Title
Development of Statistical and Deterministic Approaches to Uncertainty Quantification under Bound-to-Bound Data Collaboration

Author
Li, Wenyu

Publication Date
2021

Peer reviewed|Thesis/dissertation

Development of Statistical and Deterministic Approaches to Uncertainty Quantification under Bound-to-Bound Data Collaboration

by

Wenyu Li

A dissertation submitted in partial satisfaction of the

requirements for the degree of

Doctor of Philosophy

in

Mechanical Engineering

and the Designated Emphasis

in

Computational Data Science & Engineering

in the

Graduate Division

of the

University of California, Berkeley

Committee in charge:

Professor Michael Frenklach, Chair
Professor Jyh-Yuan Chen
Professor Lin Lin

Spring 2021

Development of Statistical and Deterministic Approaches to Uncertainty Quantification under Bound-to-Bound Data Collaboration

Wenyu Li

Abstract

Development of Statistical and Deterministic Approaches to Uncertainty Quantification under Bound-to-Bound Data Collaboration

by

Wenyu Li

Doctor of Philosophy in Mechanical Engineering

and the Designated Emphasis in

Computational Data Science & Engineering

University of California, Berkeley

Professor Michael Frenklach, Chair

This dissertation is focused on developing methods under the uncertainty quantification framework of Bound-to-Bound Data Collaboration (B2BDC). The framework systematically combines models and data to validate the consistency of a dataset (i.e., the collection of data and models) and generates more predictive models. Uncertainties in model parameters and experimental data are characterized by deterministic bounds and propagated to bounds of prediction uncertainty, resonating "Bound-to-Bound" in the name. Solution mapping techniques are used to create polynomial and rational quadratic surrogate models, with which advanced optimization techniques can be implemented to compute provable bounds.

The bound-form uncertainty adopted in the B2BDC framework naturally generates inequality constraints on model parameters. The collection of all the constraints, derived from prior knowledge about model parameters and from requiring model prediction within experimental uncertainty, defines a region in the model parameter space termed the feasible set. The agreement/disagreement among models and data is determined by inspecting whether there exist parameter vectors in the feasible set: The dataset is consistent if the feasible set is not empty and inconsistent otherwise. Numerically, examination of dataset consistency is accomplished by calculating a quantity termed scalar consistency measure, defined as the solution to a constrained optimization problem, and evaluating its sign. The dataset is inconsistent if the scalar consistency measure is negative and otherwise if it is positive. Prediction uncertainty is computed by finding minimum and maximum values of the prediction models in the feasible set. The constrained optimization problem is nonconvex and difficult to solve globally in general as nonlinear optimization solvers usually converge to a local optimum.

With quadratic, polynomial, and rational quadratic surrogate models, convex relaxation techniques are used to derive semidefinite programming problems whose solution can be computed efficiently and is a conservative bound on the solution of the original nonconvex problems. As a result, dataset inconsistency can be proved if the conservative bound of the scalar consistency measure is negative.

Starting from the bound-type uncertainty, more informative assumptions can be made to obtain more informative results. For example, if a prior distribution is selected to represent the prior uncertainty in model parameters and a likelihood function is selected to model the measurement error in the data, Bayesian inference produces a posterior distribution of the model parameters. Two physically inspired likelihood functions are investigated and compared in the thesis. For the likelihood functions and surrogate models considered in the thesis, the posterior distribution does not have a closed-form expression. Therefore, efficient sampling methods are developed to generate samples from the posterior distribution for further uncertainty quantification computations, for example, evaluating the uncertainty in model predictions.

A dataset can be inconsistent in practice, which implies that something is wrong with the system: the model (e.g., the model does not simulate the underlying process accurately), the data (e.g, a misreported measurement), or both. Efficient strategies for resolving dataset inconsistency are therefore necessary to use the framework. Methods motivated by physical reasoning can be advantageous since they may provide guidance on what factors cause the trouble. The vector consistency measure strategy aims to recover dataset consistency by relaxing the fewest experimental uncertainty bounds. Data points whose experimental uncertainty bounds are suggested to be changed by the solution vector are labelled as potentially suspicious to be examined further. Suspicious data points can also be determined by comparing their influence to the computed scalar consistency measure. A new method, suitable when the model is suspect, is developed in the dissertation that resolves dataset inconsistency by including a scenario-dependent discrepancy function, which modifies model output in a structured manner.

Syngas, a mixture of H_2 and CO, is a popular candidate for high efficiency power generation in hybrid turbines. A comprehensive and accurate knowledge of its combustion kinetics is necessary for designing optimal operating conditions in different applications. In one study, a B2BDC application to a syngas combustion dataset is carried out collaboratively by me and a research group in the German Aerospace Center. A syngas reaction mechanism is created by the German group with assessed uncertainty in the reaction rate parameters. A set of experimental measurements, including ignition delay times and laminar flame speeds, is collected by the German group with systematically assessed experimental uncertainty. I apply the B2BDC methods to the dataset and examine its feasible set to obtain a more predictive model of syngas combustion. In another study, I construct a different syngas combustion dataset including only ignition delay time measurements, using which the vector consistency measure method and the discrepancy function method are compared.

Contents

Contents **i**

List of Figures **iv**

List of Tables **x**

1 Introduction **1**

2 Bound-to-Bound Data Collaboration **5**
2.1 Introduction . . . 5
2.2 Setup and Nomenclature . . . 6
2.3 Prior Uncertainty of Parameters . . . 6
2.4 Dataset Consistency . . . 7
2.5 Prediction . . . 8
2.6 Vector Consistency Measure . . . 8
2.7 Numerical Implementation . . . 10
2.7.1 Surrogate Models . . . 10
2.7.2 Outer Bound with Quadratic Surrogates . . . 16
2.7.3 Outer Bound with Rational Quadratic Surrogates . . . 18
2.7.4 Outer Bound with Higher Order Polynomials . . . 20
2.7.5 Sensitivity Analysis . . . 21
2.7.6 Parameter Optimization . . . 25
2.8 Example: GRI-Mech Dataset . . . 27
2.9 Chapter Summary . . . 31

3 Statistical Analysis in Bound-to-Bound Data Collaboration **33**
3.1 Bayesian Inference . . . 34
3.2 Uniform Versus Gaussian Likelihood . . . 35
3.3 Sampling Methods . . . 36
3.4 Convergence Diagnosis . . . 41
3.5 Exploiting Sparsity and Generalization with Polynomial Surrogates . . . 43
3.6 A Toy Example . . . 44

3.7 GRI-Mech Example . . . 47
3.7.1 Hit-and-run Versus Gibbs . . . 48
3.7.2 Gaussian Versus Uniform Likelihood . . . 55
3.8 B2BDC Versus Bayesian with Uniform Likelihood . . . 62
3.9 Chapter Summary . . . 66

4 Syngas Combustion Application 67
4.1 Reaction Model . . . 67
4.2 Experimental Data . . . 68
4.3 Simulation and Surrogate Models . . . 68
4.4 Consistency Analysis . . . 70
4.5 Uncertainty Quantification . . . 72
4.6 Sampling the Feasible Set . . . 77
4.7 Reaction Model Optimization . . . 81
4.8 Chapter Summary . . . 90

5 Representation of Model Discrepancy 91
5.1 Definition of Model Discrepancy . . . 91
5.2 B2BDC with Model Discrepancy . . . 92
5.3 One-dimensional Mass-Spring-Damper System . . . 96
5.3.1 Problem Statement . . . 96
5.3.2 Dataset Consistency and QOI Prediction . . . 99
5.3.3 Posterior Bounds of Model Parameter and Discrepancy-Function Coefficients . . . 102
5.3.4 Posterior Uncertainty of Model Discrepancy . . . 106
5.3.5 Additional Constraints on Model Discrepancy . . . 107
5.4 Hydrogen Combustion Example . . . 108
5.4.1 Problem Statement . . . 108
5.4.2 Dataset Consistency and QOI Prediction . . . 112
5.4.3 Inference of Model Discrepancy . . . 113
5.5 Discrepancy As a Consistency Measure . . . 115
5.6 Chapter Summary . . . 116

6 Syngas Combustion Dataset with Discrepancy Functions 117
6.1 Experimental Data . . . 117
6.2 Simulation Model and Model Discrepancy . . . 123
6.3 Surrogate models, model and scenario parameters, and discrepancy function 123
6.4 Consistency Analysis . . . 126
6.5 Prediction . . . 128
6.6 Sensitivity Analysis . . . 130
6.7 Discrepancy Function Behavior . . . 132
6.8 Feasible Set Analysis . . . 135

6.9 Chapter Summary 141

7 Summary and Conclusions **143**

A GRI-Mech Dataset **146**

B Syngas Combustion Datasets **151**

C The MATLAB Toolbox **165**

D B2BDC Application: GRI-Mech **195**

Bibliography **199**

List of Figures

2.1 Ranked sensitivity of scalar consistency measure (SCM) inner-bound solutions with respect to the quantity of interest (QOI) and model parameter uncertainty bounds. 28
2.2 Ranked sensitivity of scalar consistency measure (SCM) outer-bound solutions with respect to the quantity of interest (QOI) and model parameter uncertainty bounds. 29
2.3 Computed prediction interval of model parameters whose posterior uncertainty is reduced compared to its prior. The blue and red vertical bars represent inner- and outer-bound solutions, respectively. 30
2.4 The ranked sensitivity of the outer-bound solution for the posterior upper bound of parameter x_{20}. 30
2.5 Leave-one-out prediction of quantities of interest (QOIs) in the GRI-Mech dataset. The black, blue, and red bars are experimental uncertainty bounds and bound-to-bound data collaboration (B2BDC) predicted inner and outer bounds, respectively. 31

3.1 Sketch plot of a scalar quadratic function $\widetilde{\mathcal{Q}}(t) = \widetilde{c}_0 + \widetilde{c}_1 t + \widetilde{c}_2 t^2$ with two distinct real roots. The solid black line represents the quadratic function and the dashed red line represents $\mathcal{Q}(t) = 0$. Roots are labeled (i) and (ii) for a negative a value and (iii) and (iv) for a positive a value. 39
3.2 Convergence test results of the hit-and-run (HR), Gibbs, and adaptive metropolis (AM) samples based on 10 Markov chain Monte Carlo (MCMC) chains. The black line is the multivariate potential scale reduction factor. The blue and green lines are the logarithmic determinants of the between-sample and within-sample covariance matrices, respectively. 45
3.3 Marginal histograms of the generated samples and computed Bound-to-Bound data collaboration (B2BDC) prediction intervals for x_1 and x_2. 46
3.4 Scatter plots of hit-and-run (HR), Gibbs, and adaptive metropolis (AM) samples and the prior $\mathcal{H}$ (shaded gray) and the feasible set $\mathcal{F}$ (shaded red). 47
3.5 Trace (blue line) and sampled autocorrelation (red line) of parameter x_{32}. The left and right columns contain results in a chain starting from an MCMC and optimized point, respectively. The top and bottom two rows are results for the hit-and-run (HR) and Gibbs samples, respectively. 49

3.6 Component-wise step sizes in the generated Markov chain Monte Carlo (MCMC) chains starting from MCMC points. The points and vertical bars are the computed means and 1σ confidence intervals. 50
3.7 Component-wise step sizes in the generated Markov chain Monte Carlo (MCMC) chains starting from optimized points. The points and vertical bars are the computed means and 1σ confidence intervals. 51
3.8 Computed multivariate potential scale reduction factors and logarithm determinants of covariance matrices V and W in HR samples. The vertical bars represent the mean and 1σ confidence interval over 10 repeated runs. The blue and green $\times$ symbols mark the cases in which the determinant is smaller than machine precision. 53
3.9 Computed multivariate potential scale reduction factors and logarithm determinants of covariance matrices V and W in Gibbs samples. The vertical bars represent the mean and 1σ confidence interval over 10 repeated runs. 54
3.10 Marginal empirical probability density function of the GRI-Mech model parameters based on samples with the uniform likelihood (red lines) and samples with the Gaussian likelihood (blue lines). All axes are scaled to the prior uncertainty range [-1, 1]. 57
3.11 Distribution of the calculated p-values of the two-sample Kolmogorov-Smirnov tests for model parameters. The red dashed vertical line indicates the 0.05 significance level. 58
3.12 Projected probability distribution function on two-dimensional model parameter pairs based on samples with the uniform likelihood (top panel) and samples with the Gaussian likelihood (second panel). All axes are scaled to the prior uncertainty range [-1, 1]. 59
3.13 Marginal empirical probability density function of 76 GRI-Mech quantity of interest predictions based on posterior samples with the Gaussian (blue line) and uniform (red line) likelihood functions. The black horizontal bar represents the experimental uncertainty bounds. 60
3.14 Distribution of the calculated p-values of the two-sample Kolmogorov-Smirnov tests for prediction quantities of interest. The red dashed vertical line indicates the 0.05 significance level. 61
3.15 Marginal histograms and Bound-to-Bound Data Collaboration posterior prediction intervals of GRI-Mech model parameters. The green histograms are based on 5×10^4 samples uniformly distributed on the feasible set. The blue and red bars are computed inner- and outer-bound intervals, respectively. All axes are scaled by the prior uncertainty range [-1, 1]. 64
3.16 Leave-one-out distribution, Bound-to-Bound Data Collaboration prediction, and experimental data bounds of 76 GRI-Mech quantities of interest. The green histograms are based on samples uniformly distributed on the feasible set. The blue, red, and black bars are the calculated inner- and outer-bound prediction intervals and experimental uncertainty bounds, respectively. 65

4.1 Distribution of the estimated fitting errors for ignition delay time and laminar flame speed quantities of interest (QOIs). 69
4.2 Ranked sensitivity of the shrunk posterior bounds (the lower or upper uncertainty bound marked red in Table 4.3) of parameters x_3, x_4, x_6, x_{10}, x_{11}, x_{17}, x_{23} and x_{24} with respect to the experimental uncertainty bounds and parameter prior bounds. The red and blue horizontal bars denote the upper and lower uncertainty bounds, respectively, of the contributing experimental uncertainty bounds or parameter prior bounds. 74
4.3 Ranked sensitivity of prediction lower bound for the four quantities of interest listed in Table 4.4 with respect to experimental uncertainty bounds and parameter prior bounds. The red and blue horizontal bars denote the upper and lower uncertainty bounds, respectively, of the contributing experimental uncertainty bounds or parameter prior bounds. 76
4.4 Convergence test results of samples from the DLR-SynG 2 feasible set. The results are based on 4×10^5 sampled points using the second half of the 10 Markov chain Monte Carlo chains. 77
4.5 Marginal histograms and Bound-to-Bound Data Collaboration predicted inner-bound (blue lines) and outer-bound (red lines) posterior intervals of model parameters. The axis limits are scaled by the prior uncertainty bounds of each x_i. 79
4.6 Observed two-dimensional correlations between model parameters (first row), between quantities of interest (second row), and between a model parameter and a quantity of interest (third row). The axis limits are scaled to the prior and experimental uncertainty bounds (including fitting error) for model parameters and quantities of interest, respectively. 80
4.7 Left: Average squared deviation of the optimized model predictions from the experimental observations. Right: Number of optimized model predictions that are outside of their experimental uncertainty bounds. Red and blue denote models computed using the DLR-SynG 1 and DLR-SynG 2 datasets, respectively. . . . 81
4.8 Relative model parameter (x) adjustments in the LS-H (left) and 1N-F (right) optimized models. Both models were computed using the DLR-SynG 2 dataset. 82
4.9 Ignition delay time data in [58, 73] simulated using the original model (black line), Varga's model (gray line), LS-H model (dotted red line), vector consistency measure (VCM) model (red dashed-dotted line), LS-F model (dashed blue line), and 1N-F model (short-dashed blue line). Symbols are experimental data with uncertainty represented by vertical bars. Black stars are quantities of interest (QOIs) in the DLR-SynG 2 dataset. Red stars are self-inconsistent QOIs; green stars are QOIs detected through VCM analysis. 83

4.10 Ignition delay time data in [54, 127] simulated using the original model (black line), Varga's model (gray line), LS-H model (dotted red line), vector consistency measure (VCM) model (dash-dotted red line), LS-F model (dashed blue line), and 1N-F model (short-dashed blue line). Symbols are experimental data with uncertainty represented by vertical bars. Black stars are quantities of interest (QOIs) in the DLR-SynG 2 dataset. Green stars are QOIs detected through VCM analysis. 84
4.11 Ignition delay time data in [65, 75] simulated using the original model (black line), Varga's model (gray line), LS-H model (dotted red line), vector consistency measure (VCM) model (dashed-dotted red line), LS-F model (dashed blue line), and 1N-F model (short-dashed blue line). Symbols are experimental data with uncertainty represented by vertical bars. Black stars are quantities of interest (QOIs) in the DLR-SynG 2 dataset. Red stars are self-inconsistent QOIs. Green stars are QOIs detected through VCM analysis. 85
4.12 Laminar flame speed data in [123] simulated using the original model (black line), Varga's model (gray line), LS-H model (dotted red line), vector consistency measure (VCM) model (dashed-dotted red line), LS-F model (dashed blue line), and 1N-F model (short-dashed blue line). Symbols are experimental data with uncertainty represented by vertical bars. Black stars are quantities of interest (QOIs) in the DLR-SynG 2 dataset. Green stars are QOIs detected through VCM analysis. 86
4.13 Laminar flame speed data in [82, 133, 131] simulated using the original model (black line), Varga's model (gray line), LS-H model (dotted red line), vector consistency measure (VCM) model (dashed-dotted red line), LS-F model (dashed blue line), and 1N-F model (short-dashed blue line). Symbols are experimental data with uncertainty represented by vertical bars. Black stars are quantities of interest (QOIs) in the DLR-SynG 2 dataset. Green stars are QOIs detected through VCM analysis. 87
4.14 Laminar flame speed data in [43, 86, 66, 44] simulated using the original model (black line), Varga's model (gray line), LS-H model (dotted red line), vector consistency measure (VCM) model (dashed-dotted red line), LS-F model (dashed blue line), and 1N-F model (short-dashed blue line). Symbols are experimental data with uncertainty represented by vertical bars. Black stars are quantities of interest (QOIs) in the DLR-SynG 2 dataset. 88
4.15 Ignition delay time predicted with the original model (black line), Varga's model (red), vector consistency measure (VCM) model (blue), LS-H model (green), LS-F model (orange), 1N-F model (purple), and bound-to-bound data collaboration (B2BDC) prediction interval (vertical black bar). 89

5.1 Sketch plot of the mass-spring-damper system. 97
5.2 The true model solution $z^*(k^*, t)$, the inadequate model solution $z(k^*, t)$ and the model discrepancy function $\delta^*(t) = z^*(k^*, t) - z(k^*, t)$. 98

5.3 Computed QOI prediction intervals for the mass-spring-damper example using the true model. The horizontal red dashed lines mark the displacement computed with the true model and true calibration parameter value, $z^*(k^*, t)$. The vertical blue solid lines designate the B2BDC predicted intervals, computed by solving optimization problems in Equations (2.7) and (2.8). 99
5.4 Predicted quantity of interest intervals at t = 1.5, 3.2 and 4. The horizontal red dashed lines are the displacement derived with the true model and evaluated at the true model parameter value, $z^*(k^*, t)$. The vertical blue solid lines designate the B2BDC predicted intervals, computed by solving the optimization problems in Equations (5.8) and (5.9). The ×'s mark dataset inconsistency. 101
5.5 Displacements computed with the true (left) and the inadequate (right) models for various k values drawn from its prior interval [0.2, 0.3] (cyan regions). The black vertical bars are observation quantity of interest bounds. The red dashed line is one feasible realization of $z(k, t) + c_0$ with $k = 0.2$ and $c_0 = 0.005$. The insets are zoomed on the last two observations for $t \in [2.3, 2.8]$. 104
5.6 Joint feasible set of k, c_0, and c_1 and its 2-dimensional projections (colored in red), computed with linear δ and $\epsilon = 0.1$. The color bar in the upper-left figure color codes the values of c_1. The axes' limits of k, c_0, and c_1 were set to their calculated posterior uncertainty bounds. 105
5.7 Uncertainty bounds of quadratic and cubic δ (blue lines). The red line is the true model discrepancy δ^*. 106
5.8 Interpolation and extrapolation intervals computed by solving Equations (5.8) and (5.9) with the extra constraint defined in Equation (5.20) for cubic δ at $\epsilon = 0.1$. The red dashed lines are the true prediction values. 108
5.9 QOI prediction intervals for the five cases in table 5.7. The black dashed lines are the true QOI values. The predicted QOI intervals are drawn as blue ($\epsilon = 0.01$) and red ($\epsilon = 0.005$) vertical lines. The red ×'s mark dataset inconsistency. . . . 113
5.10 The sign of model discrepancy function in the scenario region $(s_2, s_3) \in [-1, 1]^2$ for temperature values 1600, 1370 and 1200 K. The grey region represents scenarios where $U_\delta < 0$ and the white one indicates where the interval $[L_\delta, U_\delta]$ contains 0. The black points are design scenarios in Table 5.4. 115

6.1 Histograms of the estimated fitting error in the training and test sets of quantities of interest. 125
6.2 Percentage of dataset that remains consistent after adding a randomly selected group of quantities of interest from the test set. The computed results are based on 100 repeated runs. 130
6.3 Discrepancy function $\delta(s_1, s_3; 4, 5, 4)$ in the normalized scenario region $[-1, 1]^2$. Black points represent the scenario conditions of quantities of interest in the dataset. 132
6.4 Discrepancy function $\delta(s_1 - s_3; 4)$ in the projected s_2-s_3 space at fixed s_1 values. Black points represent scenario conditions of quantities of interest in the dataset. 133

6.5 Discrepancy function $\delta(s_1 - s_4; 3)$ in the projected s_2-s_3 space at fixed s_1-s_4 value pairs. Black points represent scenario conditions of quantities of interest (QOIs) in the dataset. 134
6.6 Discrepancy function $\delta(s_1 - s_5; 2)$ in the projected s_2-s_3 space at fixed $\{s_1, s_4, s_5\}$ value sets. Black points represent scenario conditions of quantities of interest (QOIs) in the dataset. 135
6.7 Bound-to-bound data collaboration predicted outer-bound intervals for reaction rate multipliers whose posterior uncertainty is smaller than the prior uncertainty. 136
6.8 Estimated two-sigma confidence interval truncated by prior uncertainty bounds for reaction rate multipliers whose posterior uncertainty is smaller than the prior uncertainty. 137
6.9 Estimated marginal probability density for multipliers λ_3, λ_6, λ_7, λ_{11}, λ_{12}, λ_{22}. The color codes are red lines: $\delta(s_1, s_3; 4, 5, 4)$; blue lines: $\delta(s_1 - s_3; 4)$; green lines: $\delta(s_1 - s_4; 3)$; cyan lines: $\delta(s_1 - s_5; 2)$; and black lines: D_{VCM}. 138
6.10 Estimated two-dimensional probability density functions in the λ_6-λ_7 and λ_{11}-λ_{12} space based on samples generated with D_{VCM}. The axis limits are the prior uncertainty bounds. 139
6.11 Estimated two-dimensional probability density functions in the λ_6-λ_7 space based on samples generated using a (a) dataset with $\delta(s_1, s_3; 4, 5, 4)$, (b) dataset with $\delta(s_1 - s_3; 4)$, (c) dataset with $\delta(s_1 - s_4; 3)$, and (d) dataset with $\delta(s_1 - s_5; 2)$. The axis limits are the prior uncertainty bounds. 140
6.12 Estimated two-dimensional probability density functions in the λ_{11}-λ_{12} space based on samples generated with a (a) dataset with $\delta(s_1, s_3; 4, 5, 4)$, (b) dataset with $\delta(s_1 - s_3; 4)$, (c) dataset with $\delta(s_1 - s_4; 3)$, and (d) dataset with $\delta(s_1 - s_5; 2)$. The axis limits are the prior uncertainty bounds. 141

C.1 The class diagram of the B2BDC toolbox. 166

D.1 Procedures of application of Bound-to-Bound Data Collaboration to engineering problems. 196

List of Tables

3.1 Averaged full-dimensional step sizes, consumed computer processing unit (CPU) time of generating 10^4 samples, and ratio of feasibility evaluation using modified and brute-force searching algorithms. 51

4.1 Eight self-inconsistent quantities of interest (QOIs) in the DLR-SynG 0 dataset 70
4.2 Calculated vector consistency measure result for DLR-SynG 1 dataset. 71
4.3 Reaction rate multipliers with posterior uncertainty bounds in DLR-SynG 2 that are different from their prior bounds. 72
4.4 Prediction intervals of the four selected quantities of interest. The units for ignition delay time and flame speed measurements are millisecond and centimeter per second, respectively. 75

5.1 Results of the dataset consistency analysis 100
5.2 Projection of the joint feasible set, computed with the inadequate model given in Equation (5.17) and different model discrepancy functions defined in Equation (5.19), onto coordinate directions of model parameter k and discrepancy-function coefficients $\{c_i\}_{i=1}^{n}$, as well as computed volume ratio of the joint feasible set to the box made of the projected intervals. The symbol $\varnothing$ represents an empty posterior uncertainty due to dataset inconsistency. 102
5.3 Detailed and reduced H_2-O_2 reaction sets and associated parameters of the rate coefficients, $AT^n e^{-E/RT}$, in the units of cm^3, mol, s, cal, K (from [135]). 110
5.4 Design conditions for the training data. 111
5.5 Tested model discrepancy functions. 111
5.6 Results of dataset consistency and the distance between true model parameter value λ^* and the feasible set. 112
5.7 Scenario parameter values for model prediction. 113
5.8 Projection of the joint feasible set, computed with linear δ at $\epsilon = 0.01$, onto coordinate directions of each discrepancy-function coefficient. 114

6.1 Range of the initial temperature, pressure, concentration ratio of H_2 to CO and syngas to O_2, temperature increment, and experimental measurements in the training and test datasets. 118
6.2 Summary of ignition delay time data of the training set. 118

6.3 Summary of ignition delay time data of the test set. 122
6.4 Suggested changes in experimental uncertainty bounds from the vector consistency measure (VCM) computation to obtain a consistent dataset. 127
6.5 Dataset consistency with discrepancy function $\delta(s; n_1, n_3, m)$ in scenario parameters s_1 and s_3. 127
6.6 Dataset consistency with various choices of scenario parameter combinations and the corresponding discrepancy functions. 128
6.7 Number of valid predictions computed using a discrepancy function $\delta(s; n_1, n_3, m)$ with the scenario parameters s_1 and s_3. 128
6.8 Number of valid predictions computed using a discrepancy function in three, four, and five scenario parameters. 129
6.9 Generalized 2-norm of the partial derivative function over the normalized cube. 131
6.10 Generalized 2-norm of the partial derivative function over the scenarios in the training set. 131
6.11 Reactions whose estimated posterior confidence interval in the multipliers are different for D_{VCM} compared to using discrepancy functions. 137
6.12 Reactions whose multipliers appear most frequently in the surrogate models as active parameters for the 112 training quantities of interest. 138

A.1 Quantities of interest in the GRI-Mech dataset [113]. Measurements from the same research institute are grouped together. 146
A.2 Active model parameters in GRI-Mech dataset [113] 147

B.1 The initial syngas combustion mechanism and associated reaction rate constants [110], $k = AT^n\exp(-E_a/T)$ in units of cm^3, mol, s, and K. 151
B.2 Prior uncertainty range of the reaction rate multipliers [110]. 154
B.3 List of ignition delay time quantities of interest and their estimated uncertainty. T_5 and P_5 are the initial temperature and pressure behind the reflected shock wave [110]. 155
B.4 List of laminar flame speed quantities of interest and their estimated uncertainty [110]. T_0, P_0 and ϕ are the initial temperature, pressure and equivalence ratio of the mixture. 159
B.5 The initial syngas combustion mechanism and associated reaction rate constants [110], $k = AT^n\exp(-E_a/T)$ in units of cm^3, mol, s, and K. 160
B.6 Prior uncertainty range of the reaction rate multipliers[110]. 163

Acknowledgments

I would like to thank the University of California at Berkeley, the faculty and staff from the Mechanical Engineering Department, my classmates, colleagues and many friends that make my years here so colorful and meaningful. It is impossible without the encouragement from these beloved people to keep myself always fueled with eagerness for new things and not giving up in front of difficulties.

I would like to acknowledge my sincere gratitude for my advisors, Professor Michael Frenklach and Professor Andrew Packard. Not only did they teach me the skills and expertise for the research, but also they showed me what a respectful thinker really is. I still remember, when I was frustrated as a project seems never to end and new questions kept coming out, Michael taught me that every research is an ongoing work and I should know how to take a break and summarize the things I have learned. Michael also taught me to write a paper and make a presentation with a story in mind. Andy is truly a special person and will be remembered forever. Although suffering from an aggressive cancer, he fought very bravely until the last minute. I remember that every time I presented my results confidently during the group meeting, Andy was able to make some insightful comments I never thought about.

I would also give special thanks to the best parents in the world! They have been supporting and believing in me throughout the graduate study. They have always been patient and willing to listen. They consoled my homesick and distress emotions with love and encouragement.

This work was supported by U.S. Department of Energy, National Nuclear Security Administration, under Award Number DE-NA0002375.

Chapter 1

Introduction

During the past few decades, computational capabilities and data availability have substantially increased in many scientific and engineering fields. Physics-derived models are used more frequently as the prototype of a simulation program. It is well known that errors and uncertainty in the solution result from converting a mathematical model to a programmable simulation model. For instance, discretization errors are produced when a derivative is replaced by finite difference. Moreover, approximations made to mathematical models in constructing simulation models add another level of uncertainty to the solution. Such approximations can be motivated by limited computation resources, lack of knowledge regarding some part of the underlying process, and so on.

Consider an illustrative example of a box sliding horizontally on a rough surface with an initial velocity of v_0 and an initial position at x_0. We are interested in the evolution of the velocity and position of the box. A physical model can be derived following Newton's laws of motion, Newtonian friction and the assumption that the friction force is the only force on the box along the direction of motion. The resulting mathematical model is as follows:

$$\begin{aligned} \frac{dv}{dt} &= -\text{sign}(v)\mu mg \\ \frac{dx}{dt} &= v, \end{aligned} \tag{1.1}$$

where $\text{sign}(v)$ is the sign of the velocity, m the mass of the box, g the acceleration due to gravity, and μ the coefficient of friction. We can measure m and g well, leaving only μ unknown. If the unknown model parameter μ is specified, we can integrate the differential equation system analytically to find $x(t)$.

It is difficult to estimate μ from first principles. Nonetheless, a scientist or engineer can design an experiment that measures this coefficient. The experiment may be subject to measurement error, but the uncertainty can be reduced by repeating the measurement many times, based on the law of large numbers. However, we may want to simulate μ for a different surface. The coefficient of friction varies as the roughness and material of

the surface change. Furthermore, the coefficient may also depend on other factors, such as temperature. If we want to use the model in many different simulation conditions, the strategy of measuring its value through designed experiments becomes impractical. Not only it is impossible to experiment with every potential simulation condition, but the functional form of the dependency is also rarely known. As such, it is more appropriate to accept the uncertainties in the model and solution and develop systematic approaches to quantify them. For example, we can inspect the model output at various model parameter values and evaluate its agreement with the measured data. The data can help to rule out parameter values that produce outputs that are too different from the measured data, and we are left with a smaller set of parameter values. It is also possible that none of the parameter values can generate a satisfactory agreement with the data. In the latter case, we consider the model to be proved inaccurate, and a new model must be derived.

Recently, the growing demand for predictive and validated models with quantifiable uncertainty has motivated the development of an active research area termed uncertainty quantification (UQ) [88]. Two principal objectives of UQ considered in this dissertation are inference of model parameters using a set of data (the *training* set), also known as the inverse or calibration problem, and model prediction outside such a set with quantified uncertainty.

Theories and methods have been developed from both statistical and deterministic perspectives. From a statistical perspective, for instance, the Bayesian inference framework [38], a prior distribution is selected to represent the uncertainty in model parameters, a likelihood function is derived to model the probability of the observed data for any fixed set of parameter values, and a posterior distribution characterizing the updated uncertainty in model parameters is produced using Bayes' theorem. Uncertainty in the prediction of other quantities depending on the model parameters is inferred via statistical approaches.

From a deterministic perspective, for example, the Bound-to-Bound Data Collaboration (B2BDC) method [23, 34, 35, 106] employed throughout this thesis, a prior region defined by inequality constraints represents the initial uncertainty of the model parameters. For the included data, an interval is assessed for each measurement as its uncertainty range. The data collaboration process combines the prior parameter uncertainty and data uncertainty to form a region in the parameter space. This region is defined by inequality constraints and is referred to as the feasible set that quantifies the updated uncertainty in the model parameter space. The prediction of other quantities is computed by solving constrained optimization problems over the feasible set. Solution mapping and advanced optimization techniques are implemented to circumvent the difficulty in finding a globally optimal solution to NP-hard nonconvex optimization problems. More details are given in Chapter 2.

The two perspectives and the methods derived under them address essentially the same problems while implementing different assumptions and numerical techniques. Remarked in the work comparing the B2BDC method and a Bayesian inference method [33], interpretation and comparison of the results from different methods are closely connected to the

assumptions made therein. In Chapter 3, I compare two likelihood functions inspired by realistic experimental conditions, which are based on the assumptions that the measurement error is from a Gaussian or uniform distribution, respectively. Since the resulting posterior distributions do not have a closed-form expression, efficient sampling methods are implemented to generate samples for the comparison. Similar to the setup in [33], I compare B2BDC computations to Bayesian inference with the uniform likelihood function using the same 102-dimensional natural gas combustion example. The analysis provides further insights regarding the similarities and differences between the two specific methods, as only the Gaussian likelihood function was considered in [33].

In addition to Bayesian calibration methods, B2BDC also shares conceptual similarities with Bayesian history matching [17] and methods under the set-membership framework [16, 37, 80, 105]. Bayesian history matching retains a probabilistic interpretation of the data and defines a nonimplausible region in the parameter space that contains all acceptable parameter vectors. Although Bayesian history matching and B2BDC both seek a region containing valid parameter vectors, they have some differences. Bayesian history matching uses stochastic emulators and improves the quality of the emulators through iterative updates of the nonimplausible region, whereas B2BDC employs polynomial response surfaces and focuses primarily on the evaluation of uncertainty in predictions [34, 35].

Similar to the setup in B2BDC, the set-membership framework in robust control describes uncertainty in prior information and data by constraints. Methods developed under this framework also formulate the estimation/prediction of quantities of interest (QOIs) as regions defined by inequality constraints or solutions to optimization problems [80, 128]. However, these methods differ from B2BDC in that they often pursue a simply shaped approximation of the formed complex regions (e.g., a bounding ellipsoid [25, 105] or minimum-volume bounding parallelotope [16]). In contrast, B2BDC uses polynomial surrogate models and handles the resulting nonconvexity through convex relaxation, leading to global guarantees on optimality [106]. A previous analysis using B2BDC indicates that approximation of the feasible set by a bounding ellipsoid or polytope may lead to overly conservative prediction results [100, 101].

In the B2BDC framework, an empty feasible set identifies a disagreement among the models and data and deems a dataset (i.e., the collection of models and data with assessed uncertainty) inconsistent. Dataset inconsistency can be and often is encountered based on our experience with realistic applications. We must resolve the dataset inconsistency before moving to other computations that require a nonempty feasible set, for example, UQ of QOI predictions. For an inconsistent dataset, three scenarios are possible: the models are accurate but the data are flawed; the data are accurate, but the models are inadequate; both the models and data are inaccurate. Motivated by the first scenario, strategies are developed to resolve dataset inconsistency by finding suspicious data based on computations of the scalar and vector consistency measure (VCM) [23, 52], followed by reexamining their estimated uncertainty bounds [23] or removing them from the dataset [110]. In Chapter 5, I develop

a new method, suitable when the model is inadequate, that resolves dataset inconsistency by adding a scenario-dependent term to the model output. The discrepancy function is expressed as a linear combination of basis functions, whose coefficients are assumed uncertain. The definition of the feasible set and equations for B2BDC UQ computations are modified accordingly. Strategies designed for the third scenario are a subject for future work.

The method of B2BDC has been successfully applied in several domains, including combustion science [23, 28, 35, 56, 99, 110], engineering [92], atmospheric chemistry [112], quantum chemistry [21], and system biology [22, 24]. In Chapter 4, I apply the B2BDC methods to a syngas (a mixture of H_2 and CO) combustion system. The reaction mechanism and used experimental data are selected by a collaborative research group from the German Aerospace Center (DLR) with systematically assessed uncertainty. The initial dataset inconsistency is resolved by removing VCM identified data. For the consistent dataset, I examine the feasible set based on both B2BDC predictions and samples from it. Optimized reaction models are computed and compared to a well-established reaction model over an extensive set of simulation conditions.

Different from the strategies of resolving dataset inconsistency by finding suspicious data, the method of including a discrepancy function can obtain dataset consistency without revising the data. In Chapter 6, I construct a different syngas combustion dataset with a modified reaction mechanism reported from the DLR group. I compare the two approaches by applying them to the initially inconsistent dataset and examining the obtained feasible sets. The results reveal some interesting distinctions between the two approaches.

Chapter 2

Bound-to-Bound Data Collaboration

2.1 Introduction

Experimentation is arguably the most direct method for conducting scientific research on a physical process because it reflects the underlying truth with or without knowing the physics behind it. Models derived from either first principles or empirical domain insight can be used to simulate the physical process systematically, for example, a set of differential equations whose solution completely characterizes all the quantities of interest (QOIs) the researcher is interested in. In certain situations, an analytical solution exists. However, a numerical approach is more frequently implemented to obtain a solution using a computer program.

In this dissertation, the models refer specifically to computer programs that output a solution for a given set of input conditions. The model is further assumed to be deterministic, meaning that the same solution is obtained when repeatedly running the program with the same input conditions. As valuable as experimental data are, they can also be challenging and expensive to obtain. Therefore, to improve our knowledge about the underlying physical process (i.e., the models in the current context), the development of a systematic method that uses the measured data effectively and efficiently is critical. During the process, uncertainties in the models, which can stem from compromises between the high-fidelity theory and computational feasibility or simply a lack of knowledge, must be addressed properly. Bound-to-Bound Data Collaboration (B2BDC) is an optimization-based deterministic framework that systematically combines models and experimental data with quantified uncertainty to produce more predictive models. In this chapter, the basic components of the B2BDC framework are presented, which were developed by our research group [23, 34, 35, 52, 106].

2.2 Setup and Nomenclature

A QOI is defined as a scalar quantity that is directly measured in experiments or can be deduced from experimental measurements. Each QOI, denoted by index e, is assumed to have a nominal value d_e and an assessed uncertainty. The nominal value is a point estimate of the QOI, for example, the reported experimental measurement. The uncertainty is characterized by an interval with its lower and upper bounds denoted by L_e and U_e, such that $d_e \in [L_e, U_e]$. A model $M_e(x)$ is assumed to be given for the eth QOI, which depends on a set of model parameters denoted by $x \in \mathbb{R}^n$. A prior uncertainty region of the parameter set x based on domain knowledge is given and denoted as $\mathcal{H}$. For a QOI, the nominal value and its evaluated uncertainty bounds, simulation model, and prior uncertainty of the model parameters form a *dataset unit*. The collection of all dataset units in a B2BDC analysis is referred to as a *dataset*.

The *feasible set*, denoted by $\mathcal{F}$, is defined for a dataset as

$$\mathcal{F} = \{x \mid x \in \mathcal{H},\ L_e \le M_e(x) \le U_e,\ e = 1, 2, \ldots, N\}. \tag{2.1}$$

The inequalities in Equation (2.1) are termed *model-data constraints* because they restrict the model output of points in the feasible set to be within the experimental uncertainty bounds. The feasible set represents our improved knowledge about the analyzed system as a smaller, or at least not larger, region in the parameter space compared to $\mathcal{H}$. The feasible set is an essential component in the B2BDC framework because most uncertainty quantification (UQ) computations rely on solving optimization problems over this region.

2.3 Prior Uncertainty of Parameters

The prior uncertainty region $\mathcal{H}$ is assumed to be a bounded polytope (i.e., a bounded region defined by a finite set of linear inequalities in the model parameter space):

$$\mathcal{H} = \{x \mid l_i \le a_i^T x \le u_i,\ i = 1, 2, \ldots, m\}, \tag{2.2}$$

where l_i and u_i are finite numbers. Each of the m linear inequalities is represented as two-sided in Equation (2.2) to clarify that $\mathcal{H}$ is bounded. In practice, a one-sided inequality can be converted to the two-sided form by solving a linear programming (LP) problem [8]. For example, suppose the prior uncertainty region is characterized as a collection of one-sided inequalities:

$$\mathcal{H} = \{x \mid a_j^T x \le u_j,\ j = 1, 2, \ldots, \hat{m}\}. \tag{2.3}$$

To calculate the lower bound associated with a_j, the following LP problem is solved:

$$\begin{aligned} l_j = \underset{x}{\text{minimize}} \quad & a_j^T x \\ \text{subject to} \quad & a_j^T x \le u_j,\ j = 1, 2, \ldots, \hat{m}. \end{aligned} \tag{2.4}$$

The simplest case is when $\{a_i = \mathbf{1}_i\}_{i=1}^n$, where $\mathbf{1}_i$ is the ith standard basis vector. In such a case, the prior uncertainty region is an n-dimensional orthotope:

$$\mathcal{H} = \{x \mid l_i \leq x_i \leq u_i,\ i = 1, 2, \ldots, n\}. \tag{2.5}$$

An orthotope $\mathcal{H}$ implies that the analyst determines the uncertainty interval in each model parameter independently, whereas the polytope $\mathcal{H}$ can include knowledge coupling multiple parameters. A potentially more accurate characterization of $\mathcal{H}$ can be achieved by replacing the linear form in Equation (2.2) with more flexible nonlinear forms (e.g., quadratics or higher-order polynomials). However, we deliberately restrict ourselves to the linear form in Equation (2.2) because (1) we often need to generate optimal design points from the prior uncertainty region and significantly more efficient sampling methods are available for an orthotope or a polytope $\mathcal{H}$. (2) Moreover, prior uncertainty assessment represented by nonlinear inequalities can always be included in the B2BDC analysis as model-data constraints.

2.4 Dataset Consistency

Whether the feasible set is empty or not classifies the analysis into two distinct categories. This motivated the introduction of *dataset consistency*: a dataset is termed consistent if its feasible set is not empty and is inconsistent otherwise [23]. Theoretically, we expect the feasible set to converge to a nonempty region as data are increasingly included if the models simulate the QOIs reasonably well and if the uncertainty assessments for the data and model parameters are accurate. However, an inconsistent dataset is not uncommon in realistic B2BDC applications. Dataset inconsistency is strong evidence for a disagreement among the model and the data, which must be resolved before carrying out further UQ computations. Therefore, the determination of dataset consistency is always the first step in a B2BDC analysis.

A constrained optimization problem was formulated in [23] to determine dataset consistency, which is given in Equation (2.6):

$$\begin{aligned} C_{\mathrm{D}} = \underset{x,\,\gamma}{\text{maximize}} \quad & \gamma \\ \text{subject to} \quad & l_i \leq a_i^T x \leq u_i,\ i = 1, 2, \ldots, m \\ & L_e + (d_e - L_e)\gamma \leq M_e(x) \leq U_e - (U_e - d_e)\gamma, \\ & e = 1, 2, \ldots, N. \end{aligned} \tag{2.6}$$

The maximized quantity C_{D} is referred to as the scalar *consistency measure* (SCM). It quantifies the maximal amount of relative change that all model-data constraints can afford with respect to the nominal values for any model parameter vector from the prior uncertainty region $\mathcal{H}$. When C_{D} is positive, a model parameter vector exists that satisfies all model-data constraints with tightened uncertainty bounds. Therefore, at least one model parameter vector exists that satisfies all model-data constraints with the original uncertainty bounds,

and the dataset is consistent. The dataset is inconsistent when C_{D} is negative. In that situation, the magnitude of C_{D} is the smallest amount that all model-data constraints must be relaxed to achieve a nonempty feasible set. A model parameter vector in the feasible set is equivalently referred to as a *feasible point* in this dissertation.

2.5 Prediction

When the dataset is consistent, the feasible set represents our improved knowledge about the model parameters and the underlying system after taking advantage of the data collaboration process. Uncertainty in predictions of other QOIs of the system is therefore quantified based on the feasible set. In B2BDC, prediction uncertainty is characterized as an interval, similar to that estimated for QOIs in the dataset. The simulation model for the predicted QOI is denoted by $M_p(x)$, and the prediction interval is denoted by $[L_p,\, U_p]$. The uncertainty bounds of the interval, L_p and U_p, are calculated by solving the following minimization and maximization problems [35]:

$$\begin{aligned} L_p = \underset{x}{\text{minimize}} \quad & M_p(x) \\ \text{subject to} \quad & x \in \mathcal{H}, \\ & L_e \le M_e(x) \le U_e, \quad e = 1, 2, \ldots, N. \end{aligned} \tag{2.7}$$

and

$$\begin{aligned} U_p = \underset{x}{\text{maximize}} \quad & M_p(x) \\ \text{subject to} \quad & x \in \mathcal{H}, \\ & L_e \le M_e(x) \le U_e, \quad e = 1, 2, \ldots, N. \end{aligned} \tag{2.8}$$

The meaning of the methodology, B2BDC, is now clear: the bounds in the experimental data and parameters are used collaboratively to calculate the bounds in QOI predictions. For the prediction interval, we are interested in quantifying the range of the QOI predictions and do not intend to make further comparisons among values within the interval without additional information.

2.6 Vector Consistency Measure

When a dataset is inconsistent, the analysis indicates that something is wrong with the dataset, and we want to have systematic and efficient approaches to resolve dataset inconsistency. Based on the computation of SCM, two solutions are available. (1) We can relax all model-data constraints, as suggested by the calculated SCM, or (2) we can remove some "offending" experimental data whose model-data constraints have larger impact on the calculated SCM. The impact is assessed by sensitivity coefficients, whose calculations are given in Section 2.7.5. The former strategy has the drawback that the scalar quantity

C_{D}, by its definition in Equation (2.6), only represents the amount of bound expansion needed to obtain a feasible point for the most "inconsistent" datum and lacks QOI-specific information. In addition, this strategy usually results in a very small feasible set (sometimes a single feasible point in the feasible set), which may lead to some numerical difficulties in the following UQ computations.

The latter strategy can be effective when inconsistency is caused by a few outliers as in the case of the GRI-Mech dataset presented in Section 2.8 [23]). When the dataset is massively inconsistent like the DLR-SynG datasets discussed in Chapter 4, this strategy may require tedious iterations without guarantee of any optimality of the solution [52]. For example, the calculated C_{D} usually has a relatively high sensitivity with respect to a few data. The analyst decides empirically which QOIs to remove based on the sensitivity result. For instance, one can choose to remove the QOI with the highest sensitivity value, calculate C_{D} for the new dataset, and then repeat the process until dataset consistency is obtained. The strategy quickly becomes intractable if the dataset is massively inconsistent and many iterations are required [52].

Motivated by the observed issues, another numerical quantity referred to as the *vector consistency measure* (VCM) was introduced [52]. Let us consider one of the most general formats of the VCM derived in [52], which is defined by the optimal value of the following optimization problem:

$$
\begin{aligned}
V_{\|\cdot\|_1} = \underset{x,\,\Delta_L,\,\Delta_U,\,\delta_l,\,\delta u}{\text{minimize}} \quad & \|\Delta_L\|_1 + \|\Delta_U\|_1 + \|\delta_l\|_1 + \|\delta_u\|_1 \\
\text{subject to} \quad & l_i - w_l^i \delta_l^i \le a_i^T x \le u_i + w_u^i \delta_u^i, \\
& i = 1, 2, \ldots, m, \\
& L_e - W_L^e \Delta_L^e \le M_e(x) \le U_e + W_U^e \Delta_U^e, \\
& e = 1, 2, \ldots, N,
\end{aligned}
\tag{2.9}
$$

where Δ_L, Δ_U, δ_l, and δ_u are relaxation vectors and W_L, W_U, w_l, and w_u are associated weights reflecting the subjective opinion of the analyst.

Compared to the SCM, the solution vectors to problem (2.9) provide a detailed resolution of constraint-specific relaxations over uncertainty bounds of experimental data and model parameters that can regain dataset consistency. The use of an L1 norm objective function is a well-known heuristic strategy to obtain a sparse solution [8]. In other words, it provides an approximate solution to the problem of how to regain dataset consistency with the fewest nonzero relaxations. With the solution vector, we identify suspicious uncertainty estimates in experimental data and model parameters as those associated with nonzero relaxations. We can place subjective confidence in certain data by specifying nonuniform weight vectors. For example, the assignment of zero values to w_l and w_u results in complete faith in the estimated uncertainty of model parameters. In that situation, a consistent dataset is obtainable in a single step by removing the QOIs with a nonzero relaxation.

2.7 Numerical Implementation

Thus far, we introduced pertinent nomenclatures in B2BDC, defined the feasible set, and formulated the optimization problems designed for computing prediction intervals for an unmeasured QOI and SCM and VCM of the dataset. In this section, we provide the details about the numerical techniques involved in fulfilling the B2BDC machinery.

2.7.1 Surrogate Models

In many scientific applications, the models used to simulate the underlying process can be quite complex (e.g., a system of differential equations). As a result, the evaluation of the model for any given instance of the model parameters can be computationally expensive. Unfortunately, computations in B2BDC often require a decent number of model evaluations, for example, solving the optimization problems constructed in the previous sections. In addition, the optimization problems are mostly nonconvex and NP-hard to solve numerically with general forms of the model. To alleviate these two difficulties, surrogate models are generated and used to replace the original models in the computations.

A surrogate model, denoted by $\mathcal{S}$, can be viewed in general as a cheaper simulator for the original model. It approximates the model output with reasonable accuracy in a specified parameter region and has a shorter runtime. The core technique involved is referred to as *Solution Mapping* [32, 26], which includes running the original model at the designed parameter points followed by fitting the numerical results with an algebraic function. In the context of B2BDC, the implemented surrogate models are classified to three cases: (1) quadratic models, (2) rational quadratic models, and (3) higher-order polynomial models. The reasons behind the classification become clearer after reading the following subsections, where the technical details about the strategies of circumventing the NP-hard optimization problem are presented for different surrogate models.

The procedures for fitting a surrogate model include active parameter selection, design point generation, and model coefficient calculation. The parameter vector x defined for the feasible set and dataset represents the union of model parameters from all models included in the analysis. A particular model may depend on a subset of x, whose influence on the simulated QOI value is substantially stronger than other model parameters due to the effect sparsity [6, 84]. Model parameters in this subset are referred to as *active parameters*. The number of coefficients in a surrogate model and the number of design points are reduced if fitting the surrogate model in the potentially lower-dimensional active parameter space. For the following discussion, the surrogate model is constructed over the prior uncertainty region $\mathcal{H}$, an orthotope (2.5). The space-filling designs were employed in the present study, the Latin hypercube sampling [76], and the Sobol quasi-random sequence [9].

To determine the active parameters for a model, a set of design points are generated from $\mathcal{H}$ using the space-filling design, and the original model is evaluated at these points. A

linear model $\mathcal{S}_l$ is calculated using the least squares regression such that

$$\mathcal{S}_l = \sum_{i=1}^{n} c_i x_i + c_0. \tag{2.10}$$

The computed coefficients define impact factors [36]:

$$\mathrm{IF}_i = |c_i| \cdot (u_i - l_i) = |c_i| \cdot \Delta x_i. \tag{2.11}$$

The coefficients c_i and the impact factors IF_i can be interpreted as the estimated partial derivative with respect to x_i and the change in model output if varying x_i alone from its lower bound to its upper uncertainty bound. Active parameters are selected by screening the ranked impact factors with a preset threshold (e.g., 5% of the largest impact factor or 10% of length of the associated experimental uncertainty interval).

Once the active parameters are selected, a polynomial surrogate model with n_p terms in the active parameter space can be expressed as follows:

$$\mathcal{P}(x_a) = \sum_{i=1}^{n_p} c_i \mathcal{M}_i(x_a), \tag{2.12}$$

where x_a is the active parameter vector and $\mathcal{M}(x_a)$ is a monomial. New design points are then generated in the active parameter space, with the nonactive parameters not fixed at selected nominal values. A rule of thumb is to set the number of design points at least 2 times the number of monomials in the surrogate model. However, it is beneficial to use a larger number of designs when affordable (e.g., more than 10 times the number of monomials in the surrogate model). A training basis matrix X with n_s design points is defined as follows:

$$X = \begin{bmatrix} \mathcal{M}_1(x_{a,1}) & \mathcal{M}_2(x_{a,1}) & \cdots & \mathcal{M}_{n_p}(x_{a,1}) \\ \mathcal{M}_1(x_{a,2}) & \mathcal{M}_2(x_{a,2}) & \cdots & \mathcal{M}_{n_p}(x_{a,2}) \\ \vdots & \vdots & \ddots & \vdots \\ \mathcal{M}_1(x_{a,n_s}) & \mathcal{M}_2(x_{a,n_s}) & \cdots & \mathcal{M}_{n_p}(x_{a,n_s}) \end{bmatrix} \tag{2.13}$$

where $x_{a,j}$ is the subset of the jth design point projected on the active parameter space. A training prediction vector Y is defined as follows:

$$Y = \begin{bmatrix} M(x_1) \\ M(x_2) \\ \vdots \\ M(x_{n_s}) \end{bmatrix}, \tag{2.14}$$

where $M(x_j)$ is the model output with the jth design point.

The coefficients of the surrogate model are computed by minimizing the error measure between the prediction vector Y and the surrogate model output $\hat{Y} = Xc$ over the training data, where c is the coefficient vector. Norm-based measures are used in B2BDC, such that the obtained surrogate model minimizes the L2 norm or the L-infinity norm of the error vector. To minimize the L2 norm of the error, the following optimization problem is solved:

$$c^* = \underset{c}{\operatorname{argmin}} \quad \frac{1}{2}(Xc - Y)^T(Xc - Y), \tag{2.15}$$

which has a well-known analytic solution $c^* = (X^TX)^{-1}X^TY$ that can be calculated very efficiently. To minimize the L-infinity norm of the error, the following optimization problem is solved:

$$c^* = \underset{c}{\operatorname{argmin}} \quad |Xc - Y|_{\text{inf}}. \tag{2.16}$$

Problem (2.16) is equivalent to

$$\begin{aligned} c^* = \underset{c,\,t}{\operatorname{argmin}} \quad & t \\ \text{subject to} \quad & X_{i.}c - Y_i \le t \\ & -(X_{i.}c - Y_i) \le t,\ i = 1, 2, \ldots, n_s, \end{aligned} \tag{2.17}$$

where $X_{i.}$ represents the ith row in matrix X. The optimization problem (2.17) is an LP problem and can be solved efficiently.

A rational quadratic surrogate model, denoted by $\mathcal{S}_{rq}$, is defined as a ratio of two quadratic functions $N(x_a)$ and $D(x_a)$ [24]:

$$\begin{aligned} & \mathcal{S}_{rq}(x_a) = \frac{N(x_a)}{D(x_a)} \\ \text{subject to} \quad & 1 \le D(x_a) \le K,\ \forall x_a \in \mathcal{H}_a, \end{aligned} \tag{2.18}$$

where $\mathcal{H}_a$ is the projection of $\mathcal{H}$ onto the active parameter space. The constraint ensures $D(x_a)$ is positive and does not behave erratically over the region $\mathcal{H}_a$. The constant K is a user-specified regularization parameter that can be selected from a set of candidate values by comparing their corresponding fitting performance. Only the L-infinity norm error measure is used for the rational quadratic surrogate model. To better demonstrate the process, we express the quadratic function in matrix multiplication form hereafter. The resulting optimization problem can be written as follows:

$$\begin{aligned} Z_n^*,\, Z_d^* = \underset{Z_n,\, Z_d,\, t}{\operatorname{argmin}} \quad & t \\ \text{subject to} \quad & -t \le \frac{\left[\begin{smallmatrix} 1 \\ x_{a,i} \end{smallmatrix}\right]^T Z_n \left[\begin{smallmatrix} 1 \\ x_{a,i} \end{smallmatrix}\right]}{\left[\begin{smallmatrix} 1 \\ x_{a,i} \end{smallmatrix}\right]^T Z_d \left[\begin{smallmatrix} 1 \\ x_{a,i} \end{smallmatrix}\right]} - Y_i \le t, \\ & i = 1, 2, \ldots, n_s, \\ & 1 \le \left[\begin{smallmatrix} 1 \\ x_a \end{smallmatrix}\right]^T Z_d \left[\begin{smallmatrix} 1 \\ x_a \end{smallmatrix}\right] \le K,\ \forall\, l_a^j \le x_a^j \le u_a^j,\ j = 1, 2, \ldots, n_a, \end{aligned} \tag{2.19}$$

where Z_n and Z_d are symmetric matrices containing the coefficients of the quadratic numerator and denominator. The subscript i and superscript j are indices associated with design points and active parameters, respectively. Despite its relatively simple form, the optimization problem (2.19) is difficult to solve because the regularity constraint on $D(x_a)$ is equivalent to an infinite number of inequalities.

One approach is to replace the regularity constraint with a semidefinite constraint and solve the resulting problem using the semidefinite programming (SDP) technique [8]. The orthotope constraint in the active parameter space can be equivalently described by n_a quadratic inequalities:

$$l_a^j \le x_a^j \le u_a^j \Leftrightarrow (x_a^j - l_a^j)(x_a^j - u_a^j) \le 0 \Leftrightarrow \left[\begin{smallmatrix}1\\x_a\end{smallmatrix}\right]^T Z_j \left[\begin{smallmatrix}1\\x_a\end{smallmatrix}\right] \le 0,\ j = 1, 2, \ldots, n_a. \tag{2.20}$$

If we further define two symmetric matrices $Z_{\mathbf{1}}$ and Z_K such that

$$\left[\begin{smallmatrix}1\\x_a\end{smallmatrix}\right]^T Z_{\mathbf{1}} \left[\begin{smallmatrix}1\\x_a\end{smallmatrix}\right] = 1,\ \left[\begin{smallmatrix}1\\x_a\end{smallmatrix}\right]^T Z_K \left[\begin{smallmatrix}1\\x_a\end{smallmatrix}\right] = K. \tag{2.21}$$

then the regularity condition is satisfied if we only search over matrices Z_d where

$$\begin{aligned} Z_L &= Z_d - Z_1 + \sum_{j=1}^{n_a} \lambda_{\mathbf{1}}^j Z_j \succeq \mathbf{0}, \\ \lambda_{\mathbf{1}}^j &\ge 0,\ j = 1, 2, \ldots, n_a, \\ Z_U &= Z_k - Z_d + \sum_{j=1}^{n_a} \lambda_K^j Z_j \succeq \mathbf{0}, \\ \lambda_K^j &\ge 0,\ j = 1, 2, \ldots, n_a, \end{aligned} \tag{2.22}$$

where $\succeq \mathbf{0}$ stands for the matrix being positive semidefinite. We can demonstrate this by multiplying $\left[\begin{smallmatrix}1\\x_a\end{smallmatrix}\right]^T$ and $\left[\begin{smallmatrix}1\\x_a\end{smallmatrix}\right]$ on both sides of Z_L in Equation (2.22). For any $x_a \in \mathcal{H}_a$, we have $\left[\begin{smallmatrix}1\\x_a\end{smallmatrix}\right]^T (\sum_{j=1}^{n_a} \lambda_{\mathbf{1}}^j Z_j) \left[\begin{smallmatrix}1\\x_a\end{smallmatrix}\right] \le 0$; therefore, $\left[\begin{smallmatrix}1\\x_a\end{smallmatrix}\right]^T Z_d \left[\begin{smallmatrix}1\\x_a\end{smallmatrix}\right] \ge \left[\begin{smallmatrix}1\\x_a\end{smallmatrix}\right]^T Z_1 \left[\begin{smallmatrix}1\\x_a\end{smallmatrix}\right] = 1$. Because the denominator is enforced by the regularity constraint to be positive, we multiply it in all the

related constraints and obtain the following optimization problem:

$$
\begin{aligned}
Z_n^*,\, Z_d^* = \underset{Z_n,\, Z_d,\, t}{\operatorname{argmin}} \quad & t \\
\text{subject to} \quad & \left[\begin{smallmatrix} 1 \\ x_{a,i} \end{smallmatrix}\right]^T (Z_n - (t + Y_i) Z_d) \left[\begin{smallmatrix} 1 \\ x_{a,i} \end{smallmatrix}\right] \leq 0, \\
& \left[\begin{smallmatrix} 1 \\ x_{a,i} \end{smallmatrix}\right]^T (Z_n + (t - Y_i) Z_d) \left[\begin{smallmatrix} 1 \\ x_{a,i} \end{smallmatrix}\right] \leq 0, \\
& i = 1, 2, \ldots, n_s, \\
& Z_d - Z_1 + \sum_{j=1}^{n_a} \lambda_{\mathbf{1}}^j Z_j \succeq 0, \\
& \lambda_{\mathbf{1}}^j \geq 0,\ j = 1, 2, \ldots, n_a \\
& Z_k - Z_d + \sum_{j=1}^{n_a} \lambda_K^j Z_j \succeq 0, \\
& \lambda_K^j \geq 0,\ j = 1, 2, \ldots, n_a.
\end{aligned}
\tag{2.23}
$$

In Equation (2.23), the two semidefinite regularity constraints are convex, but the $2n_s$ constraints associated with the prediction error are not, making the optimization problem nonconvex and NP-hard to solve. This is because the terms $(t + Y_i)Z_d$ and $(t - Y_i)Z_d$ are quadratic in the optimized variables. If t is fixed, the constraints are linear in Z_d, and the optimization problem is convex. To determine whether the solution coefficient matrices Z_n^* and Z_d^* exist for a given $t = t^*$, we can solve the following feasibility problem by setting a constant objective function:

$$
\begin{aligned}
Z_n^*,\, Z_d^* = \underset{Z_n,\, Z_d}{\operatorname{argmin}} \quad & 0 \\
\text{subject to} \quad & \left[\begin{smallmatrix} 1 \\ x_{a,i} \end{smallmatrix}\right]^T (Z_n - (t^* - Y_i) Z_d) \left[\begin{smallmatrix} 1 \\ x_{a,i} \end{smallmatrix}\right] \leq 0, \\
& \left[\begin{smallmatrix} 1 \\ x_{a,i} \end{smallmatrix}\right]^T (Z_n + (t^* - Y_i) Z_d) \left[\begin{smallmatrix} 1 \\ x_{a,i} \end{smallmatrix}\right] \leq 0, \\
& i = 1, 2, \ldots, n_s, \\
& Z_d - Z_1 + \sum_j \lambda_{\mathbf{1}}^j Z_j \succeq 0,\ \lambda_{\mathbf{1}}^j \geq 0, \\
& Z_k - Z_d + \sum_j \lambda_K^j Z_j \succeq 0,\ \lambda_K^j \geq 0, \\
& j = 1, 2, \ldots, n_a.
\end{aligned}
\tag{2.24}
$$

If the problem is feasible, the returned Z_n^* and Z_d^* specify a rational quadratic surrogate model whose infinite-norm error over the training data is less than t^*. The optimization problem (2.24) is an SDP problem and can be solved efficiently.

Based on the above discussion, an iterative algorithm is developed to compute a rational quadratic surrogate with a gradually decreasing infinite-norm error and is summarized in

Algorithm 2.1. A practical choice of $\hat{t}$ (the initial upper bound of the error norm) is the infinite-norm error obtained with a quadratic surrogate model. This upper bound is always valid because the rational quadratic model is guaranteed to have a lower error norm. The computational effort for fitting a rational quadratic surrogate is generally significantly larger than that for fitting a polynomial surrogate. This is attributed to not only the more expensive SDP problems but also the additional iterations required for computing the regularity constant K and coefficient matrices Z_n and Z_d. Consequently, the rational quadratic surrogate model is advised only when the polynomial surrogate model, especially the quadratic surrogate model, produces unacceptably large errors.

Algorithm 2.1 Calculating Z_n and Z_d for a rational quadratic surrogate model

Setting $t_l \leftarrow 0$, $t_u \leftarrow \hat{t}$.
Setting $\epsilon \leftarrow 10^{-4} t_u$.
while $(t_u - t_l) \geq \epsilon$ **do**
    Solve the feasibility problem with $t = \frac{1}{2}(t_l + t_u)$.
    if The problem is feasible **then**
        Z_n, $Z_d \leftarrow Z_n^*$, Z_d^*.
        $t_u \leftarrow \frac{1}{2}(t_l + t_u)$.
    else
        $t_l \leftarrow \frac{1}{2}(t_l + t_u)$.
    end if
end while
Return Z_n, Z_d.

The quality of the generated surrogate model is evaluated by estimating its fitting error. The cross-validation method [64] is used to provide a more realistic estimate compared to the fitting error obtained over the training data. Once the surrogate models are generated, they are used in the derived optimization problems in place of the original models. Although the resulting optimization problems are still nonconvex and NP-hard to solve, a bounding interval containing the global optimum can be computed with a tractable computational expense.

The two endpoints of the bounding interval are referred to as the *inner bound* and *outer bound*. The inner bound is a sub-optimal estimate of the global optimum, whereas the outer bound is a conservative estimate. An inner bound can be computed by implementing general nonconvex constrained optimization algorithms that produce a local optimal solution. In practice, starting at multiple initial points can improve the quality of the calculated inner bound. In addition, analytic gradient information, which is available for the three types of surrogate models considered in the B2BDC, can further reduce the computational time. The derivation for the outer bound is more involved and requires different techniques for different types of surrogate models. This is addressed in the following three subsections.

2.7.2 Outer Bound with Quadratic Surrogates

Let us consider the optimization problem for computing the SCM and replace the original models with the quadratic surrogate models:

$$\begin{aligned} C_{\mathrm{D}} = \underset{x,\gamma}{\text{maximize}} \quad & \gamma \\ \text{subject to} \quad & l_i \le a_i^T x \le u_i,\ i = 1, 2, \ldots, m, \\ & L_e + (d_e - L_e)\gamma \le \begin{bmatrix} 1 \\ x \end{bmatrix}^T \begin{bmatrix} Z_{e,0} & Z_{e,\mathcal{L}}^T \\ Z_{e,\mathcal{L}} & Z_{e,\mathcal{Q}} \end{bmatrix} \begin{bmatrix} 1 \\ x \end{bmatrix} \le U_e - (U_e - d_e)\gamma, \\ & e = 1, 2, \ldots, N. \end{aligned} \tag{2.25}$$

The coefficient matrix of the quadratic surrogate model is intentionally decomposed into the constant $Z_{e,0}$, the linear part $Z_{e,\mathcal{L}}$, and the quadratic part $Z_{e,\mathcal{Q}}$ for the following derivation. Although individual surrogate models depend on their own set of active parameters, we represented all of them in the full-dimensional parameter space for simpler notation. Applying the same trick used in Equation (2.20) for the linear inequalities and converting the two-sided quadratic inequalities into the one-sided form, the problem is reformulated with only one-sided quadratic inequalities in the augmented parameter vector $y = \begin{bmatrix} \gamma \\ x \end{bmatrix}$:

$$\begin{aligned} C_{\mathrm{D}} = \underset{y}{\text{maximize}} \quad & \begin{bmatrix} 1 \\ y \end{bmatrix}^T Z_\gamma \begin{bmatrix} 1 \\ y \end{bmatrix} \\ \text{subject to} \quad & \begin{bmatrix} 1 \\ y \end{bmatrix}^T Z_i \begin{bmatrix} 1 \\ y \end{bmatrix} \le 0,\ i = 1, 2, \ldots, m, \\ & \begin{bmatrix} 1 \\ y \end{bmatrix}^T Z_e^L \begin{bmatrix} 1 \\ y \end{bmatrix} \le 0, \\ & \begin{bmatrix} 1 \\ y \end{bmatrix}^T Z_e^U \begin{bmatrix} 1 \\ y \end{bmatrix} \le 0,\ e = 1, 2, \ldots, N, \end{aligned} \tag{2.26}$$

where Z_γ, Z_i, Z_e^L, and Z_e^U are defined as follows:

$$\begin{aligned} Z_\gamma &= \begin{bmatrix} 0 & 0.5 & \mathbf{0}^T \\ 0.5 & 0 & \mathbf{0}^T \\ \mathbf{0} & \mathbf{0} & \mathbf{0_n} \end{bmatrix}, \\ Z_i &= \begin{bmatrix} l_i \cdot u_i & 0 & -0.5(l_i + u_i)a_i^T \\ 0 & 0 & \mathbf{0}^T \\ -0.5(l_i + u_i)a_i & \mathbf{0} & a_i a_i^T \end{bmatrix}, \\ Z_e^L &= \begin{bmatrix} L_e - Z_{e,0} & 0.5(d_e - L_e) & -Z_{e,\mathcal{L}}^T \\ 0.5(d_e - L_e) & 0 & \mathbf{0}^T \\ -Z_{e,\mathcal{L}} & \mathbf{0} & -Z_{e,\mathcal{Q}} \end{bmatrix}, \\ Z_e^U &= \begin{bmatrix} Z_{e,0} - U_e & 0.5(U_e - d_e) & Z_{e,\mathcal{L}}^T \\ 0.5(U_e - d_e) & 0 & \mathbf{0}^T \\ Z_{e,\mathcal{L}} & \mathbf{0} & Z_{e,\mathcal{Q}} \end{bmatrix}. \end{aligned} \tag{2.27}$$

The problem in (2.27) is a quadratically constrained quadratic program (QCQP). Because the quadratics (i.e., Z_γ, $\{Z_i\}_{i=1}^m$, $\{Z_e^L\}_{e=1}^N$, and $\{Z_e^U\}_{e=1}^N$) are generally not positive semidefinite, the QCQP is nonconvex.

Two convex relaxation strategies can be applied to convert the QCQP to a convex optimization problem whose solution is a conservative estimate of that of the original QCQP.

We observe that the quadratic form $\left[\begin{smallmatrix}1\\y\end{smallmatrix}\right]^T Z \left[\begin{smallmatrix}1\\y\end{smallmatrix}\right]$ can be also expressed as $\mathrm{Tr}(ZY)$, where $\mathrm{Tr}(\cdot)$ is the trace of a matrix and $Y = \left[\begin{smallmatrix}1\\y\end{smallmatrix}\right]\left[\begin{smallmatrix}1\\y\end{smallmatrix}\right]^T$. The matrix Y is a rank-one positive semidefinite matrix. We can now rewrite the QCQP in variable Y by replacing the quadratic forms with the trace expression for both the objective function and constraints. If we remove the rank-one requirement, a convex optimization problem referred to as the SDP relaxation is obtained:

$$\begin{aligned}\overline{C}_{\mathrm{D,S}} = \underset{Y \succeq \mathbf{0}}{\text{maximize}} \quad & \mathrm{Tr}(Z_\gamma Y) \\ \text{subject to} \quad & \mathrm{Tr}(Z_i Y) \leq 0,\ i = 1, 2, \ldots, m, \\ & \mathrm{Tr}(Z_e^L Y) \leq 0, \\ & \mathrm{Tr}(Z_e^U Y) \leq 0,\ e = 1, 2, \ldots, N.\end{aligned} \tag{2.28}$$

The second strategy is to first linearize the objective function with an additional variable, then combine all quadratic constraints to one quadratic constraint using Lagrangian multipliers, followed by replacing the quadratic constraint with a linear matrix inequality. The resulting problem is given in (2.29). The optimization problem (2.29) is convex and is referred to as the Lagrangian relaxation:

$$\begin{aligned}\overline{C}_{\mathrm{D,L}} = \underset{\rho,\,\lambda}{\text{minimize}} \quad & \rho \\ \text{subject to} \quad & \lambda_i \geq 0,\ i = 1, 2, \ldots, m, \\ & \lambda_e^L \geq 0,\ \lambda_e^L \geq 0,\ e = 1, 2, \ldots, N, \\ & \rho \widetilde{Z}_0 - \widetilde{Z}_\gamma + \sum_{i=1}^{m} \lambda_i \widetilde{Z}_i + \sum_{e=1}^{N} (\lambda_e^L \widetilde{Z}_e^L + \lambda_e^U \widetilde{Z}_e^U) \succeq \mathbf{0},\end{aligned} \tag{2.29}$$

where the tilde matrices are defined by

$$\begin{aligned}\widetilde{Z}_0 &= \left[\begin{smallmatrix}1 & \mathbf{0}^T \\ \mathbf{0} & \mathbf{0}\end{smallmatrix}\right], \\ \widetilde{Z}_\gamma &= \left[\begin{smallmatrix}0 & \mathbf{0}^T \\ \mathbf{0} & Z_\gamma\end{smallmatrix}\right], \\ \widetilde{Z}_e^L &= \left[\begin{smallmatrix}0 & \mathbf{0}^T \\ \mathbf{0} & Z_e^L\end{smallmatrix}\right], \\ \widetilde{Z}_e^U &= \left[\begin{smallmatrix}0 & \mathbf{0}^T \\ \mathbf{0} & Z_e^U\end{smallmatrix}\right].\end{aligned} \tag{2.30}$$

The SDP and Lagrangian relaxations form a primal-dual pair and can be solved efficiently by available SDP solvers, such as SeDuMi [122]. The derivation for the outer-bound solution of the VCM and prediction uncertainty bounds is similar to that of the SCM and, therefore, is not repeated.

2.7.3 Outer Bound with Rational Quadratic Surrogates

We first consider the SCM problem and replace the original models with the rational quadratic surrogate models:

$$\begin{aligned} C_{\mathrm{D}} = \underset{x,\gamma}{\text{maximize}} \quad & \gamma \\ \text{subject to} \quad & l_i \le a_i^T x \le u_i,\ i = 1, 2, \ldots, m, \\ & L_e + (d_e - L_e)\gamma \le \frac{\left[\begin{smallmatrix}1\\x\end{smallmatrix}\right]^T Z_{n,e} \left[\begin{smallmatrix}1\\x\end{smallmatrix}\right]}{\left[\begin{smallmatrix}1\\x\end{smallmatrix}\right]^T Z_{d,e} \left[\begin{smallmatrix}1\\x\end{smallmatrix}\right]} \le U_e - (U_e - d_e)\gamma, \\ & e = 1, 2, \ldots, N. \end{aligned} \tag{2.31}$$

The linear constraints are converted to quadratic constraints using Equation (2.27). Because $\{Z_{d,e}\}_{e=1}^N$ is positive definite over the searched region, we can multiply the denominator on both sides of the model-data constraints. By doing so, the constraints become cubic in x and γ due to the product of $(d_e - L_e)\gamma$ or $(U_e - d_e)\gamma$ and the quadratic terms in $\left[\begin{smallmatrix}1\\x\end{smallmatrix}\right]^T Z_{d,e} \left[\begin{smallmatrix}1\\x\end{smallmatrix}\right]$. If we fix $\gamma = \gamma^*$, the optimization problem becomes a QCQP, and its feasibility is ensured if the corresponding SDP or Lagrangian relaxed problems are feasible. The resulting optimization problems for the two relaxations are as follows:

$$\begin{aligned} \underset{Y \succeq \mathbf{0}}{\text{maximize}} \quad & 0 \\ \text{subject to} \quad & \mathrm{Tr}(Z_i Y) \le 0,\ i = 1, 2, \ldots, m, \\ & \mathrm{Tr}(Z_e^L Y) \le 0, \\ & \mathrm{Tr}(Z_e^U Y) \le 0,\ e = 1, 2, \ldots, N \end{aligned} \tag{2.32}$$

and

$$\begin{aligned} \underset{\lambda}{\text{minimize}} \quad & \sum_{i=1}^n \lambda_i + \sum_{e=1}^N (\lambda_e^L + \lambda_e^U) \\ \text{subject to} \quad & \lambda_i \ge 0,\ i = 1, 2, \ldots, m, \\ & \lambda_e^L \ge 0,\ \lambda_e^L \ge 0,\ e = 1, 2, \ldots, N, \\ & \sum_{i=1}^n \lambda_i + \sum_{e=1}^N (\lambda_e^L + \lambda_e^U) \ge 1 \\ & \sum_{i=1}^n \lambda_i Z_i + \sum_{e=1}^N (\lambda_e^L Z_e^L + \lambda_e^U Z_e^U) \succeq \mathbf{0}, \end{aligned} \tag{2.33}$$

where Z_i, Z_e^L, and Z_e^U are defined by the following:

$$\begin{aligned} Z_i &= \left[\begin{smallmatrix} -l_i \cdot u_i & -0.5(l_i + u_i)a_i^T \\ -0.5(l_i + u_i)a_i & a_i a_i^T \end{smallmatrix}\right], \\ Z_e^L &= (L_e + (d_e - L_e)\gamma^*) Z_{d,e} - Z_{n,e} \\ Z_e^U &= Z_{n,e} - (U_e - (U_e - d_e)\gamma^*) Z_{d_e}. \end{aligned} \tag{2.34}$$

For the Lagrangian relaxation, γ^* is a valid outer bound if the computed minimum is 1.

Similar to the procedures of fitting a rational quadratic surrogate model, an iterative algorithm is developed and summarized in Algorithm 2.2 to find an outer bound $C_{\mathrm{D,S}}$ or $C_{\mathrm{D,L}}$, depending on which relaxation is used. A practical recommendation for $\hat{\gamma}$, the initial

Algorithm 2.2 Calculating an outer-bound $C_{\mathrm{D,S}}$ or $C_{\mathrm{D,L}}$

Setting $\gamma_l \leftarrow \hat{\gamma}$, $\gamma_u \leftarrow 1$.
Setting a tolerance $\epsilon \leftarrow 10^{-4}$.
while $(\gamma_u - \gamma_l) \geq \epsilon$ **do**
    Solve the optimization problem (2.32) or (2.33) with $\gamma^* = 0.5(\gamma_l + \gamma_u)$.
    if problem (2.32) is feasible or the minimum of problem (2.33) is 1 **then**
        $\gamma_l \leftarrow \gamma^*$.
    else
        $\gamma_u \leftarrow \gamma^*$.
    end if
end while
Return γ_l.

lower bound for $C_{\mathrm{D,S}}$ or $C_{\mathrm{D,L}}$, is to compute the largest γ that makes a randomly selected point in $\mathcal{H}$ satisfy all model-data constraints.

Computation of the outer bounds for the prediction uncertainty bounds of an unmeasured QOI is simpler because no iteration is required compared to the computation for the SCM. Without loss of generality, we considered the case in which the lower bound L_p is calculated. After linearizing the objective function with an additional variable and replacing the original models with the rational quadratic surrogates, the optimization problem (2.7) becomes

$$\begin{aligned} L_p = \underset{x}{\text{minimize}} \quad & \frac{\left[\begin{smallmatrix}1\\x\end{smallmatrix}\right]^T Z_{n,p} \left[\begin{smallmatrix}1\\x\end{smallmatrix}\right]}{\left[\begin{smallmatrix}1\\x\end{smallmatrix}\right]^T Z_{d,p} \left[\begin{smallmatrix}1\\x\end{smallmatrix}\right]} \\ \text{subject to} \quad & l_i \leq a_i^T x \leq u_i, \ i = 1, 2, \ldots, m, \\ & L_e \leq \frac{\left[\begin{smallmatrix}1\\x\end{smallmatrix}\right]^T Z_{n,e} \left[\begin{smallmatrix}1\\x\end{smallmatrix}\right]}{\left[\begin{smallmatrix}1\\x\end{smallmatrix}\right]^T Z_{d,e} \left[\begin{smallmatrix}1\\x\end{smallmatrix}\right]} \leq U_e, \\ & e = 1, 2, \ldots, N. \end{aligned} \tag{2.35}$$

After applying Equation (2.20) to the linear inequalities and multiplying the denominator in constraints containing a rational quadratic surrogate model, we convert all constraints into quadratic constraints and are left with only a rational quadratic model in the objective function. An additional constraint is included to enforce that, with the solution vector x^*, the denominator of the predicted model equals 1, and the objective function becomes quadratic.

The SDP relaxation is then applied to this QCQP, resulting in the following:

$$\begin{aligned} \overline{L}_{p,\mathrm{S}} = \underset{Y \succeq \mathbf{0}}{\text{minimize}} \quad & \mathrm{Tr}(Z_{n,p}Y) \\ \text{subject to} \quad & \mathrm{Tr}(Z_{d,p}Y) = 1, \\ & \mathrm{Tr}(Z_i Y) \leq 0,\ i = 1, 2, \ldots, m, \\ & \mathrm{Tr}(Z_e^L Y) \leq 0, \\ & \mathrm{Tr}(Z_e^U Y) \leq 0,\ e = 1, 2, \ldots, N. \end{aligned} \tag{2.36}$$

The matrices Z_i, Z_e^L, and Z_e^U are calculated by Equation (2.34) using $\gamma^* = 0$.

The Lagrangian relaxation is derived similarly to the case with quadratic surrogates, resulting in the following convex optimization problem:

$$\begin{aligned} \overline{L}_{p,\mathrm{L}} = \underset{\rho,\,\lambda}{\text{maximize}} \quad & \rho \\ \text{subject to} \quad & \lambda_i \geq 0,\ i = 1, 2, \ldots, m, \\ & \lambda_e^L \geq 0,\ \lambda_e^L \geq 0,\ e = 1, 2, \ldots, N, \\ & Z_{p,n} - \rho Z_{p,d} + \sum_{i=1}^{n} \lambda_i Z_i + \sum_{e=1}^{N} (\lambda_e^L Z_e^L + \lambda_e^U Z_e^U) \succeq \mathbf{0}. \end{aligned} \tag{2.37}$$

Again, the two relaxations form a primal-dual pair that can be solved efficiently using SDP solvers. Both $\overline{L}_{p,\mathrm{S}}$ and $\overline{L}_{p,\mathrm{L}}$ are valid outer-bound solutions to L_p.

2.7.4 Outer Bound with Higher Order Polynomials

When the surrogate models are higher-order polynomials, the technique used to compute an outer-bound solution is a generalization of the technique used in the derivation of the Lagrangian relaxation for a QCQP. We consider the case of predicting the lower bound L_p of a polynomial surrogate model with all the constraints expressed by one-sided polynomial inequalities:

$$\begin{aligned} L_p = \underset{x}{\text{minimize}} \quad & \mathcal{P}_0(x) \\ \text{subject to} \quad & \mathcal{P}_i(x) \geq 0,\ i = 1, 2, \ldots, \hat{m}. \end{aligned} \tag{2.38}$$

The outer-bound derivation includes a key concept: the sum-of-squares (SOS) polynomial. A polynomial is a SOS polynomial if it can be written as the sum of squared polynomials and is nonnegative. However, a nonnegative polynomial is not necessarily an SOS polynomial. More importantly, consider the following quadratic form of a polynomial $\mathcal{P}(x)$ with degree $2d$:

$$\mathcal{P}(x) = \mathbf{v}^T P_M \mathbf{v}, \tag{2.39}$$

where $\mathbf{v}$ is a vector containing all monomials with degree not higher than d, and P_M is a symmetric matrix. The polynomial $\mathcal{P}(x)$ is an SOS polynomial if and only if the matrix P_M is positive semidefinite.

Similar to the procedures involved in deriving the Lagrangian relaxation for a QCQP, we linearize the objective function with an additional variable and combine all the polynomial constraints into a single polynomial constraint with the generalized Lagrangian multipliers (i.e., SOS polynomials). The last step is to replace the nonnegativity condition with the SOS condition, resulting in the following optimization problem:

$$\begin{aligned} \overline{L}_{p,L} = \underset{\phi,\,\rho}{\text{maximize}} \quad & \rho \\ \text{subject to} \quad & \phi_i(x) \in \text{SOS}_{\omega - d_i},\ i = 1, 2, \ldots, \hat{m}, \\ & \mathcal{P}_0(x) - \rho - \sum_{i=1}^{\hat{m}} \phi_i(x)\mathcal{P}_i(x) \in \text{SOS}_{\omega}, \end{aligned} \tag{2.40}$$

where SOS_ω ($\omega \in 2\mathbb{Z}$) is the set of SOS polynomials whose degree is not higher than ω, and d_i is the degree of polynomial $\mathcal{P}_i(x)$. Problem (2.40) is convex and can be solved using general SDP solvers. However, in practice, the difference between the calculated outer-bound solution and the true optimum can be unacceptably large if the relaxation order ω is too low, whereas the computational burden can become unaffordable if ω is too high. As a result, the use of higher-order polynomial surrogate models is not frequently encountered in B2BDC applications and is usually limited to smaller problems.

2.7.5 Sensitivity Analysis

Sensitivity analysis contains a broad range of techniques that investigate the effect of input perturbations on the output variations in a system or computational model [103]. In B2BDC, we are interested in evaluating the influence of estimated uncertainty bounds to computed quantities (e.g., consistency measures and prediction interval bounds) [99, 101]. The main course of the following derivation relies on the ability to compute the derivative of the inner- and outer-bound solutions with respect to perturbations in uncertainty bounds associated with data and model parameters. For illustration, we consider the optimization problem of calculating the lower bound of a prediction interval.

$$\begin{aligned} L_p = \underset{x}{\text{minimize}} \quad & \frac{\left[\begin{smallmatrix}1\\x\end{smallmatrix}\right]^T Z_{n,p} \left[\begin{smallmatrix}1\\x\end{smallmatrix}\right]}{\left[\begin{smallmatrix}1\\x\end{smallmatrix}\right]^T Z_{d,p} \left[\begin{smallmatrix}1\\x\end{smallmatrix}\right]} \\ \text{subject to} \quad & x_i - u_i \le 0, \\ & l_i - x_i \le 0,\ i = 1, 2, \ldots, n, \\ & L_e - \frac{\left[\begin{smallmatrix}1\\x\end{smallmatrix}\right]^T Z_{n,e} \left[\begin{smallmatrix}1\\x\end{smallmatrix}\right]}{\left[\begin{smallmatrix}1\\x\end{smallmatrix}\right]^T Z_{d,e} \left[\begin{smallmatrix}1\\x\end{smallmatrix}\right]} \le 0, \\ & \frac{\left[\begin{smallmatrix}1\\x\end{smallmatrix}\right]^T Z_{n,e} \left[\begin{smallmatrix}1\\x\end{smallmatrix}\right]}{\left[\begin{smallmatrix}1\\x\end{smallmatrix}\right]^T Z_{d,e} \left[\begin{smallmatrix}1\\x\end{smallmatrix}\right]} - U_e \le 0,\ e = 1, 2, \ldots, N. \end{aligned} \tag{2.41}$$

The prior uncertainty region $\mathcal{H}$ is assumed to be the orthotope defined in Equation (2.5), and all surrogate models are rational quadratic functions. Results for the case with quadratic surrogates are obtained by setting all denominators to 1.

A perturbed problem (2.41) parameterized by the perturbation vector $\theta = [\delta u,\, \delta l,\, \Delta U,\, \Delta L]$ is given in (2.42). The vectors δu and δl are perturbations associated with the uncertainty upper and lower bounds of model parameters; ΔU and ΔL are associated with the uncertainty upper and lower bounds of the experimental data. The unperturbed problem corresponds to $\theta = \mathbf{0}$:

$$
\begin{aligned}
L_p(\theta) = \underset{x}{\text{minimize}} \quad & \frac{\left[\begin{smallmatrix}1\\x\end{smallmatrix}\right]^T Z_{n,p} \left[\begin{smallmatrix}1\\x\end{smallmatrix}\right]}{\left[\begin{smallmatrix}1\\x\end{smallmatrix}\right]^T Z_{d,p} \left[\begin{smallmatrix}1\\x\end{smallmatrix}\right]} \\
\text{subject to} \quad & x_i - u_i \le (\delta u)_i, \\
& l_i - x_i \le (\delta l)_i,\ i = 1, 2, \ldots, n, \\
& L_e - \frac{\left[\begin{smallmatrix}1\\x\end{smallmatrix}\right]^T Z_{n,e} \left[\begin{smallmatrix}1\\x\end{smallmatrix}\right]}{\left[\begin{smallmatrix}1\\x\end{smallmatrix}\right]^T Z_{d,e} \left[\begin{smallmatrix}1\\x\end{smallmatrix}\right]} \le (\Delta L)_e, \\
& \frac{\left[\begin{smallmatrix}1\\x\end{smallmatrix}\right]^T Z_{n,e} \left[\begin{smallmatrix}1\\x\end{smallmatrix}\right]}{\left[\begin{smallmatrix}1\\x\end{smallmatrix}\right]^T Z_{d,e} \left[\begin{smallmatrix}1\\x\end{smallmatrix}\right]} - U_e \le (\Delta U)_e,\ e = 1, 2, \ldots, N.
\end{aligned}
\tag{2.42}
$$

We first consider the inner-bound solution, which calculates a local optimum for (2.42) with $\theta = \mathbf{0}$ using general nonlinear constrained optimization solvers. Many such solvers, for example, the MATLAB function `fmincon`, return a vector of Lagrangian multipliers associated with the found solution. These multipliers, denoted by λ^l, λ^u, λ^L, and λ^U, are partial derivatives of the optimum with respect to the corresponding perturbations:

$$
\begin{aligned}
\left.\frac{\partial L_p}{\partial (\delta l)_i}\right|_{\theta=\mathbf{0}} &= \lambda_i^l, \\
\left.\frac{\partial L_p}{\partial (\delta u)_i}\right|_{\theta=\mathbf{0}} &= \lambda_i^u, \\
\left.\frac{\partial L_p}{\partial (\Delta L)_e}\right|_{\theta=\mathbf{0}} &= \lambda_e^L, \\
\left.\frac{\partial L_p}{\partial (\Delta U)_e}\right|_{\theta=\mathbf{0}} &= \lambda_e^U.
\end{aligned}
\tag{2.43}
$$

Derivations of the partial derivatives are more complicated for the outer-bound solution because the optimization problem (2.42) is converted to a somewhat different problem using SDP or Lagrangian relaxation before solving. Following similar procedures derived in

Section 2.7.3, the following two relaxations are obtained:

$$\begin{aligned}
\overline{L}_{p,\mathrm{S}}(\theta) = \underset{Y \succeq \mathbf{0}}{\text{minimize}} \quad & \mathrm{Tr}(Z_{n,p}Y) \\
\text{subject to} \quad & \mathrm{Tr}(Z_{d,p}Y) = 1, \\
& \mathrm{Tr}(Z_i Y) \leq \mathrm{Tr}(\hat{Z}_i Y),\ i = 1, 2, \ldots, n, \\
& \mathrm{Tr}(Z_e^L Y) \leq (\Delta L)_e \mathrm{Tr}(Z_{d,e} Y), \\
& \mathrm{Tr}(Z_e^U Y) \leq (\Delta U)_e \mathrm{Tr}(Z_{d,e} Y),\ e = 1, 2, \ldots, N,
\end{aligned} \tag{2.44}$$

and

$$\begin{aligned}
\overline{L}_{p,\mathrm{L}}(\theta) = \underset{\rho,\,\lambda}{\text{maximize}} \quad & \rho \\
\text{subject to} \quad & \lambda_i \geq 0,\ i = 1, 2, \ldots, n, \\
& \lambda_e^L \geq 0,\ \lambda_e^L \geq 0,\ e = 1, 2, \ldots, N, \\
& Z_{p,n} - \rho Z_{p,d} + \sum_{i=1}^{n} \lambda_i (Z_i - \hat{Z}_i) \\
& \qquad + \sum_{e=1}^{N} (\lambda_e^L (Z_e^L - (\Delta L)_e Z_{d,e}) + \lambda_e^U (Z_e^U - (\Delta U)_e Z_{d,e})) \succeq \mathbf{0}.
\end{aligned} \tag{2.45}$$

The matrices Z_i, Z_e^L, and Z_e^U are presented in Equation (2.34), whereas the perturbation matrix $\hat{Z}_i$ is a sparse matrix with only three nonzero elements:

$$\begin{aligned}
&\hat{Z}_i(1,1) = (\delta l)_i u_i - (\delta u)_i l_i + (\delta l)_i (\delta u)_i, \\
&\hat{Z}_i(1, i+1) = \hat{Z}_i(i+1, 1) = 0.5((\delta u)_i - (\delta l)_i).
\end{aligned} \tag{2.46}$$

The convex optimization problems [(2.44) and (2.45)] form a primal-dual pair and can be framed in the context of a conic linear program. The primal and dual variables, denoted by $V \in \mathbb{R}^{n+2N} \times \mathbb{S}^{n+1}$ and $\lambda \in \mathbb{R}^{n+2N+1}$, are constructed as follows:

$$\begin{aligned}
&V = (r, Y) = (r_i,\, r_e^L,\, r_e^U,\, Y), \\
&\lambda = (\rho,\, \lambda_i,\, \lambda_e^L,\, \lambda_e^U).
\end{aligned} \tag{2.47}$$

With the cone being $\mathcal{K} = \mathbb{R}_+^{n+2N} \times \mathbb{S}_+^{n+1}$, the problems (2.44) and (2.45) can be written in variables V and λ:

$$\begin{aligned}
\overline{L}_{p,\mathrm{S}}(\theta) = \underset{V}{\text{minimize}} \quad & C \cdot V, \\
\text{subject to} \quad & V \in \mathcal{K}, \\
& b - AV = 0,
\end{aligned} \tag{2.48}$$

$$\begin{aligned}
\overline{L}_{p,\mathrm{L}}(\theta) = \underset{\lambda}{\text{maximize}} \quad & b^T \lambda, \\
\text{subject to} \quad & C - A^T \lambda \in \mathcal{K}.
\end{aligned}$$

The coefficient matrices A, b, and C are defined as follows:

$$AV = \begin{bmatrix} \mathrm{Tr}(Z_{d,p}Y) \\ -r_1 - \mathrm{Tr}(Z_1 Y) \\ \vdots \\ -r_n - \mathrm{Tr}(Z_n Y) \\ -r_1^L - \mathrm{Tr}(Z_1^L Y) \\ \vdots \\ -r_N^L - \mathrm{Tr}(Z_N^L Y) \\ -r_1^U - \mathrm{Tr}(Z_1^U Y) \\ \vdots \\ -r_N^U - \mathrm{Tr}(Z_N^U Y) \end{bmatrix} + \begin{bmatrix} 0 \\ \mathrm{Tr}(\hat{Z}_1 Y) \\ \vdots \\ \mathrm{Tr}(\hat{Z}_i Y) \\ (\Delta L)_1 \mathrm{Tr}(Z_{d,1} Y) \\ \vdots \\ (\Delta L)_N \mathrm{Tr}(Z_{d,N} Y) \\ (\Delta U)_1 \mathrm{Tr}(Z_{d,1} Y) \\ \vdots \\ (\Delta U)_N \mathrm{Tr}(Z_{d,N} Y) \end{bmatrix}, \tag{2.49}$$

$$b = \begin{bmatrix} 1 \\ 0 \\ \vdots \\ 0 \end{bmatrix}, \quad C = \begin{bmatrix} 0 \\ \vdots \\ 0 \\ Z_{n,p} \end{bmatrix}.$$

The parameterized Lagrangian function $L(V, \lambda, \theta)$ associated with problem (2.48) is defined as follows:

$$L(V, \lambda, \theta) = b^T \lambda + (C - A^T \lambda) \cdot V. \tag{2.50}$$

For the current discussion, we further assume the following:

1. There is a strictly feasible point for the optimization problem (2.48) with $\theta = \mathbf{0}$.
2. The denominators of all rational quadratic surrogates are strictly positive on the perturbed domain (i.e., $\{x \,|\, l_i - (\delta l)_i \leq x_i \leq u_i + (\delta u)_i,\ i = 1, 2, \ldots n\}$).

With the above assumptions, the values of $\overline{L}_{p,\mathrm{S}}(\theta)$ and $\overline{L}_{p,\mathrm{D}}(\theta)$ coincide for all θ in a sufficiently small neighborhood of $\theta = \mathbf{0}$. Let $\overline{L}_p(\theta)$ denote this common optimal value and suppose that $L(V, \lambda, \theta)$ is a continuously differentiable function. Then, $\overline{L}_p(\theta)$ is directionally differentiable at $\theta = \mathbf{0}$ [42, 107], and its directional derivative along a unit vector u is given in Equation (2.51):

$$\overline{L}_p'(\theta = \mathbf{0}; u) = \inf_{V \in \mathrm{Sol(P)}} \sup_{\lambda \in \mathrm{Sol(D)}} u^T \Delta_\theta L(V, \lambda, \theta), \tag{2.51}$$

where Sol(P) and Sol(D) are the solution sets for the primal and dual problems, respectively. The partial derivative with respect to each perturbation parameter is calculated based on

Equation (2.51):

$$\begin{aligned}
\left.\frac{\partial \overline{L}_p}{\partial(\delta l)_i}\right|_{\theta=\mathbf{0}} &= \lambda_i(u_i Y(1,1) - Y(1,i+1)),\\
\left.\frac{\partial \overline{L}_p}{\partial(\delta u)_i}\right|_{\theta=\mathbf{0}} &= \lambda_i(Y(1,i+1) - l_i Y(1,1)),\\
\left.\frac{\partial \overline{L}_p}{\partial(\Delta L)_e}\right|_{\theta=\mathbf{0}} &= \lambda_e^L \mathrm{Tr}(Z_{d,e} Y),\\
\left.\frac{\partial \overline{L}_p}{\partial(\Delta U)_e}\right|_{\theta=\mathbf{0}} &= \lambda_e^U \mathrm{Tr}(Z_{d,e} Y),
\end{aligned} \tag{2.52}$$

where λ_i, λ_e^L, λ_e^U, and Y are extracted from the optimal primal and dual variables.

The sensitivity of the inner- or outer-bound solution with respect to the perturbation in uncertainty bounds is computed by scaling the partial derivative with the associated uncertainty interval length:

$$\begin{aligned}
S_{l,i} &= (u_i - l_i)\left.\frac{\partial L_p}{\partial(\delta l)_i}\right|_{\theta=\mathbf{0}},\\
S_{u,i} &= (u_i - l_i)\left.\frac{\partial L_p}{\partial(\delta u)_i}\right|_{\theta=\mathbf{0}},\\
S_{L,e} &= (U_e - L_e)\left.\frac{\partial L_p}{\partial(\Delta L)_e}\right|_{\theta=\mathbf{0}},\\
S_{U,e} &= (U_e - L_e)\left.\frac{\partial L_p}{\partial(\Delta U)_e}\right|_{\theta=\mathbf{0}}.
\end{aligned} \tag{2.53}$$

As a result, the derived sensitivity coefficients consider not only the effect of reducing an uncertainty bound locally but also the maximal amount of reduction that the uncertainty interval can achieve, as have been referred to as impact factors [36].

2.7.6 Parameter Optimization

The philosophy of B2BDC is to quantify and propagate uncertainties through the formation of the feasible set, which generally contains an infinite number of parameter vectors for a consistent dataset. However, the analyst may be confronted with a situation in which a single parameter vector must be selected, for example, if the analyst wants to design a power plant with a new fuel mixture based on simulation results. To characterize the burning process of the fuel, the analyst constructs a reaction mechanism whose reaction rate parameters are determined by reviewing the existing literature. As typically seen in combustion science, the rate parameters are accompanied by uncertainty. However, a bit different from the goal of UQ in B2BDC, the analyst simply needs some approaches to choose a set of rate parameters to simulate the performance of the power plant at various operating conditions for the design. The infrastructure of B2BDC helps in such application scenarios [136].

The approach of using numerical optimization techniques to improve combustion models was first proposed by Frenklach [27, 31, 81]. Since then, this class of methods has been developed and applied extensively in chemical kinetics research (e.g., [12, 69, 98, 108, 109, 110, 113, 126, 135, 136]). Many of the applications propose searching an optimal set of rate parameters over a prior uncertainty region in the rate parameter space that minimizes some user-defined error functions. An error function that is often encountered is the sum of squared differences between model predictions and experimental measurements, and between model parameters and their nominal values. This error function was applied by You et al. [136] in B2BDC and this class of optimized parameter vectors was denoted as $x_{\text{LS-H}}$, where the subscript "LS" stands for least squares, and "H" represents the prior uncertainty region. The associated optimization problem is given in Equation (2.54):

$$x_{\text{LS-H}} = \underset{x\in\mathcal{H}}{\operatorname{argmin}} \sum_e w_e(M_e(x) - d_e)^2 + \sum_i w_i(x_i - x_{i,0})^2, \tag{2.54}$$

where w_e and w_i are nonnegative scalar weights associated with the eth experimental datum and ith model parameter. Despite its simple mathematical form, the optimization framework Equation (2.54) is quite flexible and can consider numerous subjective opinions. For example, domain expertise and user preference can be reflected by specifying different weights in the problem. A larger weight implies that the analyst prefers a model parameter vector that generates a smaller error with respect to the associated term.

In B2BDC, the feasible set is a region containing acceptable parameter vectors with respect to the estimated experimental uncertainty. Therefore, we take advantage of the data collaboration effort of B2BDC by searching in the feasible set instead of in the prior uncertainty region. This error function was applied by You et al. [136] and this class of optimized parameter vectors was denoted as $x_{\text{LS-F}}$ because it minimizes the weighted squared differences between model predictions and experimental observations and between the optimal parameter values and their nominal values over the feasible set $\mathcal{F}$:

$$x_{\text{LS-F}} = \underset{x\in\mathcal{F}}{\operatorname{argmin}} \sum_e w_e(M_e(x) - d_e)^2 + \sum_i w_i(x_i - x_{i,0})^2. \tag{2.55}$$

Besides the squared difference used in Equations (2.54) and (2.55), the relative or percentage error is also a commonly reported error measure in experimental literature. The error is defined by the following:

$$\epsilon_{\text{r}} = \left| \frac{y_p - y_{\text{obs}}}{y_{\text{obs}}} \right|, \tag{2.56}$$

where y_p and y_{obs} are the model prediction and experimental observation, respectively. Motivated by this error form, we develop the following two classes of optimized parameter vectors, denoted by $x_{\text{Rel-H}}$ and $x_{\text{Rel-F}}$. The two methods search for a parameter vector that minimizes the weighted sum of relative errors over $\mathcal{H}$ and $\mathcal{F}$, respectively. The corresponding

optimization problems are the following:

$$x_{\text{Rel-H}} = \underset{x\in\mathcal{H}}{\operatorname{argmin}} \sum_e w_e \left| \frac{M_e - d_e}{d_e} \right|, \tag{2.57}$$

and

$$x_{\text{Rel-F}} = \underset{x\in\mathcal{F}}{\operatorname{argmin}} \sum_e w_e \left| \frac{M_e - d_e}{d_e} \right|. \tag{2.58}$$

The one-norm heuristic was applied to obtain a sparsely perturbed parameter vector with respect to a nominal parameter vector [101, 136]. The optimized parameter vector, denoted by $x_{\text{1N-F}}$, is calculated by solving the following optimization problem:

$$x_{\text{1N-F}} = \underset{x\in\mathcal{F}}{\operatorname{argmin}} \sum_i w_i |x_i - x_{i,0}|. \tag{2.59}$$

In the parameter optimization process, the goal is to obtain an optimal parameter vector in the parameter space. As a result, we do not derive any outer-bound solutions for parameter optimization because the relaxed problem is often in a different parameter space. The optimization problems are solved directly using nonlinear constrained optimization solvers. If a global optimum is preferred, we can initialize the optimization problems at multiple starting points and select the one with the smallest error measure. In other cases, a local optimum is sufficient. For example, the error measure may present itself as a long, narrow, gently sloping valley in many applications in chemical kinetics [32]. Thus, the parameter vector can change dramatically without discernible changes in the error measure, making the desire for a global optimum less meaningful [26].

2.8 Example: GRI-Mech Dataset

The GRI-Mech dataset was created along with the work of developing an optimized reaction mechanism for natural gas combustion modeling [113]. The dataset was initially consisted of 77 experimental data with well-assessed uncertainty by domain experts. The QOIs are listed in Table A.1 and cover a wide range of combustion-related phenomena, for example, ignition delay times, species profiles, and laminar flame speeds. The estimated uncertainty in QOIs is taken from the work by You et al. [136] and more details can be found in the references cited above.

The reaction model [113] is based on a mechanism consisting of 325 chemical reactions in 53 species, resulting in more than 650 model parameters, including rate constants, species thermodynamic properties, and instrumental constants (e.g., absorption coefficients). A quadratic surrogate model was generated for each QOI in the selected active parameter space. A total of 102 active parameters remain in the final dataset, and all model parameters are normalized to have the prior uncertainty interval $[-1, 1]$. The 102 active model

parameters are listed in Table A.2, where they are either logarithm of the pre-exponential factor associated with a chemical reaction or enthalpy of formation of a species. If we denote the pre-exponential factor of reaction rate coefficient and enthalpy of formation associated with the ith entry in Table A.2 by A_i and h_i, respectively, then the active model parameters, denoted by x_i, are

$$x_i = \begin{cases} \dfrac{\log A_i - (\log A_{i,\max} + \log A_{i,\min})/2}{(\log A_{i,\max} - \log A_{i,\min})/2}, & i = 1, 2, \ldots, 78, 80, \ldots, 102 \\ \dfrac{h_i - (h_{i,\max} + h_{i,\min})/2}{(h_{i,\max} - h_{i,\min})/2}, & i = 79 \end{cases} . \tag{2.60}$$

The MATLAB source codes used for the GRI-Mech example can be found in Appendix D and at `https://github.com/B2BDC/B2BDC/tree/master/GRIexample`.

The dataset generates an SCM interval $[-0.37, -0.27]$ and is therefore inconsistent. The sensitivity of the computed SCM inner- and outer-bound solutions with respect to uncertainty bounds is calculated using the formulas derived in Section 2.7.5. The ranked results are given in Figures 2.1 and 2.2. The sensitivity results of the inner- and outer-bound solutions are qualitatively similar.

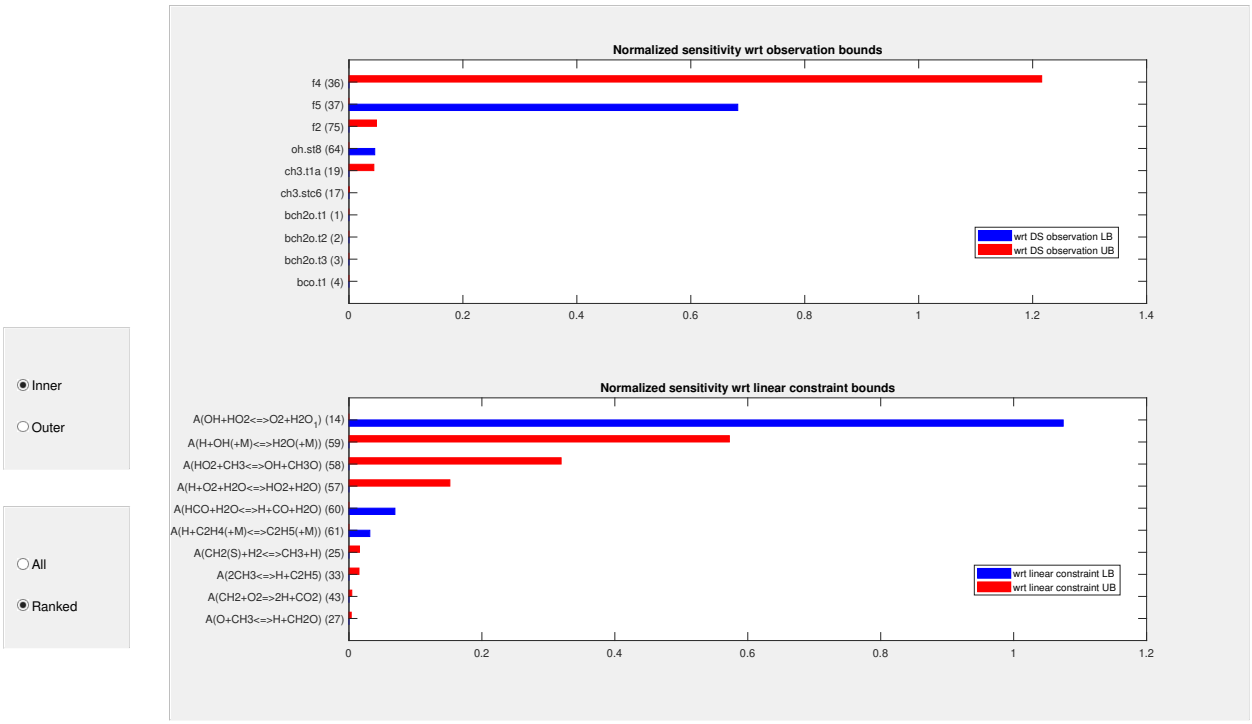

Figure 2.1: Ranked sensitivity of scalar consistency measure (SCM) inner-bound solutions with respect to the quantity of interest (QOI) and model parameter uncertainty bounds.

As presented in [23], the two top-ranked QOIs with largest sensitivity of SCM (i.e., QOI f4 and f5) were examined. Inspection of the two QOIs revealed that the removal of QOI

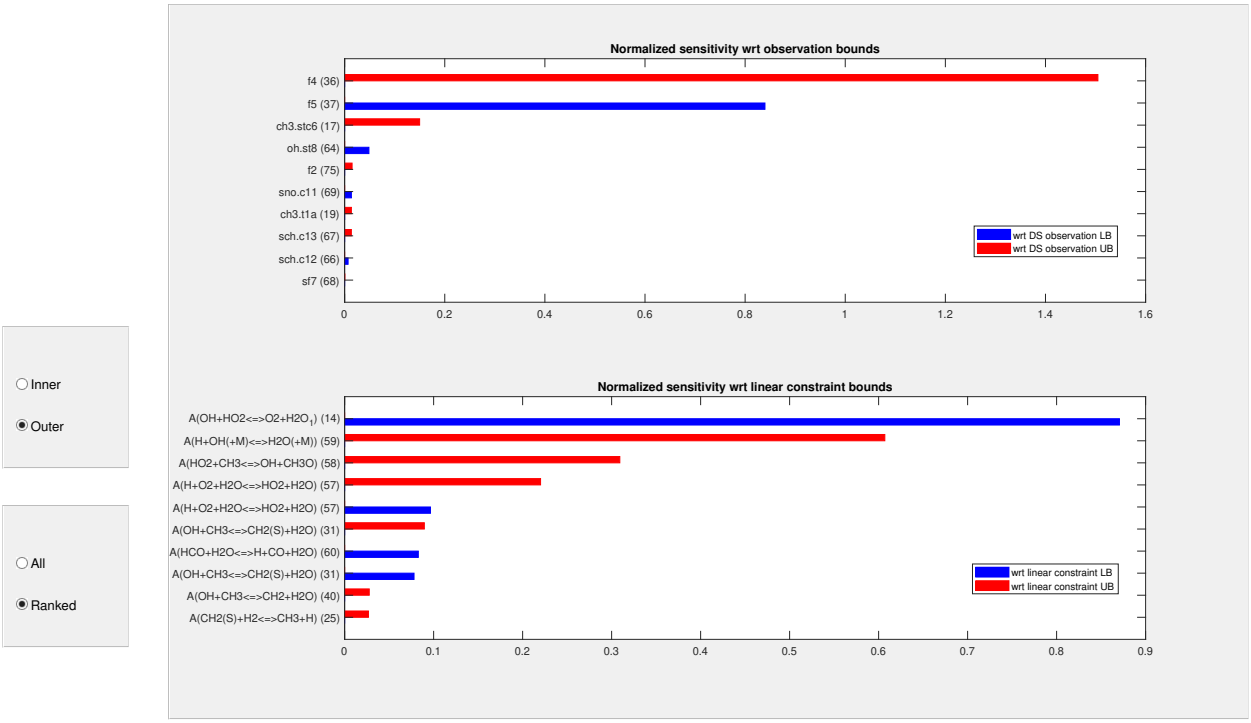

Figure 2.2: Ranked sensitivity of scalar consistency measure (SCM) outer-bound solutions with respect to the quantity of interest (QOI) and model parameter uncertainty bounds.

f5 results in a consistent dataset with the computed SCM within $[0.12, 0.24]$, whereas the removal of QOI f4 cannot regain dataset consistency. Using the consistent dataset obtained by removing f5, the prediction interval of each model parameter is calculated by replacing $M_p(x)$ with $\{x_i\}_{i=1}^{102}$ in Equations (2.7) and (2.8). The computed intervals are the projection of the feasible set along the one-dimensional (1D) coordinate directions. Among all 102 parameters, we select those whose prediction intervals are smaller than the prior uncertainty interval $[-1, 1]$ and present them in Figure 2.3. As another example, Figure 2.4 presents the ranked sensitivity of the predicted outer-bound solution of the upper uncertainty bound for parameter x_{20}.

To demonstrate the practice of predicting unmeasured QOIs, a leave-one-out calculation was conducted for the 76 QOIs in the consistent dataset. For each QOI, a new (consistent) dataset was generated by removing the predicted QOI. The prediction interval of the selected QOI was then calculated using the new dataset. The results are presented in Figure 2.5. The results reveal that, in most cases, experimental uncertainty is completely contained by both the inner- and outer-bound B2BDC prediction intervals with a noticeable margin. This implies that the inclusion of the selected QOI benefits the data collaboration process because feasible parameter vectors for the other 75 QOIs predict the target QOI outside its experimental uncertainty interval. Adding the target QOI shrinks the feasible set and

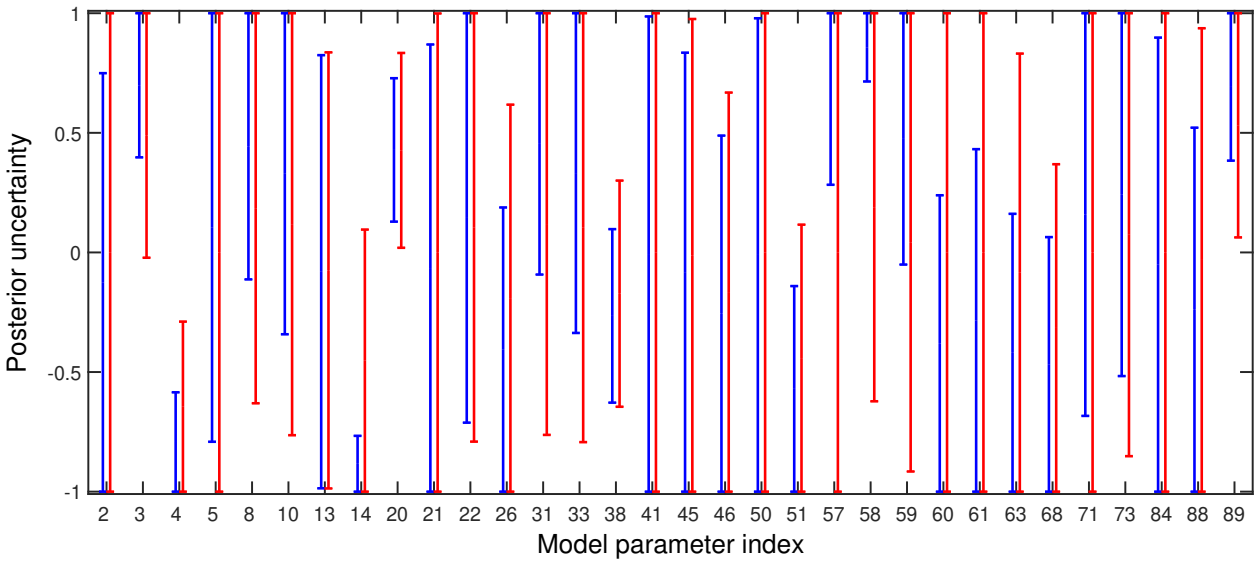

Figure 2.3: Computed prediction interval of model parameters whose posterior uncertainty is reduced compared to its prior. The blue and red vertical bars represent inner- and outer-bound solutions, respectively.

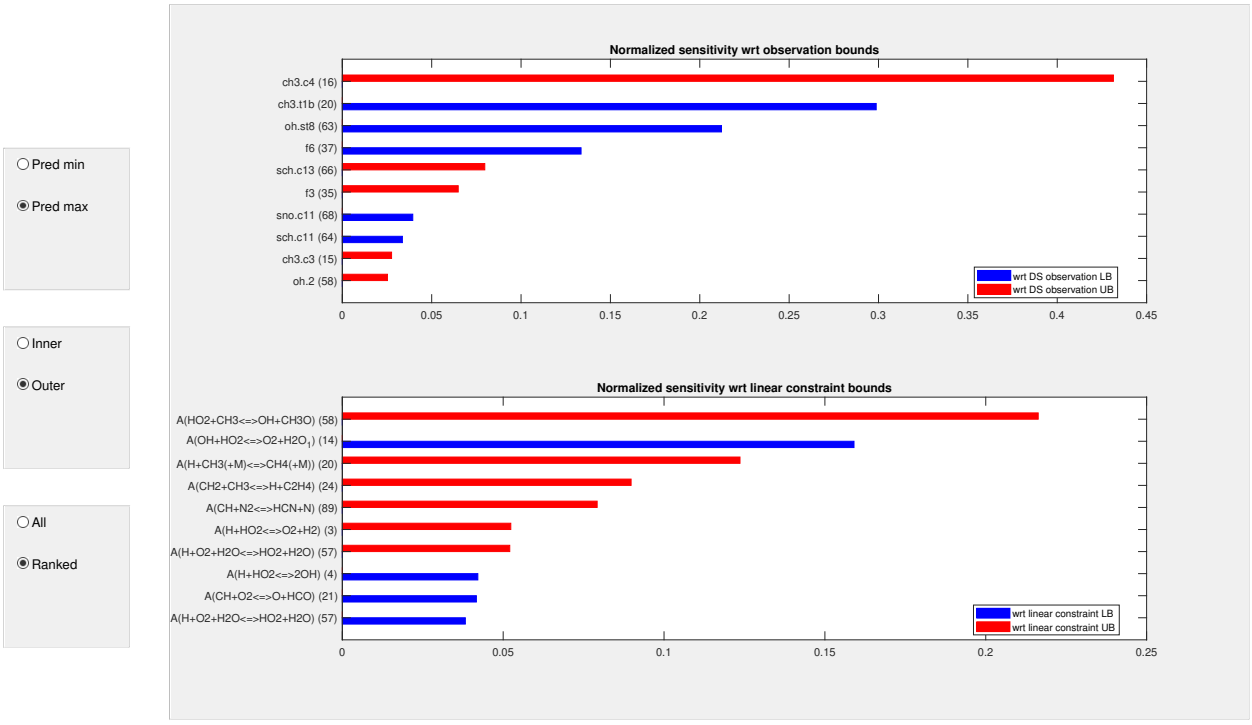

Figure 2.4: The ranked sensitivity of the outer-bound solution for the posterior upper bound of parameter x_{20}.

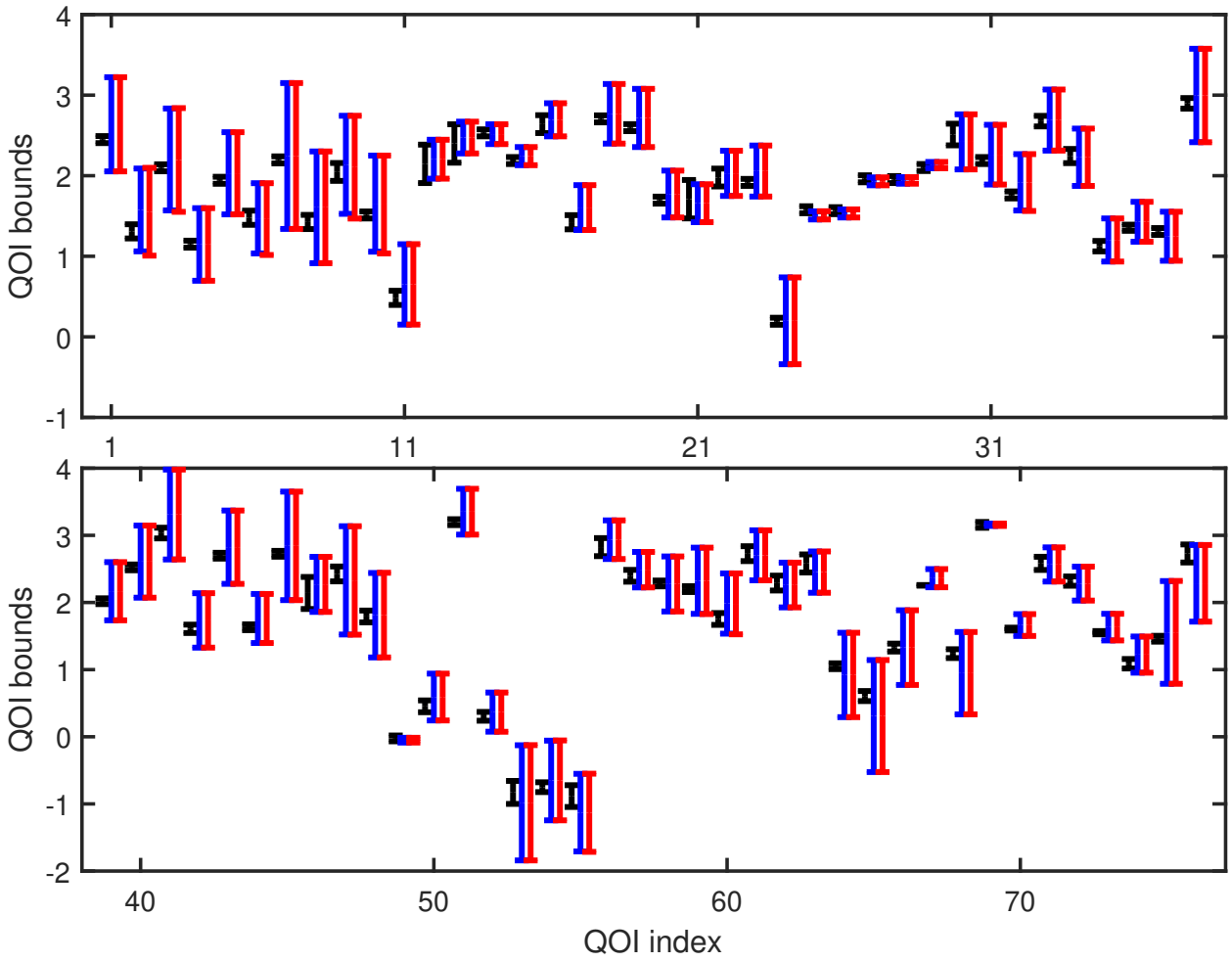

Figure 2.5: Leave-one-out prediction of quantities of interest (QOIs) in the GRI-Mech dataset. The black, blue, and red bars are experimental uncertainty bounds and bound-to-bound data collaboration (B2BDC) predicted inner and outer bounds, respectively.

improves our knowledge of the system. For QOI SR.10c, on the other hand, the outer-bound prediction interval is completely contained by the experimental uncertainty interval. For such a case, adding the target QOI to the dataset makes no change to the feasible set.

2.9 Chapter Summary

The advancement in modern computers and explosive growth in data availability offer the opportunity to improve our knowledge about the uncertainty in a physical system using data collaboration. The B2BDC framework provides a systematic approach to learning the underlying system, which is to a) progressively reduce the uncertainty in the model parameter space, b) identify cases where models and data are in disagreement, and c) quantify

uncertainty in model predictions. This chapter depicts the roadmap of the methodology and details the numerical techniques implemented for its practical use, in particular, the Solution Mapping technique and numerical optimization methods.

The essence of the B2BDC framework is (1) requiring a feasible point to reproduce all QOIs within the estimated uncertainty intervals, and (2) quantifying uncertainty from the bounds of model parameters and experimental QOIs to the bounds of the predicted QOIs. Minimal attempts have been made to differentiate feasible points except for the parameter optimization section, where subjective opinion from the analyst is included by selecting different error measures and associated weights. Consequently, the obtained knowledge after data collaboration and UQ computations (i.e., the feasible set and prediction intervals) can be used as starting points on which more subjective/informative assumptions are based. These assumptions can stem from domain expertise in specific applications. For example, statistical assumptions about the prior uncertainty in model parameters and measurement error distribution can be made, which, via the use of Bayes' theorem, produces a more nuanced probability characterization of the updated uncertainty in model parameters. The topic is discussed in the next chapter.

Chapter 3

Statistical Analysis in Bound-to-Bound Data Collaboration

The method of Bound-to-Bound Data Collaboration (B2BDC) presented in Chapter 2 uses inequality constraints to characterize the uncertainty in model parameters and experimental measurements. The set-form characterization of uncertainty is quite "uniformative" compared to the statistical assumptions made in Bayesian inference frameworks. If the given information and domain expertise allow us to select a prior distribution of the model parameters and make a statistical assumption about the measurement error distribution (i.e., to determine a likelihood function), the method of Bayesian inference can produce a posterior distribution of the model parameters. Based on the posterior distribution, not only credible intervals of quantities of interest (QOIs) can be estimated, but also subjective belief in different QOI values is reflected as the associated probability.

A comparison between the method of B2BDC and a Bayesian inference method was made in [33]. Detailed derivation of the assumed uncertainty in both methods were presented and discussed in that work. The same surrogate models were used in the B2BDC and the Bayesian frameworks. In the Bayesian framework, a uniform distribution over the prior uncertainty region $\mathcal{H}$ is employed to represent an unbiased belief in model parameter vectors from $\mathcal{H}$. The 102-dimensional GRI-Mech dataset was used for a numerical study with the Gaussian measurement error distribution considered for the Bayesian framework. The results revealed a qualitative agreement between the two methods. The B2BDC prediction intervals and the Bayesian credible intervals are similar to each other for many model parameters and QOIs, although a wide discrepancy between the two intervals was observed in a few cases. The statistical nature of the Bayesian inference provides a tool for comparing different QOI and model parameter values using their associated probability, which is not available from B2BDC computations.

In this chapter, I compare two physically inspired measurement error distributions within the context of Bayesian inference: the Gaussian and the uniform error distributions. For

both likelihood functions investigated, the resulting posterior distributions do not have a closed-form expression. Therefore, efficient sampling methods are developed based on well-known algorithms to generate samples from both posterior distributions. The results from the Bayesian inference with the two likelihood functions are compared using the GRI-Mech dataset. The case with the uniform error distribution assumption, which results in a posterior distribution of the model parameters that is uniformly distributed in the feasible set, is also compared with the B2BDC computations to provide further insights of the two frameworks in addition to the results reported in [33].

3.1 Bayesian Inference

We select the Bayesian inference framework [38, 89] in the current study. This class of statistical methods was initiated in the statistical literature by Kennedy and O'Hagan [60] and has since received substantial interest in the uncertainty quantification (UQ) field [1, 11, 55]. The method is founded on Bayes' theorem, through which a posterior distribution of model parameters is calculated by combining the prior distribution of the model parameters and a likelihood function specifying the probability of observing the included experimental data at any given parameter values.

Because we are interested in applying the method of Bayesian inference within the framework of B2BDC, it is assumed that the Bayesian analysis starts from the B2BDC dataset (i.e., the model and the experimental data with assessed uncertainty). The prior distribution of model parameters, denoted by $\pi(x)$, is assumed to be the uniform distribution over the prior uncertainty region $\mathcal{H}$:

$$\pi(x) = \mathcal{U}(\mathcal{H}) = \begin{cases} \frac{1}{V(\mathcal{H})}, & x \in \mathcal{H} \\ 0, & \text{otherwise,} \end{cases} \tag{3.1}$$

where $V(\cdot)$ is the volume of a region. The likelihood function is denoted by $\mathbb{L}(\{\mathcal{D}_e\}_{e=1}^N|x)$, and its selection is discussed in the next section. The posterior distribution, denoted by $P(x|\{\mathcal{D}_e\}_{e=1}^N)$, is computed as follows:

$$P(x|\{\mathcal{D}_e\}_{e=1}^N) = \frac{\pi(x)\mathbb{L}(\{\mathcal{D}_e\}_{e=1}^N|x)}{P(\{\mathcal{D}_e\}_{e=1}^N)} \propto \pi(x)\mathbb{L}(\{\mathcal{D}_e\}_{e=1}^N|x)). \tag{3.2}$$

The posterior distribution $P(x|\{\mathcal{D}_e\}_{e=1}^N)$ characterizes the updated uncertainty of model parameters for the Bayesian inference, conceptually similar to the feasible set for B2BDC. Uncertainty in prediction QOIs that depend on the model parameters can be inferred using general statistical approaches. Unlike the feasible set or the prediction interval, we can now compare different values in model parameters or QOI predictions by evaluating their probabilities: we believe more in values with a higher probability than those with a lower probability. However, this extra analytical availability does not come for free: it relies on the validity of the selected statistical assumptions.

3.2 Uniform Versus Gaussian Likelihood

In Bayesian inference, the likelihood function characterizes the probability of observing a given set of experimental measurements for a given model parameter vector and is the bridge connecting model and data. We investigate two measurement error distributions here: the Gaussian and the uniform distributions, and refer to the corresponding likelihood functions as the Gaussian and the uniform likelihood hereafter. The Gaussian likelihood assumption is probably the most well-known and widely applied distribution for representing errors in experimental measurements [90, 119]. The assumption has a solid foundation in the central limit theorem and provides many analytical benefits in theory development. However, situations exist where the uniform likelihood may characterize experimental measurement error more appropriately, for example, the ignition delay-time measurements in shock tubes [2, 19, 33]. In the shock tube setup, the shock propagation is initiated by a random diaphragm rupture, and the same experiment usually cannot be statistically reproduced. As a result, the uncertainty in the measurement is often reported in a $\pm$ interval expressing the maximum-error assessed based on various experimental factors [110] and/or the scattering of a series of data points measured at close but not exact conditions (see, e.g., [36, 95]).

For both likelihood functions, we assume that the experimental observations are independent of each other. For the Gaussian likelihood function, the information contained in the eth dataset unit (i.e., $\{L_e,\, d_e,$ and $U_e\}$) is used to define the distribution of the eth measurement [33]. In this study, we assume the measurement is from a Gaussian distribution centered at d_e with standard deviation $\sigma_e = 0.25(U_e - L_e)$ (i.e., the measurement error is from a zero-mean Gaussian distribution with the same standard deviation). Different choices of the mean and standard deviation of the measurement distribution are also possible but are not considered here. The resulting likelihood function, denoted by $\mathbb{L}_{\mathcal{N}}$, is as follows:

$$\mathbb{L}_{\mathcal{N}}(\{\mathcal{D}_e\}_{e=1}^N|x) = \prod_{e=1}^{N} \frac{1}{\sqrt{2\pi\sigma_e^2}} e^{-\frac{(M_e(x)-d_e)^2}{2\sigma_e^2}}, \tag{3.3}$$

where $M_e(x)$ is the model for the eth QOI. With the Gaussian likelihood defined in Equation (3.3), the posterior distribution is proportional to an exponential function whose exponent is the sum of the negative squared prediction error divided by the scaled measurement variance over all QOIs if $x \in \mathcal{H}$:

$$P_{\mathcal{N}}(x|\{\mathcal{D}_e\}_{e=1}^N) \propto \begin{cases} e^{-\sum_{e=1}^{N} \frac{(M_e(x)-d_e)^2}{2\sigma_e^2}}, & x \in \mathcal{H} \\ 0, \quad \text{otherwise} \end{cases}. \tag{3.4}$$

For the uniform likelihood, we assume the eth measurement comes from a uniform distribution within $[L_e,\, U_e]$. The likelihood function, denoted by $\mathbb{L}_{\mathcal{U}}$, is as follows:

$$\mathbb{L}_{\mathcal{U}}(\{\mathcal{D}_e\}_{e=1}^N|x) = \begin{cases} \prod_{e=1}^{N} \frac{1}{(U_e-L_e)}, & M_e(x) \in [L_e,\, U_e]\ \forall e \\ 0, \quad \text{otherwise} \end{cases}. \tag{3.5}$$

Inserting the uniform likelihood function into Equation (3.2) results in a posterior distribution that is uniformly distributed over the feasible set:

$$P_{\mathcal{U}}(x|\{\mathcal{D}_e\}_{e=1}^N) = \begin{cases} \frac{1}{V(\mathcal{F})}, & x \in \mathcal{F} \\ 0, & \text{otherwise} \end{cases} . \tag{3.6}$$

Examination of Equations (3.4) and (3.5) reveals that $P_{\mathcal{N}}(x|\{\mathcal{D}_e\}_{e=1}^N)$ and $P_{\mathcal{U}}(x|\{\mathcal{D}_e\}_{e=1}^N)$ have a nonzero probability over $\mathcal{H}$ and $\mathcal{F}$, respectively. Because the feasible set specifies the boundary for separating acceptable parameter vectors from unacceptable vectors, a posterior distribution that only generates feasible parameter vectors is preferred for a potential joint UQ analysis. Such a posterior distribution is defined as *comparable* with B2BDC in this dissertation.

The uniform likelihood function is not the unique assumption that generates a comparable posterior distribution. Any likelihood function that assumes the measurement having nonzero probability only within the B2BDC assessed uncertainty interval generates a comparable posterior distribution (e.g. a Gaussian distribution truncated by the uncertainty bounds). However, these likelihood functions are less justifiable by realistic experimental setups compared to the uniform likelihood. Therefore, among all likelihood functions that generate a comparable posterior distribution, we only considered the uniform likelihood function in this dissertation. Furthermore, the resulting posterior distribution—the uniform distribution over the feasible set—is itself an intuitively appealing choice for representing our belief about model parameters as described by bounds in B2BDC.

3.3 Sampling Methods

The UQ of a QOI depending on the model parameters usually includes the computation of its statistical moments and credible intervals. The computation often requires the integration of functions over the posterior distribution. Except for limited cases where an analytical solution exists, numerical approaches, such as the Monte Carlo methods, are applied to accomplish the computation. The Monte Carlo methods rely on the ability to generate samples from the posterior distribution, which can be quite an elaborate task, in particular, for high-dimensional applications.

The rejection sampling method with bounding geometry is a conceptually simple strategy to generate independent and identically distributed samples. However, numerical investigation (e.g., the work done in Russi's thesis [101]) reveals that the method with a bounding orthotope, ellipse, or polytope quickly becomes inefficient for a moderate problem dimension (> 7). After examining some popular sampling methods, the class of Markov chain Monte Carlo (MCMC) methods was selected to generate samples from the two posterior distributions investigated in the current study (i.e., $P_{\mathcal{N}}(x|\{\mathcal{D}_e\}_{e=1}^N)$ and $P_{\mathcal{U}}(x|\{\mathcal{D}_e\}_{e=1}^N)$).

To generate samples from $P_{\mathcal{U}}(x|\{\mathcal{D}_e\}_{e=1}^N)$, the hit-and-run (HR) sampler and the Gibbs sampler were considered. The HR sampler was proposed independently by Boneh and Golan [5], and Smith [114, 115] for uniformly sampling a bounded region. The sampler has been reported to have an outstanding mixing time in the literature [3, 4, 15, 137] and is considered the most efficient algorithm for generating uniformly distributed samples if the region is convex [71, 72]. The algorithm is summarized in Algorithm 3.1. The algorithm generates

Algorithm 3.1 The hit-and-run (HR) sampler

$X_s \leftarrow \varnothing$.
Find a starting point $x_0 \in \mathcal{F}$.
while $|X_s| < N_s$ **do**
    Generate a direction $d \sim \mathcal{N}(\mathbf{0}, \mathbb{I}_n)$.
    Calculate the line set $L_d = \{x \,|\, x \in \mathcal{F}\} \cap \{x \,|\, x = x_0 + td,\ t \in \mathbb{R}\}$.
    Choose x uniformly from L_d.
    $X_s \leftarrow X_s \cup \{x\}$ and $x_0 \leftarrow x$.
end while
Return X_s.

the candidate direction d from a standard Gaussian distribution and updates all coordinate components simultaneously in one step.

The Gibbs sampler, proposed by Geman and Geman [40], was selected due to its practical popularity in high-dimensional problems [13] despite being computationally more intensive. The Gibbs sampler updates each coordinate component sequentially according to its conditional distribution and is summarized in algorithm 3.2. For our target distribution $P_{\mathcal{U}}$, the

Algorithm 3.2 The Gibbs sampler

$X_s \leftarrow \varnothing$.
Find a starting point $x_0 \in \mathcal{F}$.
while $|X_s| < N_s$ **do**
    for $i = 1$ to n **do**
        Set $d = \mathbf{1}_i$.
        Calculate the line set $L_d = \{x \,|\, x \in \mathcal{F}\} \cap \{x \,|\, x = x_0 + td,\ t \in \mathbb{R}\}$.
        Choose x uniformly from L_d and set $x_0 \leftarrow x$.
    end for
    $X_s \leftarrow X_s \cup \{x_0\}$.
end while
Return X_s.

conditional distribution of the ith coordinate component conditioned on all other coordinates

becomes the uniform distribution over the line set $L_{\mathbf{1}_i}$ along that coordinate direction:

$$P_{\mathcal{U}}(x^i|x^1,\dots x^{i-1},x^{i+1},\dots,x^n)=\begin{cases}\frac{1}{|L_{\mathbf{1}_i}|}, & \text{if } [x^1,\dots,x^i,\dots,x^n]\in L_{\mathbf{1}_i},\\ 0, & \text{otherwise,}\end{cases} \tag{3.7}$$

where $\mathbf{1}_i$ is the ith standard basis vector. The symbol | represents "conditioned on" and $|L_{\mathbf{1}_i}|$ is the length of the line set. It is observed that both samplers involve almost identical computation steps, which are addressed next.

In both samplers, a starting feasible point is required. For a consistent dataset, this starting point is always available as an auxiliary output when we compute the inner-bound solution of the scalar consistency measure (SCM). We assume only quadratic or rational quadratic surrogate models are used for the following derivation. Thus, the feasible set is described by a finite set of linear and quadratic inequalities:

$$\begin{aligned}&\mathcal{F}=\{x\mid \mathcal{L}_\alpha(x)\le 0,\ \mathcal{Q}_\beta(x)\le 0,\ \alpha=1,2,\dots,n_l,\ \beta=1,2,\dots,n_q\},\\ &\mathcal{L}_\alpha(x)=b_\alpha+a_\alpha^T x,\\ &\mathcal{Q}_\beta(x)=c_{0,\beta}+c_{1,\beta}^T x+x^T C_{2,\beta}x,\end{aligned} \tag{3.8}$$

where b_α and $c_{0,\beta}$ are scalars, a_α and $c_{1,\beta}$ are vectors, and $C_{2,\beta}$ is a symmetric matrix with proper dimensions.

Once a direction d is generated, the line set in model parameters x can be equivalently expressed in a scalar variable t:

$$\begin{aligned}&L_t=\{t\mid \widetilde{\mathcal{L}}_\alpha(t)\le 0,\ \widetilde{\mathcal{Q}}_\beta(t)\le 0,\ \alpha=1,2,\dots,n_l,\ \beta=1,2,\dots,n_q\},\\ &\widetilde{\mathcal{L}}_\alpha(t)=\widetilde{b}_\alpha+\widetilde{a}_\alpha t,\\ &\widetilde{\mathcal{Q}}_\beta(t)=\widetilde{c}_{0,\beta}+\widetilde{c}_{1,\beta}t+\widetilde{c}_{2,\beta}t^2.\end{aligned} \tag{3.9}$$

The tilde coefficients in eq. (3.9) are calculated by the following Equation (3.10):

$$\begin{aligned}&\widetilde{a}_\alpha=a_\alpha^T d,\\ &\widetilde{b}_\alpha=b_\alpha+a_\alpha^T x_0,\\ &\widetilde{c}_{0,\beta}=c_{0,\beta}+c_{1,\beta}^T x_0+(x_0)^T C_{2,\beta}x_0,\\ &\widetilde{c}_{1,\beta}=c_{1,\beta}^T d+2d^T C_{2,\beta}x_0,\\ &\widetilde{c}_{2,\beta}=d^T C_{2,\beta}d.\end{aligned} \tag{3.10}$$

The line set L_t can be represented as a union of finite disjoint intervals whose endpoints are the roots of one of the linear or quadratic functions in Equation (3.9). To calculate the union, the roots of all linear functions $\{\widetilde{\mathcal{L}}_\alpha(t)\}_{\alpha=1}^{n_l}$ are calculated first. We denote the largest negative and smallest positive roots by $\underline{t}$ and $\overline{t}$, respectively. If no negative or positive roots

exist, $\underline{t}$ and $\bar{t}$ are set to $-\infty$ and ∞ accordingly. Because $t = 0$ is feasible and linear functions are monotonic, the line set L_t is contained in $[\underline{t}, \bar{t}]$. The roots of the quadratic functions $\{\widetilde{\mathcal{Q}}_\beta(t)\}_{\beta=1}^{n_q}$ are then calculated and the distinct real roots that lie within $[\underline{t}, \bar{t}]$ are retained for the subsequent computation. The remaining roots are sorted and denoted by $\{t_k\}_{k=1}^{r}$ such that $\underline{t} = t_1 < t_2 < \ldots < t_r = \bar{t}$.

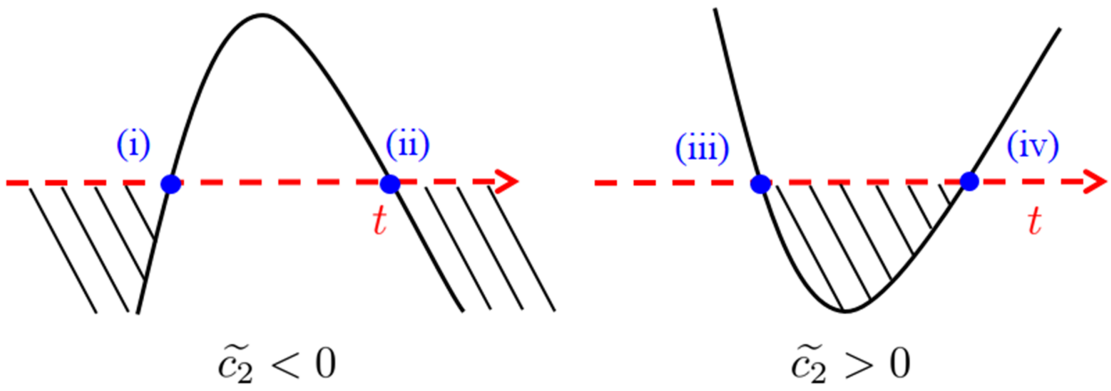

Figure 3.1: Sketch plot of a scalar quadratic function $\widetilde{\mathcal{Q}}(t) = \widetilde{c}_0 + \widetilde{c}_1 t + \widetilde{c}_2 t^2$ with two distinct real roots. The solid black line represents the quadratic function and the dashed red line represents $\mathcal{Q}(t) = 0$. Roots are labeled (i) and (ii) for a negative a value and (iii) and (iv) for a positive a value.

An interval made of two adjacent roots, $[t_k, t_{k+1}]$, is contained in L_t and is referred to as a feasible interval if its midpoint is in L_t. A brute-force check over all these intervals scales with the number of distinct real roots, r, can become inefficient when r is large. To accelerate the computation, the search algorithm is modified based on the following observation. Consider a scalar quadratic function with roots labeled as shown in Figure 3.1 depending on the sign of $\widetilde{c}_2$, with the shaded regions denoting t values satisfying the feasibility condition in Equation (3.9). When t increases, roots (i) and (iv) correspond to a transition from feasible t values to infeasible values, whereas roots (ii) and (iii) do the opposite. A feasible interval is termed isolated if it moves outside the interval from both endpoints corresponding to a transition from feasible t values to infeasible values. Suppose moving toward smaller t values violates the feasibility condition at a root t_k. Therefore, t_k is the left endpoint of an isolated feasible interval in L_t. The corresponding right endpoint can be found by sequentially checking the roots t_{k+1}, t_{k+2}, and so on until the first type (i) or (iv) root is found, denoted by t_k^*. If t_k^* is a type (iv) root, no further isolated feasible intervals exist beyond t_k^* because any t value greater than t_k^* breaks at least the quadratic inequality associated with t_k^*. If t_k^* is a type (i) root, the left endpoint of the next isolated feasible interval must be no smaller than the type (ii) root associated with the same quadratic function. Hence, we can start our

Algorithm 3.3 Modified search algorithm

$L_t \leftarrow \varnothing$.
Find the index k such that $t_k \leq 0 < t_{k+1}$.
Set $\underline{k} \leftarrow k$ and $\overline{k} \leftarrow k+1$.
while $\underline{k} > 1$ and $t = (t_{\underline{k}} + t_{\underline{k}-1})/2$ is feasible **do**
    $\underline{k} \leftarrow \underline{k} - 1$.
end while
while $\overline{k} < r$ and $t = (t_{\overline{k}} + t_{\overline{k}+1})/2$ is feasible **do**
    $\overline{k} \leftarrow \overline{k} + 1$.
end while
$L_t \leftarrow L_t \cup [t_{\underline{k}}, t_{\overline{k}}]$.
while $t_{\underline{k}}$ is a type (ii) root and the type (i) root of the same quadratic is in $\{t_k\}_{k=1}^r$ **do**
    Find index k such that t_k is the type (i) root and set $\underline{k} \leftarrow k$.
    while $\underline{k} > 1$ and $t = (t_{\underline{k}} + t_{\underline{k}-1})/2$ is infeasible **do**
        $\underline{k} \leftarrow \underline{k} - 1$
    end while
    if $\underline{k} > 1$ **then**
        Set $L_r \leftarrow t_{\underline{k}}$.
        while $\underline{k} > 1$ and $t = (t_{\underline{k}} + t_{\underline{k}-1})/2$ is feasible **do**
            $\underline{k} \leftarrow \underline{k} - 1$.
        end while
        $L_t \leftarrow L_t \cup [t_{\underline{k}}, L_r]$
    end if
end while
while $t_{\overline{k}}$ is a type (i) root and the type (ii) root of the same quadratic is in $\{t_k\}_{k=1}^r$ **do**
    Find index k such that t_k is the type (ii) root and set $\overline{k} \leftarrow k$.
    while $\overline{k} < r$ and $t = (t_{\overline{k}} + t_{\overline{k}+1})/2$ is infeasible **do**
        $\overline{k} \leftarrow \overline{k} + 1$
    end while
    if $\overline{k} < r$ **then**
        Set $L_l \leftarrow t_{\overline{k}}$.
        while $\overline{k} < r$ and $t = (t_{\overline{k}} + t_{\overline{k}+1})/2$ is feasible **do**
            $\overline{k} \leftarrow \overline{k} + 1$.
        end while
        $L_t \leftarrow L_t \cup [L_l, t_{\overline{k}}]$
    end if
end while
Return L_t.

check from the type (ii) root if it is in the root list, and all the roots between are skipped.

The procedure for a given right endpoint, moving along the decreasing t direction, follows similar arguments. The modified search algorithm is summarized in Algorithm 3.3.

To generate samples from $P_{\mathcal{N}}$, we selected the component-wise adaptive metropolis (AM) method [47]. The AM sampler is summarized in Algorithm 3.4. The variance is updated

Algorithm 3.4 Adaptive metropolis sampler

$X_s \leftarrow \varnothing$.
Find a starting point $x_0 \in \mathcal{H}$.
Define an initial variance v_i for each coordinate component x_i.
while $|X_s| < N_s$ **do**
    for $i = 1$ to n **do**
        Draw a candidate component $\Delta x^i \sim \mathcal{N}(0, v^i)$.
        Define the candidate point x' by $x' = x_0 + \Delta x_i \mathbf{1}_n$.
        Accept the candidate with probability $\gamma = \frac{P_{\mathcal{N}}(x')}{P_{\mathcal{N}}(x_0)}$ and update $x_0 \leftarrow x'$.
    end for
    $X_s \leftarrow X_s \cup \{x_0\}$.
    Update the variance v_i based on all samples.
end while
Return X_s.

according to Equation (3.11)

$$v_t^i = \begin{cases} v_0^i, & t \le t_0 \\ s(\mathrm{Var}(x_0^i, x_1^i, \ldots, x_{t-1}^i) + \epsilon), & t > t_0, \end{cases} \tag{3.11}$$

where v_0^i and t_0 are the user-initiated variance and number of burning samples. The symbol $\mathrm{Var}(x_0^i, x_1^i, \ldots, x_{t-1}^i)$ calculates the variance of samples $\{x_j^i\}_{j=0}^{t-1}$. The parameter s is set to 2.4, and ϵ is set to a smaller number depending on the application. With the notation that $g_t = \mathrm{Var}(x_0^i, x_1^i, \ldots, x_{t-1}^i)$ and $\overline{x}_t = \mathrm{Mean}(x_0^i, x_1^i, \ldots, x_{t-1}^i)$, the variance term in Equation (3.11) has a simple recursive formula:

$$g_{t+1} = \frac{t-1}{t} g_t + \overline{x}_t^2 + \frac{1}{t} x_t^2 - \frac{t+1}{t} \overline{x}_{t+1}^2, \tag{3.12}$$

which is used to accelerate the computation.

3.4 Convergence Diagnosis

Iterative sampling methods, for example MCMC, converge to the stationary distribution only asymptotically. Therefore, it is necessary to monitor the convergence of the generated samples to validate the following inference analysis. We adopted the convergence test approach proposed by Gelman and Rubin [39] and Brooks and Gelman [10]. The idea is to

generate multiple MCMC chains and monitor calculable statistics that should converge to 1 as the samples converge to the target distribution. The after-sample calculation is summarized in Equation (3.13), with the notation that x_{pq} ($p = 1, 2, \ldots, N_s$, $q = 1, 2, \ldots, m$) represents the pth sampled parameter vector in the qth MCMC chain.

$$\begin{aligned}
x_{\cdot q} &= \frac{1}{N_s}\sum_{p=1}^{N_s} x_{pq}, \\
x_{\cdot\cdot} &= \frac{1}{N_s m}\sum_{p=1}^{N_s}\sum_{q=1}^{m} x_{pq}, \\
B &= \frac{1}{m-1}\sum_{q=1}^{m}(x_{\cdot q} - x_{\cdot\cdot})(x_{\cdot q} - x_{\cdot\cdot})^T, \\
W &= \frac{1}{m(N_s-1)}\sum_{p=1}^{N_s}\sum_{q=1}^{m}(x_{pq} - x_{\cdot q})(x_{pq} - x_{\cdot q})^T, \\
V &= \frac{N_s-1}{N_s}W + \frac{m+1}{m}B, \\
\lambda_1 &= \lambda_{\max}(W^{-1}B), \\
R &= \frac{N_s-1}{N_s} + \frac{m+1}{m}\lambda_1.
\end{aligned} \tag{3.13}$$

The symbols $x_{\cdot q}$ and $x_{\cdot\cdot}$ are averages in the qth MCMC chain and for all m chains. Moreover, V and W are the estimated among-chain and within-chain covariance matrices, and $\sqrt{R}$ is the monitored statistic referred to as the *multivariate potential scale reduction factor* (MPSRF). The notation $\lambda_{\max}(\cdot)$ denotes the largest eigenvalue of a matrix. The MPSRF provides a scalar distance measure between the two covariance matrices as follows:

$$R = \max_a \quad \frac{a^T V a}{a^T W a}. \tag{3.14}$$

We present two strategies to generate the initial points. The first strategy is to generate one MCMC chain, for example, starting from the feasible point obtained by calculating the inner-bound solution of the SCM, and choosing multiple points from that chain randomly or with a preset step size. The second strategy is motivated by the emphasis addressed in [10, 39] that the initial points should be over-dispersed relative to the target distribution. For the uniform distribution in the feasible set, we aim to distribute the initial points to be as widespread in the feasible set as possible. To achieve this goal, the following optimization problem is solved for m initial feasible points where $\mathcal{C}$ is the estimated covariance matrix

based on these m initial points:

$$\begin{aligned} \underset{\{x_j\}_{j=1}^m}{\text{maximize}} \quad & \sum_{j=1}^{m-1} \log \lambda_j(\mathcal{C}) \\ \text{subject to} \quad & x_j \in \mathcal{F},\ j = 1, 2, \ldots, m. \end{aligned} \tag{3.15}$$

The formula is similar to the D-optimal design [62] over the feasible set. However, because the covariance matrix can be singular when $m + 1$ is smaller than the problem dimension, we maximize the product of the first $m - 1$ nonzero eigenvalues.

The initial points generated by the two strategies are respectively referred to as the MCMC and optimized starting points. The computation is usually more costly for the second strategy, in particular, for situations in which the number of model parameters and/or the initial points is large.

3.5 Exploiting Sparsity and Generalization with Polynomial Surrogates

As demonstrated in the GRI-Mech example given in Section 2.8, models for an individual QOI can depend on a much smaller set of active parameters despite the dataset containing a parameter list in a quite higher dimension (102). Detailed in Section 2.7.1, this sparsity feature is exploited in our strategies for generating surrogate models. Shown in [33], evaluating surrogate models in the active parameter space compared to the full-dimensional parameter space can result in substantial computational savings in MCMC calculations, for example, the number of algebraic operations involved in evaluating a quadratic function with input parameter vector scales with the square of its parameter dimension. In the HR and Gibbs samplers, converting the line set in x to the line set in t using Equation (3.10) has the highest computational cost, which, by the definitions given in Equations (3.9) and (3.10), has the benefit of using active parameters similarly to surrogate model evaluations. For the AM sampler, the step that involves the most computations is the calculation of the acceptance probability γ, which essentially contains only surrogate model evaluations and, therefore, is also enhanced. The Gibbs and AM sampler can further take advantage of such a sparsity feature. When updating a coordinate component x^i in the Gibbs sampler, roots are computed only for quadratic (linear) functions that depend on x^i. When the AM sampler is used, the summation in the acceptance probability γ can be performed only over QOIs that depend on x^i.

The line set calculation in the HR and Gibbs samplers can be very challenging for models whose complete list of roots along a given direction is difficult to compute. Fortunately, the strategy discussed for quadratic surrogate models can be generalized for real-coefficient polynomials with moderate modifications. In that situation, the line set L_t is defined by a

finite number of scalar polynomial inequalities. Following similar logic, linear inequalities are used first to calculate a bounding interval for L_t. The list of candidate roots is then generated by considering the distinct real roots of the constraining polynomials. For a scalar polynomial, efficient tools exist for computing all these roots (e.g., MATLAB function `roots`). The search algorithm is modified accordingly. The calculation of the first isolated interval remains unchanged (lines 2-10) in Algorithm 3.3). For a right endpoint of an isolated interval, the roots of the same polynomial greater than this right endpoint are checked sequentially to determine a lower bound for the next potential left endpoint: the first root of the same polynomial that corresponds to a transition from infeasible to feasible and is in the root list, or infinity if no such root is found. The same argument applies to the left endpoint. The procedure of finding an isolated interval from one endpoint remains the same.

The developed HR and Gibbs samplers can generate samples from the B2BDC feasible set defined with all three types of surrogate models. A set defined by a finite number of polynomial inequalities is also known as a *semi-algebraic set*, which has gathered extensive research interest in other scientific domains, such as control [53] and semidefinite programming [91]. The developed HR and Gibbs samplers may also be applied in other applications.

3.6 A Toy Example

A 2D toy example is used in this section for illustration. The feasible set is described by the following four quadratic inequalities with a prior uncertainty region for model parameters at $[-1,\, 1]^2$:

$$\begin{aligned} -5.23 \le S_1(x) = 4x_1^2 - 11x_2^2 + 2.5x_1x_2 - 1.8x_1 - 1.2x_2 - 0.4 \le -3.23 \\ -1.45 \le S_2(x) = 4x_1^2 - x_2^2 - 7.5x_1x_2 + 2.2x_1 - 1.2x_2 - 0.2 \le 0.55 \end{aligned}. \tag{3.16}$$

The Gaussian likelihood is based on the assumption that the two "measurements" are from a Gaussian distribution centered at $d_1 = -4.23$ and $d_2 = -0.45$ with $\sigma_1 = \sigma_2 = 0.5$, whereas the uniform likelihood assumes that they are from a uniform distribution within the corresponding uncertainty intervals given in Equation (3.16). The HR, Gibbs, and AM samplers were applied with 10 starting points. An MCMC chain with 200 samples was generated from each initial point. The sample set including the second half of all 10 MCMC chains was used for the convergence test. The calculated MPSRF and the determinant of the among-chain and within-chain covariance matrices are presented in Figure 3.2. The results suggest that the samples generated from all three samplers converged. The MPSRF decreases to close to 1, and the two determinants have stabilized and reached values close to each other.

This converged sample set of 10^3 total parameter vectors is used to further demonstrate a typical analysis in UQ. The 1D projections of the samples on x_1 and x_2 are examined first. The sample-based histograms and the computed outer-bound prediction intervals are illustrated in Figure 3.3. The results reveal that the histograms of HR and Gibbs samples

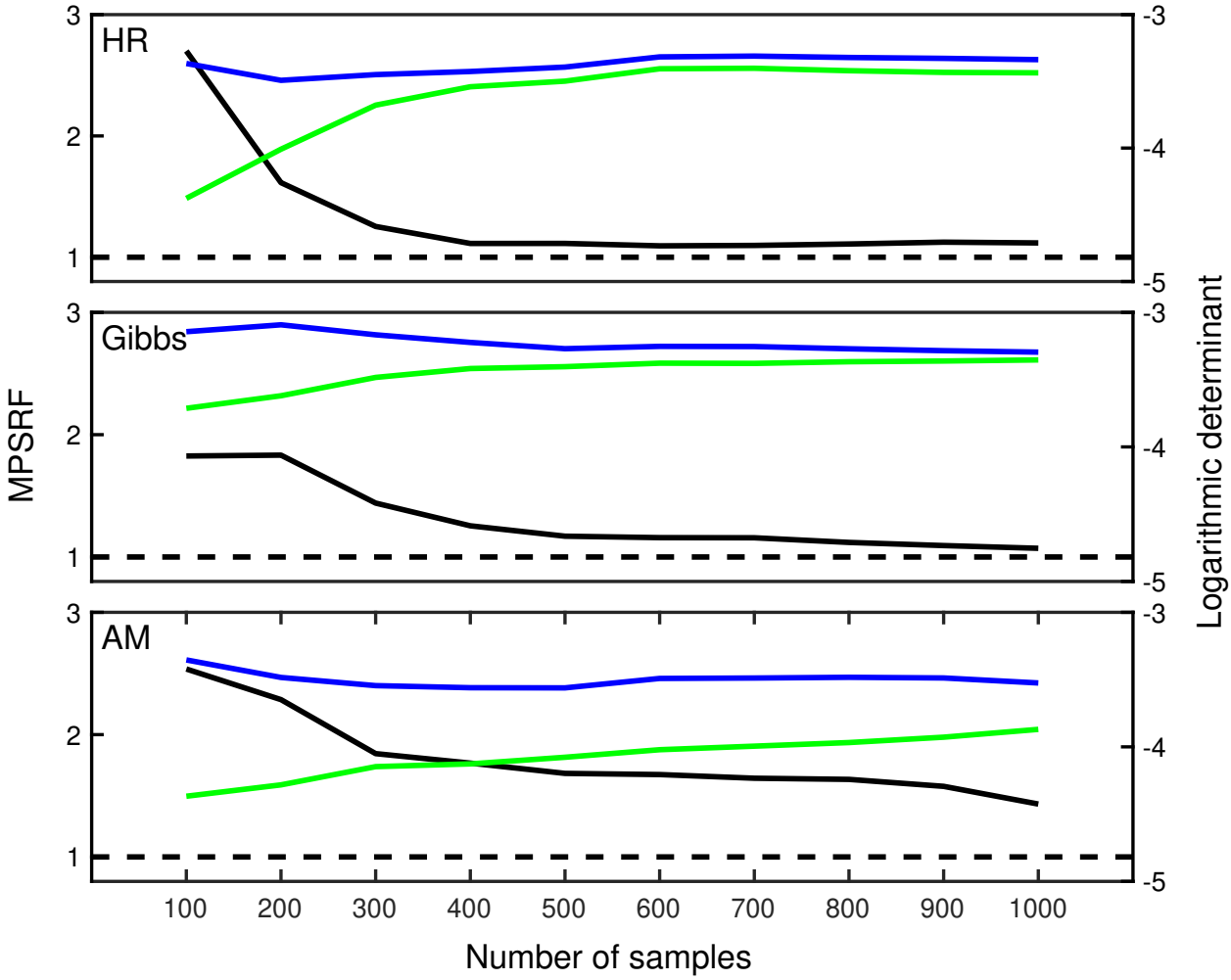

Figure 3.2: Convergence test results of the hit-and-run (HR), Gibbs, and adaptive metropolis (AM) samples based on 10 Markov chain Monte Carlo (MCMC) chains. The black line is the multivariate potential scale reduction factor. The blue and green lines are the logarithmic determinants of the between-sample and within-sample covariance matrices, respectively.

cover an identical range of prediction intervals, whereas the histogram of the AM samples goes slightly beyond the predicted bounds. Considering the random effects caused by the finite sample size, the histograms based on the HR and Gibbs samples for x_1 are reasonably similar to each other and are different from the histogram based on the AM samples. The histogram based on the AM samples exhibits a higher frequency of larger x_1 values. The three histograms of x_2 display no significant differences among the three sample sets.

The samples are then visualized in the 2D space, and their scatter plots are given in Figure 3.4 with the prior region $\mathcal{H}$ and feasible set $\mathcal{F}$. The HR and Gibbs samples cover the feasible set quite uniformly and completely, as expected from a converged sample set.

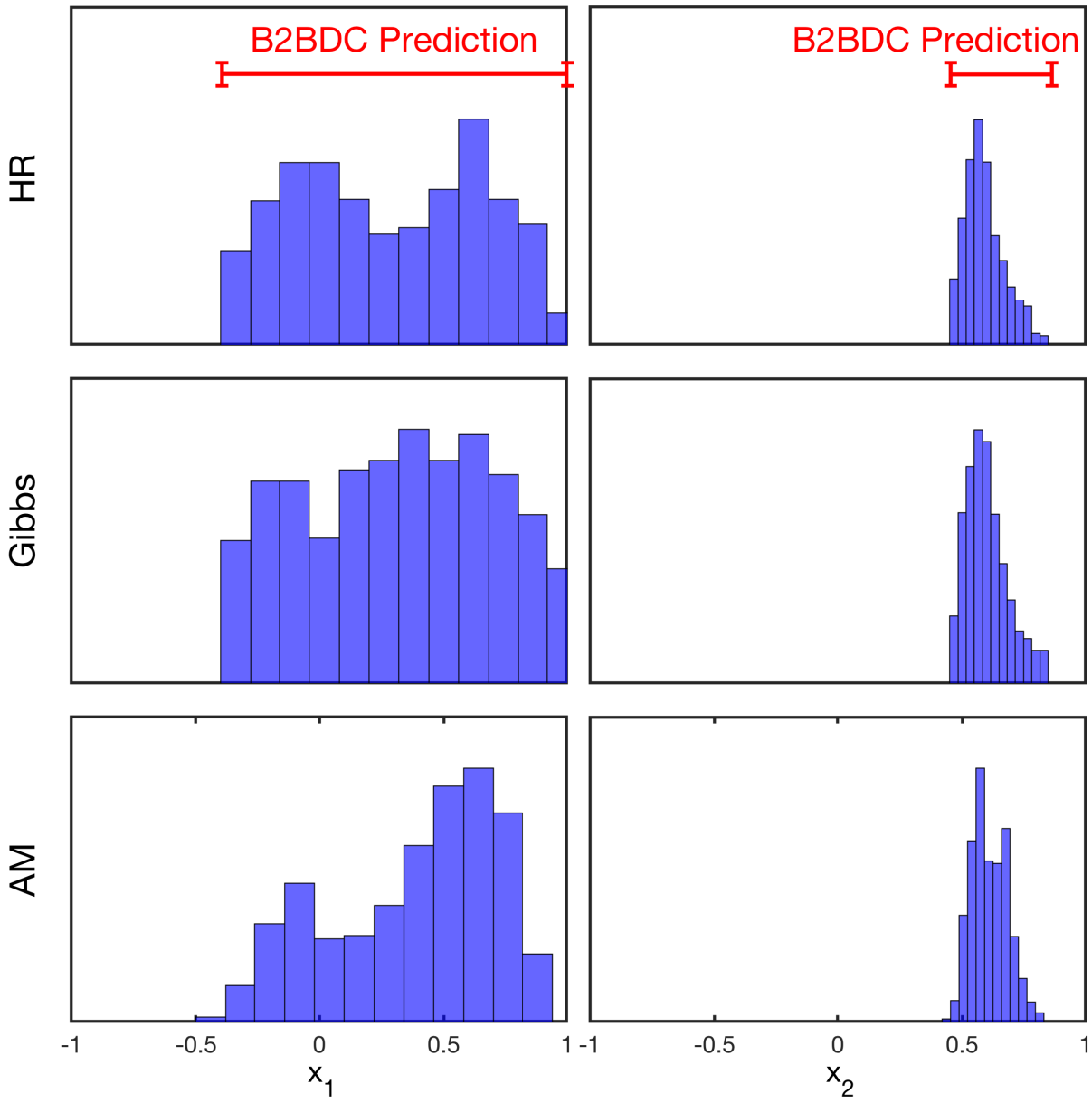

Figure 3.3: Marginal histograms of the generated samples and computed Bound-to-Bound data collaboration (B2BDC) prediction intervals for x_1 and x_2.

However, the AM samples exhibit a mild clustering at some interior regions of the feasible set. A small portion of the AM samples (58 out of 1000) is outside the feasible set but remains reasonably adjacent.

There are a couple of interesting observations from this 2D toy example. First, the

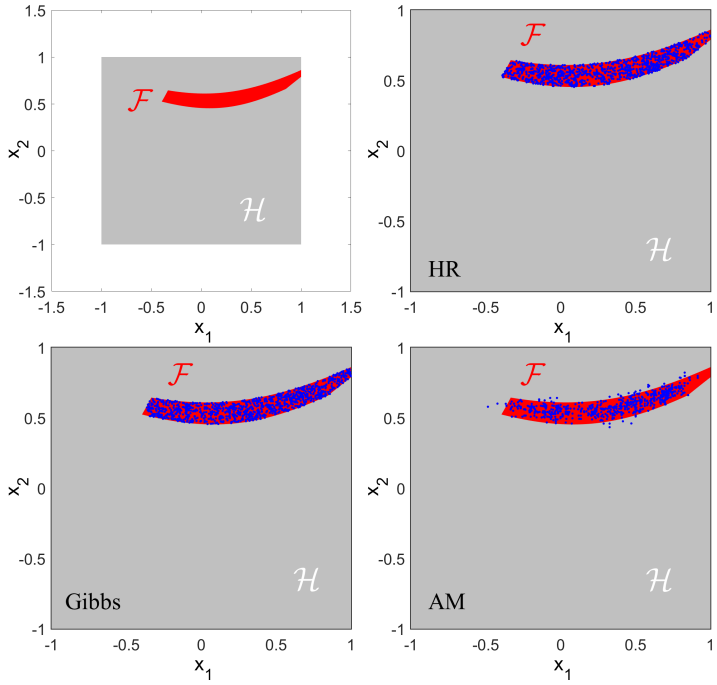

Figure 3.4: Scatter plots of hit-and-run (HR), Gibbs, and adaptive metropolis (AM) samples and the prior $\mathcal{H}$ (shaded gray) and the feasible set $\mathcal{F}$ (shaded red).

optimization-based prediction interval of any QOI is reproducible using the HR and Gibbs samples because they cover almost the whole feasible set. Second, most of the AM samples still fall in the feasible set. To determine whether the above observations hold for higher-dimensional problems, in the next section, we use the 102-dimensional GRI-Mech dataset for the demonstration.

3.7 GRI-Mech Example

Introduced in Section 2.8, the GRI-Mech dataset has 102 model parameters and 77 QOIs. The prior uncertainty region of the model parameters is $\mathcal{H} = [-1, 1]^{102}$, and quadratic surrogate models were generated for all QOIs. To obtain a consistent dataset with a nonempty feasible set, QOI f5 was removed as detailed in Section 2.8. We first evaluate and compared the performance of the HR and Gibbs samplers on generating uniform samples from the GRI-Mech feasible set. The posterior distributions with the Gaussian and with the uniform likelihoods are then compared. At last, we compare the B2BDC prediction intervals with the statistical inferences based on uniformly distributed samples in the feasible set.

3.7.1 Hit-and-run Versus Gibbs

To investigate the mixing performance of the HR and Gibbs samplers, multiple chains were generated from both the MCMC and optimized starting points. The MCMC starting points were generated with a step size of 100 from the MCMC chain initiated at the SCM inner-bound solution point. The optimized points were computed as solutions to the optimization problem (3.15). The number of starting points was set to 10. For each starting point, an MCMC chain of length $N_s = 10^4$ was generated, applying both samplers.

The trace and sampled autocorrelation $\hat{A}_k$, defined by Equation (3.17) for a scalar quantity y, where $\overline{y}$ and k are the mean of the samples and the lag number, are displayed in Figure 3.5 for parameter x_{32}:

$$\begin{aligned} A_k &= \frac{1}{N_s} \sum_{j=1}^{N_s-k} (y_j - \overline{y})(y_{j+k} - \overline{y}), \\ \hat{A}_k &= \frac{A_k}{A_0}. \end{aligned} \tag{3.17}$$

The results indicate that the autocorrelation is significantly higher in the HR samples than in the Gibbs samples. The Gibbs samples traverse the entire prior uncertainty interval, whereas the HR samples move within a much narrower region close to the upper uncertainty bound. The chain starts from an optimized point (right column in Figure 3.5) that has a slightly higher autocorrelation than from an MCMC point for the HR sampler. The difference is negligibly small for the Gibbs sampler.

The component-wise and full-dimensional step sizes, denoted by Δx^i and $\Delta \|x\|_2$, are calculated for each MCMC chain using Equation (3.18), and the results are given in Figures 3.6 and 3.7:

$$\begin{aligned} \Delta x^i &= \frac{1}{N_s - 1} \sum_{j=2}^{N_s} |x_j^i - x_{j-1}^i|, \\ \Delta \|x\|_2 &= \frac{1}{N_s - 1} \sum_{j=2}^{N_s} \|x_j - x_{j-1}\|_2 . \end{aligned} \tag{3.18}$$

The results reveal that the component-wise step sizes are distributed more unevenly in the Gibbs samples compared to those in the HR samples, independent of the starting-point type. The mean and standard deviation of component-wise step sizes are similar across all coordinates for the HR samples; however, they are quite different for the Gibbs samples. The results demonstrate that the Gibbs sampler can explore different coordinates with different lengths of scales. The mean component-wise step sizes of the Gibbs samples exhibit negligible dependence on the starting-point type, varying within 4% from one to another. In contrast, roughly twice larger mean step sizes are observed across all coordinates for the HR samples starting from an MCMC point compared to an optimized point. Using all 20 MCMC chains,

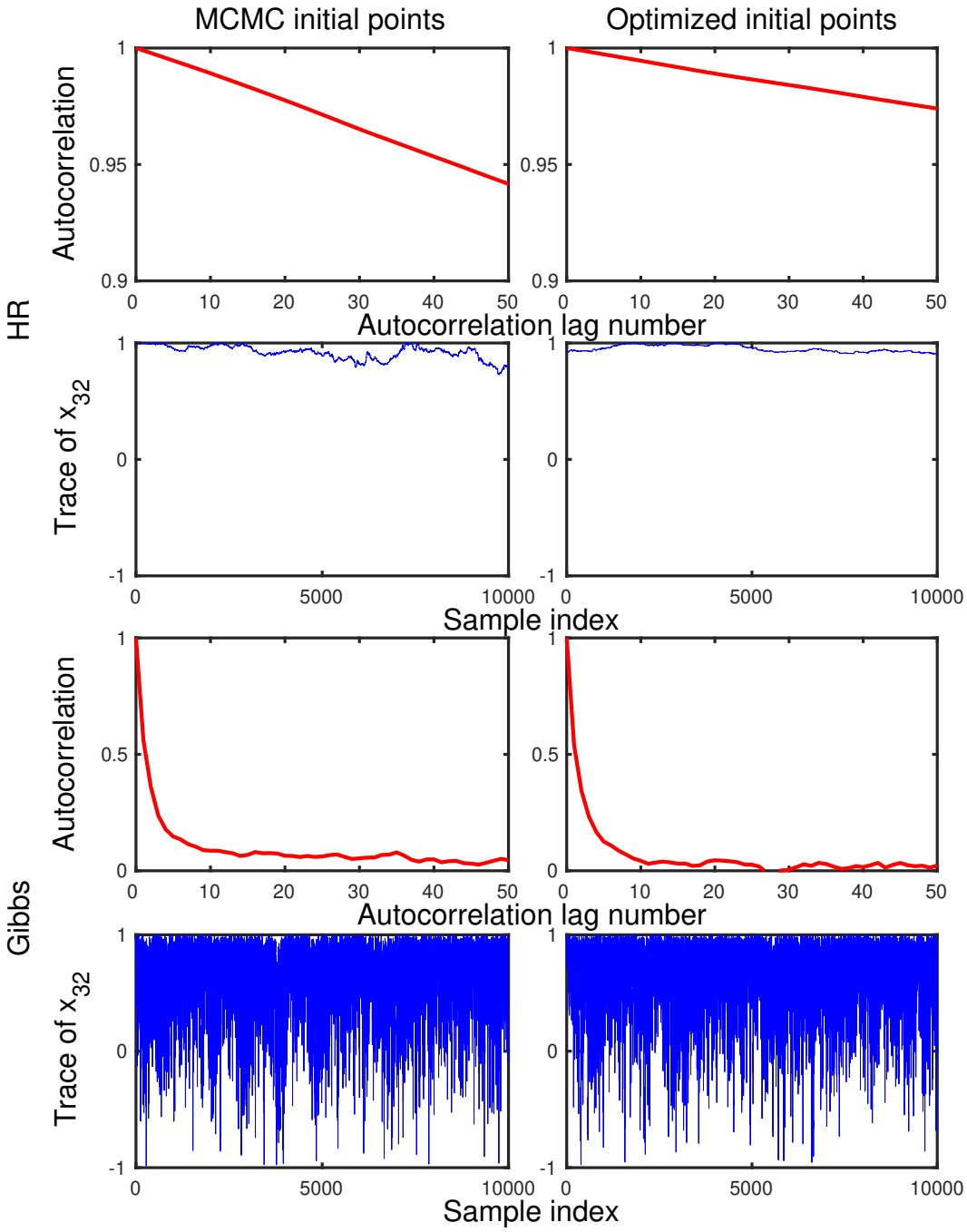

Figure 3.5: Trace (blue line) and sampled autocorrelation (red line) of parameter x_{32}. The left and right columns contain results in a chain starting from an MCMC and optimized point, respectively. The top and bottom two rows are results for the hit-and-run (HR) and Gibbs samples, respectively.

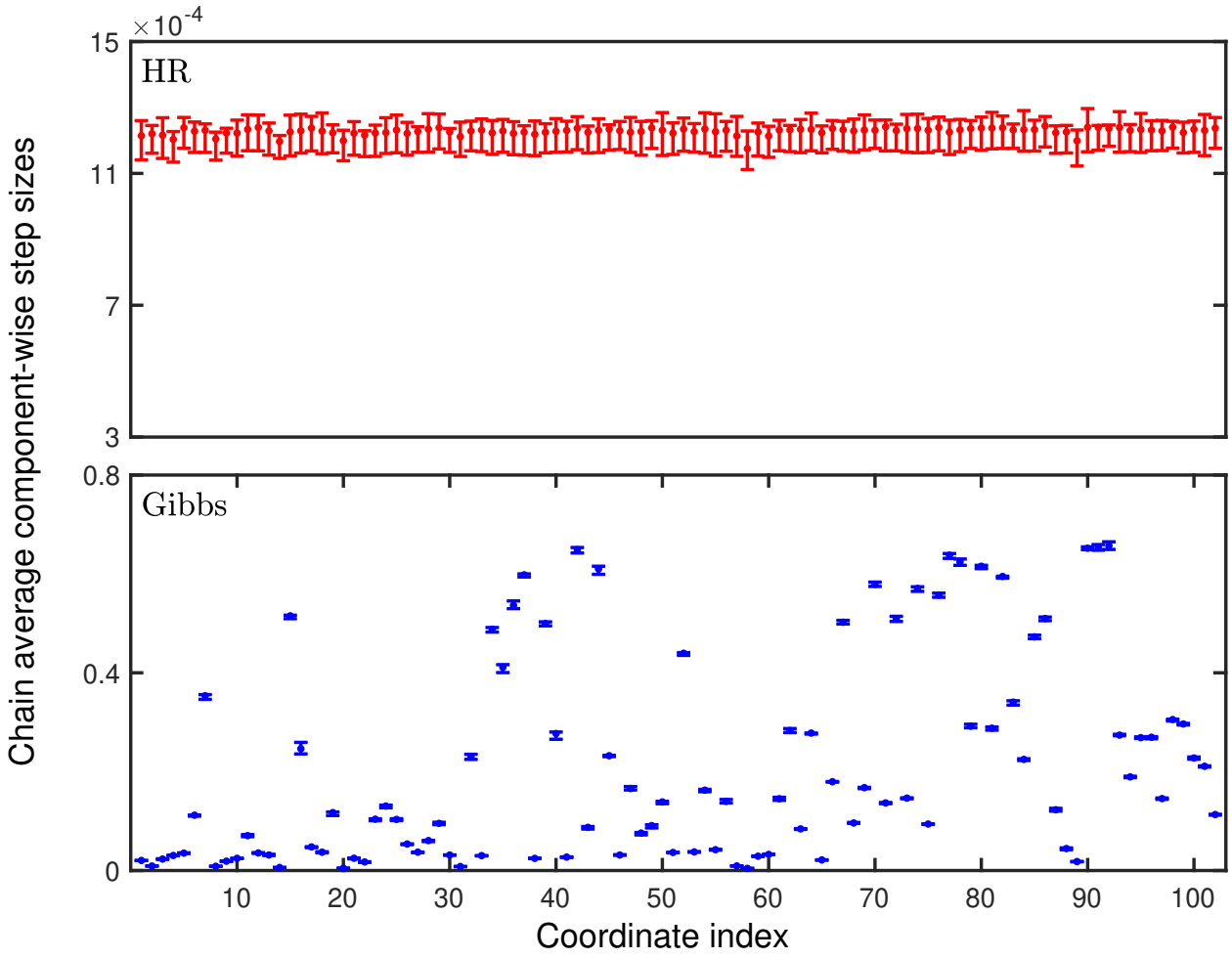

Figure 3.6: Component-wise step sizes in the generated Markov chain Monte Carlo (MCMC) chains starting from MCMC points. The points and vertical bars are the computed means and 1σ confidence intervals.

the computed ratio of the mean step sizes in the Gibbs samples compared to those in the HR samples varies from 3.7 to over 1500 across the coordinates with an average value of over 300.

The averaged full-dimensional step sizes, consumed computer processing unit (CPU) time, and ratio of feasibility evaluations in the modified to the brute-force search algorithms are reported in Table 3.1 based on all chains. Examination of Table 3.1 shows that the full-dimensional step size in the Gibbs samples is about 360 times of that in the HR samples. The modified search algorithm provides 75% and 60% computation savings for the Gibbs and HR sampler, respectively. The Gibbs sampler, which computes the line set 101 times more than the HR sampler in generating one new sample point, only results in a computational time of 30 times longer. Considering the relatively comparable savings obtained from using the

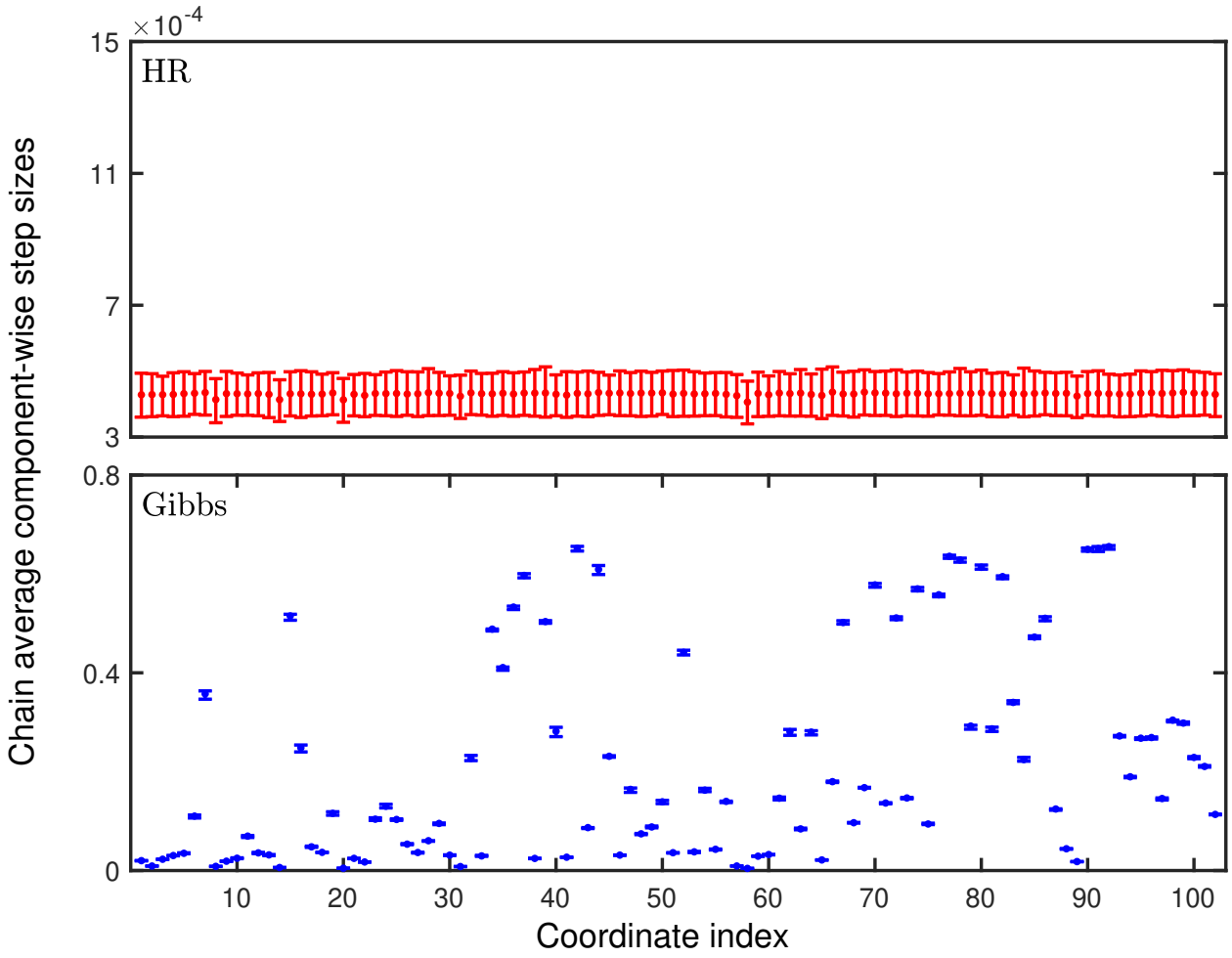

Figure 3.7: Component-wise step sizes in the generated Markov chain Monte Carlo (MCMC) chains starting from optimized points. The points and vertical bars are the computed means and 1σ confidence intervals.

Table 3.1: Averaged full-dimensional step sizes, consumed computer processing unit (CPU) time of generating 10^4 samples, and ratio of feasibility evaluation using modified and brute-force searching algorithms.

Sampler	$\Delta \|x\|_2$	CPU time (s)	Ratio of feasibility evaluations (%)
HR	1.05×10^{-2}	11.0	43.2
Gibbs	3.85	335.3	25.4

modified search algorithm, the observed acceleration in CPU time for the Gibbs sampler is likely attributed to the further exploitation of the active parameter pattern while computing the candidate roots.

The MPSRF was computed for both the HR and Gibbs samples to evaluate their convergence. Only the last half of each chain was used, as suggested by Gelman and Rubin [39]. In addition to the MPSRF, the determinants of the estimated among-chain and within-chain covariance matrices, V and W, were also calculated for examination. The logarithmic determinant of a matrix is proportional to the logarithm of the geometric mean of its eigenvalues and is interpreted as a relative measure of how dispersed the samples are. The process was repeated 10 times to reduce random effects, and the results are depicted in Figures 3.8 and 3.9.

For the HR sampler, runs with optimized initial points consistently result in a larger MPSRF and smaller determinants of both V and W, at any given instance of the sampling history. The HR sampler with optimized initial points also exhibits a larger variance over repeated runs. The computed convergence result exhibits no sign of convergence with 10^4 samples. The MPSRF is still far from 1, and the logarithmic determinants have not stabilized. For the Gibbs sampler, the computed MPSRF and the determinants of V and W exhibit negligible dependence on the starting-point types. Both the mean and variance are similar over the 10 repeated runs. The logarithmic determinants are also substantially larger than those with the HR sampler, indicating the Gibbs samples are more widespread. The test suggests the chain converged with 10^4 samples. The MPSRF decreases to a value close to 1, and the logarithmic determinants of V and W stabilized and achieved values close to each other.

Based on the chain mixing and convergence performance, the Gibbs sampler is strongly favored in the relatively high-dimensional (102) GRI-Mech example. The chains generated with the Gibbs sampler are significantly closer to convergence (i.e., achieving a much smaller MPSRF) when the same amount of CPU time is consumed. The Gibbs sampler provided a satisfactory performance by generating 5×10^3 converged samples in this 102-dimensional example within 6 minutes. This may be attributed to its observed ability to explore each coordinate component with self-adjusted, significantly larger step sizes compared to the HR sampler. Starting multiple chains at optimized initial points provides no benefit for the Gibbs sampler in this test case. This is likely due to the outstanding mixing performance of the Gibbs sampler, such that any influence from the initial points dissipates in the first half of the chain. Among the 10 repeated runs, we selected the one with the smallest MPSRF for the following analysis. The collection contains 5×10^4 total samples after discarding the first half of each chain.

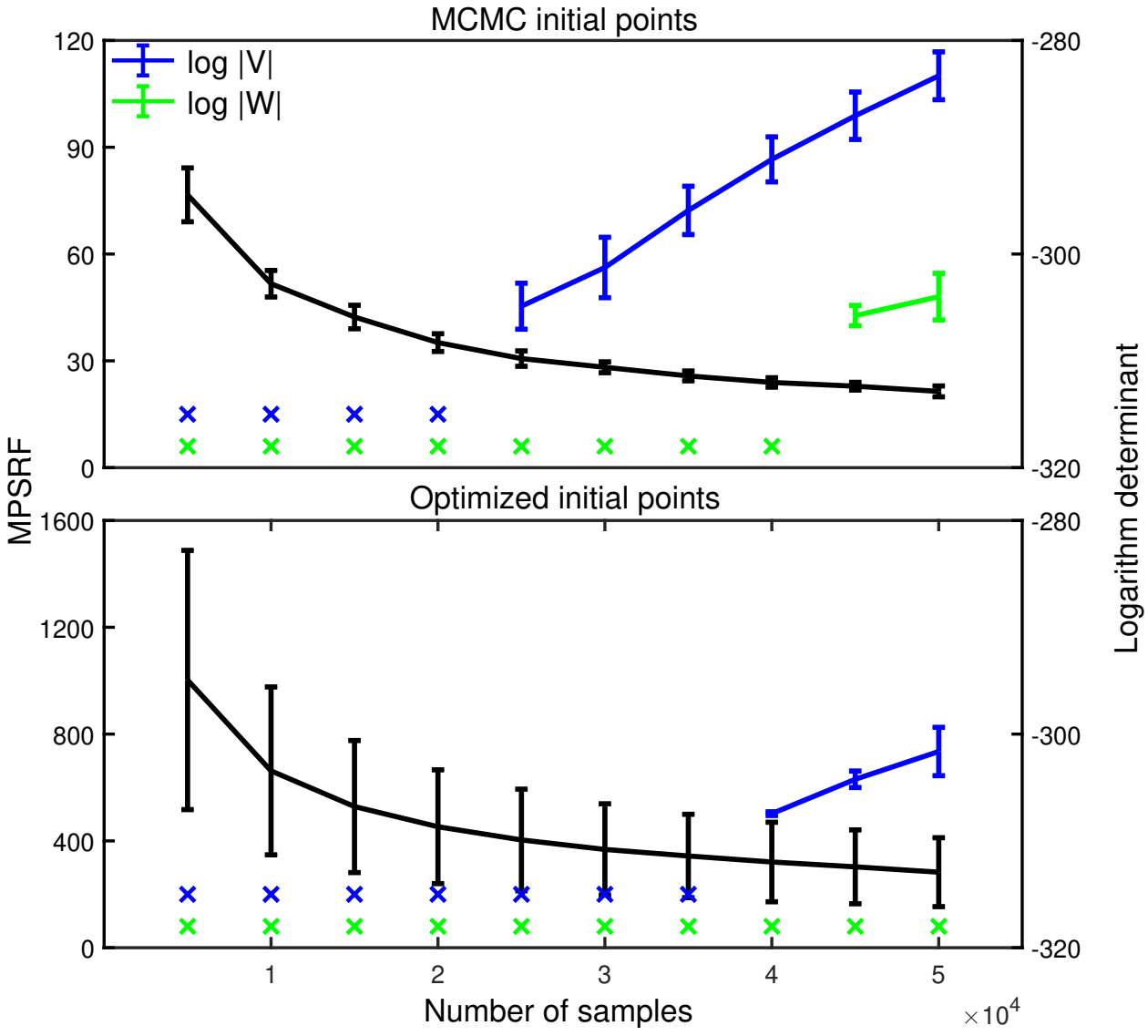

Figure 3.8: Computed multivariate potential scale reduction factors and logarithm determinants of covariance matrices V and W in HR samples. The vertical bars represent the mean and 1σ confidence interval over 10 repeated runs. The blue and green $\times$ symbols mark the cases in which the determinant is smaller than machine precision.

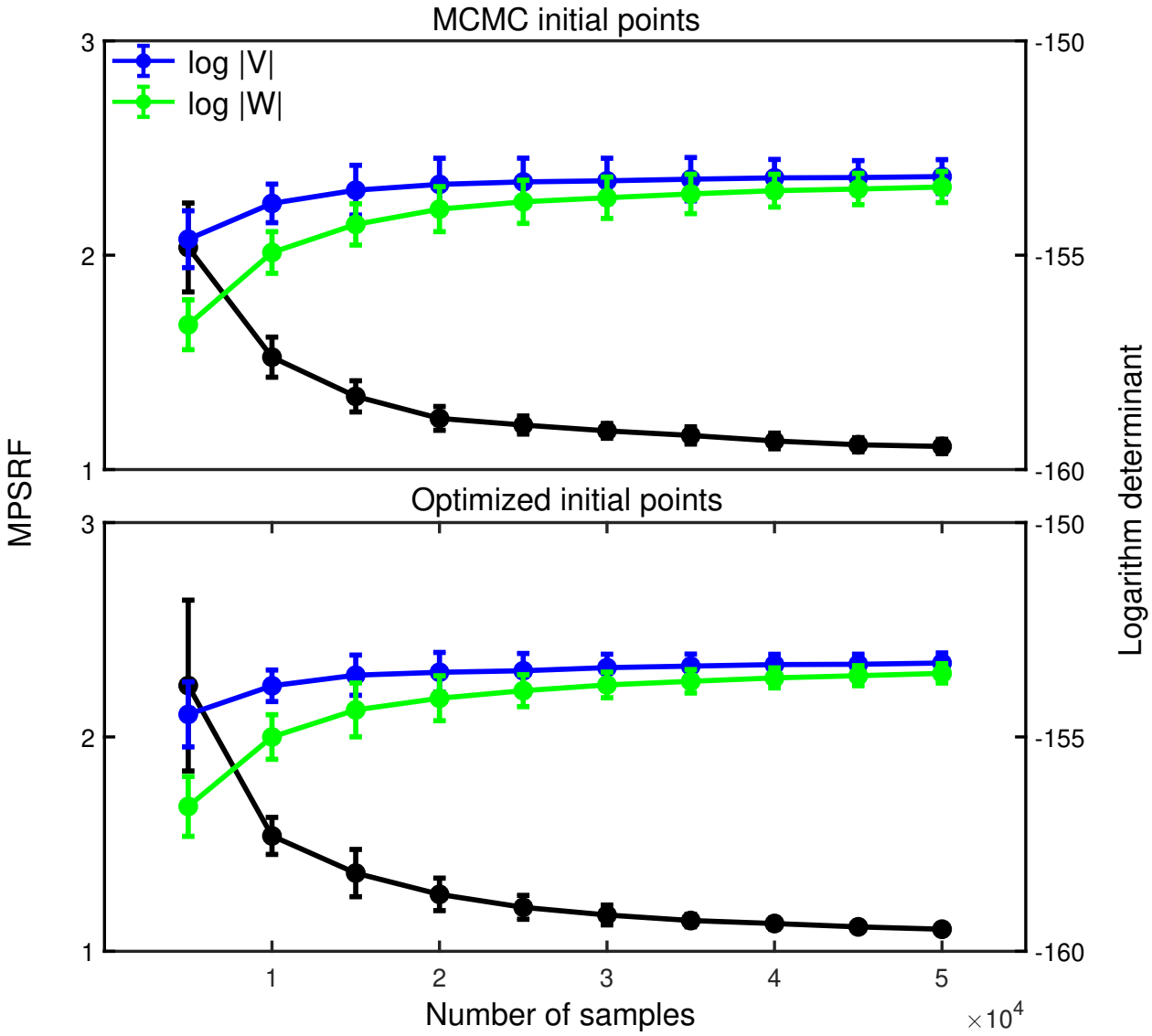

Figure 3.9: Computed multivariate potential scale reduction factors and logarithm determinants of covariance matrices V and W in Gibbs samples. The vertical bars represent the mean and 1σ confidence interval over 10 repeated runs.

3.7.2 Gaussian Versus Uniform Likelihood

A converged set of 5×10^4 samples was generated from $P_{\mathcal{N}}$ using the AM sampler for the comparison of the two posterior distributions. The MCMC chain takes 2×10^4 samples to converge compared to 10^4 for the Gibbs sampler. Thus, only the last quarter of the AM samples in each chain are used to maintain an identical sample size. The 1D marginal empirical probability density functions (PDFs) for all model parameters were estimated based on the samples, and the results are given in Figure 3.10.

The results show that the marginal posterior empirical PDFs are unimodal in most cases for both likelihood assumptions, suggesting many parameters form a most probable value in their posterior distributions. The unique mode of the PDF, however, can be located on either side or in the middle of the prior uncertainty interval. Overall, the posterior distribution with the Gaussian likelihood displays a lower peak and larger variance than the posterior distribution with the uniform likelihood across the 1D projections. An observable difference exists between the two PDFs in more than half of the parameters, more significantly for parameters with a smaller index. As shown in Table A.2, in the GRI-Mech dataset, parameters with a smaller index are associated with chemical reactions that are more influential to the measured QOIs and are expected to experience a stronger influence from the Bayesian analysis. To provide a quantifiable measure of the similarity between the two PDFs for each model parameter, the two-sample Kolmogorov-Smirnov (KS) test [74] was applied to each model parameter and the p-value of the test (i.e., the largest probability of incorrectly rejecting the null hypothesis that the two histograms come from the same distribution) was calculated. For each model parameter, both the Gibbs and the AM samples were thinned (i.e., generating a subset of the original set by taking subsequent samples with a selected step size) such that the generated subsets are almost independent (with a autocorrelation less than 0.05). Since the marginal PDFs of parameters x_{37}, x_{44}, x_{77}, x_{78}, x_{90} and x_{91} are close to their prior distributions, they are excluded from the KS tests since the effect of likelihood function on them has not yet occurred. The distribution of the calculated p-values is shown in Figure 3.11. If a typically used 0.05 significance level is employed, the results imply that 85 out of the 96 (88.5%) cases the two marginal PDFs are different.

Four parameters, x_2, x_{12}, x_{41}, and x_{55}, were selected to investigate the pairwise correlated PDFs, which are associated with reactions H + O_2 → O + OH, H + CH_2O → H_2 + HCO, O_2 + CH_3 → CH_3O + O, and HO_2 + CH_3 → O_2 + CH_4, respectively. These four parameters exhibit comparable variances but slightly different modal locations in the two sample sets. The results are provided in Figure 3.12 where the PDFs were computed using a box kernel function with support over the prior uncertainty domain $[-1, 1]^2$. Consistent with the observation in the 1D results, the 2D PDF with the Gaussian likelihood has a relatively larger variance because it covers a larger region with nontrivial probabilities. The shape and location of the nontrivial region are more noticeably different than in the 1D case between the two sample sets. The 2D PDFs in Figure 3.12 display a relatively weaker pairwise correlation for the Gibbs samples. For example, parameter x_2 is almost uncorrelated

with the other three parameters because the contours are very close to concentric circles, suggesting that adjusting the rate parameter associated with reaction $H + O_2 \rightarrow O + OH$ in one direction barely results in adjusting the rate parameters associated with the other three reactions in the same or opposite direction. Only parameters x_{41} and x_{55} exhibit an observable negative correlation, implying that increasing the rate parameter associated with reaction $O_2 + CH_3 \rightarrow CH_3O + O$ is likely to cause the decrease of the rate parameter associated with reaction $HO_2 + CH_3 \rightarrow O_2 + CH_4$. The results are caused by that both reactions are competing over a common species, CH_3. In comparison, the contours from the AM samples are more distorted and asymmetrical.

The effect of the two likelihood assumptions on model prediction was evaluated using the leave-one-out method. Each of the 76 QOIs was removed from the dataset, resulting in a new dataset containing the remaining 75 QOIs. MCMC chains of 10^4 and 2×10^4 samples were generated from the posterior distribution with the uniform and Gaussian likelihoods, respectively. For both cases, the last 5000 samples of the chain were used, and the prediction of the removed QOI was characterized by evaluating the model at the sampled parameter vectors. The estimated empirical PDFs of all QOIs are provided in Figure 3.13.

The results show that the prediction PDFs are unimodal in most cases for both likelihood assumptions. For both sample sets, the prediction PDF has a sizable probability over the experimental uncertainty bounds, except for QOI sf7, sno.c11, and nfr4. The prediction PDFs with the Gaussian likelihood have larger variances overall, consistent with the larger variance observed in the posterior parameter distributions. In a considerable number of cases, the prediction PDF with the uniform likelihood covers a smaller region with noticeable density than the experimental uncertainty interval. Similar to the case with model parameters, the two-sample KS test was applied to each prediction QOI and the distribution of the calculated p-values are shown in Figure 3.14. The results imply that all of the prediction QOI PDFs are different with a significance level 0.05.

In addition to the observed differences in parameter and prediction PDFs, none of the 5×10^4 samples with the Gaussian likelihood are in the feasible set. This is quite different from our experience with the 2D toy example given in Section 3.6, where the majority of the samples are in the feasible set.

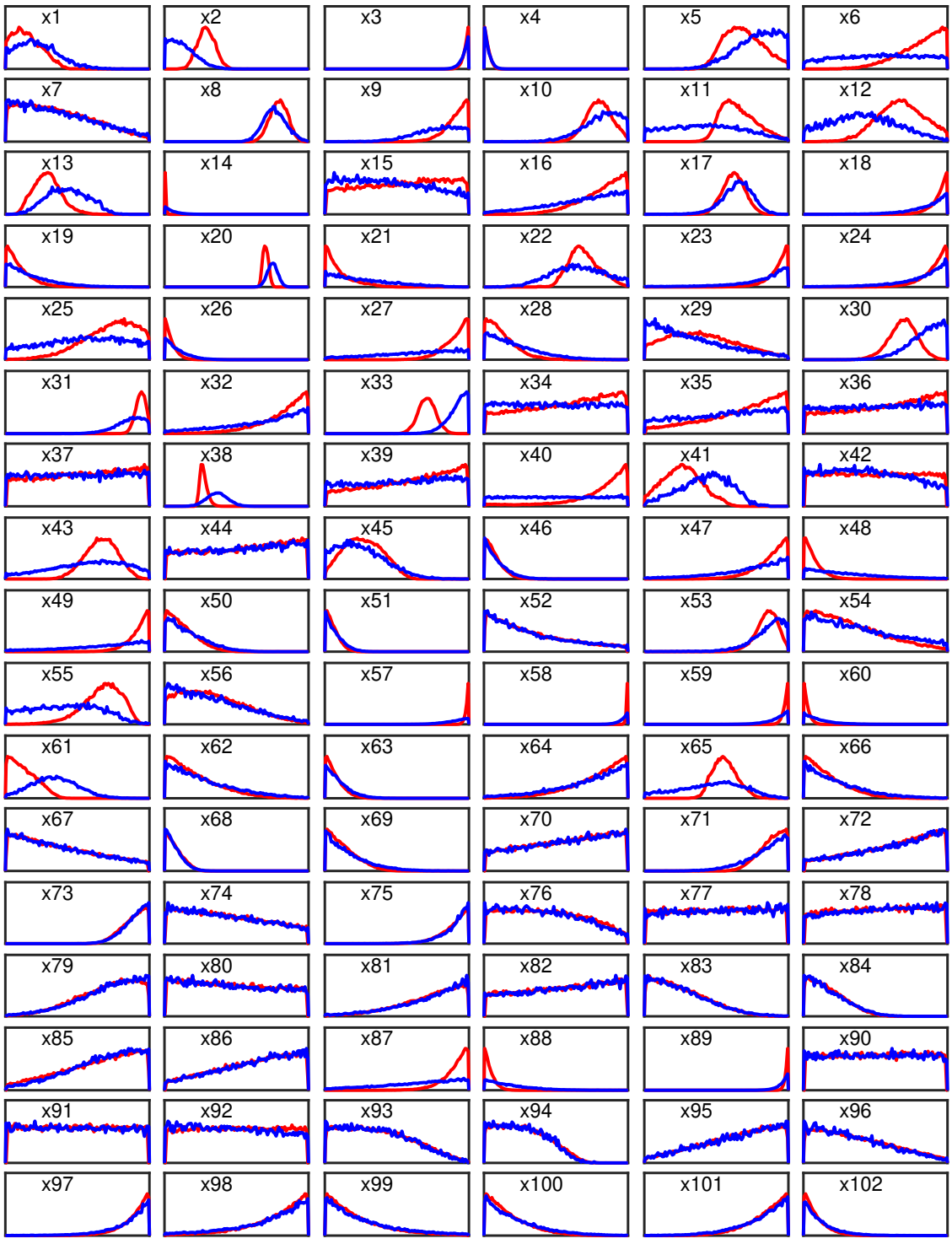

Figure 3.10: Marginal empirical probability density function of the GRI-Mech model parameters based on samples with the uniform likelihood (red lines) and samples with the Gaussian likelihood (blue lines). All axes are scaled to the prior uncertainty range [-1, 1].

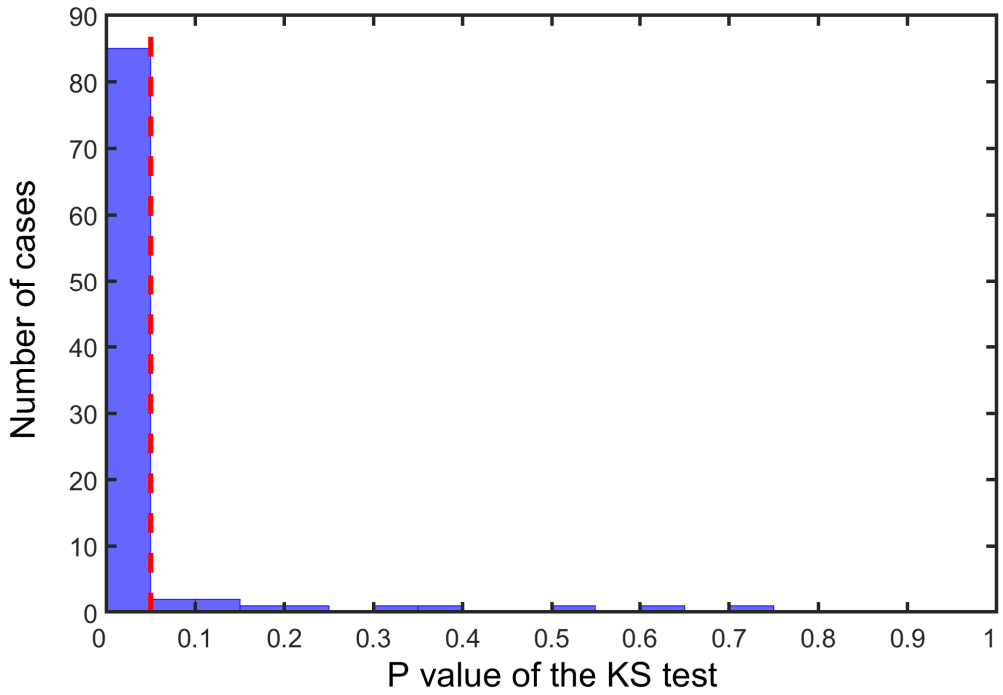

Figure 3.11: Distribution of the calculated p-values of the two-sample Kolmogorov-Smirnov tests for model parameters. The red dashed vertical line indicates the 0.05 significance level.

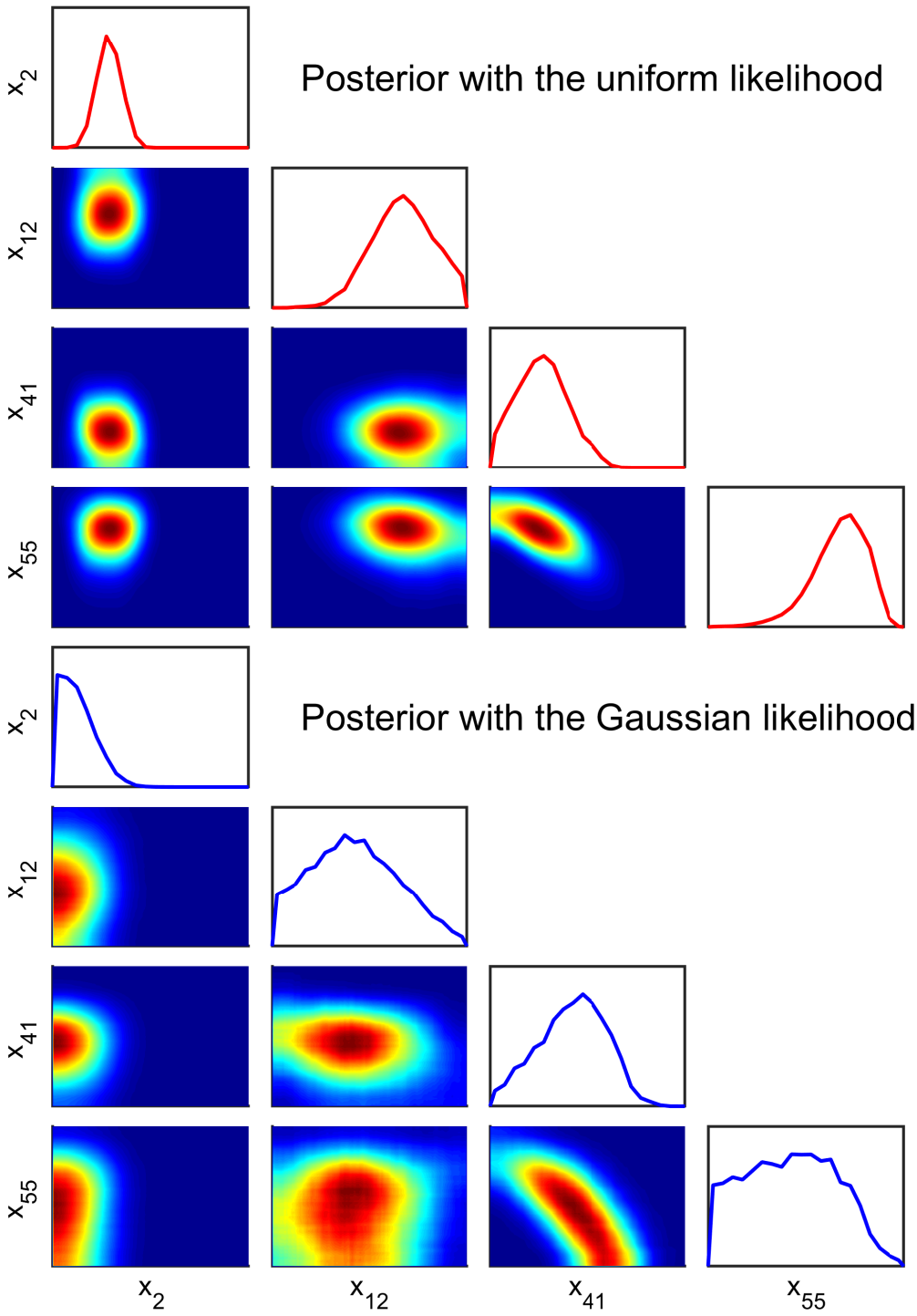

Figure 3.12: Projected probability distribution function on two-dimensional model parameter pairs based on samples with the uniform likelihood (top panel) and samples with the Gaussian likelihood (second panel). All axes are scaled to the prior uncertainty range [-1, 1].

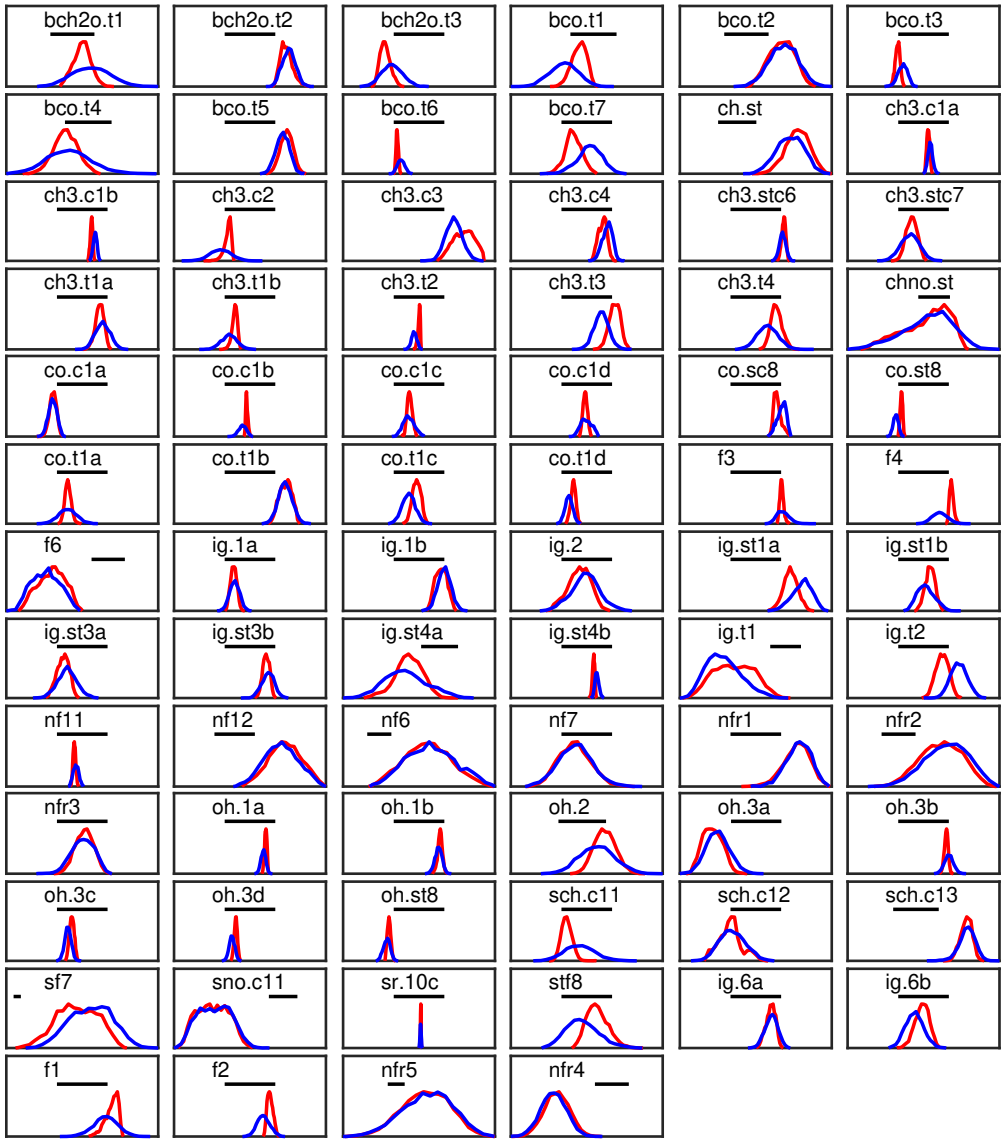

Figure 3.13: Marginal empirical probability density function of 76 GRI-Mech quantity of interest predictions based on posterior samples with the Gaussian (blue line) and uniform (red line) likelihood functions. The black horizontal bar represents the experimental uncertainty bounds.

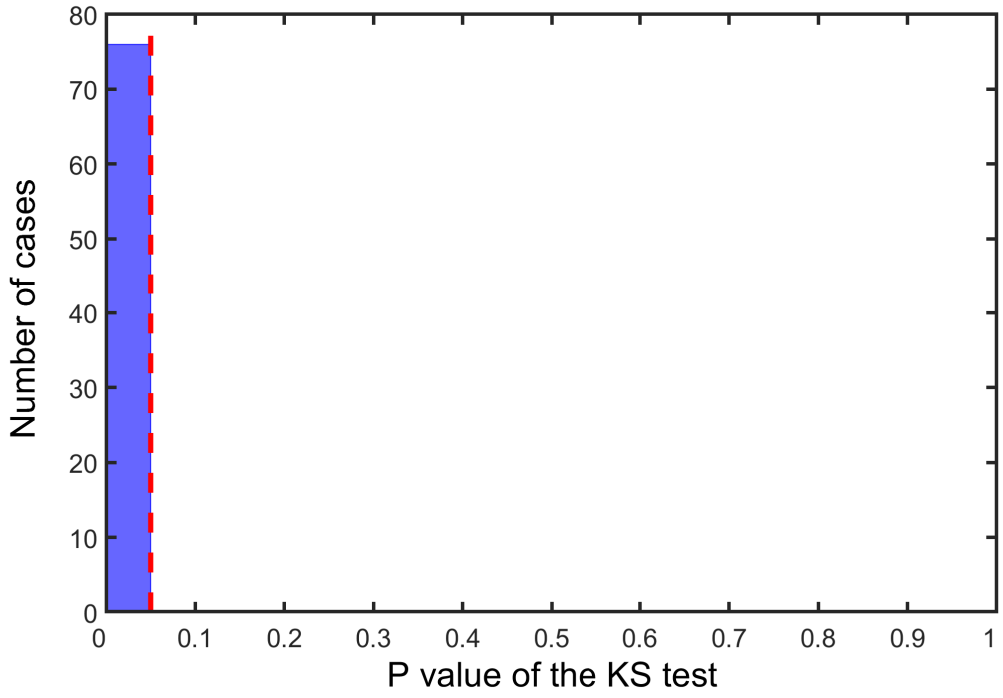

Figure 3.14: Distribution of the calculated p-values of the two-sample Kolmogorov-Smirnov tests for prediction quantities of interest. The red dashed vertical line indicates the 0.05 significance level.

3.8 B2BDC Versus Bayesian with Uniform Likelihood

The method of B2BDC and the Bayesian inference method with the uniform likelihood are compared in this section. The posterior distribution is approximated by the converged Gibbs samples. The prediction interval of each model parameter was first calculated and compared to the marginal histograms in Figure 3.15.

Examination of Figure 3.15 indicates that, different from the results in [33] but expected from the present setup, the prediction intervals consistently contain the regions covered by the histograms. In addition, a noticeable gap typically exists between the ranges covered by the histogram and by both the inner-bound (blue) and outer-bound (red) prediction intervals. The inner-bound prediction intervals are based on the found feasible points and therefore have a nonzero probability from $P_{\mathcal{U}}$. The results suggest, as remarked in [117], that the uniform assumption for representing prior parameter uncertainty region $\mathcal{H}$ and the experimental uncertainty bounds is not equivalent to the constraints. With these more informative assumptions and the resulting posterior distribution, typically used credible intervals (e.g., a 95% credible interval) tend to be noticeably shorter than B2BDC prediction intervals computed based on inequality constraints. Compared to the results observed in the 2D toy example presented in Section 3.6, replacing B2BDC constraints by the more informative uniform assumptions on model parameters and QOIs induces a stronger impact on the generated results for higher dimensional problems.

The implemented statistical assumptions generated results that are more informative than the B2BDC prediction intervals. Although the B2BDC prediction intervals remain unchanged compared to the prior uncertainty interval for some parameters, the corresponding Bayesian posterior histograms can tell a different story. For example, parameters x_{90}, x_{91} and x_{92} show a relatively uniform histogram over the B2BDC prediction interval, whereas the histograms of parameters x_9, x_{11} and x_{50} are quite nonuniform and display negligible probability over some portions of the prediction interval. The nonuniform histograms can peak toward either side of the prior uncertainty interval despite the associated model parameters having identical B2BDC prediction intervals (e.g., parameters x_{100} and x_{101}). This feature is also observed and reported in [33] between B2BDC computations and Bayesian inference with the Gaussian likelihood. Therefore, it suggests that the more informative results are due to the more informative assumptions adopted in a Bayesian inference, but not specific to a particular likelihood function.

The leave-one-out prediction interval of each QOI was computed following a similar procedure defined in the previous section. The results are provided in Figure 3.16 with the experimental uncertainty intervals. Examination of Figure 3.16 shows that, similar to the case for model parameters, the computed prediction intervals consistently cover a larger enclosed uncertainty region than the sample-based credible intervals with a noticeable gap for most QOI predictions. The histograms provide a quantifiable measure (the probability) to the prediction values within B2BDC prediction intervals. The histograms provide an

instrument for evaluating and comparing values within the B2BDC prediction intervals. For cases in which the B2BDC outer-bound prediction interval is completely contained within the experimental uncertainty bounds (e.g., QOI ch3.c1b, ch3.c1a, and sr.10c), removal of the QOI has provable effect on the feasible set; every feasible point without the QOI generates a model prediction within its experimental uncertainty. Similar provable arguments are difficult to make with statistical samples. For example, considering QOI f6, sch.c13, and nfr4, although the ranges covered by the prediction histogram and experimental bounds are disjoint, we cannot argue that the QOIs are inconsistent with the remaining QOIs. In fact, we know that these QOIs are consistent with the remaining QOIs because the dataset including all 76 QOIs is consistent. Unlike for the model parameters, the prediction histograms are centered roughly around the midpoint of the corresponding B2BDC inner-bound prediction intervals.

The results shown in Figures 3.15 and 3.16 are different from those reported in [33], where the B2BDC computations were compared to Bayesian inference with the Gaussian likelihood. In that case, the credible intervals were comparable to, or sometimes longer than the B2BDC prediction intervals for model parameters and for leave-one-out predictions. The results resonate with the observations given in Section 3.7.2 that the two likelihood functions have a substantial influence on the subsequent UQ analysis, and imply that the comparison between B2BDC and Bayesian inference depends on the implemented statistical assumptions.

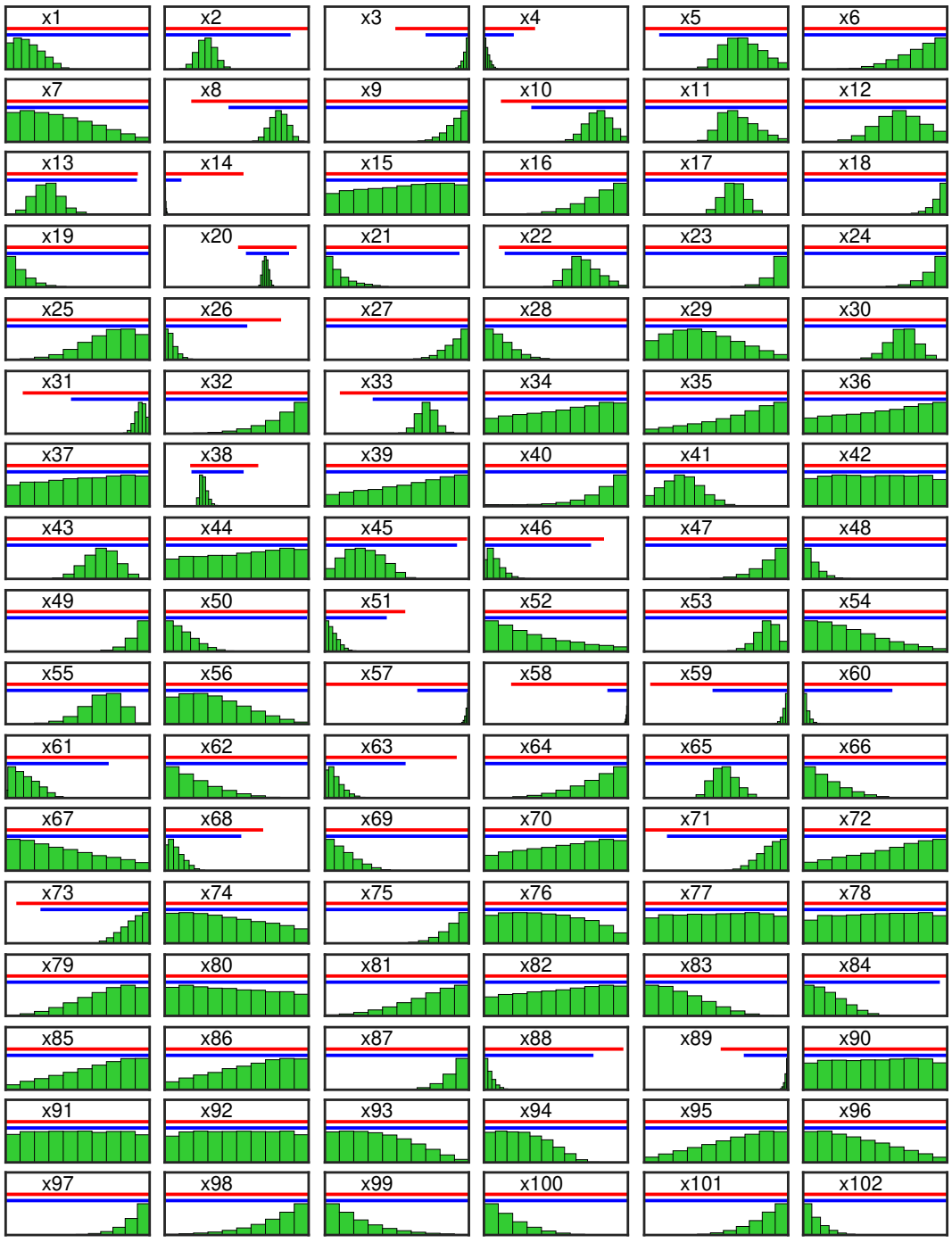

Figure 3.15: Marginal histograms and Bound-to-Bound Data Collaboration posterior prediction intervals of GRI-Mech model parameters. The green histograms are based on 5×10^4 samples uniformly distributed on the feasible set. The blue and red bars are computed inner- and outer-bound intervals, respectively. All axes are scaled by the prior uncertainty range [-1, 1].

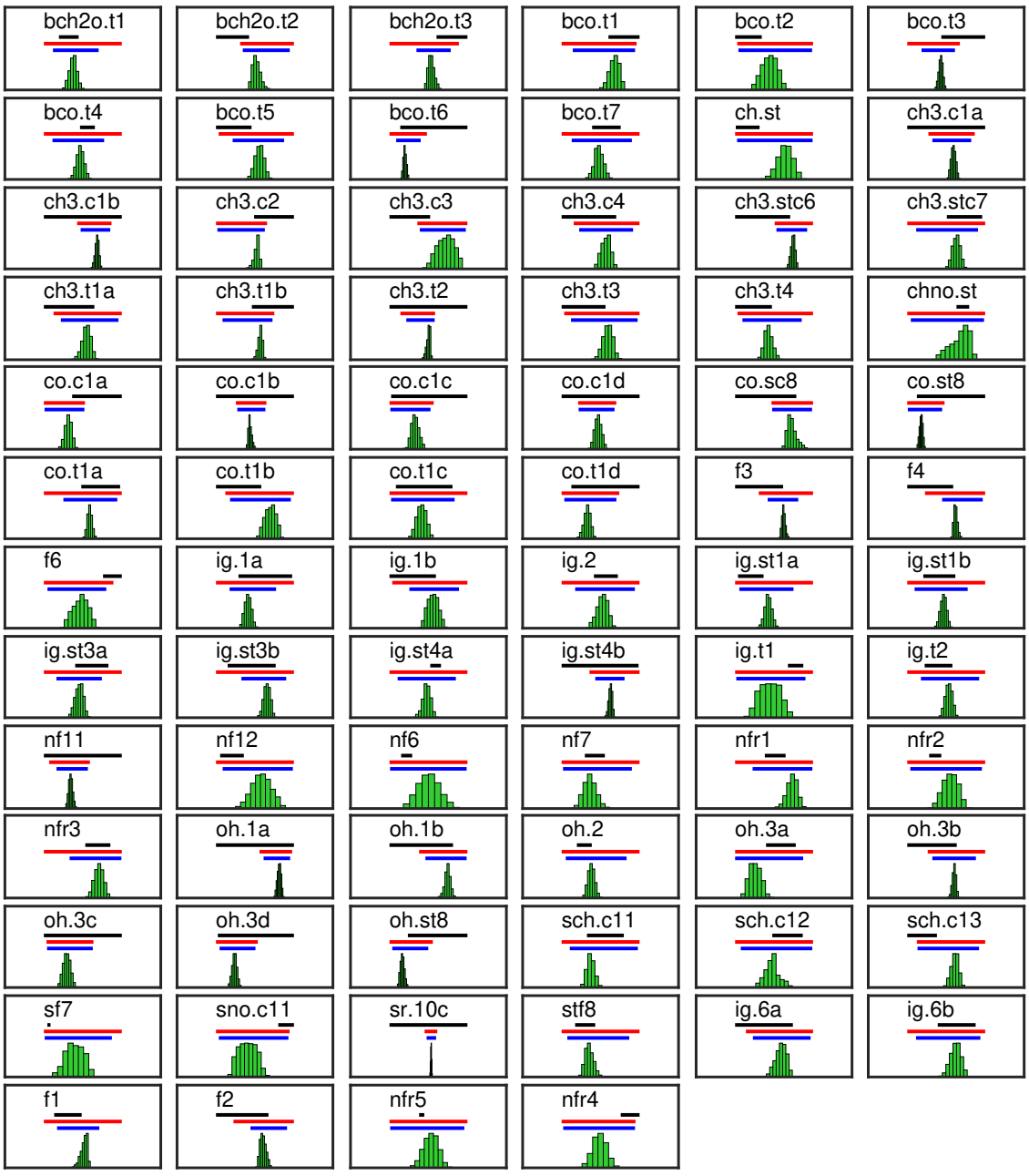

Figure 3.16: Leave-one-out distribution, Bound-to-Bound Data Collaboration prediction, and experimental data bounds of 76 GRI-Mech quantities of interest. The green histograms are based on samples uniformly distributed on the feasible set. The blue, red, and black bars are the calculated inner- and outer-bound prediction intervals and experimental uncertainty bounds, respectively.

3.9 Chapter Summary

We presented a Bayesian inference workflow starting from a B2BDC dataset, in which uncertainties in model parameters and experimental QOIs are characterized by inequalities. In the Bayesian inference, we assumed a uniform prior distribution over the prior parameter uncertainty region. Two physically motivated likelihood assumptions, the Gaussian and uniform likelihoods, were investigated and compared. Efficient samplers were developed to generate samples from the resulting posterior distributions. We demonstrated that the two posterior distributions exhibit a growing difference in their lower dimensional projections with increased problem dimension. In the 102-dimensional GRI-Mech example, via the two-sample KS tests, the resulting posterior distributions exhibited substantial differences in their 1D projections on many model parameters and all leave-one-out predictions. The difference between the two posterior distributions in 2D projections can be more noticeable than in the 1D case. The comparison between the B2BDC prediction intervals and the Bayesian marginal histograms with the uniform likelihood shows that the credible intervals are consistently contained by the prediction intervals with noticeable gaps. The gaps are more significant in the higher dimensional case (the GRI-Mech example) than in the lower dimensional case (the 2D toy example). The results complements the previous work [33] by demonstrating that the comparison of the UQ analysis from B2BDC and Bayesian inference depends strongly on the implemented assumptions.

The HR and Gibbs samplers performed comparably for the illustrative 2D toy example. However, the latter dominated the former in the 102-dimensional GRI-Mech dataset by generating much quickly converged MCMC chains. Although both samplers are capable in principle of moving from one feasible point to any other feasible point along the proposed direction in one step, the Gibbs sampler can generate a coordinate-dependent step size that is orders of magnitude larger than that generated by the HR sampler. Thus, it provided a much faster-converged set of samples. The developed search algorithm for the line set calculation exhibited promising efficiency improvement compared to a brute-force implementation. Although only quadratic inequalities were considered in this case study, the developed sampler can be generalized to the situation with general polynomial inequalities with modest modifications.

The GRI-Mech example demonstrates benefits of combining B2BDC prediction intervals and Bayesian inference with the uniform likelihood. The optimization techniques efficiently compute the boundary of the uncertainty in QOIs, whereas the samples provides a quantifiable measure of subjective belief for values within the uncertainty region. In the next chapter, the B2BDC methods are applied to a syngas combustion dataset, implementing both optimization-based computations and Bayesian inference based on samples from the feasible set.

Chapter 4

Syngas Combustion Application

Syngas (a mixture of H_2 and CO) is a popular candidate for high efficiency power generation in hybrid turbines. In this chapter, I apply the methods of Bound-to-Bound Data Collaboration (B2BDC) to a syngas combustion system. A syngas reaction mechanism and a set of related experimental data were generated by a research group from the German Aerospace Center (DLR), with systematically assessed uncertainty. The dataset contains 55 model parameters and 167 quantities of interest (QOIs), including shock-tube ignition delay time and laminar flame speed measurements. The initial dataset was found to be inconsistent, and the vector consistency measure (VCM) method was used to resolve the inconsistency. The feasible set of the resulting consistent dataset was examined via both prediction interval computations and Bayesian inference with the uniform likelihood function. Optimized models were computed and compared to a well-established reaction model obtained with a different set of data.

4.1 Reaction Model

The study of syngas combustion has received increased interest in recent years [20, 61, 70, 104, 116, 123, 126]. The work is of great practical value because the syngas mixture (i.e., the mixture of primarily H_2 and CO) is a popular fuel in many industrial fields. In addition, the work contributes to general combustion research because the syngas mixture constitutes the next complex system other than the hydrogen system. Because the combustion mechanism of larger fuels inevitably includes the combustion mechanism of smaller fuels generated from them, comprehensive knowledge about the chemical kinetics of syngas plays an essential role in developing reliable reaction models of larger hydrocarbons.

The assembled reaction model for syngas combustion is a submodel of the DLR C_0-C_2 reaction model [111], which is the base chemistry of the DLR reaction database for heavy-hydrocarbon oxidation. The syngas reaction model contains 55 chemical reactions in 17 species. The reaction mechanism and the nominal reaction rate parameters are summarized

in Table B.1 and more details can be found in [110].

For each reaction in the mechanism, an uncertain multiplier λ_i is defined to represent the uncertainty in the associated reaction rate such that

$$k_i = \lambda_i k_{i,0}, \quad i = 1, 2, \ldots, 55, \tag{4.1}$$

where $k_{i,0}$ is the nominal rate constant computed using the parameter values given in Table B.1. The prior uncertainty range of each λ_i was assessed separately [110], and the results are summarized in Table B.2.

The model parameters x_i are selected as logarithms of λ and denoted by $x \in \mathbb{R}^{55}$:

$$x_i = \ln \lambda_i, \quad i = 1, 2, \ldots, 55. \tag{4.2}$$

In the present study, each model parameter x_i has a nominal value 0, resulting in the prior uncertainty region $\mathcal{H}$ being a 55-dimensional orthotope with the nominal value at the origin.

4.2 Experimental Data

As detailed in [110], two types of commonly used QOIs in a combustion reaction kinetics study were collected: the ignition delay time measurements in a shock-tube facility and laminar flame speed measurements. The selected ignition delay time QOIs [41, 54, 58, 65, 73, 75, 78, 82, 93, 95, 125, 127, 136] cover a wide range of temperatures (800 to 2500 K), pressures (0.5 to 50 bar) and equivalence ratios (ϕ = 0.5 to 1.5). The laminar flame speed QOIs included in the dataset [18, 43, 44, 48, 50, 51, 66, 68, 77, 85, 86, 123, 124, 130, 131, 133, 134, 138] were measured at 0.1 to 0.5 MPa using a variety of techniques. The selected laminar flame speed QOIs cover the full range of operating conditions available in the literature. The uncertainties in the experimental data were taken from [110] and are reproduced in Tables B.3 and B.4. The current analysis includes a total of 122 ignition delay time QOIs and 45 laminar flame speed QOIs.

4.3 Simulation and Surrogate Models

Ignition delay time QOIs were simulated using ReactionLab [29] with the homogeneous constant-volume adiabatic reaction model, and the laminar flame speed QOIs were simulated using the Chemkin software [59]. Quadratic surrogate models were selected for the current analysis. Because the ignition delay time QOIs can vary by orders of magnitude for different parameter vectors in $\mathcal{H}$, the corresponding response surfaces were constructed with the logarithmic transformation of the QOIs. The response surfaces of laminar flame speed QOIs were generated without the logarithmic transformation. As a result,

$$S_e(x) \approx y_e(x) = \begin{cases} \log_{10} t_{\text{ign}}(x), & e = 1, 2, \ldots, 122 \\ v(x), & e = 123, 124, \ldots, 167, \end{cases} \tag{4.3}$$

where $t_{\text{ign}}(x)$ and $v(x)$ denote the simulated ignition delay time and laminar flame speed with parameter vector x, respectively.

The maximum absolute fitting error ϵ_e, defined as

$$\epsilon_e := \max_{x \in \mathcal{H}} \left| y_e(x) - S_e(x) \right|, \tag{4.4}$$

was estimated as $\hat{\epsilon_e}$ using a test set of design points denoted by $\mathbb{X}_{\text{test}}$:

$$\hat{\epsilon_e} = \max_{x \in \mathbb{X}_{\text{test}}} \left| y_e(x) - S_e(x) \right|. \tag{4.5}$$

The distribution of the estimated fitting errors for ignition delay time and flame speed QOIs is given in Figure 4.1. The calculated $\hat{\epsilon_e}$ was included in the corresponding model-data

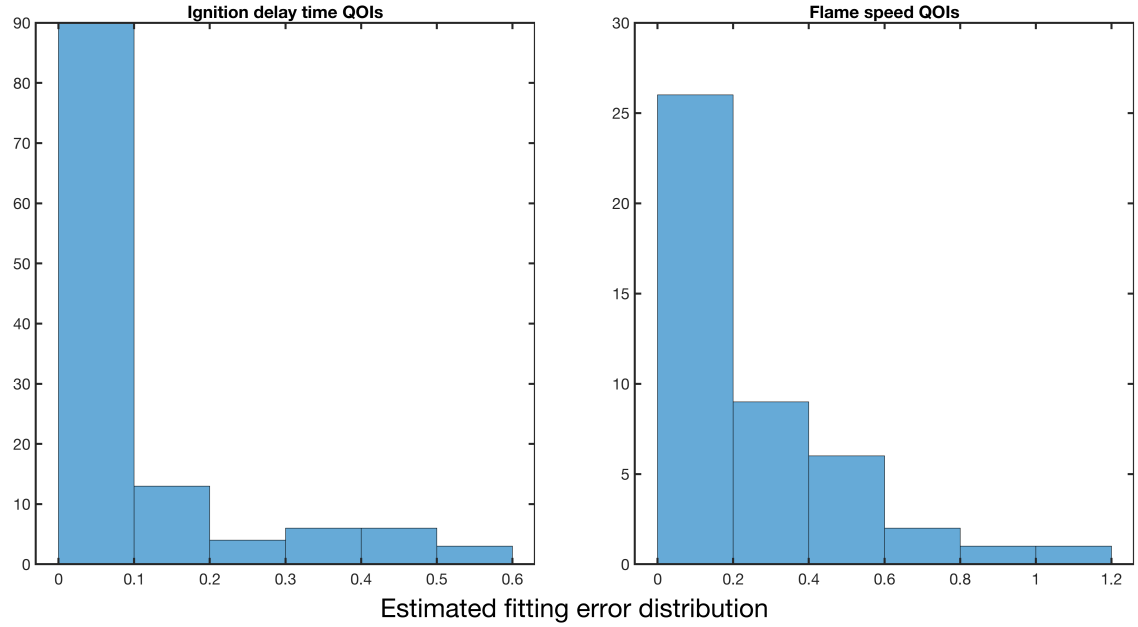

Figure 4.1: Distribution of the estimated fitting errors for ignition delay time and laminar flame speed quantities of interest (QOIs).

constraints to maintain their validity with respect to the surrogate model. The model-data constraint with fitting error is as follows:

$$L_e - \hat{\epsilon_e} \leq S_e(x) \leq U_e + \hat{\epsilon_e}, \quad e = 1, 2, \ldots, 167. \tag{4.6}$$

The initial dataset with all 167 QOIs is denoted as DLR-SynG 0.

4.4 Consistency Analysis

The dataset DLR-SynG 0 turned out to be massively inconsistent with the computed scalar consistency measure (SCM) being within [-2.84, -2.25]. Eight QOIs, listed in Table 4.1, were found to be self-inconsistent: no parameter vector exists in $\mathcal{H}$ to predict these QOIs individually within their respective experimental uncertainty bounds. The self-inconsistent QOIs were removed and the resulting dataset was denoted as DLR-SynG 1. Moreover, DLR-SynG 1 was also proven to be inconsistent, with the computed SCM within [-2.29, -1.62]. The VCM method (Section 2.6) was then applied to the DLR-SynG 1 dataset with a unit weight for relaxation associated with QOI uncertainty bounds and a zero weight for relaxation associated with model parameter uncertainty bounds. An inner-bound solution was found using a nonlinear constrained optimization solver, where the optimal relaxation vector has 37 nonzero entries. The corresponding QOIs and their suggested change of uncertainty bounds are given in Table 4.2.

Table 4.1: Eight self-inconsistent quantities of interest (QOIs) in the DLR-SynG 0 dataset

PrIMe ID	QOI type
a00000309	ignition delay time
a00000352	ignition delay time
a00000355	ignition delay time
a00000358	ignition delay time
a00000359	ignition delay time
a00000360	ignition delay time
a00000503	ignition delay time
a00000504	ignition delay time

A consistent dataset was obtained by removing these 37 QOIs from the DLR-SynG 1 dataset. The resulting consistent dataset is denoted as DLR-SynG 2 and contains 122 QOIs, of which 84 and 38 are the ignition delay time and laminar flame speed QOIs, respectively.

Table 4.2: Calculated vector consistency measure result for DLR-SynG 1 dataset.

PrIMe ID	QOI type	Estimated uncertainty (%)	Lower bound change (%)	Upper bound change (%)
a00000110	ignition delay time	50	-14.84	
a00000113	ignition delay time	40		13.00
a00000189	ignition delay time	30		0.92
a00000190	ignition delay time	30		10.14
a00000191	ignition delay time	50		431.95
a00000228	ignition delay time	35	-12.78	
a00000236	ignition delay time	30	-2.56	
a00000237	ignition delay time	35	-13.48	
a00000241	ignition delay time	30		86.11
a00000308	ignition delay time	30		1.46
a00000310	ignition delay time	40		187.12
a00000311	ignition delay time	30		28.59
a00000312	ignition delay time	30		48.63
a00000316	ignition delay time	35		175.15
a00000335	ignition delay time	25		11.94
a00000353	ignition delay time	30		17.76
a00000354	ignition delay time	40		44.21
a00000356	ignition delay time	25		6.02
a00000357	ignition delay time	35		28.49
a00000490	ignition delay time	30	-4.55	
a00000498	ignition delay time	30	-16.77	
a00000499	ignition delay time	30	-1.25	
a00000500	ignition delay time	30		51.79
a00000505	ignition delay time	30		51.07
a00000507	ignition delay time	30		14.50
a00000491	ignition delay time	20	-79.93	
a00000492	ignition delay time	50	-6.40	
a00000495	ignition delay time	50	-34.47	
a00000496	ignition delay time	50	-44.16	
a00000497	ignition delay time	50	-10.55	
a00000128	flame speed	10	-0.73	
a00000129	flame speed	10	-0.30	
a00000260	flame speed	10		2.43
a00000269	flame speed	10		4.74
a00000271	flame speed	10	-6.75	
x00000471	flame speed	20	-6.18	
a00000534	flame speed	10		5.34

4.5 Uncertainty Quantification

The feasible set of DLR-SynG 2 is embedded in a 55-dimensional parameter space and is difficult to visualize. Instead, its 1D projections onto each model parameter coordinate were examined. The projections are the prediction intervals of the model parameters and were computed by solving the prediction problems in Equations (2.7) and (2.8) with $M_p = x_i$. The multipliers whose outer-bound prediction intervals are different from their corresponding prior uncertainty intervals are listed in Table 4.3, with the changed uncertainty bounds marked in red.

Table 4.3: Reaction rate multipliers with posterior uncertainty bounds in DLR-SynG 2 that are different from their prior bounds.

Index	Reaction	λ prior bounds		λ posterior bounds	
		lower	upper	lower	upper
3	H_2+O $\rightarrow$ OH+H	0.63	1.58	0.81	1.58
4	H_2+OH $\rightarrow$ H_2O+H	0.65	1.63	0.65	1.52
6	O_2+H $\rightarrow$ OH+O	0.80	1.26	0.90	1.26
10	H+O $\rightarrow$ OH	0.20	5.00	0.96	5.00
11	HO_2+H $\rightarrow$ H_2+O_2	0.50	2.00	0.56	2.00
17	HO_2+OH $\rightarrow$ H_2O+O_2	0.32	3.16	0.39	3.16
23	CO+OH $\rightarrow$ CO_2+H	0.80	1.26	0.80	1.08
24	CO+O $\rightarrow$ CO_2	0.50	2.00	0.50	1.97

The sensitivity of these eight changed bounds with respect to experimental or model parameter uncertainty bounds was computed using the formulas given in Section 2.7.5. The ranked results are illustrated in Figure 4.2 for the top 15 contributors. The results reveal that both experimental uncertainty bounds and prior uncertainty bounds of parameters can exhibit comparable influence on the predicted parameter bounds. A few entries appear frequently in all subplots. For example, the ignition delay time QOI a00000107 appears in 6 out of 8 cases. The flame speed QOI a00000261 appears in 7 out of 8 cases. Model parameter x_{10}, which is associated with reaction H+O $\rightarrow$ OH, appears 6 out of 8 cases. The model parameter x_{11}, which is associated with reaction HO_2+H $\rightarrow$ H_2+O_2, appears in 6 out of 8 cases. Entries exist that are unique to one of the eight subplots (e.g., the flame speed QOI a00000282 for the predicted lower bounds of reaction HO_2+H $\rightarrow$ H_2+O_2).

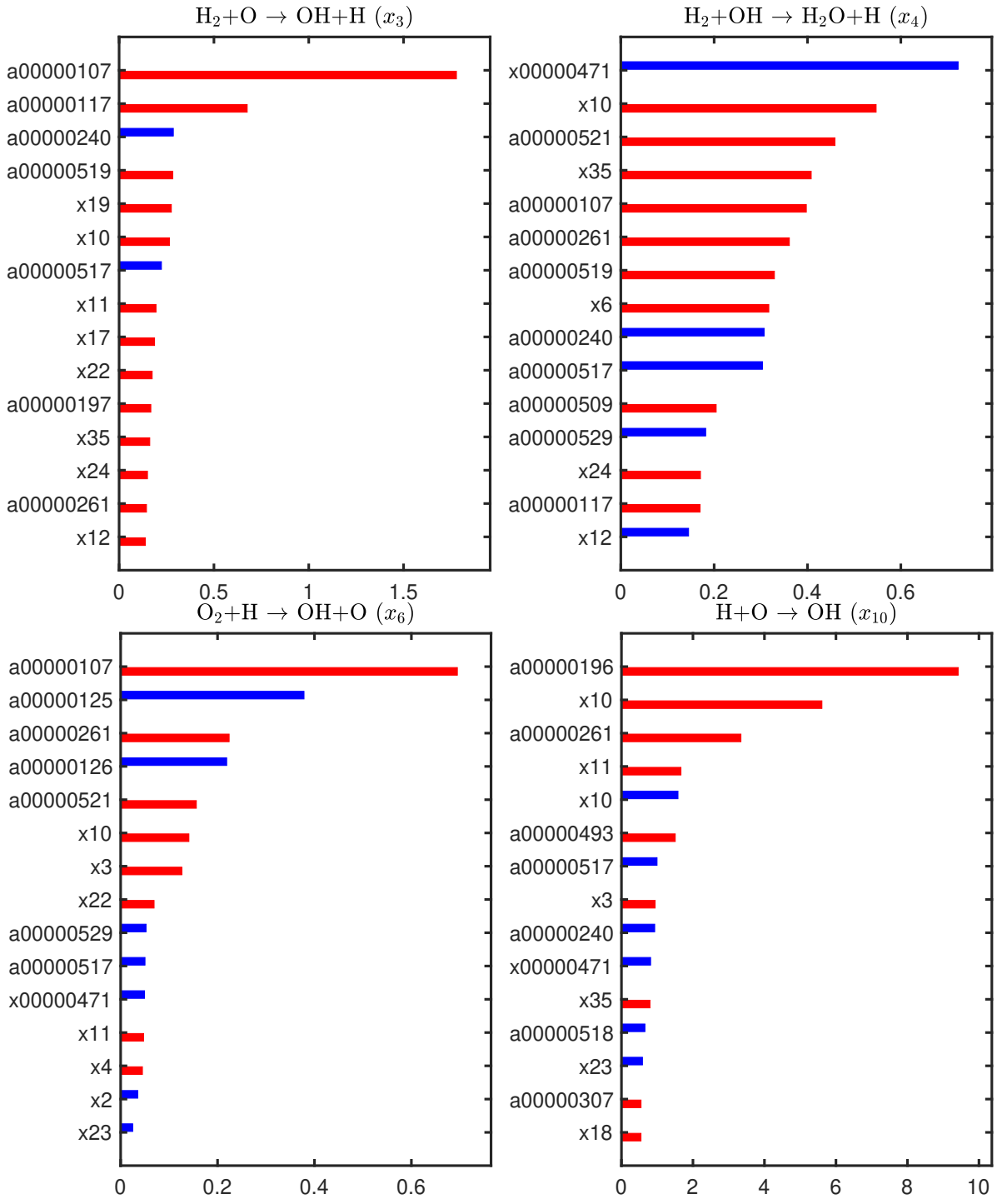
H_2+O → OH+H (x_3)
a00000107
a00000117
a00000240
a00000519
x19
x10
a00000517
x11
x17
x22
a00000197
x35
x24
a00000261
x12
0
0.5
1
1.5
H_2+OH → H_2O+H (x_4)
x00000471
x10
a00000521
x35
a00000107
a00000261
a00000519
x6
a00000240
a00000517
a00000509
a00000529
x24
a00000117
x12
0
0.2
0.4
0.6
O_2+H → OH+O (x_6)
a00000107
a00000125
a00000261
a00000126
a00000521
x10
x3
x22
a00000529
a00000517
x00000471
x11
x4
x2
x23
0
0.2
0.4
0.6
H+O → OH (x_{10})
a00000196
x10
a00000261
x11
x10
a00000493
a00000517
x3
a00000240
x00000471
x35
a00000518
x23
a00000307
x18
0
2
4
6
8
10

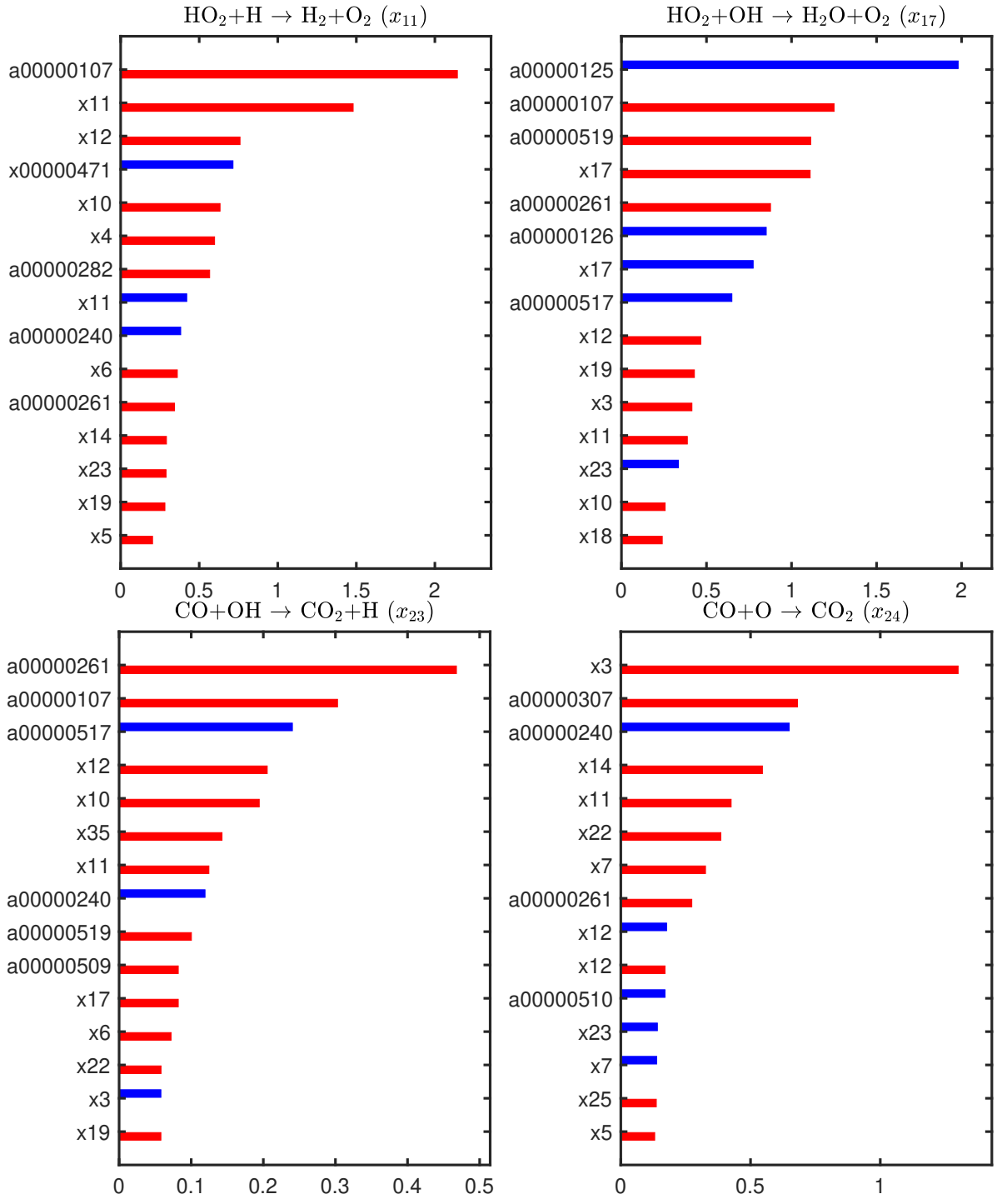

Figure 4.2: Ranked sensitivity of the shrunk posterior bounds (the lower or upper uncertainty bound marked red in Table 4.3) of parameters x_3, x_4, x_6, x_{10}, x_{11}, x_{17}, x_{23} and x_{24} with respect to the experimental uncertainty bounds and parameter prior bounds. The red and blue horizontal bars denote the upper and lower uncertainty bounds, respectively, of the contributing experimental uncertainty bounds or parameter prior bounds.

Four QOIs that were removed using the VCM method were selected to investigate their prediction intervals and the associated sensitivity using the DLR-SynG 2 dataset. The prediction intervals are given in Table 4.4 along with the experimental uncertainty intervals. The results indicate that the inner-bound prediction intervals of a00000308 and a00000129

Table 4.4: Prediction intervals of the four selected quantities of interest. The units for ignition delay time and flame speed measurements are millisecond and centimeter per second, respectively.

PrIMe ID	QOI type	Prediction interval		Exp. interval
		Inner bound	Outer bound	
a00000236	ignition delay time	[955.7, 1216.2]	[715.7, 2052.9]	[1267, 2353]
a00000308	ignition delay time	[408.8, 437.4]	[372.2, 504.4]	[221.9, 412.1]
a00000129	flame speed	[132.3, 136.1]	[126.5, 139.2]	[135.9, 166.1]
a00000260	flame speed	[35.4, 36.2]	[33.4 37.5]	[28.8, 35.2]

share some common regions with the experimental uncertainty intervals, whereas the other two do not. All outer-bound prediction intervals are partially overlapped with the associated experimental uncertainty interval. The sensitivity of the prediction outer lower bound of the four QOIs is presented in Figure 4.3. Again, the results suggest that both the experimental uncertainty bounds and parameter prior uncertainty bounds can contribute comparably to the prediction intervals. Experimental data from the same type of QOI are more influential on the prediction interval bounds. The sensitivity results for the ignition delay time QOI a00000236 demonstrate that 7 out of 8 experimental data entries in the plot are QOIs of the same type, except for QOI x00000471. For ignition delay time QOI a00000308, 5 out of 7 experimental data entries are from the same type, except for QOIs a00000261 and a00000517. For flame speed QOIs, a00000129 and a00000260, QOIs of the same type occupy 6 out of the top 10 and 5 out of the top 8 contributing experimental data entries, respectively. These observations underlie the collaborative part of the B2BDC methodology.

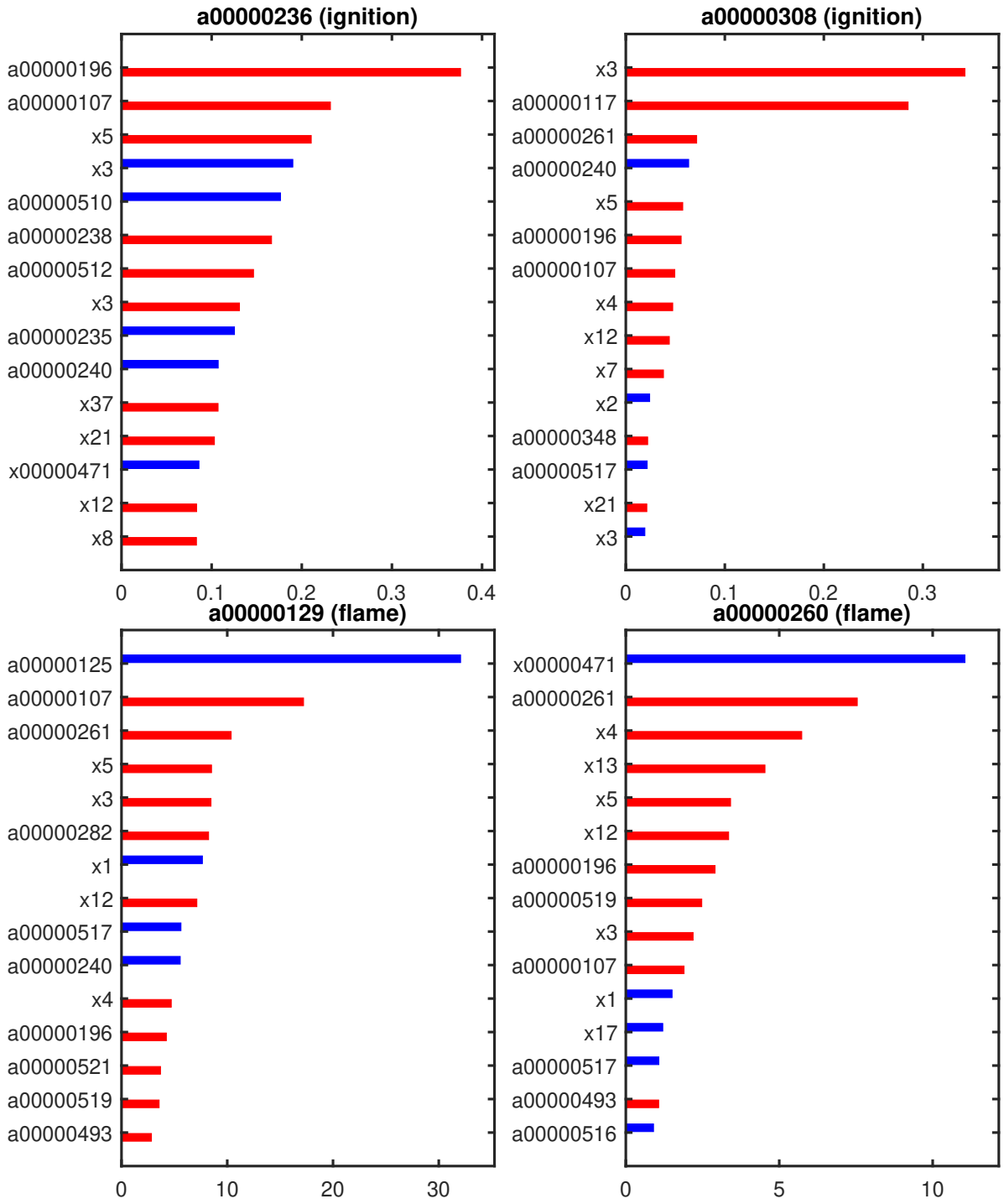

Figure 4.3: Ranked sensitivity of prediction lower bound for the four quantities of interest listed in Table 4.4 with respect to experimental uncertainty bounds and parameter prior bounds. The red and blue horizontal bars denote the upper and lower uncertainty bounds, respectively, of the contributing experimental uncertainty bounds or parameter prior bounds.

4.6 Sampling the Feasible Set

The Bayesian inference method was applied to the DLR-SynG 2 dataset with the uniform prior distribution and uniform likelihood function, resulting in a posterior distribution that is uniformly distributed over the feasible set. The Gibbs sampler developed in Section 3.3 was used to generate samples from the posterior distribution. To monitor the convergence, 10 starting points were generated by drawing every 100th point from the Markov chain Monte Carlo (MCMC) chain initialized at the feasible point obtained while computing the SCM. For each starting point, an MCMC chain of length 8×10^4 was generated. The convergence test results are presented in Figure 4.4 based on a sample set including the second half of each chain. An examination of Figure 4.4 indicates that the chain has converged to the target distribution. The MPSRF decreases to close to 1, and the logarithmic determinants of the among-chain and within-chain covariance matrices have stabilized and reached values close to each other. The converged sample set of 4×10^5 total points was used for the following analysis.

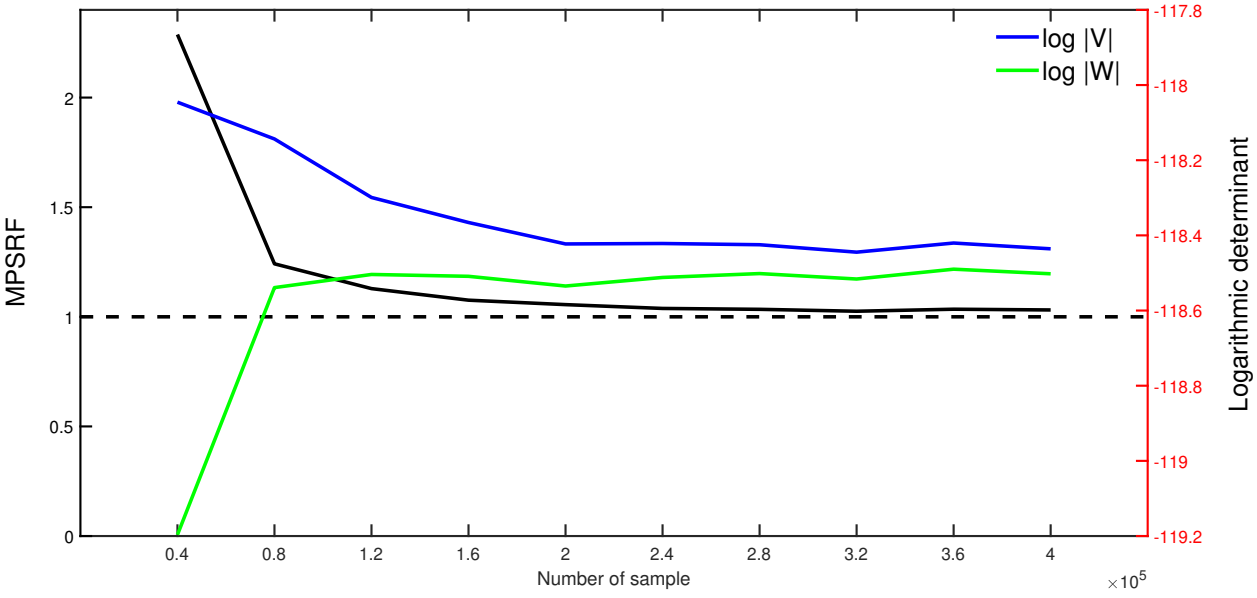

Figure 4.4: Convergence test results of samples from the DLR-SynG 2 feasible set. The results are based on 4×10^5 sampled points using the second half of the 10 Markov chain Monte Carlo chains.

The marginal histogram of each model parameter x_i is presented in Figure 4.5 with the B2BDC inner-bound and outer-bound prediction intervals. Besides the model parameters listed in Table 4.3 whose outer-bound prediction intervals are different compared to the prior uncertainty intervals, other parameters exhibit a reduced uncertainty in their inner-bound prediction intervals (e.g., x_5 and x_{12}). The histograms indicate that more parameters have a different posterior distribution compared to the prior uniform distribution compared to

the observation with the inner-bound prediction intervals. For example, parameters x_5, x_8, x_9, x_{16}, x_{30}, x_{22}, x_{30}, x_{40} have a posterior distribution concentrated toward the prior upper bound whereas parameters x_{14}, x_{20}, x_{24}, x_{25}, x_{33} have a posterior distribution concentrated toward the prior lower bound.

Correlations among model parameters and QOI predictions based on the generated samples were investigated. A couple of cases are displayed in Figure 4.6 where a relatively strong correlation is observed between model parameters, between QOI predictions, and between a model parameter and a QOI prediction. Because the model parameters have a uniform prior distribution in $\mathcal{H}$, the observed correlation among model parameters and the small occupation of the histograms compared to $\mathcal{H}$ are direct consequences of data collaboration.

The first row in Figure 4.6 reveals that, to be consistent with all experimental data, increasing the rate of reaction HO_2+O $\rightarrow$ OH+O_2 (x_{19}) is likely to require increasing and decreasing rates of reactions HO_2+HO_2 $\rightarrow$ H_2O_2+O_2 (x_{21}) and CO+OH $\rightarrow$ CO_2+H (x_{23}), respectively. The subplots in the second row reveal that the 8th and 23rd, and the 33rd and 48th ignition delay QOIs have a positive correlation over feasible parameter vectors. A parameter vector that predicts a longer ignition delay time for QOI_8 and QOI_{33} is likely to result in predicting a longer ignition delay time for QOI_{23} and QOI_{48}. Inspection of the last row indicates that, QOI_{40} and QOI_4 are (linearly) dependent on the rate constants of reactions CH+ O_2 $\rightarrow$ CO_2+H (x_1) and H_2+OH $\rightarrow$ H_2O+H (x_{32}). A larger reaction rate of CH+ O_2 $\rightarrow$ CO_2+H or H_2+OH $\rightarrow$ H_2O+H in the feasible set is more likely to increase or decrease the respective QOI prediction. Correlations are the simplest coupled information on two scalar quantities. Although coupled relations involving more quantities are difficult to visualize, they are, in principle, fully calculable from the samples.

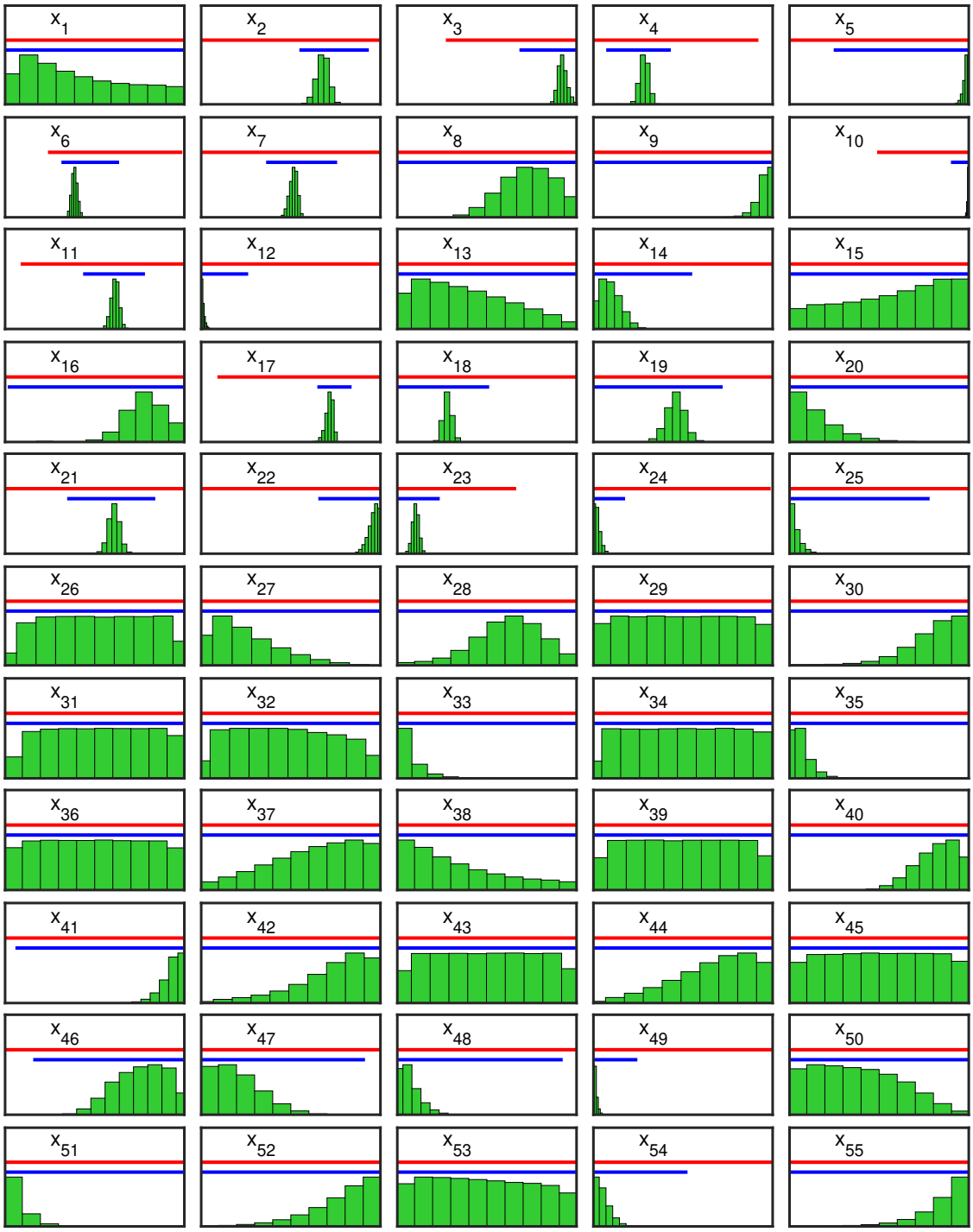

Figure 4.5: Marginal histograms and Bound-to-Bound Data Collaboration predicted inner-bound (blue lines) and outer-bound (red lines) posterior intervals of model parameters. The axis limits are scaled by the prior uncertainty bounds of each x_i.

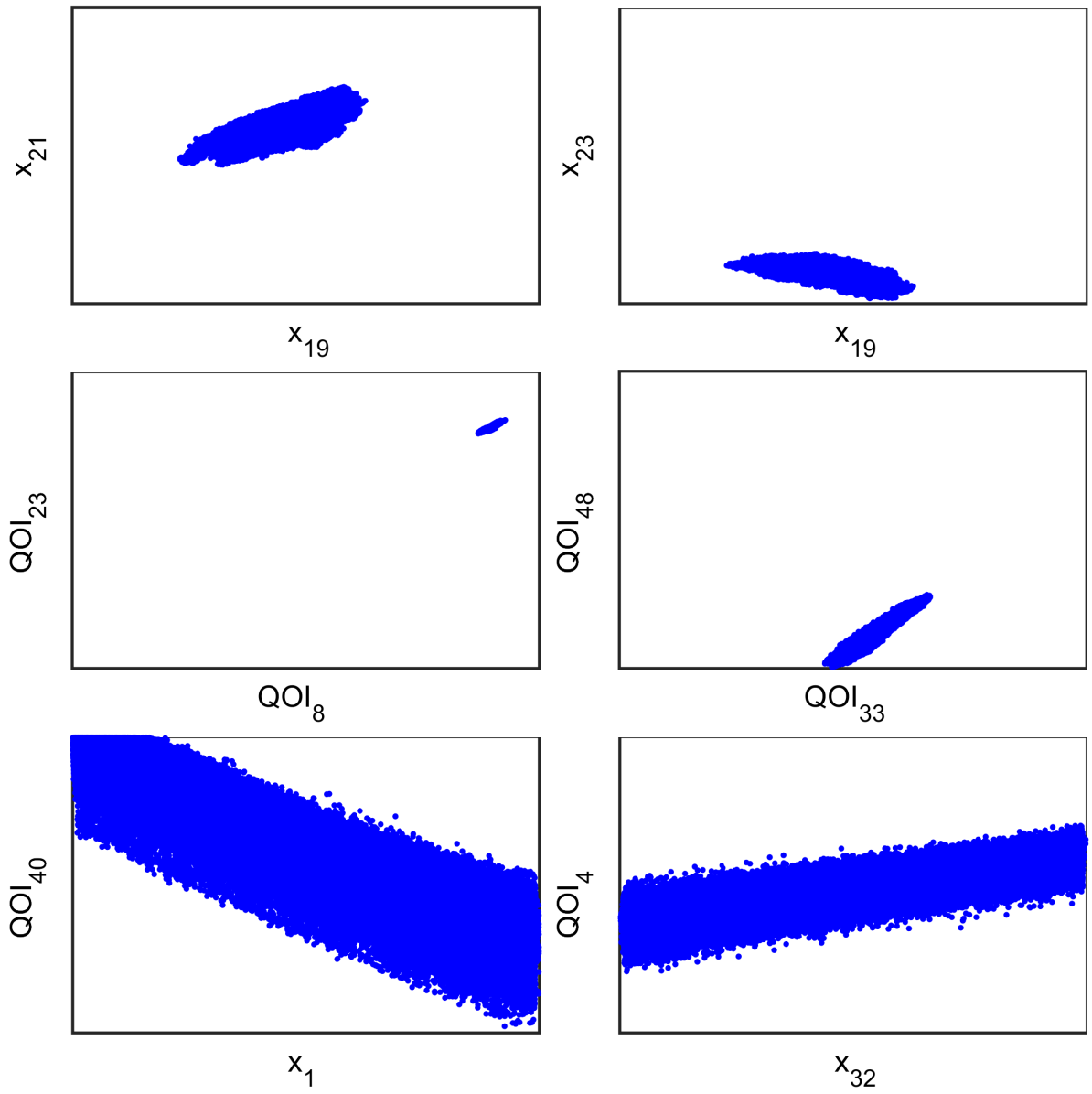

Figure 4.6: Observed two-dimensional correlations between model parameters (first row), between quantities of interest (second row), and between a model parameter and a quantity of interest (third row). The axis limits are scaled to the prior and experimental uncertainty bounds (including fitting error) for model parameters and quantities of interest, respectively.

4.7 Reaction Model Optimization

Optimized reaction models were obtained using the criteria presented in Section 2.7.6. The DLR-SynG 1 dataset is inconsistent, and only the $\mathcal{H}$-based methods are applicable in this case, whereas both $\mathcal{H}$- and $\mathcal{F}$-based optimization methods apply to DLR-SynG 2. Therefore, the LS-H optimized models were computed for both the DLR-SynG 1 and DLR-SynG 2 datasets. For DLR-SynG 2, 1N-F and LS-F optimized models were also computed. Their performance was evaluated by calculating (1) the average squared prediction error, and (2) the number of QOI predictions that violate the experimental uncertainty interval. The results are presented in Figure 4.7 for the optimized and original models (with nominal rate constants) and the VCM model (the model parameter vector obtained in solving the inner-bound solution of the VCM).

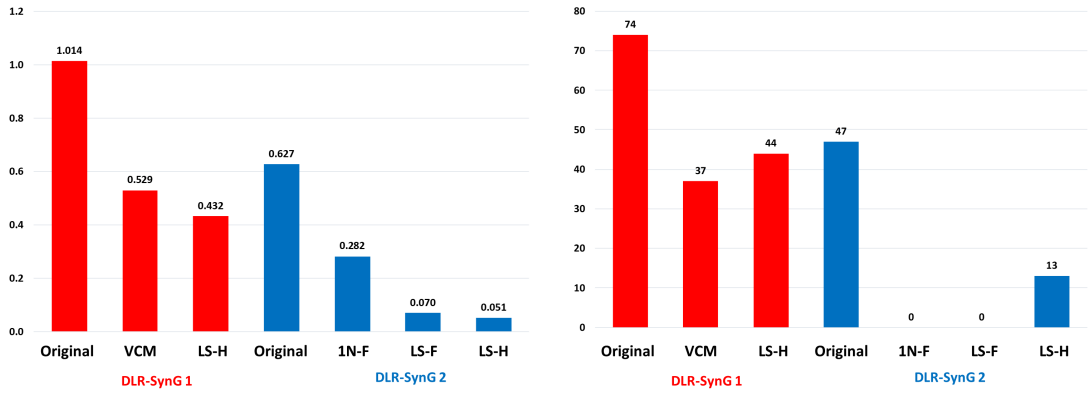

Figure 4.7: Left: Average squared deviation of the optimized model predictions from the experimental observations. Right: Number of optimized model predictions that are outside of their experimental uncertainty bounds. Red and blue denote models computed using the DLR-SynG 1 and DLR-SynG 2 datasets, respectively.

Comparison of both performance criteria indicates that, for both datasets, DLR-SynG 1 and DLR-SynG 2, all optimized models (including the VCM model) produce a significantly better agreement with the experimental data than the original model. As remarked in [28], the results imply that simply putting together the literature-recommended rate constants in a derived syngas combustion mechanism is insufficient to guarantee its predictivity for macroscopic syngas combustion properties, such as the ignition delay time and laminar flame speed. As in [136], the LS-H models generate a smaller average prediction error compared to the LS-F and 1N-F models because the method searches an enclosed region ($\mathcal{H}$ compared to $\mathcal{F}$). However, the LS-H models predict 44 and 13 QOIs outside of their experimental

uncertainty bounds for DLR-SynG 1 and DLR-SynG 2, respectively. The LS-F and 1N-F models, by design, generate predictions within all QOI uncertainty bounds.

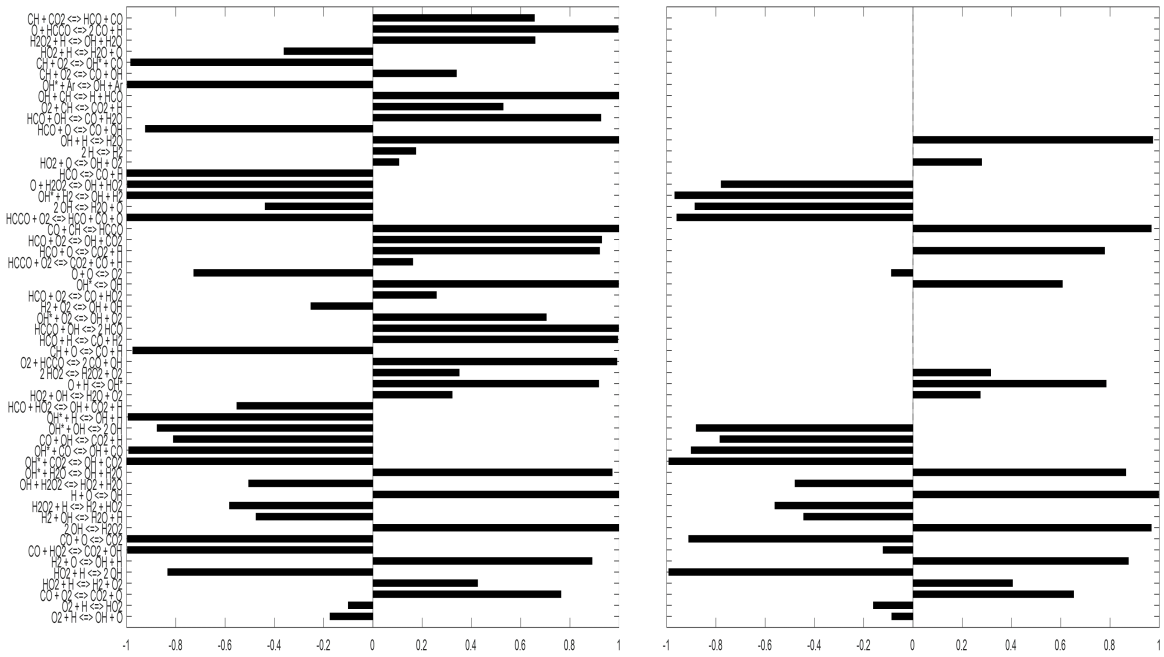

Figure 4.8: Relative model parameter (x) adjustments in the LS-H (left) and 1N-F (right) optimized models. Both models were computed using the DLR-SynG 2 dataset.

The model parameter vectors associated with the LS-H and 1N-F model computed for the DLR-SynG 2 dataset are depicted in Figure 4.8. The parameter vector of the LS-H model changes all model parameters, and many of them are adjusted to their respective lower or upper prior uncertainty bounds. In comparison, the parameter vector of the 1N-F model suggests a sparser change across the model parameters and retains a noticeable number of the parameters at their nominal values.

The original model and the LS-H, LS-F, 1N-F, and VCM optimized models were compared with another recently published syngas reaction model [126] that has been reported to outperform 19 other models. This model is referred to as Varga's model, and its prediction performance was calculated for the data collected in this study. The results for the ignition delay times and laminar flame speeds are given in Figures 4.9 to 4.11 and Figures 4.12 to 4.14, respectively.

The results demonstrate that all optimized models perform with about the same overall quality. Some models perform better in one set of conditions, whereas others make predictions closer to the experimental observations for different sets of conditions. The results highlight the focus of B2BDC on systematically quantifying uncertainty in model parameters

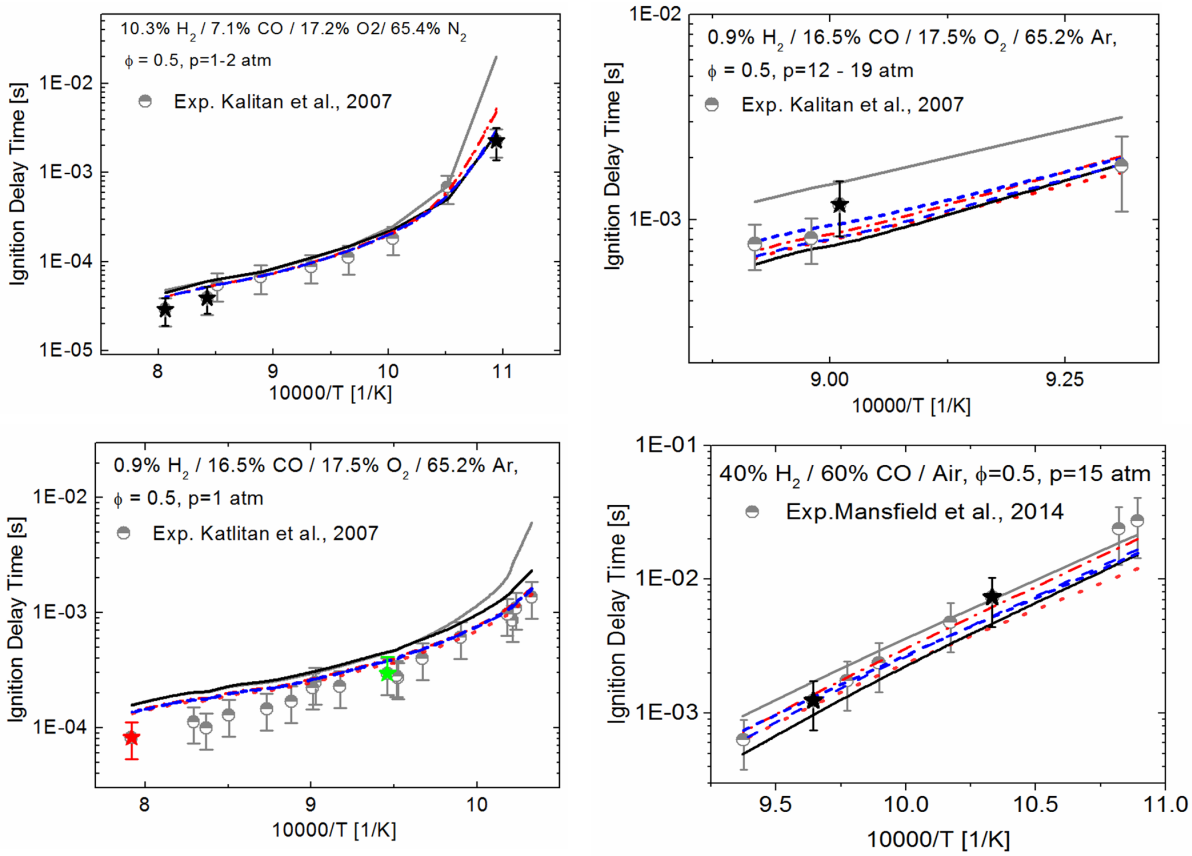

Figure 4.9: Ignition delay time data in [58, 73] simulated using the original model (black line), Varga's model (gray line), LS-H model (dotted red line), vector consistency measure (VCM) model (red dashed-dotted line), LS-F model (dashed blue line), and 1N-F model (short-dashed blue line). Symbols are experimental data with uncertainty represented by vertical bars. Black stars are quantities of interest (QOIs) in the DLR-SynG 2 dataset. Red stars are self-inconsistent QOIs; green stars are QOIs detected through VCM analysis.

through data collaboration instead of computing a solution that best fits the experimental observations.

We then tested all models at relatively extreme operating conditions of a combustor, with a fuel with a low heating value initialized at low temperatures and high pressures. Specifically, we selected a fuel mixture containing 1.0% H_2, 5.3% CO, 42.7% H_2O, and 51.1% CO_2 that is mixed with preheated air under fuel-lean conditions with $\phi = 0.5$, $P = 12$ bar, and T=720 to 820K. The prediction results are illustrated in Figure 4.15. The LS-H model, which produces the smallest prediction error over the dataset, significantly underpredicts all

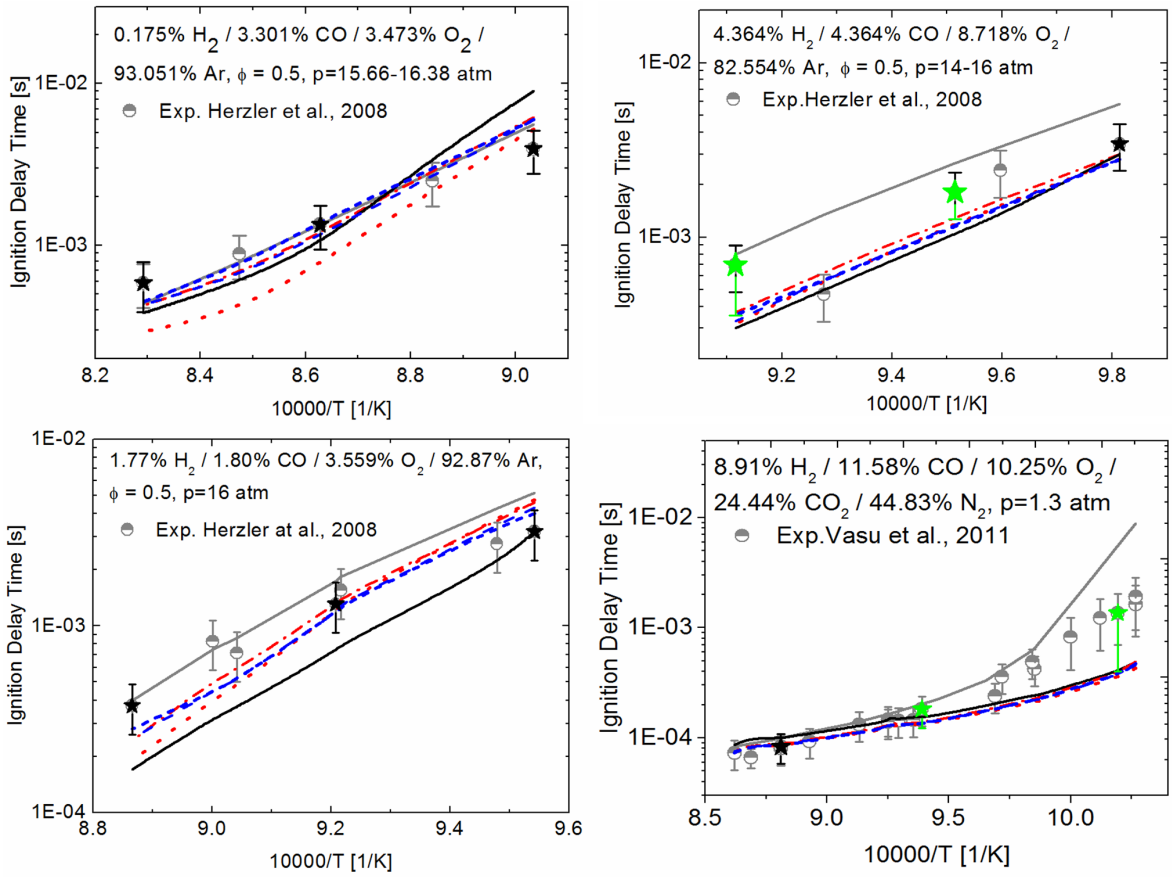

Figure 4.10: Ignition delay time data in [54, 127] simulated using the original model (black line), Varga's model (gray line), LS-H model (dotted red line), vector consistency measure (VCM) model (dash-dotted red line), LS-F model (dashed blue line), and 1N-F model (short-dashed blue line). Symbols are experimental data with uncertainty represented by vertical bars. Black stars are quantities of interest (QOIs) in the DLR-SynG 2 dataset. Green stars are QOIs detected through VCM analysis.

targets relative to their B2BDC prediction intervals.

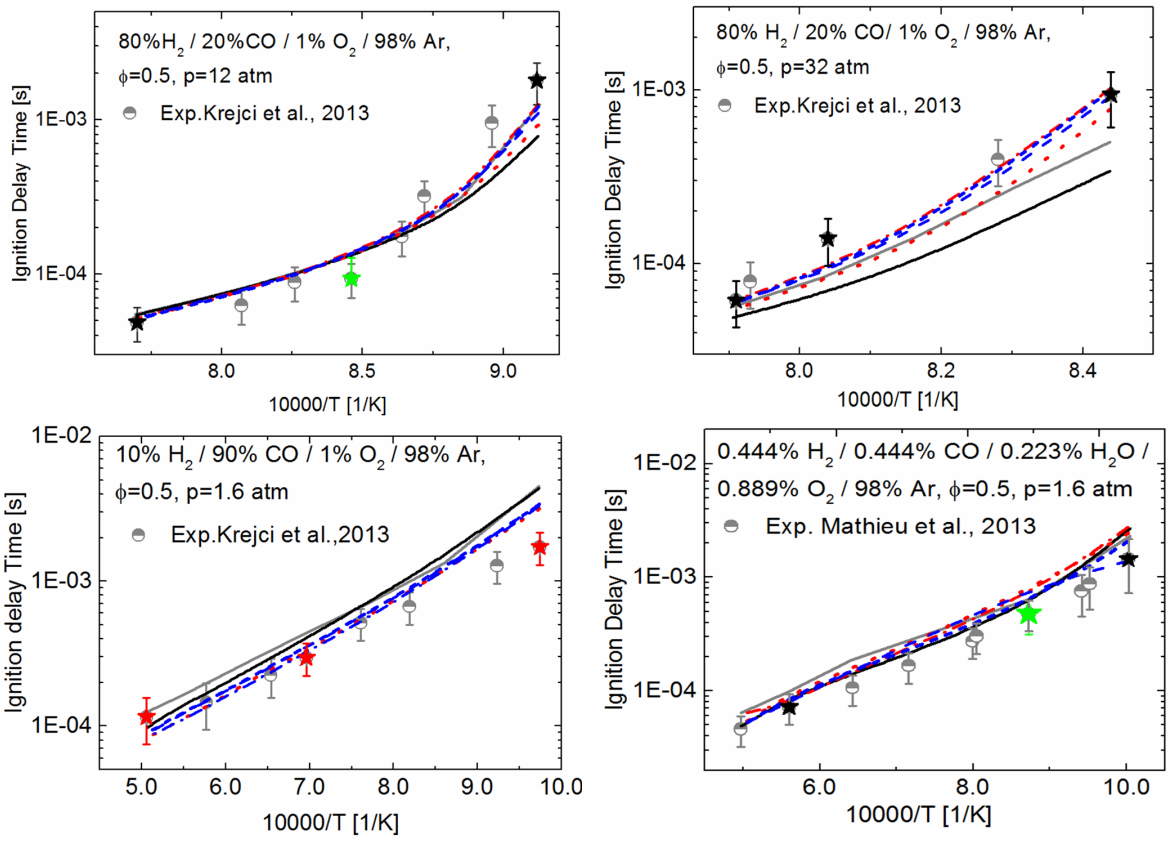

Figure 4.11: Ignition delay time data in [65, 75] simulated using the original model (black line), Varga's model (gray line), LS-H model (dotted red line), vector consistency measure (VCM) model (dashed-dotted red line), LS-F model (dashed blue line), and 1N-F model (short-dashed blue line). Symbols are experimental data with uncertainty represented by vertical bars. Black stars are quantities of interest (QOIs) in the DLR-SynG 2 dataset. Red stars are self-inconsistent QOIs. Green stars are QOIs detected through VCM analysis.

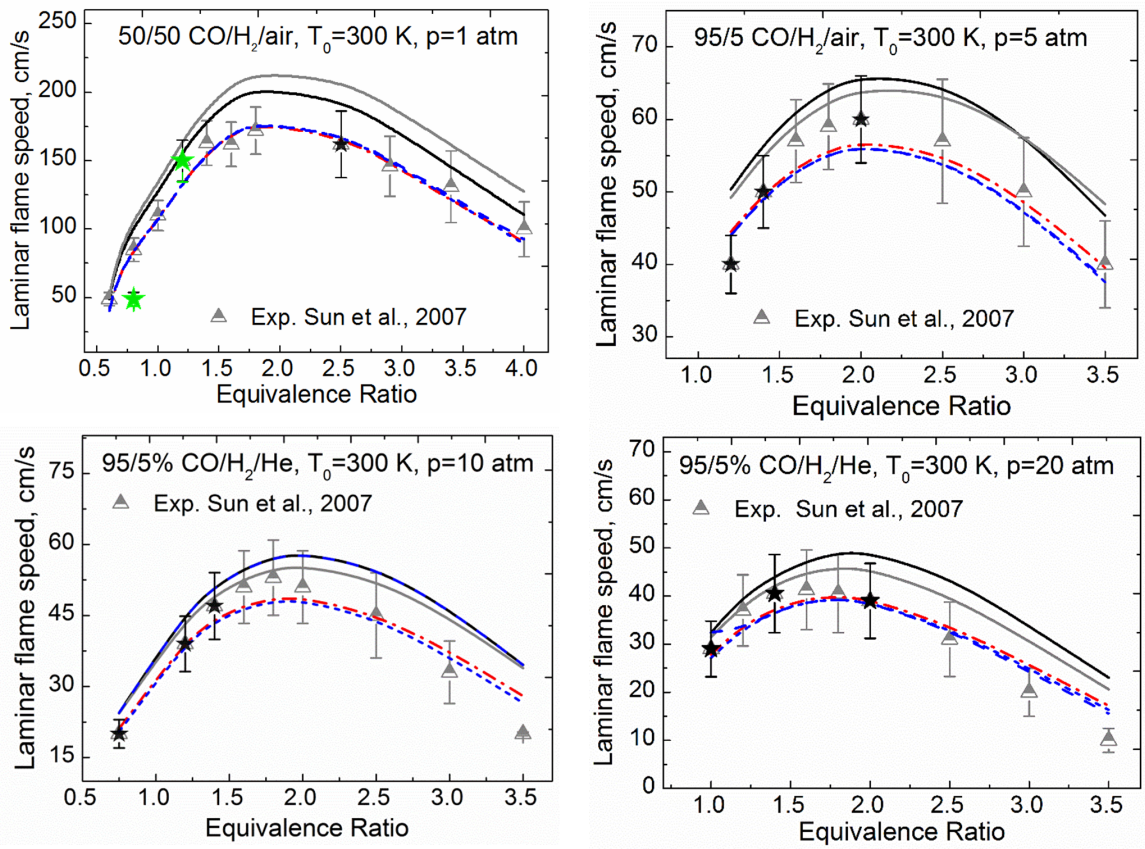

Figure 4.12: Laminar flame speed data in [123] simulated using the original model (black line), Varga's model (gray line), LS-H model (dotted red line), vector consistency measure (VCM) model (dashed-dotted red line), LS-F model (dashed blue line), and 1N-F model (short-dashed blue line). Symbols are experimental data with uncertainty represented by vertical bars. Black stars are quantities of interest (QOIs) in the DLR-SynG 2 dataset. Green stars are QOIs detected through VCM analysis.

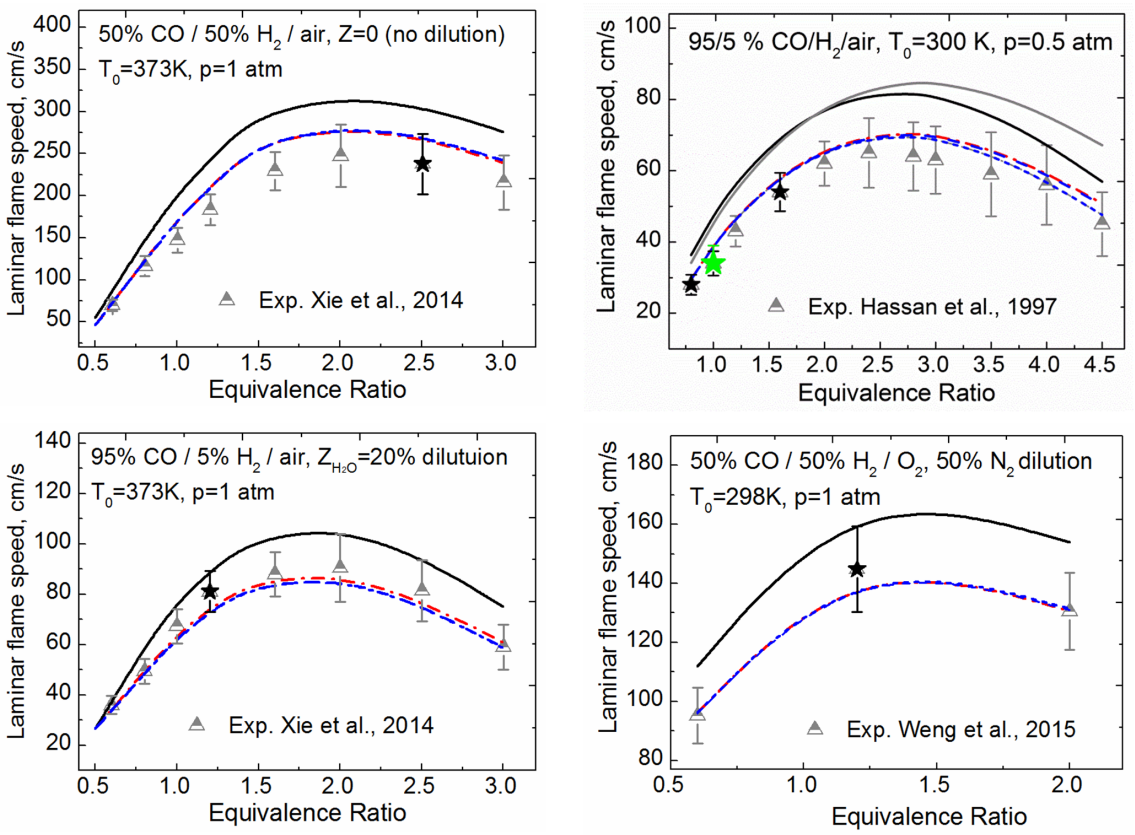

Figure 4.13: Laminar flame speed data in [82, 133, 131] simulated using the original model (black line), Varga's model (gray line), LS-H model (dotted red line), vector consistency measure (VCM) model (dashed-dotted red line), LS-F model (dashed blue line), and 1N-F model (short-dashed blue line). Symbols are experimental data with uncertainty represented by vertical bars. Black stars are quantities of interest (QOIs) in the DLR-SynG 2 dataset. Green stars are QOIs detected through VCM analysis.

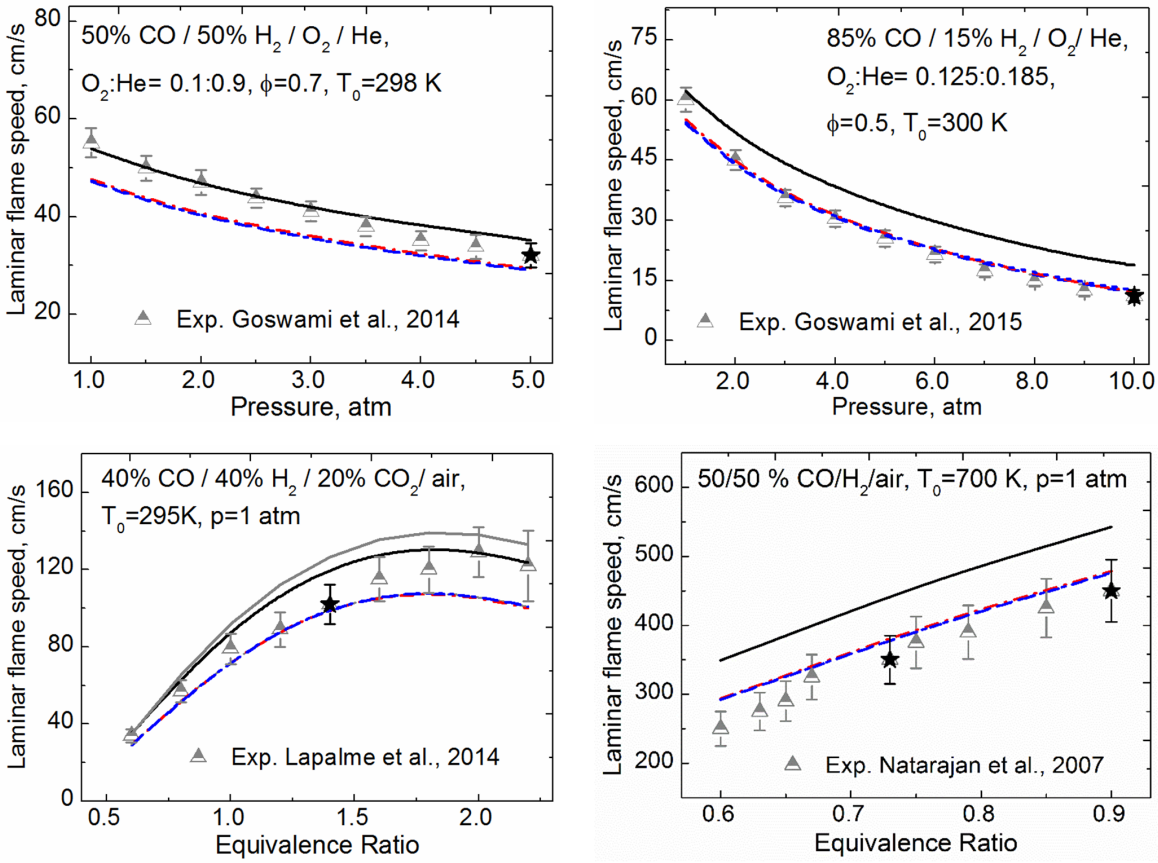

Figure 4.14: Laminar flame speed data in [43, 86, 66, 44] simulated using the original model (black line), Varga's model (gray line), LS-H model (dotted red line), vector consistency measure (VCM) model (dashed-dotted red line), LS-F model (dashed blue line), and 1N-F model (short-dashed blue line). Symbols are experimental data with uncertainty represented by vertical bars. Black stars are quantities of interest (QOIs) in the DLR-SynG 2 dataset.

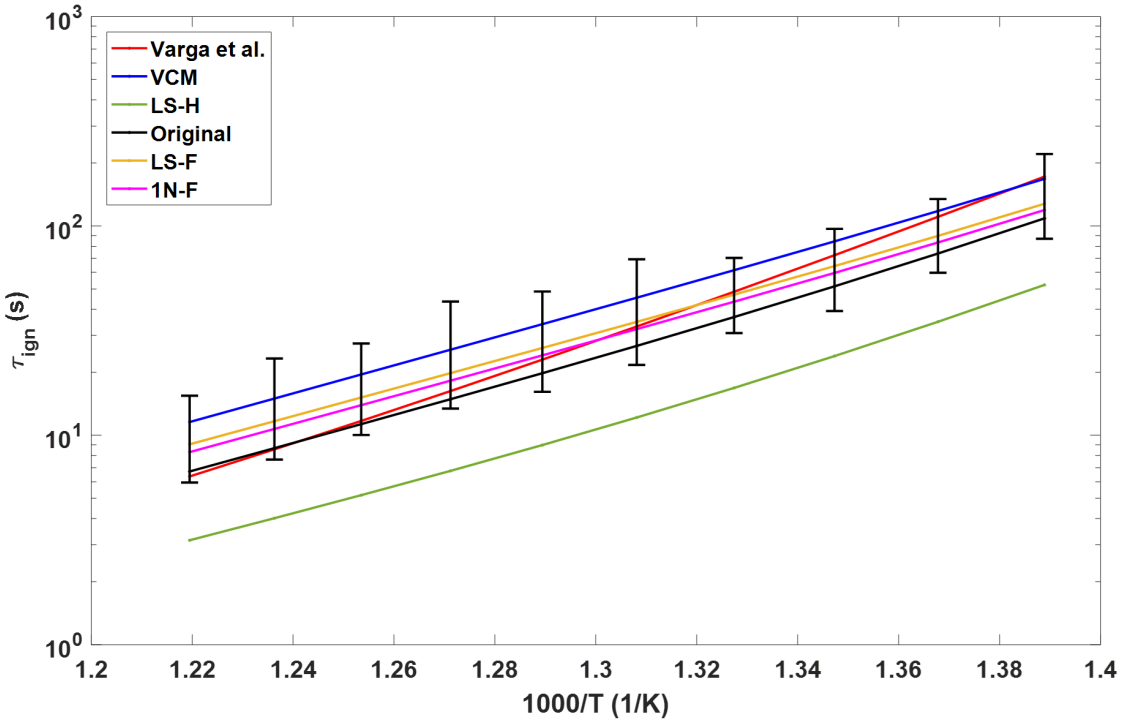

Figure 4.15: Ignition delay time predicted with the original model (black line), Varga's model (red), vector consistency measure (VCM) model (blue), LS-H model (green), LS-F model (orange), 1N-F model (purple), and bound-to-bound data collaboration (B2BDC) prediction interval (vertical black bar).

4.8 Chapter Summary

The B2BDC method was applied to a syngas combustion dataset with shock-tube ignition delay time and laminar flame speed QOIs. The initial dataset turned out to be massively inconsistent, and dataset inconsistency was effectively resolved using the VCM method. The feasible set of the consistent dataset was examined by computing the prediction intervals of model parameters and a few VCM-identified QOIs. A converged set of samples was generated using the Gibbs sampler that is uniformly distributed in the feasible set. Marginal histograms of model parameters and 2D correlations were examined based on the sample set. Optimized models were obtained and compared to another well-established model. All compared models perform comparably over the data in the dataset. However, the LS-H model exhibits a significantly deteriorated performance at conditions different from those considered in the dataset.

In addition to the eight self-inconsistent QOIs, the VCM method detects a sizable number of data with a nonzero uncertainty bound relaxation: 37 out of 159 ($\approx$23%). Removal of experimental data from an analysis is always the last choice, especially when no strong evidence supports such an operation. For example, in the present analysis, the identified QOIs exhibit no obvious similarities among them. They are not from the same research institute, nor do they have similar experimental conditions. Yet we must remove the QOIs suggested by the VCM computation to proceed with computations that apply only to a consistent dataset. However, the inconsistency may not, or at least may not entirely be caused by the incorrectly assessed experimental uncertainty. The underlying model may be inadequate to represent the experimental measurements faithfully. The question is whether we can compensate for the influence of model discrepancy in B2BDC and resolve the inconsistency without discarding experimental data. This is the topic of the next chapter.

Chapter 5

Representation of Model Discrepancy

The uncertainty quantification (UQ) analysis with the syngas combustion dataset in Chapter 4 demonstrates a situation where a large number of data (37 out of 159) are detected by the vector consistency measure (VCM) method in addition to eight self-inconsistent ones. Removal of such a considerable number of experimental data without a clear justification is accompanied with serious concern and raises the question: is there any missing factors in the analysis that we have not considered? In this chapter, I investigate another source of uncertainty caused by the potential difference between the model and the underlying physical process it simulates, termed as model discrepancy, and develop new methods in Bound-to-Bound Data Collaboration (B2BDC) framework to explicitly compensate for the model inadequacy in the computations.

5.1 Definition of Model Discrepancy

In the work of Kennedy and O'Hagan [60], experimental observations are assumed to be noisy measurement of the underlying true process which represents reality,

$$y = \mathcal{R}(s) + \epsilon, \tag{5.1}$$

where ϵ is the measurement noise, s are the scenario parameters, and $\mathcal{R}(s)$ represents reality. The scenario parameters are controllable properties known from the experimental setup and can vary from experiment to experiment, for example the initial temperature and pressure for a shock tube ignition delay time measurement. In any scientific endeavor, knowledge of the true process is an idealization; a model, considered as tentatively entertained [7], may have a systematic error in its prediction. Kennedy and O'Hagan [60] suggest to describe the uncertainty in the model form as an additive term δ, referred to as *model discrepancy*, to the model output,

$$\mathcal{R}(s) = M(x^*, s) + \delta(s), \tag{5.2}$$

where x^* is the underlying true calibration parameter vector. The model parameters are uncertain parameters intrinsic to the model, $M(\cdot)$, and share a common set of values across all experiments.

The assumption that the discrepancy term δ depends on scenario parameters s is an important characteristic of the setup: it attempts to describe systematic errors at different scenarios by a structured function. This structure puts an implicit constraint on values the discrepancy term can take at different experimental conditions and provides an opportunity to infer the discrepancy through UQ analysis. Discrepancy with different types of quantity of interest (QOI), for example the ignition delay time and laminar flame speed QOIs encountered in the syngas application in Chapter 4, should be compensated for by different discrepancy terms since the systematic error associated with them is unlikely to be correlated.

This approach of compensating for model discrepancy has received substantial interest and following under the Bayesian calibration framework (see, e.g., [1, 11, 55, 57, 63, 96, 97, 121, 129]). While referring to model discrepancy as model inadequacy, model bias, model form uncertainty, model error, and model form error, some use a Gaussian process (GP) [102, 118] to represent $\delta(s)$ [11, 55, 96, 97, 121, 129] and others a functional decomposition [57, 63]. Efforts have also been made to overcome the difficulty in identifying model discrepancy and model parameters individually, and to improve prediction performance at conditions different from the training data. For example, Brynjarsdóttir and O'Hagan [11] put constraints on the GP realization of model discrepancy at specific conditions derived from domain knowledge. Plumlee [96] argued that the prior distribution of model discrepancy should be orthogonal to the gradient of the model under certain assumptions. Wang et al. [129] estimated the model discrepancy and model parameters separately. Joseph and Melkote [57] constructed a statistical model of discrepancy in a sequential manner, limiting its contribution to the prediction.

5.2 B2BDC with Model Discrepancy

We adopt the definition of model discrepancy proposed by Kennedy and O'Hagan in Equation (5.2) and on that basis introduce a scenario-dependent *discrepancy function* $\delta(s)$ into the model-data constraint,

$$L_e \leq M_k(x, s_e) + \delta_k(s_e) \leq U_e, \tag{5.3}$$

where the subscript k is the index representing the type of the eth QOI. We assume that the discrepancy takes the form of a linear combination of n_k basis functions, $\{\Phi_i^k\}_{i=1}^{n_k}$,

$$\delta_k(s) = \sum_{i=1}^{n_k} c_i^k \Phi_i^k(s), \tag{5.4}$$

where $c^k = \{c_i^k\}_{i=1}^{n_k}$ are unknown coefficients, and $n_k = 0$ refers hereafter to a zero discrepancy function (i.e., $\delta_k = 0$). Substitution of Equation (5.4) into Equation (5.3) results in,

$$L_e \leq M_k(x, s_e) + \sum_{i=1}^{n_k} c_i^k \Phi_i^k(s_e) \leq U_e. \tag{5.5}$$

Let c denote the vector containing all discrepancy related coefficients. The linear form in Equation (5.4) is motivated by the fact that existing tools in B2BDC are directly applicable with Equation (5.5) in the extended parameter space (x, c). While $\{\Phi_i^k\}_{i=1}^{n_k}$ can be any set of nonlinear functions, the modified model-data constraints are linear in c. Representing model discrepancy by a linear combination of basis functions has also been used by others [57]. However, our method is different that it does not fit a particular model discrepancy function during the analysis. As a result, orthogonality among basis functions that provides a better performance regarding function estimation is not required.

We define the joint feasible set in the extended parameter space of x and c by combining the prior uncertainty and modified model-data constraints,

$$\mathcal{F}_\delta = \{(x, c) \,|\, x \in \mathcal{H},\, c \in \mathcal{H}_c,\, L_e \leq M_k(x, s_e) + \sum_{i=1}^{n_k} c_i^k \Phi_i^k(s_e) \leq U_e,\, e = 1, 2, \ldots, N\}, \tag{5.6}$$

where $\mathcal{H}_c$ represents the prior uncertainty region of the discrepancy-function coefficients c. The projection of $\mathcal{F}_\delta$ on the model parameter space is,

$$\widetilde{\mathcal{F}} = \{x \,|\, \exists \hat{c} : (x, \hat{c}) \in \mathcal{F}_\delta\}, \tag{5.7}$$

which represents the set of feasible model parameters after including the discrepancy functions. When the joint feasible set is not empty, prediction at an unmeasured scenario s_p can be obtained by solving the modified versions of Equations (2.7) and (2.8) as following:

$$\begin{aligned} L_p = \underset{x,\,c}{\text{minimize}} \quad & M_{k'}(x, s_p) + \sum_{i=1}^{n_{k'}} c_i^{k'} \Phi_i^{k'}(s_p) \\ \text{subject to} \quad & x \in \mathcal{H}, \\ & c \in \mathcal{H}_c, \\ & L_e \leq M_k(x, s_e) + \sum_{i=1}^{n_k} c_i^k \Phi_i^k(s_e) \leq U_e, \quad e = 1, 2, \ldots, N, \end{aligned} \tag{5.8}$$

and

$$\begin{aligned} U_p = \underset{x,\,c}{\text{maximize}} \quad & M_{k'}(x, s_p) + \sum_{i=1}^{n_{k'}} c_i^{k'} \Phi_i^{k'}(s_p) \\ \text{subject to} \quad & x \in \mathcal{H}, \\ & c \in \mathcal{H}_c, \\ & L_e \leq M_k(x, s_e) + \sum_{i=1}^{n_k} c_i^k \Phi_i^k(s_e) \leq U_e, \quad e = 1, 2, \ldots, N, \end{aligned} \tag{5.9}$$

where k' represents the QOI type of the prediction model. To simplify the notation for a more concise demonstration of the method, we assume a unique type of QOIs and remove the index k hereafter.

The proposed method treats the observed data as the sum of model output and discrepancy function as implied by Equation (5.2). The joint feasible set, defined over the extended parameter space $(x,\, c)$, therefore represents only combinations of the model and discrepancy function that are consistent with the data. It is not possible to learn the model or the discrepancy function separately without further assumptions and/or information.

Conceptually, the discrepancy function should be included whenever an analyst is aware of any potential model inadequacy based on domain expertise. However, this criterion is rather overoptimistic and can be difficult to operate with: if the prior knowledge is enough to indicate the existence of a systematic error, why don't we improve the implemented model before the analysis; if it is not evident enough, how can we make the judgement? Therefore, from a practical perspective the developed method simply provides another resolution to dataset inconsistency in addition to the VCM method, motivated by that model discrepancy can be a competitive contributor to the observed disagreement between data and models. With this interpretation, a challenge is the choice of basis functions since there are infinitely many sets of basis functions that can regain dataset consistency. An analyst may simply choose the set with the least number of basis functions that resolves dataset inconsistency following similar logic in developing Akaike's criterion: to penalize larger number of parameters and prevent overfitting. If extra insight is provided, various forms of discrepancy function can be investigated before making the final decision based on considerations besides the requirement that dataset consistency is recovered.

The developed framework with model discrepancy expressed using Equation (5.4) has a general feature that, for a given dataset and a prediction QOI, the prediction interval $[L_p,\, U_p]$ becomes systematically wider if additional basis functions are included. To understand this, suppose two sets of basis functions are used in an analysis, with the second being a superset of the first. Let vector c represent the coefficients for the shared basis functions $\{\Phi_i\}_{i=1}^{n}$ and c' the coefficient vector for the additional basis functions $\{\Phi'_j\}_{j=1}^{n'}$ as following:

$$\begin{aligned} \delta^1(s) &= \sum_{i=1}^{n} c_i \Phi_i(s) \\ \delta^2(s) &= \delta^1(s) + \sum_{j=1}^{n'} c'_j \Phi'_j(s). \end{aligned} \tag{5.10}$$

The corresponding joint feasible sets formed by Equation (5.6) are denoted by $\mathcal{F}_\delta^1$ and $\mathcal{F}_\delta^2$. Any feasible point $(x,\, c) \in \mathcal{F}_\delta^1$ is also feasible for $\mathcal{F}_\delta^2$ by setting c' to a zero vector, i.e., $(x,\, c,\, c')|_{c'=0} \in \mathcal{F}_\delta^2$. Therefore, the prediction interval of a QOI computed over $\mathcal{F}_\delta^1$ is always contained by that computed over $\mathcal{F}_\delta^2$. The increased uncertainty in the prediction interval

can depend on the prediction model, the dataset, and the selected basis functions, as will be demonstrated in Sections 5.3 and 5.4.

Previous work (e.g., [11, 96]) has demonstrated the value of including prior knowledge of the model discrepancy function when applying statistical UQ methods. In B2BDC, this can be accomplished by incorporating additional constraints. For example, sign constraints on the discrepancy function, or its derivatives, can be enforced at specified scenario conditions by introducing linear inequalities in c. An example of forcing model discrepancy function to be positive at selected scenarios is

$$\sum_{i=1}^{n} c_i \phi_i(s_j) > 0, \;\; j = 1, 2, \ldots. \tag{5.11}$$

The effect of such constraints is automatically propagated to predictions through augmenting the feasibility constraint in Equations (5.8) and (5.9). Another example of constraining the magnitude of model discrepancy function is given in Section 5.3.

The posterior uncertainty of the model discrepancy function at any specified scenario s_p can be calculated by solving the prediction problems in Equations (5.8) and (5.9) with the objective function replaced by $\delta(s_p)$ as following:

$$\begin{aligned} L_\delta = \underset{x,\,c}{\text{minimize}} \quad & \sum_{i=1}^{n} c_i \Phi_i(s_p) \\ \text{subject to} \quad & x \in \mathcal{H}, \\ & c \in \mathcal{H}_c, \\ & L_e \leq M_k(x, s_e) + \sum_{i=1}^{n_k} c_i^k \Phi_i^k(s_e) \leq U_e, \quad e = 1, 2, \ldots, N, \end{aligned} \tag{5.12}$$

and

$$\begin{aligned} U_\delta = \underset{x,\,c}{\text{maximize}} \quad & \sum_{i=1}^{n} c_i \Phi_i(s_p) \\ \text{subject to} \quad & x \in \mathcal{H}, \\ & c \in \mathcal{H}_c, \\ & L_e \leq M_k(x, s_e) + \sum_{i=1}^{n_k} c_i^k \Phi_i^k(s_e) \leq U_e, \quad e = 1, 2, \ldots, N, \end{aligned} \tag{5.13}$$

Repeating this computation at various conditions in the scenario parameter space can identify regions where uncertainty in the model discrepancy function is large. In a similar manner, the posterior uncertainty can be calculated for each discrepancy-function coefficient c_i.

Application of this developed method is demonstrated with two examples in the following sections: an illustrative mass-spring-damper system and a realistic hydrogen combustion

system. In each example, we started with a postulated "true" model to represent the underlying true process. An inadequate model for the analysis was then created by omitting some parts of the true model and a true calibration parameter value was selected. The developed framework was applied to the inadequate model and the following results are reported and discussed for different choices of basis functions:

1. Dataset consistency
2. If the dataset is consistent, a) the prediction intervals at interpolated and extrapolated conditions; b) whether the true process values are contained in the prediction intervals, and to a secondary point, whether the true calibration parameter x^* is in the (projected) feasible set.

The computation was conducted for two levels of experimental uncertainty to provide a more comprehensive characterization of the developed method. To clarify the nomenclature, δ^* and δ are used to represent the true model discrepancy defined in Equation (5.2) and the linear combination in Equation (5.4), respectively. We also differentiate between *interpolated* and *extrapolated* predictions, where the former refers to s_p lying within the training domain and the latter outside. For the simpler mass-spring-damper example, no surrogate models were used; quadratic surrogate models were used for the hydrogen combustion example. In both examples, only the inner-bound solutions were calculated and examined.

5.3 One-dimensional Mass-Spring-Damper System

5.3.1 Problem Statement

The force, F, needed to extend or compress a spring by a small distance, z, is expressed using Hooke's law

$$F = -kz, \tag{5.14}$$

where k is a constant characteristic of the spring, its stiffness. We now consider a simple system: a ball attached to a spring, whose other end is fixed at a wall, sketched in Figure 5.1. The ball has a mass $m = 1$ and is placed initially at $z_0 = -1.5$ with an initial velocity $v_0 = 1$. In addition to the force exerted by the spring, the motion of the ball is also affected by a damping force proportional to the ball's velocity. Thus, the evolution of the ball's displacement is described by

$$\begin{aligned} &\frac{d^2z}{dt} = -kz - b\frac{dz}{dt}, \\ &z|_{t=0} = z_0 = -1.5, \\ &\left.\frac{dz}{dt}\right|_{t=0} = v_0 = 1, \end{aligned} \tag{5.15}$$

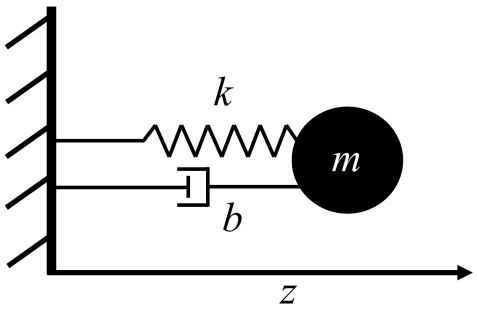

Figure 5.1: Sketch plot of the mass-spring-damper system.

where b is the constant coefficient of the damping force and its value is set to 0.05. For a given k, displacement evolution of the system described in Equation (5.15)—the "true" model in this example—is the solution to a second order, constant coefficient, ordinary differential equation and has analytic form

$$z^*(k,t) = e^{-bt/2}\left[\frac{v_0 + 0.5bz_0}{\sqrt{k - b^2/4}}\sin\left(\sqrt{k - b^2/4}\ t\right) + z_0\cos\left(\sqrt{k - b^2/4}\ t\right)\right]. \tag{5.16}$$

The "inadequate" model is constructed by neglecting the damping force (i.e., $b = 0$), which results in the solution

$$z(k,t) = \frac{v_0}{\sqrt{k}}\sin\left(\sqrt{k}\ t\right) + z_0\cos(\sqrt{k}\ t). \tag{5.17}$$

In both the true and inadequate models, the stiffness k is the model parameter and the time t is the scenario parameter. The true stiffness of the spring — the true calibration parameter value — is selected to be $k^* = 0.25$ with the prior uncertainty interval $\mathcal{H} = [0.2, 0.3]$. The real displacement is evaluated with $z^*(k^*, t)$. The displacements computed by the two models with $k = k^*$ and their difference, the model discrepancy defined by Equation (5.2), are demonstrated in Figure 5.2 for $t \in [0, 4]$.

The QOIs for this example were chosen to be the displacements of the ball at specified times t_e. The dataset is composed of twenty of these QOIs in the scenario region $t \in [0, 3]$. For each QOI, an "observed" value was generated by adding uniform noise with a prescribed maximum magnitude ϵ to the true process value,

$$\begin{aligned} &z_e = z^*(k^*, t_e) + \epsilon\, u_e, \\ &u_e \sim \mathcal{U}(-1,\, 1), \quad e = 1, 2, \ldots, 20. \end{aligned} \tag{5.18}$$

QOI uncertainty bounds were generated by setting $L_e = z_e - \epsilon$ and $U_e = z_e + \epsilon$. The analysis was performed with ϵ values of 0.05 and 0.1. Three prediction QOIs were generated for t

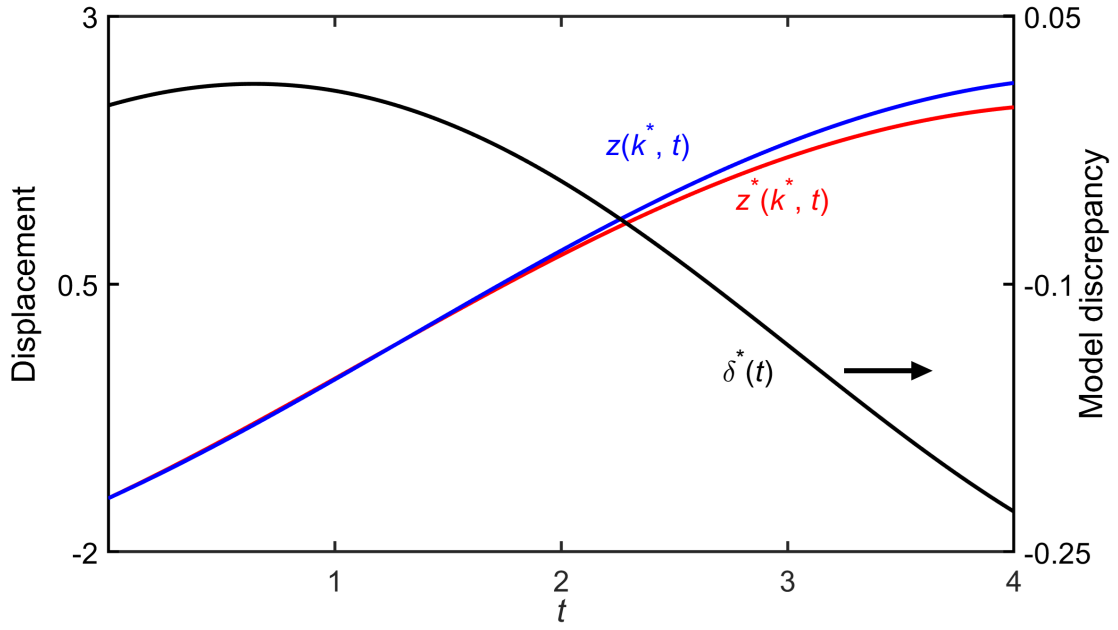

Figure 5.2: The true model solution $z^*(k^*, t)$, the inadequate model solution $z(k^*, t)$ and the model discrepancy function $\delta^*(t) = z^*(k^*, t) - z(k^*, t)$.

values of 1.5, 3.2, and 4. The first prediction case occurs at a scenario within the training-set domain of [0, 3] and is an interpolated prediction. The second and third cases occur at scenarios outside the training-set domain and are extrapolated predictions.

5.3.2 Dataset Consistency and QOI Prediction

I first consider the ideal situation where the true model, given by Equation (5.16), and the formulas in Chapter 2 are used in the B2BDC calculations. The computed prediction intervals for the three prediction QOIs are displayed in Figure 5.3. With this setup, the dataset is consistent with k^* being feasible and the prediction intervals contain the true process values at all three times for both tested ϵ's. The length of the prediction intervals at each prediction scenario is shorter for a smaller value of ϵ, indicating that more accurate measurements produce more accurate predictions.

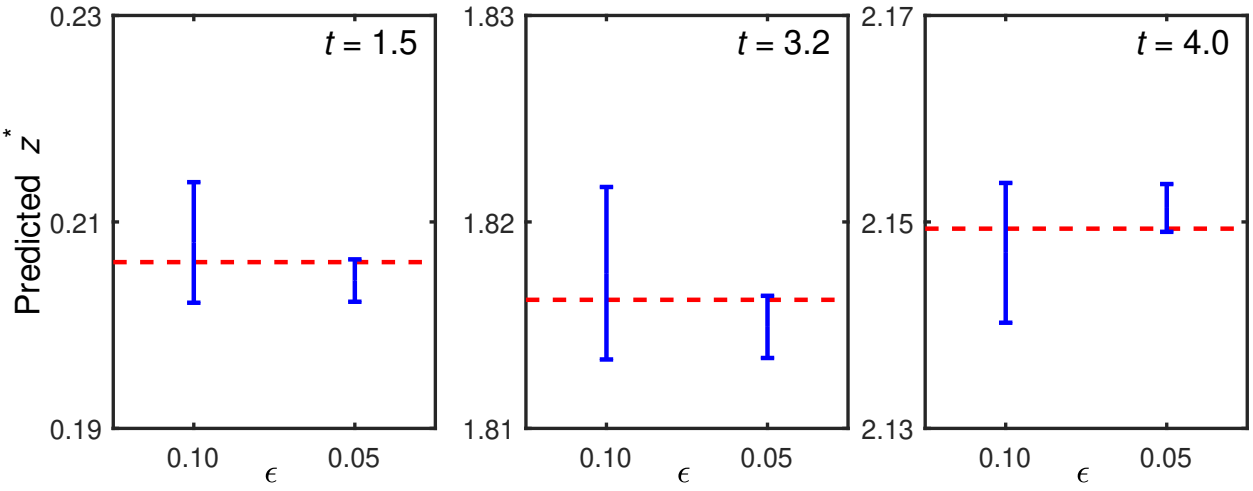

Figure 5.3: Computed QOI prediction intervals for the mass-spring-damper example using the true model. The horizontal red dashed lines mark the displacement computed with the true model and true calibration parameter value, $z^*(k^*, t)$. The vertical blue solid lines designate the B2BDC predicted intervals, computed by solving optimization problems in Equations (2.7) and (2.8).

I then move to a more realistic situation where an inadequate model, given by Equation (5.17), was examined with the new method proposed and described in Section 5.2. Four different model discrepancy functions,

$$\delta(t) = \sum_{i=1}^{n} c_{i-1} t^{i-1}, \quad n = 1, 2, 3, 4, \tag{5.19}$$

were tested in addition to the case where $\delta = 0$. The discrepancy function is a polynomial in t of degree $n - 1$.

The outcome of the dataset consistency analysis is summarized in table 5.1. Examination of these results shows that the dataset is inconsistent for both values of ϵ when $n = 0$, i.e., when no model discrepancy function is used. For $\epsilon = 0.05$, a quadratic δ is required to obtain dataset consistency. In this case, k^* is also found to be feasible. For $\epsilon = 0.1$, a constant δ

Table 5.1: Results of the dataset consistency analysis

ϵ	n				
	0	1	2	3	4
0.05	inconsistent	inconsistent	inconsistent	$k^* \in \widetilde{\mathcal{F}}$	$k^* \in \widetilde{\mathcal{F}}$
0.10	inconsistent	$k^* \notin \widetilde{\mathcal{F}}$	$k^* \in \widetilde{\mathcal{F}}$	$k^* \in \widetilde{\mathcal{F}}$	$k^* \in \widetilde{\mathcal{F}}$

is enough to achieve consistency. However, k^* becomes a feasible point only after using a linear δ.

The computed QOI prediction intervals are displayed in fig. 5.4 for $t = 1.5$, 3.2, and 4. As expected, the prediction intervals with a higher order δ are wider for both ϵ values. In the cases where δ produces a consistent dataset for both ϵ values, a shorter prediction interval is observed with the smaller ϵ. For $\epsilon = 0.1$, the calculated QOI prediction interval using a constant δ does not contain the true value at all time instances. With a linear δ, the prediction interval contains the true value at all three time instances. The prediction interval contains the true value for all tested times and for both values of ϵ with a quadratic and cubic δ.

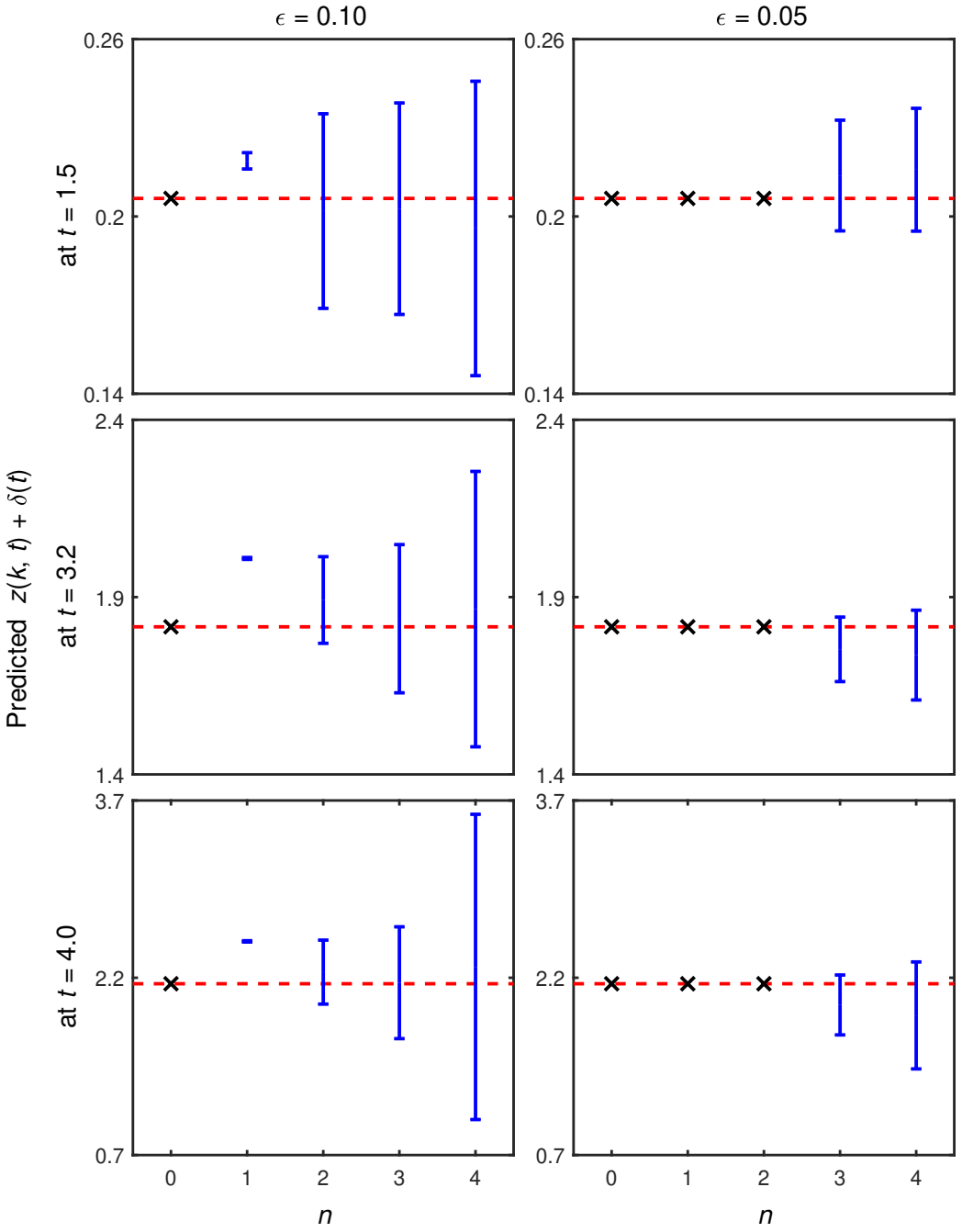

Figure 5.4: Predicted quantity of interest intervals at t = 1.5, 3.2 and 4. The horizontal red dashed lines are the displacement derived with the true model and evaluated at the true model parameter value, $z^*(k^*, t)$. The vertical blue solid lines designate the B2BDC predicted intervals, computed by solving the optimization problems in Equations (5.8) and (5.9). The $\times$'s mark dataset inconsistency.

5.3.3 Posterior Bounds of Model Parameter and Discrepancy-Function Coefficients

I now examine the posterior uncertainty bounds of model parameter k and discrepancy-function coefficients $\{c_i\}_{i=1}^n$ obtained for different polynomial orders of δ. These bounds are the 1D projection of the joint feasible set $\mathcal{F}_\delta$ onto coordinate directions. The volume ratio of the joint feasible set and the multidimensional orthotope, whose sides are the posterior projections of the parameters, was calculated as the fraction of 10^6 samples uniformly distributed in the orthotope, that lay in $\mathcal{F}_\delta$. The results are presented in Table 5.2. For comparison, the prediction interval of k obtained with the true model is also listed. The computed volume ratio results show that the joint feasible set becomes progressively smaller relative to the orthotope as dimension increases.

Table 5.2: Projection of the joint feasible set, computed with the inadequate model given in Equation (5.17) and different model discrepancy functions defined in Equation (5.19), onto coordinate directions of model parameter k and discrepancy-function coefficients $\{c_i\}_{i=1}^n$, as well as computed volume ratio of the joint feasible set to the box made of the projected intervals. The symbol $\varnothing$ represents an empty posterior uncertainty due to dataset inconsistency.

n	k	c_0	c_1	c_2	c_3	Volume ratio
			$\epsilon = 0.05$			
	[0.24, 0.25]*					
0	$\varnothing$					
1	$\varnothing$	$\varnothing$				
2	$\varnothing$	$\varnothing$	$\varnothing$			
3	[0.20, 0.30]	[-0.02, 0.03]	[-0.08, 0.06]	[-0.05, 0.00]		5.2×10^{-3}
4	[0.20, 0.30]	[-0.02, 0.03]	[-0.12, 0.06]	[-0.13, 0.14]	[-0.05, 0.03]	2.3×10^{-4}
			$\epsilon = 0.10$			
	[0.24, 0.26]*					
0	$\varnothing$					
1	[0.20, 0.21]	[0.00, 0.01]				5.2×10^{-1}
2	[0.20, 0.30]	[-0.01, 0.04]	[-0.11, 0.01]			4.9×10^{-2}
3	[0.20, 0.30]	[-0.02, 0.04]	[-0.13, 0.06]	[-0.05, 0.03]		1.2×10^{-2}
4	[0.20, 0.30]	[-0.04, 0.05]	[-0.19, 0.19]	[-0.31, 0.22]	[-0.07, 0.09]	2.0×10^{-4}

*Posterior uncertainty interval obtained with the true model.

The B2BDC analysis with the true model results in a significantly narrower posterior uncertainty interval for model parameter k as compared to its prior; the interval in this case,

by design, contains the true calibration parameter value. With the inadequate model and a constant model discrepancy function ($n = 1$) at $\epsilon = 0.1$, an even narrower posterior interval is obtained. However, the true value k^* is completely missed. With a higher order δ, the posterior interval covers the same range as the prior. This outcome can be explained by considering two factors that affect the prediction interval of k.

Firstly, the inadequate model has a different functional dependency on the model parameter k, resulting in a problem specific change of the posterior bounds: feasible k values for the true model can become infeasible for the inadequate model and vice versa. In the current example, this can be visually observed by comparing the displacement predicted using the true and inadequate models and its dependency on model parameter k, as demonstrated in Figure 5.5. Plotted in this figure are $z^*(k,t)$ and $z(k,t)$ computed for different k's drawn from its prior interval along with the experimental uncertainty intervals for the case where $\epsilon = 0.1$. For a given t, larger k values produce larger displacements for both models. The resulting displacement bands (shown in cyan) cover similar vertical regions at smaller t values but the band for the inadequate model gradually shifts upward with increasing magnitude at larger t values comparing to that for the true model. For the last two observations, shown in the right inset plot, only a small portion of the band satisfies the QOI uncertainty bounds. Note that this portion corresponds to smaller k values. However, predictions with these smaller k values invalidate at least one other QOI bound since the dataset is inconsistent, motivating the use of δ to resolve inconsistency.

The second factor, as discussed in Section 5.2, is that inclusion of a higher order δ always results in a wider prediction interval. For a constant δ at $\epsilon = 0.1$, the posterior interval widens from the empty set (with a zero δ) to an interval with finite length. With the constant δ, feasible (k, c_0) can be found with k limited to a very small region close to the prior lower bound. The red dashed curve in Figure 5.5 corresponds to the prediction with one of the feasible (k, c_0).

The posterior uncertainty intervals of $\{c_i\}_{i=1}^n$ also become systematically wider with a higher polynomial order of δ, as expected. The enlarged posterior uncertainty intervals associated with individual parameters k and $\{c_i\}_{i=1}^n$ are related to the phenomenon usually referred to in statistical literature (e.g., [11]) as confounding, manifesting itself in the presence of a strong correlation between model parameter(s) and model discrepancy despite their relatively wider marginal posterior distributions. We demonstrate this from a deterministic perspective by the plots shown in Figure 5.6, generated for the case of a linear δ at $\epsilon = 0.1$. The plots display the joint feasible set of k, c_0 and c_1 along with its 2D projections. The three-dimensional plot clearly shows that the joint feasible set occupies only a small fraction of the enclosing cube. Inspection of the projections indicates that at a fixed k value, the uncertainty in c_0 and c_1 is reduced, on average, to 66 and 46%, of their posterior ranges. At a fixed c_0, the uncertainty in c_1 is reduced, on average, to 26% of its posterior range.

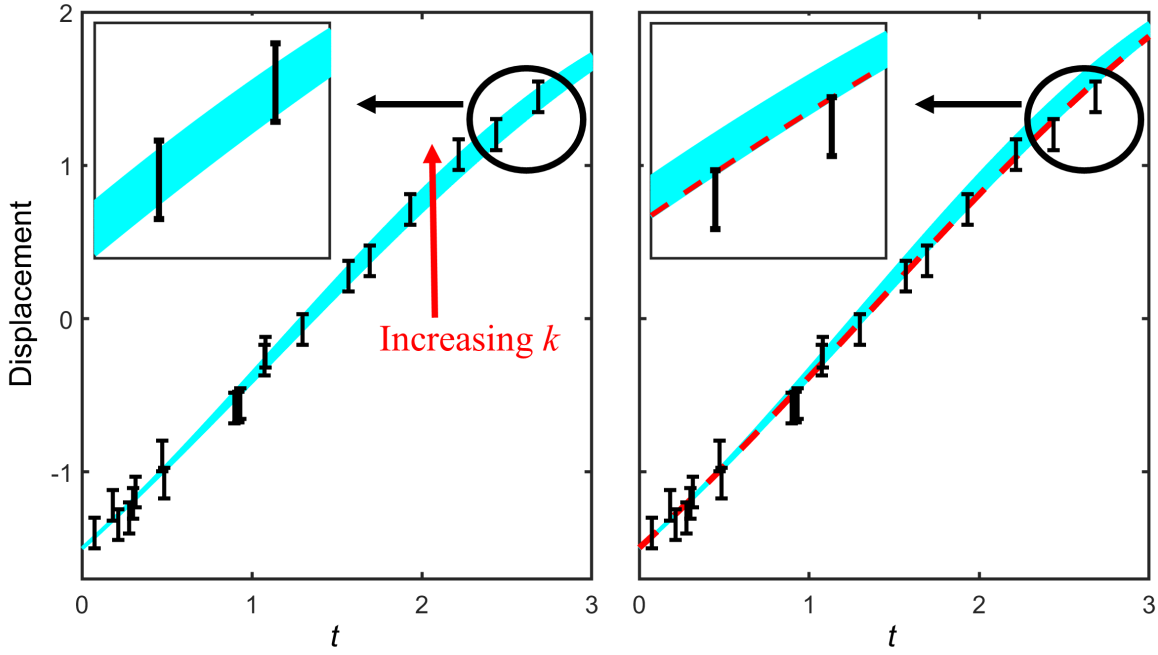

Figure 5.5: Displacements computed with the true (left) and the inadequate (right) models for various k values drawn from its prior interval [0.2, 0.3] (cyan regions). The black vertical bars are observation quantity of interest bounds. The red dashed line is one feasible realization of $z(k,t) + c_0$ with $k = 0.2$ and $c_0 = 0.005$. The insets are zoomed on the last two observations for $t \in [2.3, 2.8]$.

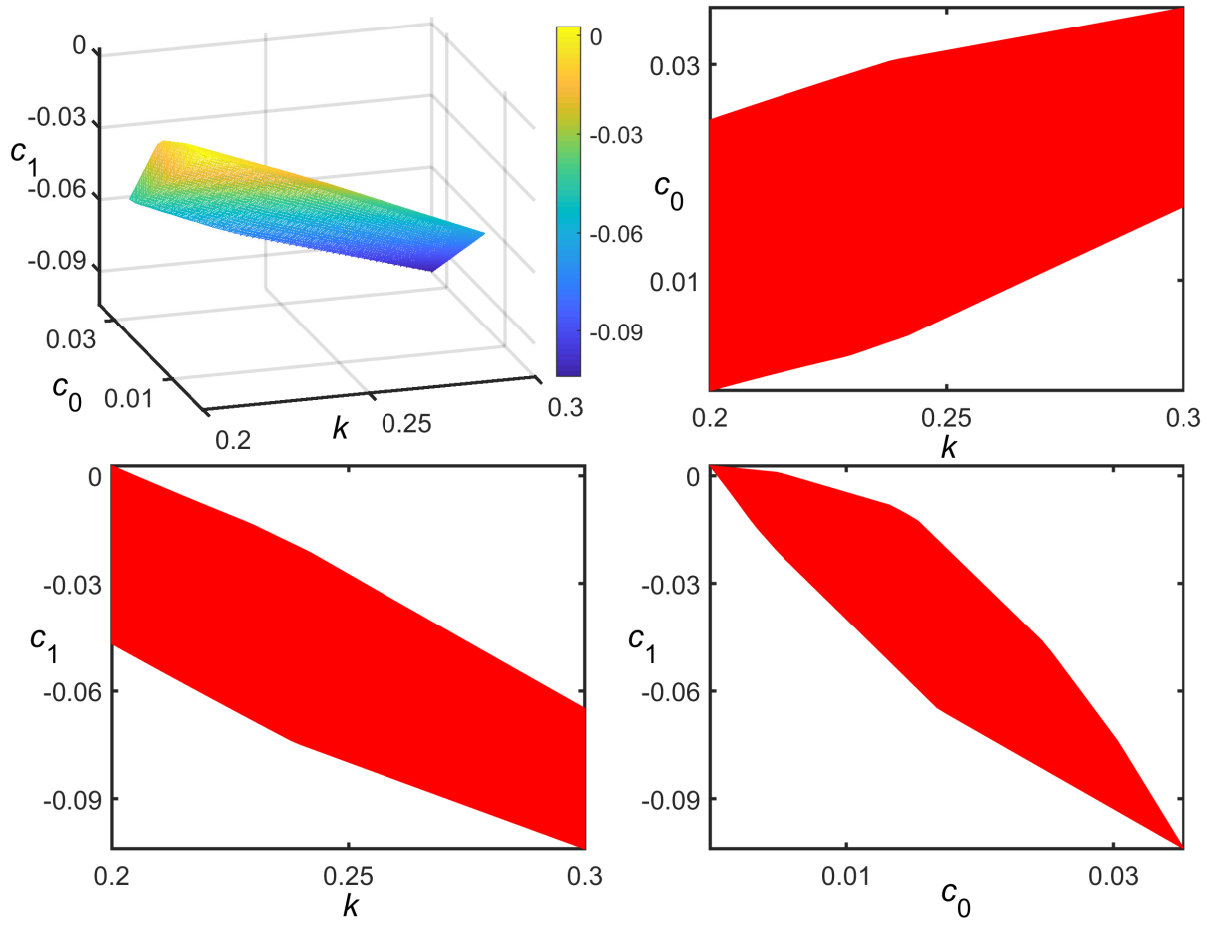

Figure 5.6: Joint feasible set of k, c_0, and c_1 and its 2-dimensional projections (colored in red), computed with linear δ and $\epsilon = 0.1$. The color bar in the upper-left figure color codes the values of c_1. The axes' limits of k, c_0, and c_1 were set to their calculated posterior uncertainty bounds.

5.3.4 Posterior Uncertainty of Model Discrepancy

I now examine the lower and upper bounds of δ predicted at 1000 discrete time points, t_i, equally spaced in [0, 4]. The inner-bound solutions were calculated by solving the problems (5.12 and 5.13) with nonlinear constrained optimization solvers. This region is divided into the interpolation zone ($t \in [0, 3]$), where data exists, and the extrapolation zone ($t \in [3, 4]$) for comparison. The uncertainty bands are shown in Figure 5.7 for quadratic and cubic δ; they were generated by linearly interpolating adjacent upper and lower bounds.

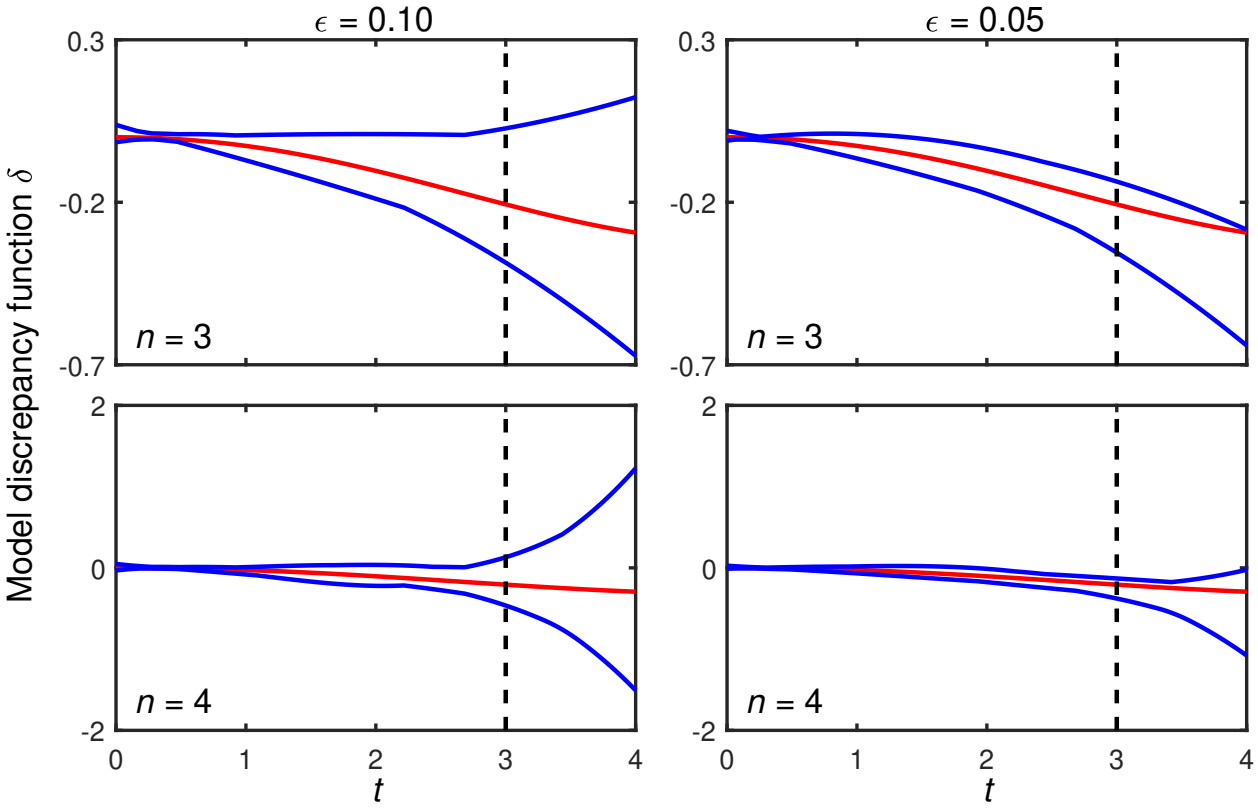

Figure 5.7: Uncertainty bounds of quadratic and cubic δ (blue lines). The red line is the true model discrepancy δ^*.

Inspection of these results shows that the computed uncertainty bounds enclose δ^* in both the interpolation and extrapolation zones for both quadratic and cubic δ. The width of the predicted uncertainty band is effectively constrained within the interpolation zone. The predicted uncertainty band starts to widen toward the end of the interpolation zone and diverges rapidly in the extrapolation zone. The observed divergence is more dramatic for a cubic δ than for a quadratic δ. The uncertainty band for a fixed δ is overall narrower with a smaller ϵ in both interpolation and extrapolation zones.

5.3.5 Additional Constraints on Model Discrepancy

As discussed in Section 5.2, constraints derived from domain knowledge about the model discrepancy can be included in the B2BDC calculations. Let us assume that although we introduce a discrepancy function, we would still like to rely on the inadequate model more than on the introduced correction when making predictions. This idea reflects the general spirit of some existing work in the literature (e.g., [57]). This requirement can be attained by selecting among all feasible values of δ those that have their magnitude, averaged over data and prediction scenarios, below a prescribed threshold, α,

$$\frac{1}{N+1}(|\delta(t_p)| + \sum_{i=1}^{N} |\delta(t_i)|) \leq \alpha, \tag{5.20}$$

where N is the number of experimental data. This constraint was added to the joint feasible set construction and prediction intervals were calculated with varying values of α. The results for $\epsilon = 0.1$ and cubic δ are shown in Figure 5.8. As expected, the prediction interval increases for larger α, reaching the value obtained without constraint eq. (5.20) eventually, as this additional constraint becomes inactive.

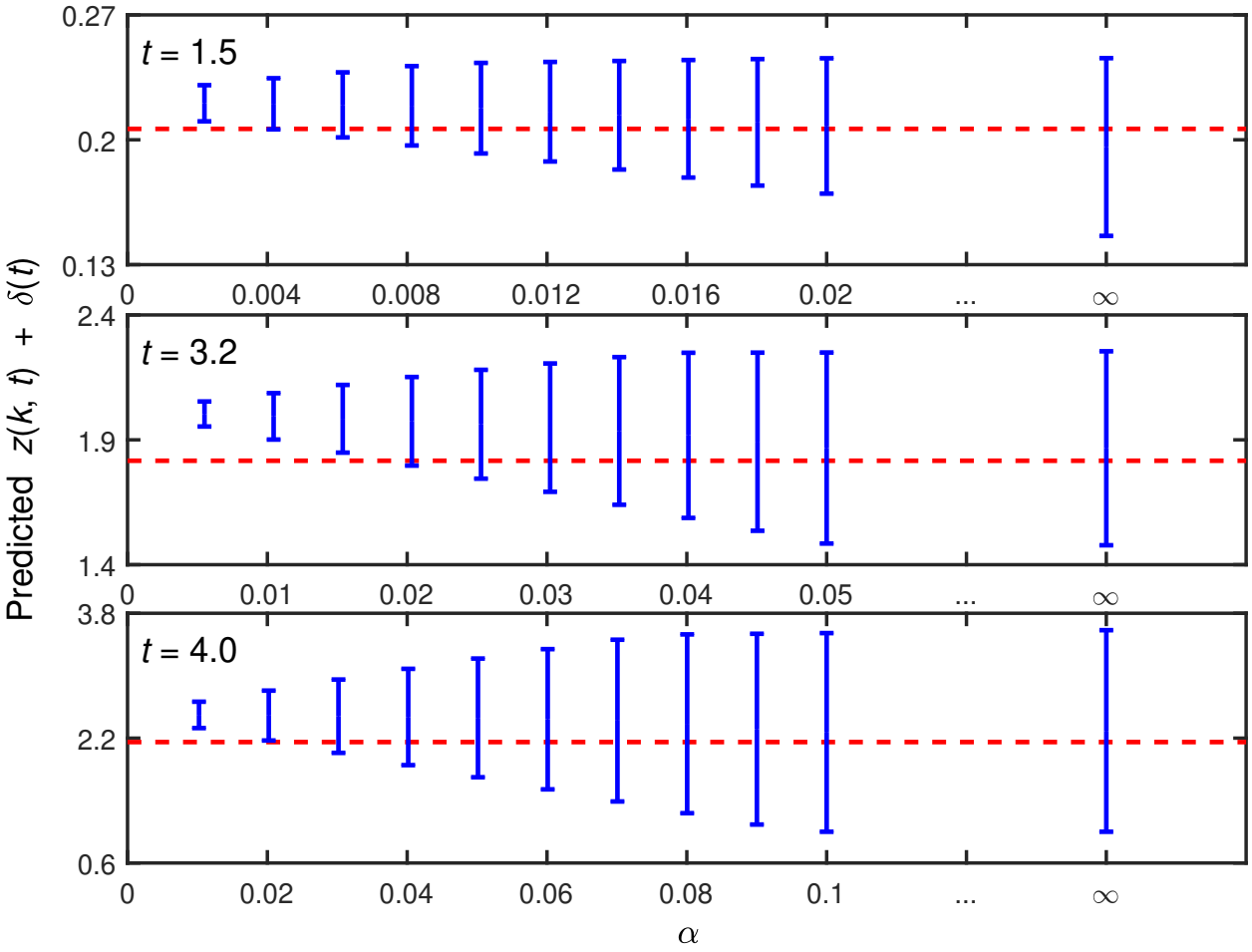

Figure 5.8: Interpolation and extrapolation intervals computed by solving Equations (5.8) and (5.9) with the extra constraint defined in Equation (5.20) for cubic δ at $\epsilon = 0.1$. The red dashed lines are the true prediction values.

5.4 Hydrogen Combustion Example

5.4.1 Problem Statement

In this section I apply the approach to a hydrogen combustion model: a homogeneous adiabatic H_2-air reaction system at constant volume. The evolution of the system states (i.e., species concentrations and temperature) was simulated numerically by solving a set of ordinary differential equations. The time derivatives of species concentrations and temperature were calculated based on the specified chemical reaction mechanism and the energy equation. Simulations with detailed (21 reactions [135]) and reduced (5 reactions [132]) mechanisms, listed in Table 5.3, are considered as the true and inadequate models, respectively. The model parameters, denoted by $\lambda \in \mathbb{R}^5$, are logarithm of the multipliers associated with the

five rate constants shared by both mechanisms, with their prior uncertainties taken from [135]. The true calibration parameter value is specified as $\lambda^* = \mathbf{0}$, where $\mathbf{0}$ is a vector of zeros.

The normalized scenario parameters, s_1, s_2 and s_3, are defined by

$$\begin{aligned} s_1 =& \frac{1000/T - 1000/T_{\text{center}}}{1000/T_{\text{low}} - 1000/T_{\text{high}}}, \\ & T_{\text{center}} = 1370 \text{ K},\ T_{\text{low}} = 1200 \text{ K},\ T_{\text{high}} = 1600 \text{ K}, \\ s_2 =& \frac{\ln P - \ln P_{\text{center}}}{\ln P_{\text{high}} - \ln P_{\text{low}}}, \\ & P_{\text{center}} = 3.2 \text{ atm},\ P_{\text{low}} = 1 \text{ atm},\ T_{\text{high}} = 10 \text{ atm}, \\ s_3 =& \frac{\phi - \phi_{\text{center}}}{\phi_{\text{high}} - \phi_{\text{low}}}, \\ & \phi_{\text{center}} = 1,\ \phi_{\text{low}} = 0.75,\ \phi_{\text{high}} = 1.25, \end{aligned} \tag{5.21}$$

where T, P and ϕ are initial temperature, initial pressure and equivalence ratio of the mixture, respectively. In this example, equivalence ratio is the ratio of hydrogen to oxygen concentrations in the initial mixture to that in a stoichiometric mixture. The use of inverse temperature and logarithmic pressure for defining s_1 and s_2 are common in the combustion field (e.g., [132]).

A dataset was constructed using a second-order orthogonal design [83] over the scenario region $[-1,\ 1]^3$. The corresponding scenario parameter values are listed in Table 5.4. For each of the scenario conditions, the corresponding QOI is defined as the time when the hydrogen concentration drops to half of its initial value. This QOI was computed numerically from the simulated hydrogen concentration profile and denoted by $t^*_{1/2}(\lambda, T, P, \phi)$ and $t_{1/2}(\lambda, T, P, \phi)$ for the true and inadequate models, respectively. Measurements of these QOIs, denoted by t_i, were generated by adding a relative noise to the true process values, specified as evaluating $t^*_{1/2}$ at the true calibration parameter value λ^*,

$$\begin{aligned} & t_i = t^*_{1/2}(\lambda^*, T_i, P_i, \phi_i)(1 + \epsilon\, u_i), \\ & u_i \sim \mathcal{U}(-1,\ 1), \quad i = 1, 2, \ldots, 15, \end{aligned} \tag{5.22}$$

where $\mathcal{U}(-1,\ 1)$ is the uniform distribution within $[-1,\ 1]$. The maximum noise magnitude, ϵ, was assigned with values of 0.01 and 0.005. As before, the data uncertainty bounds were generated by computing $[(1-\epsilon)t_i, (1+\epsilon)t_i]$. In this example the QOIs computed with the inadequate model have no analytic solution and a quadratic surrogate model S_i was generated for each QOI such that $S_i(\lambda) \approx \ln(t_{1/2}(\lambda, T_i, P_i, \phi_i))$. As in the previous example, we consider a polynomial model discrepancy function (Table 5.5), but now with the scenario parameters s_1, s_2 and s_3.

Table 5.3: Detailed and reduced H_2-O_2 reaction sets and associated parameters of the rate coefficients, $AT^n e^{-E/RT}$, in the units of cm^3, mol, s, cal, K (from [135]).

Reduced		Reactions	A	n	E
✓	1	**$H + O_2 = O + OH$**	2.65×10^{16}	-0.6707	17041
✓	2	**$O + H_2 = H + OH$**	3.87×10^{4}	2.7	6260
✓	3	**$OH + H_2 = H + H_2O$**	2.16×10^{8}	1.51	3430
	4	$OH + OH = O + H_2O$	3.57×10^{4}	2.4	-2110
	5[a]	$H + H + M = H_2 + M$	1.00×10^{18}	-1.0	0
		$H + H + H_2 = H_2 + H_2$	9.00×10^{16}	-0.6	0
		$H + H + H_2O = H_2 + H_2O$	6.00×10^{19}	-1.25	0
	6[b]	$O + O + M = O_2 + M$	1.20×10^{17}	-1.0	0
	7[c]	$O + H + M = OH + M$	4.71×10^{18}	-1.0	0
	8[d]	$H + OH + M = H_2O + M$	2.20×10^{22}	-2.0	0
✓	9[e]	**$H + O_2 + M = HO_2 + M$**	5.75×10^{19}	-1.4	0
		$H + O_2 = HO_2$	4.65×10^{12}	0.44	0
	10	$H + HO_2 = O + H_2O$	3.97×10^{12}	0.0	671
✓	11	**$H + HO_2 = H_2 + O_2$**	2.99×10^{6}	2.12	-1172
	12	$H + HO_2 = OH + OH$	8.40×10^{13}	0.0	635
	13	$O + HO_2 = OH + O_2$	2.00×10^{13}	0.0	0
	14	$OH + HO_2 = H_2O + O_2$	2.89×10^{13}	0.0	-497
	15	$HO_2 + HO_2 = H_2O_2 + O_2$	1.30×10^{11}	0.0	-1630
		$HO_2 + HO_2 = H_2O_2 + O_2$	4.20×10^{14}	0.0	12000
	16[f]	$OH + OH + M = H_2O_2 + M$	1.46×10^{11}	0.868	-8548
		$OH + OH = H_2O_2$	8.71×10^{9}	0.869	-2191
	17	$H + H_2O_2 = H_2O + OH$	1.00×10^{13}	0.0	3600
	18	$H + H_2O_2 = HO_2 + H_2$	1.21×10^{7}	2.0	5200
	19	$O + H_2O_2 = HO_2 + OH$	9.63×10^{6}	2.0	4000
	20	$OH + H_2O_2 = H_2O + HO_2$	1.74×10^{12}	0.0	318
		$OH + H_2O_2 = H_2O + HO_2$	7.59×10^{13}	0.0	7272
	21[c]	$O + OH + M = HO_2 + M$	8.00×10^{15}	0.0	0

[a]Collision efficiency: Ar = 0.63.

[b]Collision efficiencies: H_2 = 2.4, H_2O = 15.4, Ar = 0.83.

[c]Collision efficiencies: H_2 = 2, H_2O = 12, Ar = 0.7.

[d]Collision efficiencies: H_2 = 0.73, H_2O = 3.65, Ar = 0.38.

[e]Collision efficiencies: H_2O = 12, Ar = 0.53; Troe parameters: $a = 0.5$, $T^{***} = 10^{-30}$, $T^{*} = 10^{30}$, $T^{**} = 10^{100}$.

[f]Collision efficiencies: H_2 = 2, H_2O = 6, Ar = 0.67; Troe parameters: $a = 1.0$, $T^{***} = 10^{-30}$, $T^{*} = 10^{30}$, $T^{**} = 10^{30}$.

Table 5.4: Design conditions for the training data.

Design index	s_1	T (K)	s_2	P (atm)	s_3	ϕ
1	1	1200	1	10	1	1.25
2	1	1200	1	10	-1	0.75
3	1	1200	-1	1	1	1.25
4	1	1200	-1	1	-1	0.75
5	-1	1600	1	10	1	1.25
6	-1	1600	1	10	-1	0.75
7	-1	1600	-1	1	1	1.25
8	-1	1600	-1	1	-1	0.75
9	0	1370	0	3.2	0	1
10	1.215	1170	0	3.2	0	1
11	-1.215	1660	0	3.2	0	1
12	0	1370	1.215	12.8	0	1
13	0	1370	-1.215	0.78	0	1
14	0	1370	0	3.2	1.215	1.3
15	0	1370	0	3.2	-1.215	0.7

Table 5.5: Tested model discrepancy functions.

Model discrepancy	Number of basis function n
No δ	0
$\delta = c_0$	1
$\delta = c_0 + \sum_{i=1}^{3} c_i s_i$	4
$\delta = c_0 + \sum_{i=1}^{3} c_i s_i + \sum_{i,j=1; i \leq j}^{3} c_{i,j} s_i s_j$	10

5.4.2 Dataset Consistency and QOI Prediction

Dataset consistency is calculated first and the results are given in Table 5.6. Inspection

Table 5.6: Results of dataset consistency and the distance between true model parameter value λ^* and the feasible set.

n	Dataset consistency	d_{λ^*}
	$\epsilon = 0.01$	
0	Inconsistent	—
1	Inconsistent	—
4	Consistent	0.167
10	Consistent	0.047
	$\epsilon = 0.005$	
0	Inconsistent	—
1	Inconsistent	—
4	Inconsistent	—
10	Consistent	0.072

of these results shows that with $\epsilon = 0.01$, the dataset is inconsistent for both the zero δ and constant δ cases, and becomes consistent when linear and quadratic δ are used. After ϵ is lowered to 0.005, linear δ is insufficient to keep the dataset consistent. For cases where the dataset is consistent, the distance between the true calibration parameter value and the feasible set, denoted by d_{λ^*} and defined in Equation (5.23), is calculated and the results are also reported in Table 5.6. In all these cases, the true calibration parameter value is not in the feasible set. Its distance from the feasible set is larger when lower order δ or smaller ϵ is used.

$$d^2_{\lambda^*} = \min_{(\lambda,c)\in\mathcal{F}_\delta} (\lambda - \lambda^*)^T(\lambda - \lambda^*). \tag{5.23}$$

For cases where the dataset is consistent, prediction intervals are computed at one interpolated and four extrapolated scenarios, which are specified in Table 5.7. The results are depicted in Figure 5.9. Again the lengths of the prediction intervals are shorter with linear δ as compared to quadratic δ. Similarly, smaller values of ϵ produce shorter prediction intervals. At $\epsilon = 0.01$, the prediction interval with a linear δ contains the true value for cases 1, 2 and 3, but underpredicts the target for cases 4 and 5. With a quadratic δ, the prediction intervals contain the true values for all tested cases at both ϵ values.

Table 5.7: Scenario parameter values for model prediction.

Case index	Prediction	s_1	T (K)	s_2	P (atm)	s_3	ϕ
1	Interpolation	-0.6	1500	0.4	5	0	1
2	Extrapolation	-1.67	1800	0.4	5	0	1
3	Extrapolation	-1	1600	1.16	12	0	1
4	Extrapolation	-1	1600	0.4	5	1.6	1.4
5	Extrapolation	-1.67	1800	1.16	12	1.6	1.4

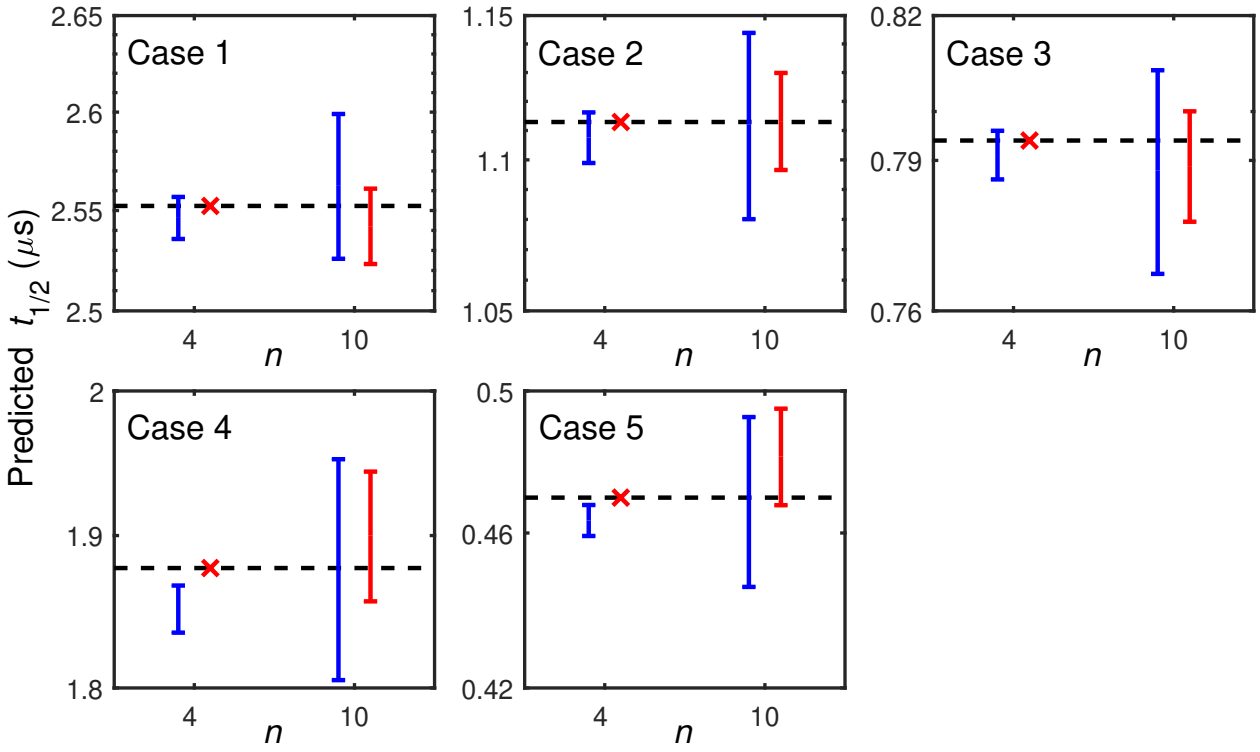

Figure 5.9: QOI prediction intervals for the five cases in table 5.7. The black dashed lines are the true QOI values. The predicted QOI intervals are drawn as blue ($\epsilon = 0.01$) and red ($\epsilon = 0.005$) vertical lines. The red $\times$'s mark dataset inconsistency.

5.4.3 Inference of Model Discrepancy

The projection of the feasible set on the parameter space of discrepancy-function coefficients, c, describes not one but a set of discrepancy functions that are consistent with the data. The following analysis with the linear δ and $\epsilon = 0.01$ shows an example of inferring model discrepancy from B2BDC calculations. The posterior uncertainty bounds of the discrepancy-function coefficients were calculated and the results are given in Table 5.8. The

volume ratio of the joint feasible set to the multidimensional orthotope, specified similarly as in Section 5.3, is 2.6×10^{-8} based on 10^9 samples. The results show that all feasible c_2 and

Table 5.8: Projection of the joint feasible set, computed with linear δ at $\epsilon = 0.01$, onto coordinate directions of each discrepancy-function coefficient.

Coefficient	Posterior uncertainty bounds
c_0	[-0.139, 0.112]
c_1	[-0.018, 0.005]
c_2	[-0.015, -0.006]
c_3	[-0.042, -0.013]

c_3 are negative since the calculated posterior upper bounds are negative for these two coefficients. For the linear δ, the coefficients are also the partial derivatives of the discrepancy function with respect to the scenario parameters, meaning

$$c_i = \frac{\partial \delta}{\partial s_i}. \tag{5.24}$$

All feasible δ's are therefore smaller at larger s_2 or s_3 values given other scenario parameters fixed.

The prediction interval of δ (i.e., $[L_\delta, U_\delta]$) defined in Equations (5.12) and (5.13), was then calculated in the s_2-s_3 (P-ϕ) space at three fixed s_1 (T) values. The computed intervals were examined to determine the sign of feasible δ's at each specified scenario condition and the results are shown in Figure 5.10. Similar patterns are observed for the three tested temperature values: except for a lower left triangle region where both pressure and equivalence ratio are relatively small, all feasible δ's are negative. As a result of dataset consistency, predictions made at the grey-region scenarios always add a negative correction to the model output, suggesting that the inadequate model systematically overpredicts the QOI. Combining the results that c_2 and c_3 are negative in the feasible set, the overprediction is likely to be stronger at larger s_2 and s_3 values (i.e., at higher pressures and equivalence ratios).

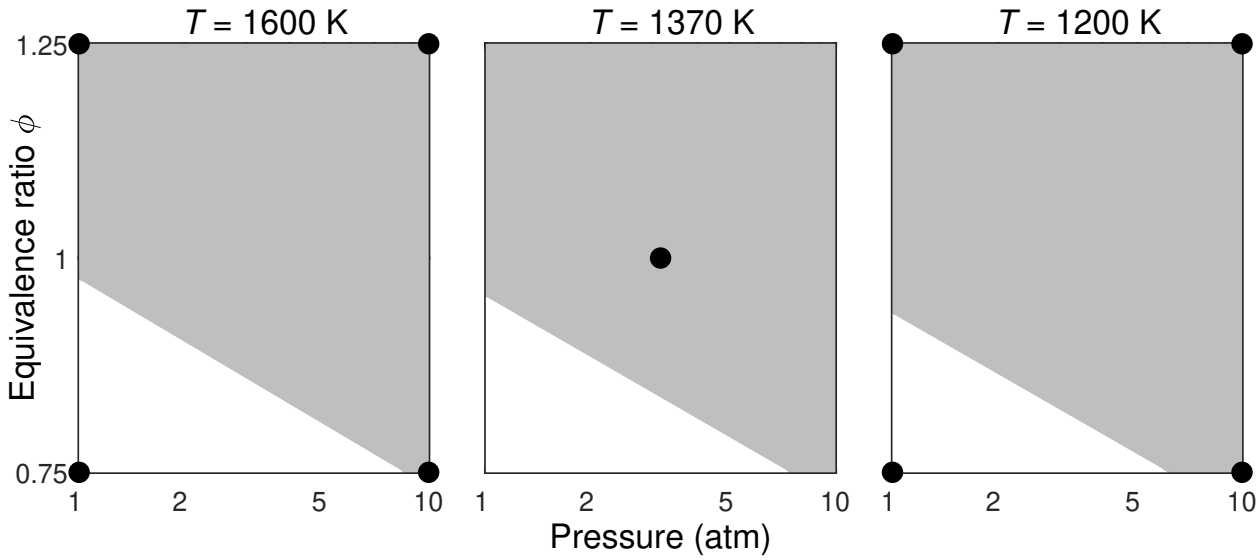

Figure 5.10: The sign of model discrepancy function in the scenario region $(s_2,\, s_3) \in [-1,\, 1]^2$ for temperature values 1600, 1370 and 1200 K. The grey region represents scenarios where $U_\delta < 0$ and the white one indicates where the interval $[L_\delta,\, U_\delta]$ contains 0. The black points are design scenarios in Table 5.4.

5.5 Discrepancy As a Consistency Measure

The above examples and discussion primarily focus on the impact of model discrepancy on predictions. The inclusion of discrepancy into B2BDC also provides the opportunity to calculate a more general consistency measure. For a given collection of basis functions $\{\Phi_i\}_{i=1}^n$, define this consistency measure as

$$\begin{aligned} \underset{x,\,c}{\text{minimize}} \quad & f(c) \\ \text{subject to} \quad & x \in \mathcal{H}, \\ & c \in \mathcal{H}_c, \\ & L_e \leq M(x, s_e) + \sum_{i=1}^{n} c_i \Phi_i(s_e) \leq U_e, \quad e = 1, 2, \ldots, N, \end{aligned} \tag{5.25}$$

where the objective $f(\cdot)$ is a function of only the coefficients c and reflects the "complexity" of the discrepancy function. In essence, Equation (5.25) asks the following question: what is the least complex discrepancy function required to recover dataset consistency? Different choices of $f(\cdot)$ and $\{\Phi_i(\cdot)\}_{i=1}^n$ produce different consistency measures. For example, defining

the complexity and discrepancy functions as

$$\begin{aligned} f(c) &= \sum_{i=1}^{N} |c_i| \\ \Phi_i(s) &= -\mathbb{1}_{\{s_i\}}(s) = \begin{cases} -1 & s = s_i \\ 0 & \text{otherwise} \end{cases} \end{aligned} \tag{5.26}$$

where $n = N$ and the $\{s_i\}_{i=1}^{N}$ are the dataset scenarios. Note that with this choice of discrepancy, the eth model-data constraint in Equation (5.25) becomes

$$L_e \leq M_e(x) - c_e \leq U_e. \tag{5.27}$$

This is exactly a version of the VCM presented in [52, Equation (4.4)]. Other choices of f, such as the integral over $\mathcal{H}_c$ of the squared discrepancy (or its squared derivatives, should each $\{\Phi_i(\cdot)\}_{i=1}^{n}$ be differentiable), can also be handled in the B2BDC framework.

Consistency measures formulated in this fashion gauges the disagreement between models and observations based on the "simplest" (or least complex) discrepancy required to render a dataset consistent. One potential application of this type of consistency measure is for model comparison. For a fixed set of basis functions $\{\Phi_i(\cdot)\}_{i=1}^{n}$, multiple models can be compared by evaluating Equation (5.25).

5.6 Chapter Summary

A new method was developed under the B2BDC framework to compensate dataset inconsistency caused by model inadequacy. The method adds a scenario-dependent discrepancy function to model output. Model-data constraints, feasible set and B2BDC computation formulas are modified accordingly. This discrepancy function is represented by a linear combination in basis functions whose coefficients are uncertain. Therefore, existing B2BDC machinery, including derivation of outer-bound solutions and developed sampling methods, is directly applicable in the extended parameter space composed of model parameters and discrepancy-function coefficients.

Application of this method shows some promising results in both the mass-spring-damper and the hydrogen examples as it resolves dataset inconsistency without removing any experimental data, the issue we struggle with the VCM method. How does the method perform in a realistic engineering application with massively inconsistent dataset, for example, the syngas combustion system analyzed in Chapter 4? In the next chapter, a syngas combustion dataset including only ignition delay time data is constructed, using which the two approaches for resolving dataset inconsistency (i.e., the method of including a discrepancy function and the VCM method) are compared.

Chapter 6

Syngas Combustion Dataset with Discrepancy Functions

The application of the Bound-to-Bound Data Collaboration (B2BDC) method to the syngas combustion dataset in Chapter 4 encountered a massively inconsistent initial dataset, which requires the removal of eight self-inconsistent quantities of interest (QOIs) and 37 QOIs detected using the vector consistency measure (VCM) method to obtain dataset consistency. The method presented in Chapter 5 provides an alternative approach for resolving dataset inconsistency without removing experimental data.

In this chapter, a syngas combustion dataset is constructed including only ignition delay time data. A homogeneous constant-volume adiabatic reaction model was used to simulate the ignition delay time QOIs. The model is valid if the experimental shock-tube design is realized ideally but can be inadequate for nonideal situations observed and reported in the literature [2, 14, 79, 94]. I apply two approaches, the method of including a discrepancy function and the VCM method, to resolve the initial inconsistency. The resulting feasible sets of the obtained consistent datasets and the B2BDC computations are analyzed and compared.

6.1 Experimental Data

Ignition delay time data measured in a shock-tube facility were collected for the current analysis. The uncertainty in the experimental measurements was estimated using the rules detailed in [110]. The investigated scenario factors are the temperature and pressure after the reflected shock wave, denoted by T_5 and P_5, respectively, the temperature increment, denoted by ΔT and defined as the temperature increase in the system after a simulation time that is 10 times the experimentally measured ignition delay time where the system has reached its steady state. Moreover, another factor is the initial concentration ratio of H_2 to CO and syngas (H_2+CO) to O_2 in the mixture, denoted respectively by $n_{\mathrm{H2/CO}}$ and

$n_{(H2+CO)/O2}$. Training and test sets of ignition delay time measurements were constructed, containing 112 and 37 data points, respectively. The range of scenario factors and measured ignition delay times is summarized in Table 6.1, and the detailed information is given in Tables 6.2 and 6.3. The test set includes primarily low temperature measurements, where the ignition delay times are relatively long and the model discrepancy is expected to be more significant.

Table 6.1: Range of the initial temperature, pressure, concentration ratio of H_2 to CO and syngas to O_2, temperature increment, and experimental measurements in the training and test datasets.

	Training set	**Test set**
T_5 (K)	900-2004	933-1319
P_5 (atm)	0.9-32.5	1-35.1
ΔT (K)	6.68-1880	16.82-1862
$n_{H2/CO}$	0.053-4	0.053-3.97
$n_{(H2+CO)/O2}$	0.989-1.999	0.989-1.999
t_{ign} (μs)	25-4340	44-3950

Table 6.2: Summary of ignition delay time data of the training set.

	T_5 (K)	P_5 (atm)	ΔT (K)	$n_{H2/CO}$	$n_{(H2+CO)/O2}$	t_{ign} (μs)	Unc. (%)	Ref.
1	956	1.44	1853.4	0.109	0.989	878	35	[78]
2	965	1.46	1847.5	0.109	0.989	629	35	[78]
3	933	1.16	1879.4	0.251	1.987	1001	40	[78]
4	947	1.21	1871.6	0.251	1.987	618	35	[78]
5	932	1.39	1869.3	0.109	0.989	1169	40	[78]
6	1008	1.9	183.7	1	0.989	1380	50	[75]
7	1361	12.1	176.6	1	0.989	43	30	[75]
8	1122	13.3	186.3	1	0.989	705	30	[75]
9	1291	30.2	178.2	1	0.989	51	30	[75]
10	1233	31.6	185.6	1	0.989	252	30	[75]
11	1150	31.9	185.1	1	0.989	1482	30	[75]
12	1784	1.5	69.0	1	0.999	72	30	[75]
13	1883	1.5	67.2	1	0.989	56	30	[75]
14	1147	2	108.4	1	0.999	480	30	[75]
15	1398	11.7	94.0	1	0.999	29	30	[75]
16	1285	12.5	63.7	1	0.999	49	30	[75]
17	1101	12.9	6.7	1	0.999	980	30	[75]
18	1299	29.4	20.0	1	0.999	38	30	[75]

Table 6.2 (continued)

	T_5 (K)	P_5 (atm)	ΔT (K)	$n_{\mathrm{H2/CO}}$	$n_{\mathrm{(H2+CO)/O2}}$	t_{ign} (μs)	Unc. (%)	Ref.
19	1186	32.5	39.5	1	0.999	504	30	[75]
20	1065	1.3	1315.9	0.769	1.999	182	20	[127]
21	1135	1.2	1268.1	0.769	1.999	80	20	[127]
22	975	1.72	1380.5	0.769	1.999	1720	20	[127]
23	999	1.8	1368.4	0.769	1.999	951	20	[127]
24	1048	1.7	1337.4	0.769	1.999	199	20	[127]
25	981	1.24	1364.3	0.769	1.999	1360	20	[127]
26	916	1	1505.1	3.971	1	2011	50	[58]
27	1126	11.9	1529.9	0.109	0.989	472	35	[58]
28	1265	17.1	1482.4	0.109	0.989	25	30	[58]
29	968	1.2	1536.4	0.055	0.994	1365	40	[58]
30	1057	1.1	1484.6	0.055	0.994	297	30	[58]
31	1263	1.1	1352.8	0.055	0.994	82	30	[58]
32	1149	2	1460.1	0.055	0.994	114	30	[58]
33	1304	1.7	1359.7	0.055	0.994	51	30	[58]
34	1110	12.7	1549.0	0.055	0.994	1186	40	[58]
35	1074	1.1	1436.3	3.971	1	68	30	[58]
36	1151	1	1395.2	3.971	1	52	30	[58]
37	914	1	1519.4	1.451	1.012	2277	50	[58]
38	951	1.1	1504.8	1.451	1.012	687	40	[58]
39	996	1.1	1483.4	1.451	1.012	181	35	[58]
40	1072	1.1	1445.9	1.451	1.012	87	30	[58]
41	1175	1	1388.1	1.451	1.012	55	30	[58]
42	1187	1	1381.6	1.451	1.012	39	30	[58]
43	1241	1	1351.7	1.451	1.012	29	30	[58]
44	900	0.9	1536.1	0.673	1	2935	50	[58]
45	954	1.2	1493.2	3.971	1	462	35	[58]
46	1026	1.1	1479.2	0.673	1	153	30	[58]
47	1162	1	1401.9	0.673	1	57	30	[58]
48	936	1.2	1545.6	0.25	1.006	1331	40	[58]
49	1015	1.1	1500.8	0.25	1.006	219	30	[58]
50	1183	1.1	1406.1	0.25	1.006	63	30	[58]
51	992	2.6	1543.6	0.25	1.006	1015	40	[58]
52	1058	2.6	1511.3	0.25	1.006	108	30	[58]
53	1063	3.1	1515.2	0.25	1.006	120	30	[58]
54	1015	13.7	1580.4	0.25	1.006	2278	50	[58]
55	993	1	1470.9	3.971	1	144	30	[58]
56	1114	14.9	1543.4	0.25	1.006	638	35	[58]
57	1190	16.8	1515.7	0.25	1.006	82	35	[58]
58	960	1.2	1531.5	0.109	0.989	1307	40	[58]
59	1052	1.1	1479.0	0.109	0.989	274	30	[58]
60	1197	1.1	1396.4	0.109	0.989	101	30	[58]

Table 6.2 (continued)

	T_5 (K)	P_5 (atm)	ΔT (K)	$n_{\mathrm{H2/CO}}$	$n_{\mathrm{(H2+CO)/O2}}$	t_{ign} (μs)	Unc. (%)	Ref.
61	981	2.7	1548.2	0.109	0.989	2284	50	[58]
62	1048	2.5	1513.1	0.109	0.989	236	30	[58]
63	1118	2.5	1477.6	0.109	0.989	94	30	[58]
64	1063	14.3	1560.7	0.109	0.989	1695	40	[58]
65	943	22.3	1537.7	0.755	1.002	3340	35	[95]
66	1033	23.7	1509.9	0.755	1.002	2150	35	[95]
67	1148	21.4	1469.0	0.755	1.002	380	35	[95]
68	1299	12.3	191.8	4	1	48.76	25	[65]
69	1264	31.3	193.0	4	1	61.39	30	[65]
70	1243	31.3	195.2	4	1	139.5	30	[65]
71	1185	31.3	196.4	4	1	938.24	35	[65]
72	1325	32.3	193.9	1	1	32.13	30	[65]
73	1204	32.3	203.4	1	1	552.85	35	[65]
74	1179	32.3	203.5	1	1	864.31	35	[65]
75	1327	31.3	195.8	0.111	1	76.42	30	[65]
76	1259	31.3	191.1	0.111	1	180.08	30	[65]
77	1166	31.3	96.6	0.111	1	1493.81	40	[65]
78	1695	1.65	121.5	4	1	51.84	30	[65]
79	1182	12.3	191.7	4	1	93.63	25	[65]
80	1351	1.65	184.6	4	1	183.92	30	[65]
81	980	1.65	194.9	4	1	1467.71	40	[65]
82	2004	1.65	67.6	1	1	40.24	25	[65]
83	1273	1.65	193.2	1	1	311.48	25	[65]
84	992	1.65	201.5	1	1	1640.74	35	[65]
85	1975	1.59	74.0	0.111	1	115.41	25	[65]
86	1436	1.59	166.3	0.111	1	296.1	25	[65]
87	1027	1.59	198.4	0.111	1	1725.99	35	[65]
88	1096	12.3	196.7	4	1	1796.82	30	[65]
89	1383	11.9	195.1	1	1	41.13	25	[65]
90	1235	11.9	196.6	1	1	86.2	25	[65]
91	1099	11.9	203.7	1	1	1060.78	30	[65]
92	1387	12	199.4	0.111	1	82.95	25	[65]
93	1228	12	199.9	0.111	1	191.9	25	[65]
94	1116	12	211.5	0.111	1	1450.14	35	[65]
95	1046	16.6	1451.1	0.053	1.001	4340	30	[54]
96	1159	16.0	692.5	0.053	1.001	1350	30	[54]
97	1206	16.2	690.7	0.053	1.001	588	35	[54]
98	1165	15.8	365.6	0.053	1.001	3900	30	[54]
99	1207	16.2	364.9	0.053	1.001	1730	30	[54]
100	1259	15.7	364.0	0.053	1.001	630	30	[54]
101	1019	13.9	1417.7	1	1.001	3430	30	[54]
102	1051	15.1	1410.9	1	1.001	1810	30	[54]

Table 6.2 (continued)

	T_5 (K)	P_5 (atm)	ΔT (K)	$n_{\mathrm{H2/CO}}$	$n_{\mathrm{(H2+CO)/O2}}$	t_{ign} (μs)	Unc. (%)	Ref.
103	1097	15.4	1399.0	1	1.001	470	35	[54]
104	1048	15.8	682.6	1.017	1.003	3210	30	[54]
105	1086	15.3	681.3	1.017	1.003	1310	30	[54]
106	1128	15.3	680.0	1.017	1.003	374	30	[54]
107	1054	15.4	346.9	1.017	1.003	3960	30	[54]
108	1090	15.6	346.6	1.017	1.003	1850	30	[54]
109	1140	15.7	346.0	1.017	1.003	448	30	[54]
110	1072	15.6	1442.4	0.053	1.001	2660	30	[54]
111	1132	15.9	1424.4	0.053	1.001	986	35	[54]
112	1107	16.0	694.5	0.053	1.001	3970	30	[54]

Table 6.3: Summary of ignition delay time data of the test set.

	T_5 (K)	P_5 (atm)	ΔT (K)	$n_{\mathrm{H2/CO}}$	$n_{\mathrm{(H2+CO)/O2}}$	t_{ign} (μs)	Unc. (%)	Ref.
1	959	1.37	1846.9	0.109	0.989	760	35	[78]
2	941	1.39	1862.3	0.109	0.989	1080	40	[78]
3	1107	13.2	187.0	1	0.989	1373	30	[75]
4	1251	1.9	105.6	1	0.999	273	30	[75]
5	1319	12.2	85.3	1	0.999	44	30	[75]
6	1252	35.1	16.8	1	0.999	72	30	[75]
7	1209	31.5	37.6	1	0.999	326	30	[75]
8	1062	1.9	181.9	1	0.989	787	50	[75]
9	1081	1.19	1302.2	0.770	1.999	139	20	[127]
10	1020	1.84	1357.1	0.770	1.999	482	20	[127]
11	1017	1.92	1360.5	0.770	1.999	823	20	[127]
12	988	1.28	1361.4	0.770	1.999	1225	20	[127]
13	1029	1.25	1335.9	0.770	1.999	358	20	[127]
14	977	1.2	1531.6	0.055	0.994	1099	40	[58]
15	1064	1	1437.9	3.971	1	80	30	[58]
16	1005	2.3	1540.8	0.055	0.994	1005	40	[58]
17	1074	19.2	1574.9	0.055	0.994	1823	40	[58]
18	936	1	1496.4	3.971	1	1085	40	[58]
19	933	1.1	1526.1	0.673	1	1471	40	[58]
20	957	1.1	1489.6	3.971	1	311	35	[58]
21	934	1.2	1546.6	0.25	1.006	1427	40	[58]
22	938	1.2	1544.6	0.25	1.006	1015	40	[58]
23	1046	1.1	1483.9	0.25	1.006	139	30	[58]
24	972	1.1	1483.0	3.971	1	191	30	[58]
25	1080	14.5	1556.3	0.25	1.006	1153	40	[58]
26	1033	1.1	1489.4	0.109	0.989	289	30	[58]
27	1053	18.7	1499.1	0.755	1.002	1560	35	[95]
28	947	20.9	1535.6	0.755	1.002	3520	35	[95]
29	987	23.8	1524.8	0.755	1.002	2010	35	[95]
30	1013	21.6	1514.9	0.755	1.002	2030	35	[95]
31	1180	16.1	691.7	0.053	1.001	884	30	[54]
32	1048	16.0	1449.9	0.053	1.001	3950	30	[54]
33	1078	15.6	1404.4	1	1.001	692	35	[54]
34	1055	15.6	682.3	1.017	1.003	2750	30	[54]
35	1064	15.5	346.8	1.017	1.003	3230	30	[54]
36	1094	15.3	346.5	1.017	1.003	1710	30	[54]
37	1131	15.5	693.6	0.053	1.001	2500	30	[54]

6.2 Simulation Model and Model Discrepancy

The ignition delay time QOIs were simulated using a homogeneous constant-volume adiabatic (CONSTVA) reaction model in the ReactionLab software [29]. The reaction mechanism proposed in [110] was used with few modifications. The complete reaction set and updated nominal rate parameters are given in Table B.5.

An uncertain multiplier, denoted by λ_i, was assigned for each reaction rate k_i such that,

$$k_i = \lambda_i k_{i,0}, \quad i = 1, 2, \ldots, 55, \tag{6.1}$$

where $k_{i,0}$ is the reaction rate coefficient computed with the nominal parameter values. The prior uncertainty of each multiplier is given in Table B.6.

Measuring the ignition delay time in a shock-tube facility has been extensively adopted in combustion chemistry studies [2, 19, 49, 113]. If the mixture after the reflected shock wave is stationary and uniform under ideal conditions, the implemented CONSTVA model is adequate to simulate the system evolution with relatively fast run-time. However, nonidealities, including boundary layer development [2, 30, 94] and inhomogeneous mild ignition [14, 79], have been observed experimentally in long ignition time scenarios (several milliseconds or longer), which supports the motivation to apply the method with a discrepancy function.

Although revised simulating strategies have been proposed to account for these nonidealities (e.g., [45, 46, 67]), we argue that the application of the discrepancy-function method is by no means limited to the CONSTVA model and may be preferred in other situations. First, the revised models can be too computationally demanding to be implemented using the B2BDC method, in which a decent number of simulation runs at various parameter vectors are required. Second, despite being relatively more rigorous than the CONSTVA model, the revised models may still miss some physical parts of the system and could be subject to a different model discrepancy.

6.3 Surrogate models, model and scenario parameters, and discrepancy function

In the current study, the model parameter x was set as the logarithm of the multipliers,

$$x_i = \ln \lambda_i, \quad i = 1, 2, \ldots, 55, \tag{6.2}$$

and the prior uncertainty region $\mathcal{H}$ is a 55-dimensional orthotope roughly centered at the origin, which represents the vector of nominal values. The simulated ignition delay times can vary by orders of magnitude with different model parameter vectors in $\mathcal{H}$. To ensure better response surface behavior [26, 32], the QOIs were specified as the logarithmic ignition delay time:

$$y_e(x) = \log_{10}\left(t_{\mathrm{ign},e}(x)\right), \quad e = 1, 2, \ldots, 149. \tag{6.3}$$

For each QOI y_e, the Latin hypercube sampling method [76] was applied to generate 10^4 design points from $\mathcal{H}$ for computer experiments. A linear model $\mathcal{L}_e(x)$ was first fitted to the 55-dimensional parameter space using the least squares method,

$$\mathcal{L}_e(x) = \sum_{i=1}^{55} a_i x_i + a_0. \tag{6.4}$$

The influence of each model parameter on the specific QOI y_e was evaluated based on the impact factor discussed in Section 2.7.1 and defined as

$$\mathrm{IF}_i = |a_i| \times \Delta x_i, \tag{6.5}$$

where Δx_i is the length of the prior uncertainty interval for model parameter x_i. A parameter is selected as active if its impact factor is greater than 5% of the largest impact factor over all model parameters or 10% of the corresponding experimental uncertainty interval length. Once active parameters x_a^e are determined, a quadratic surrogate model $\mathcal{Q}_e(x_a^e)$ is computed using the least squares method only in the active parameter space. The fitting error is denoted by ϵ and defined by the following:

$$\epsilon_e = \max_{x \in \mathcal{H}} \ |\mathcal{Q}_e(x_a^e) - y_e|. \tag{6.6}$$

The fitting error was estimated using 10-fold cross-validation criterion [120] and the distribution histograms are given in Figure 6.1. In the following analysis, the fitting error was considered by expanding the lower and upper bounds with the estimated ϵ in the model-data constraint if the QOI is in the dataset or in the prediction interval otherwise.

Five normalized scenario parameters representing the scenario factors listed in Table 6.1 are constructed as follows:

$$\begin{aligned}
s_1 =& \frac{(1000/T_5) - (1000/T_5)_{\text{center}}}{(1000/T_5)_{\max} - (1000/T_5)_{\min}}, \\
s_2 =& \frac{P_5 - P_{5,\text{center}}}{P_{5,\max} - P_{5,\min}}, \\
s_3 =& \frac{\Delta T - \Delta T_{\text{center}}}{\Delta T_{\max} - \Delta T_{\min}}, \\
s_4 =& \frac{n_{\text{H2/CO}} - (n_{\text{H2/CO}})_{\text{center}}}{(n_{\text{H2/CO}})_{\max} - (n_{\text{H2/CO}})_{\min}}, \\
s_5 =& \frac{n_{\text{(H2+CO)/O2}} - (n_{\text{(H2+CO)/O2}})_{\text{center}}}{(n_{\text{(H2+CO)/O2}})_{\max} - (n_{\text{(H2+CO)/O2}})_{\min}},
\end{aligned} \tag{6.7}$$

where the center, minimum, and maximum values are computed based on the QOIs in the training set.

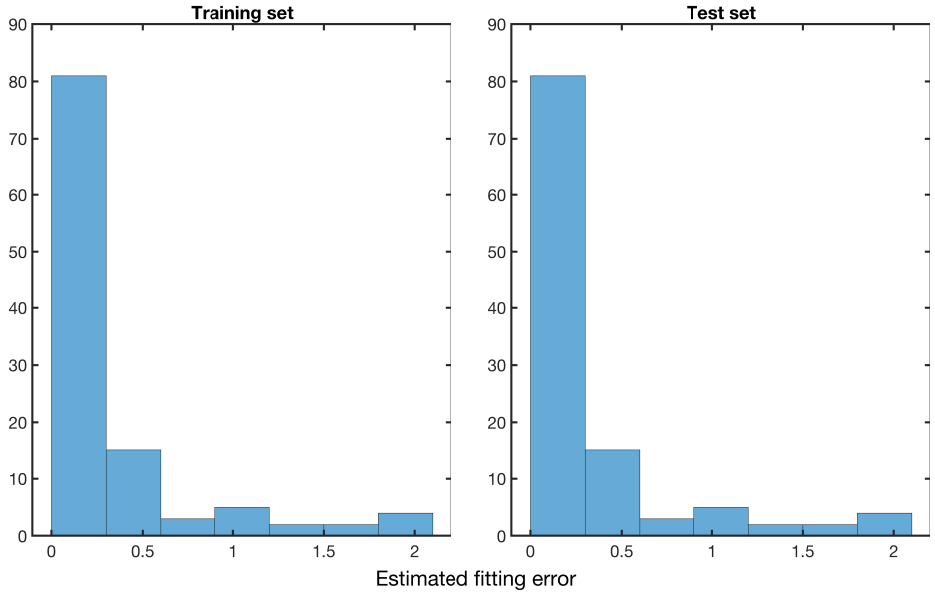

Figure 6.1: Histograms of the estimated fitting error in the training and test sets of quantities of interest.

Polynomial discrepancy functions were used in the current study. If two scenario parameters are selected, for example s_1 and s_2, the polynomial is specified by three parameters: n_1, n_2, and m, where n_1 and n_2 represent the highest power in s_1 and s_2, and m represents the highest power in the coupled monomials. The discrepancy function is described as follows:

$$\delta(s; n_1, n_2, m) = c_0 + \sum_{i=1}^{n_1} c_i s_1^i + \sum_{j=1}^{n_2} c_{n_1+j} s_2^j + \sum_{i=1,\ j=1}^{i=m-1,\ j=m-i} c_{i,j} s_1^i s_2^j. \tag{6.8}$$

If three scenario parameters are selected, for example s_1, s_2, and s_3, the following four discrepancy functions labelled by I are investigated:

$$\delta(s; I) = \begin{cases} c_0 + \sum_{i=1}^{3} c_i s_i, & I = 1, \\ c_0 + \sum_{i=1}^{3} \sum_{n=1}^{2} c_{2(i-1)+n} s_i^n + \sum_{i,j=1;i\neq j}^{3} c_{i,j} s_i s_j, & I = 2, \\ c_0 + \sum_{i=1}^{3} \sum_{n=1}^{3} c_{3(i-1)+n} s_i^n + \sum_{i,j=1;i\neq j}^{3} c_{i,j} s_i s_j + c_{1,2,3} s_1 s_2 s_3, & I = 3, \\ c_0 + \sum_{i=1}^{3} \sum_{n=1}^{3} c_{3(i-1)+n} s_i^n + \sum_{i,j=1;i<j}^{3} \sum_{n=1,\ m=1}^{n=2,\ m=3-n} c_{i,j}^{n,m} s_i^n s_j^m, & I = 4. \end{cases} \tag{6.9}$$

The discrepancy function $\delta(s; I)$ is linear and quadratic for $I = 1$ and 2. It is partial (not containing all coupled monomials) and fully cubic for $I = 3$ and 4.

If four scenario parameters are used, for example s_1 to s_4, the following four discrepancy

functions labelled by I are investigated:

$$\delta(s;I)=\begin{cases} c_0+\sum_{i=1}^{4} c_i s_i, \quad I=1, \\ c_0+\sum_{i=1}^{4}\sum_{n=1}^{2} c_{2(i-1)+n} s_i^n+\sum_{i,j=1;i\neq j}^{4} c_{i,j} s_i s_j, \quad I=2, \\ c_0+\sum_{i=1}^{4}\sum_{n=1}^{3} c_{2(i-1)+n} s_i^n+\sum_{i,j=1;i\neq j}^{4} c_{i,j} s_i s_j, \quad I=3, \\ c_0+\displaystyle\sum_{i=1}^{4}\sum_{n=1}^{3} c_{2(i-1)+n} s_i^n+\sum_{i,j=1;i\neq j}^{4} c_{i,j} s_i s_j \\ \quad +\displaystyle\sum_{i,j,k=1;i\neq j;i\neq k;j\neq k}^{4} c_{i,j,k} s_i s_j s_k, \quad I=4. \end{cases} \tag{6.10}$$

The discrepancy function $\delta(s;I)$ is linear and quadratic for $I=1$ and 2. While containing cubic monomials in a single variable, $\delta(s;I)$ includes coupled monomials of two and three variables for $I=3$ and 4.

If all five scenario parameters are used, the discrepancy function is restricted to only linear and quadratic functions:

$$\delta(s;I)=\begin{cases} c_0+\sum_{i=1}^{5} c_i s_i, \quad I=1, \\ c_0+\sum_{i=1}^{5}\sum_{n=1}^{2} c_{2(i-1)+n} s_i^n+\sum_{i,j=1;i\neq j}^{5} c_{i,j} s_i s_j, \quad I=2. \end{cases} \tag{6.11}$$

6.4 Consistency Analysis

The initial dataset with 112 QOIs and 30 active parameters produces a scalar consistency measure (SCM) C_{D} within [-0.77, -0.67] and hence is inconsistent. The VCM was then computed and an inner-bound solution is summarized in Table 6.4. A consistent dataset was obtained by removing the detected 12 QOIs and is denoted by D_{VCM}.

We examined the case in which a model discrepancy function was included in the analysis. The scenario parameters s_1 and s_2 were considered first because the temperature and pressure after the reflected shock wave (i.e., T_5 and P_5) are the properties that determine the state of the reacting system. The discrepancy functions given in Equation (6.8) were implemented with n_1 and n_2 varying from 2 to 5, and m from 2 to 4. None of the investigated discrepancy functions resolved the dataset inconsistency, suggesting that these two scenario parameters may be insufficient to characterize the inadequacy of the model.

When s_2 is replaced by s_3 (i.e., the temperature increment ΔT and T_5 are used in the discrepancy function), some tested discrepancy functions resulted in a consistent dataset. The results are summarized in Table 6.5. The results demonstrate that, although the combination of s_1 and s_3 regains dataset consistency, relatively high-order monomials are required in the corresponding discrepancy function.

The combinations of scenario parameters s_1-s_3, s_1-s_4, and s_1-s_5 were investigated using the discrepancy functions specified in Equations (6.9) to (6.11), respectively. The results are

Table 6.4: Suggested changes in experimental uncertainty bounds from the vector consistency measure (VCM) computation to obtain a consistent dataset.

QOI index	Lower bound change (%)	Upper bound change (%)
12	—	26.2
14	—	62.2
17	—	106.7
24	0.6	—
25	26.9	—
35	—	6.6
55	—	30.8
65	—	31.0
67	3.2	—
81	—	40.3
87	—	53.5
92	5.1	—

Table 6.5: Dataset consistency with discrepancy function $\delta(s; n_1, n_3, m)$ in scenario parameters s_1 and s_3.

n_1	n_3 $(m = 2)$				n_3 $(m = 3)$				n_3 $(m = 4)$			
	2	3	4	5	2	3	4	5	2	3	4	5
2	No	No	No	Yes	No	No	Yes	Yes	Yes	Yes	Yes	Yes
3	No	No	No	Yes	No	Yes	Yes	Yes	Yes	Yes	Yes	Yes
4	No	No	No	Yes	No	Yes	Yes	Yes	Yes	Yes	Yes	Yes
5	No	No	No	Yes	No	Yes	Yes	Yes	Yes	Yes	Yes	Yes

summarized in Table 6.6. The results reveal that, for three scenario parameters s_1 to s_3, the dataset consistency is not recovered with a linear ($I = 1$) or quadratic ($I = 2$) discrepancy function. The dataset inconsistency is resolved for $I = 3$ and 4. When four or five scenario parameters are used, dataset consistency is obtained with a quadratic ($I = 2$) discrepancy function.

The dataset inconsistency can be resolved by removing the VCM-detected QOIs from the dataset or adding a scenario-dependent polynomial discrepancy function (except for the case in which only s_1 and s_2 are used). The ability to maintain all experimental data in the analysis may be an advantage for the latter strategy because experiments are still considered the most accurate representation of reality. Further examination of the VCM result reveals

Table 6.6: Dataset consistency with various choices of scenario parameter combinations and the corresponding discrepancy functions.

Discrepancy function	Dataset consistency		
	s_1-s_3	s_1-s_4	s_1-s_5
$I = 1$	No	No	No
$I = 2$	No	Yes	Yes
$I = 3$	Yes	Yes	—
$I = 4$	Yes	Yes	—

that the detected QOIs are distributed over a relatively wide range of scenario conditions and are from different research groups, which makes the reasoning to label them as "suspicious" data challenging.

6.5 Prediction

For a consistent dataset obtained using the VCM method or by including a discrepancy function, the prediction intervals of the 37 QOIs of the test set were computed. To keep the analysis conservative, only the outer-bound prediction intervals were considered for the following analysis. The number of cases in which the computed outer-bound interval intersects with the experimental uncertainty bounds, termed a *valid* prediction hereafter, was computed. The dataset D_{VCM} makes a valid prediction for 32 out of 37 QOIs of the test set. The results for consistent datasets with a discrepancy function are summarized in Tables 6.7 and 6.8.

Table 6.7: Number of valid predictions computed using a discrepancy function $\delta(s; n_1, n_3, m)$ with the scenario parameters s_1 and s_3.

n_1	n_3 $(m = 2)$	n_3 $(m = 3)$			n_3 $(m = 4)$			
	5	3	4	5	2	3	4	5
2	32	—	33	34	35	35	35	36
3	32	33	33	34	35	35	35	36
4	32	33	33	34	35	35	35	37
5	32	33	33	35	35	35	36	37

The results reveal that, when a discrepancy function with s_1 and s_3 resolves dataset inconsistency, it results in at least as many valid predictions as the dataset D_{VCM}. The

Table 6.8: Number of valid predictions computed using a discrepancy function in three, four, and five scenario parameters.

Discrepancy function	Number of valid predictions		
	$\delta(s_1 - s_3; I)$	$\delta(s_1 - s_4; I)$	$\delta(s_1 - s_5; I)$
$I = 1$	—	—	—
$I = 2$	—	34	36
$I = 3$	36	37	—
$I = 4$	37	37	—

dataset can validly predict all 37 QOIs with $\delta(s; 4, 5, 4)$ and $\delta(s; 5, 5, 4)$. When three scenario parameters are used, the dataset only misses one QOI for $I = 3$ and is perfect for $I = 4$ regarding making valid predictions. When four scenario parameters are used, the dataset misses three targets with a quadratic δ and predicted all QOIs within their uncertainty bounds for $I > 2$. When all five scenario parameters are used, the dataset with a quadratic discrepancy function ($I = 2$) misses one QOI.

Another test was conducted using D_{VCM} and the dataset with the simplest discrepancy function that generates a perfect prediction performance or quadratic discrepancy function for five scenario parameters (i.e., $\delta(s_1, s_3; 4, 5, 3)$, $\delta(s_1 - s_3; 4)$, $\delta(s_1 - s_4; 3)$ and $\delta(s_1 - s_5; 2)$). Suppose a fixed number of QOIs are drawn randomly from the test set and added to the dataset, the question arises regarding whether the dataset consistency would break down. The number of added QOIs in the test varied from one to eight, and 100 runs were repeated for each case. The results are presented in Figure 6.2.

The results indicate that including a discrepancy function considerably improves the chance of maintaining dataset consistency when extra data were added to the analysis compared to using D_{VCM}. For D_{VCM}, the rate decreases to below 50% if more than three QOIs are added and to about 20% if more than six QOIs are added. The rate remains roughly above 60% for all cases with a discrepancy function. Among the four examined discrepancy functions, $\delta(s_1 - s_3; 4)$ preserves the highest rate of maintaining dataset consistency. The performance of the other three discrepancy functions is comparable across various numbers of added QOIs.

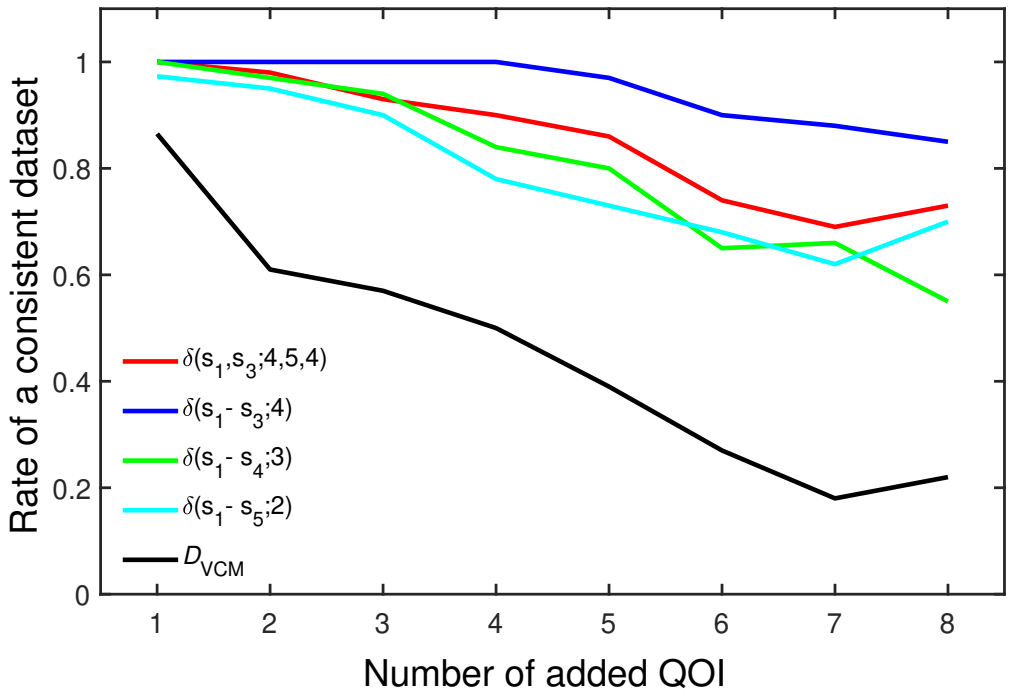

Figure 6.2: Percentage of dataset that remains consistent after adding a randomly selected group of quantities of interest from the test set. The computed results are based on 100 repeated runs.

6.6 Sensitivity Analysis

As the scenario parameters were selected a priori in this study, it is of interest to determine which scenario parameter plays a more important role in the discrepancy function once the dataset inconsistency is resolved. We compared the effect by evaluating the averaged partial derivative of the discrepancy function with respect to each scenario parameter over an ensemble of feasible discrepancy functions. The coefficient vectors of the assembled discrepancy functions were generated by projecting uniform samples from the joint feasible set onto the discrepancy-function coefficient space. Because the basis functions are differentiable, the partial derivative can be calculated for a given set of discrepancy-function coefficient vectors $\{c^j\}_{j=1}^n$ as follows:

$$\frac{\partial \delta}{\partial s_i}(s; c^j) = \sum_{j=1}^{n} c^j \frac{\partial \Phi_j(s)}{\partial s_i}. \tag{6.12}$$

The resulting partial derivatives are also functions of the scenario parameters. To provide a comparable measure of this function, we evaluated the generalized p-norm of the function over a region of interest in the scenario space, denoted by $\mathcal{S}$. For a positive value of p, this

value is calculated as follows:

$$\left\| \frac{\partial \delta}{\partial s_i} \right\|_p = \left(\int_{\mathcal{S}} \left| \frac{\partial \delta}{\partial s_i}(s) \right|^p ds \right)^{1/p}. \tag{6.13}$$

In practice, the integral is replaced by averaging it over scenario conditions either uniformly distributed in the normalized scenario box $[-1,\ 1]^{n_s}$ or over scenario conditions of QOIs in the dataset. As a result, the final formula for computing the partial derivative is given in Equation (6.14). The computation includes two levels of averaging: over feasible discrepancy functions and over scenario conditions:

$$\left\| \frac{\partial \delta}{\partial s_i} \right\|_p = \frac{1}{MN} \sum_{j=1}^{N} \left(\sum_{k=1}^{M} \left| \frac{\partial \delta}{\partial s_i}(s_k; c^j) \right|^p \right)^{1/p}. \tag{6.14}$$

The computed results with $p = 2$ over the normalized scenario cube and over the training set scenarios are summarized in Tables 6.9 and 6.10. The parameter N was set to 10^4 for both cases, and M was set to 10^4 for case with the normalized scenario cube.

Table 6.9: Generalized 2-norm of the partial derivative function over the normalized cube.

Discrepancy	$\partial\delta/\partial s_1$	$\partial\delta/\partial s_2$	$\partial\delta/\partial s_3$	$\partial\delta/\partial s_4$	$\partial\delta/\partial s_5$
$\delta(s_1, s_3; 4, 5, 4)$	5.31	—	8.09	—	—
$\delta(s_1 - s_3; 4)$	2.08	1.63	3.15	—	—
$\delta(s_1 - s_4; 3)$	0.69	1.10	1.35	0.31	—
$\delta(s_1 - s_5; 2)$	0.81	2.06	0.91	1.24	2.20

Table 6.10: Generalized 2-norm of the partial derivative function over the scenarios in the training set.

Discrepancy	$\partial\delta/\partial s_1$	$\partial\delta/\partial s_2$	$\partial\delta/\partial s_3$	$\partial\delta/\partial s_4$	$\partial\delta/\partial s_5$
$\delta(s_1, s_3; 4, 5, 4)$	1.71	—	3.11	—	—
$\delta(s_1 - s_3; 4)$	0.81	1.61	1.81	—	—
$\delta(s_1 - s_4; 3)$	0.57	1.43	1.48	0.40	—
$\delta(s_1 - s_5; 2)$	0.55	1.03	0.77	0.59	2.58

The results reveal that the 2-norm partial derivatives are qualitatively similar over the two investigated regions in the scenario space. The values reduced significantly when more than two scenario parameters were included in the discrepancy function. The partial derivative with respect to s_3, the scenario parameter representing the temperature increment of

the system, displays the largest value in both Tables 6.9 and 6.10 except for $\delta(s_1 - s_5; 2)$. The partial derivative with respect to s_2 exhibits a relatively large value consistently for all tested δ values, implying that the initial pressure P_5 is an important factor for the discrepancy function. When both the ratio of H_2 to CO (s_4) and syngas to O_2 (s_5) are included, the partial derivatives with respect to s_5 and s_2 become the largest and second-largest derivatives, suggesting that the mixture composition, in particular the fuel to oxygen ratio, is also important to the discrepancy function. The results demonstrate that the partial derivative values can be affected nontrivially by the selection of the scenario parameters. The order among them arranged by magnitude can change if other scenario parameters are added or removed.

6.7 Discrepancy Function Behavior

The behavior of the discrepancy functions was examined within the normalized scenario cube for different numbers of scenario parameters. The same group of discrepancy functions was used, and the sampled mean discrepancy-function coefficient vectors were chosen to represent the feasible discrepancy functions. The function $\delta(s_1, s_3; 4, 5, 4)$ is plotted in Figure 6.3. The discrepancy function is relatively smooth over the region where data are

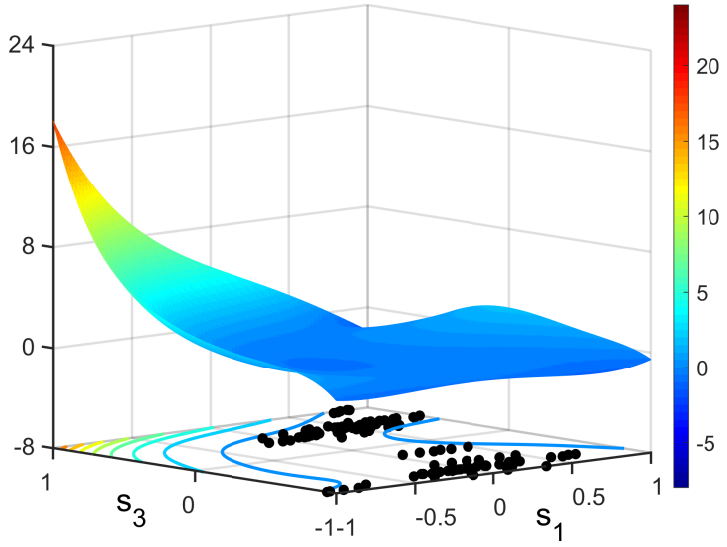

Figure 6.3: Discrepancy function $\delta(s_1, s_3; 4, 5, 4)$ in the normalized scenario region $[-1,\ 1]^2$. Black points represent the scenario conditions of quantities of interest in the dataset.

provided, although higher-order monomials exist in the basis functions. The function changes quickly outside this training domain, reaching significantly larger values toward the corner specified by $s_1 = -1$ and $s_3 = 1$, indicating that the discrepancy function puts a substan-

tially positive correction on the model output at low initial temperature and high initial pressure conditions.

The discrepancy function $\delta(s_1 - s_3; 4)$ is plotted in the projected space of s_2 and s_3 at three fixed s_1 values considering their relatively larger partial derivative values. Each dataset QOI was assigned to the closest s_1 slice. The results are displayed in Figure 6.4. The function is again relatively smooth over regions where the data exist. However, this effective training domain becomes smaller compared to that observed in Figure 6.3 due to the diluted data density in the projected slices embedded in a higher-dimensional scenario space. A significantly larger curvature is observed outside the training domain, and the behavior of the function surface can be quite different for different slices. The value of the discrepancy function quickly increases toward the $[s_2 = 1, s_3 = 1]$ corner for the $s_1 = -0.75$ and $s_1 = 0$ slices, indicating that the discrepancy function makes a positive correction to the model output at high initial pressure conditions with large temperature increase if the initial temperature is relatively low. The value decreases toward the $[s_2 = 1, s_3 = -1]$ corner at $s_1 = 0.75$, implying that a negative correction is placed on the model output by the discrepancy function at high initial pressure conditions with small temperature increase if the initial temperature is relatively high. Figure 6.4.

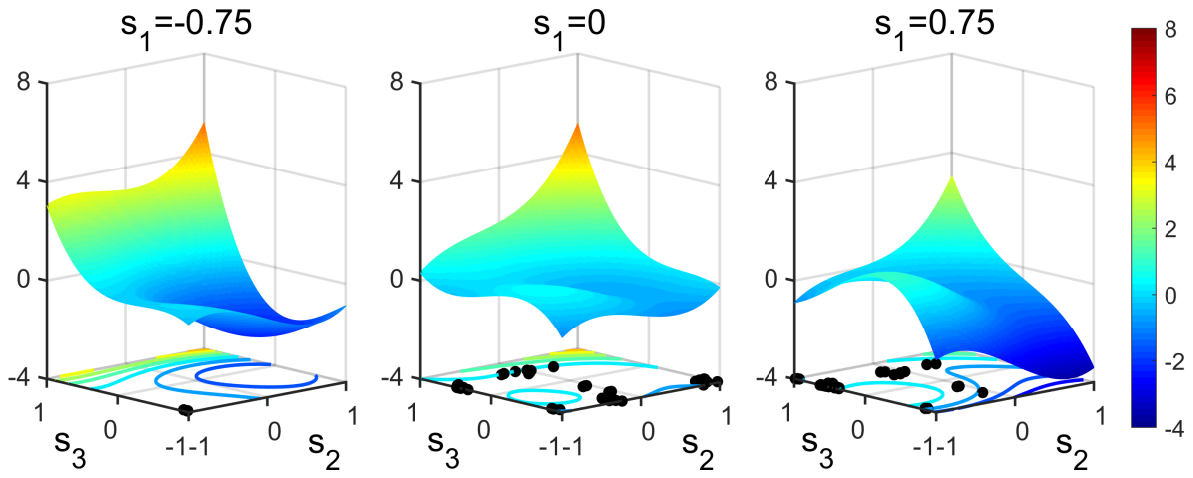

Figure 6.4: Discrepancy function $\delta(s_1 - s_3; 4)$ in the projected s_2-s_3 space at fixed s_1 values. Black points represent scenario conditions of quantities of interest in the dataset.

The discrepancy function $\delta(s_1 - s_4, 3)$ is plotted in the projected space of s_2-s_3 at centers of the four quadrants in the s_1-s_4 space. Dataset QOIs were assigned to each case based on the shortest Euclidean distance in the s_1-s_4 space. The results are given in Figure 6.5. Although the training data density in each case is further diluted due to another increment of the scenario parameter dimension, the function displays overall smoother behavior in the 2D projected scenario space compared to that observed in Figures 6.3 and 6.4. The

function remains comparably flat over the whole normalized square region for $s_1 = 0.5$ and $s_4 = \pm 0.5$. The value of the function increases moderately toward the $[s_2 = 1, s_3 = 1]$ corner for $s_1 = -0.5$ and $s_4 = \pm 0.5$. The observed results may be attributed to the addition of another scenario parameter in the analysis, the reduced complexity in the basis functions and the moderated irregularity of the function behavior.

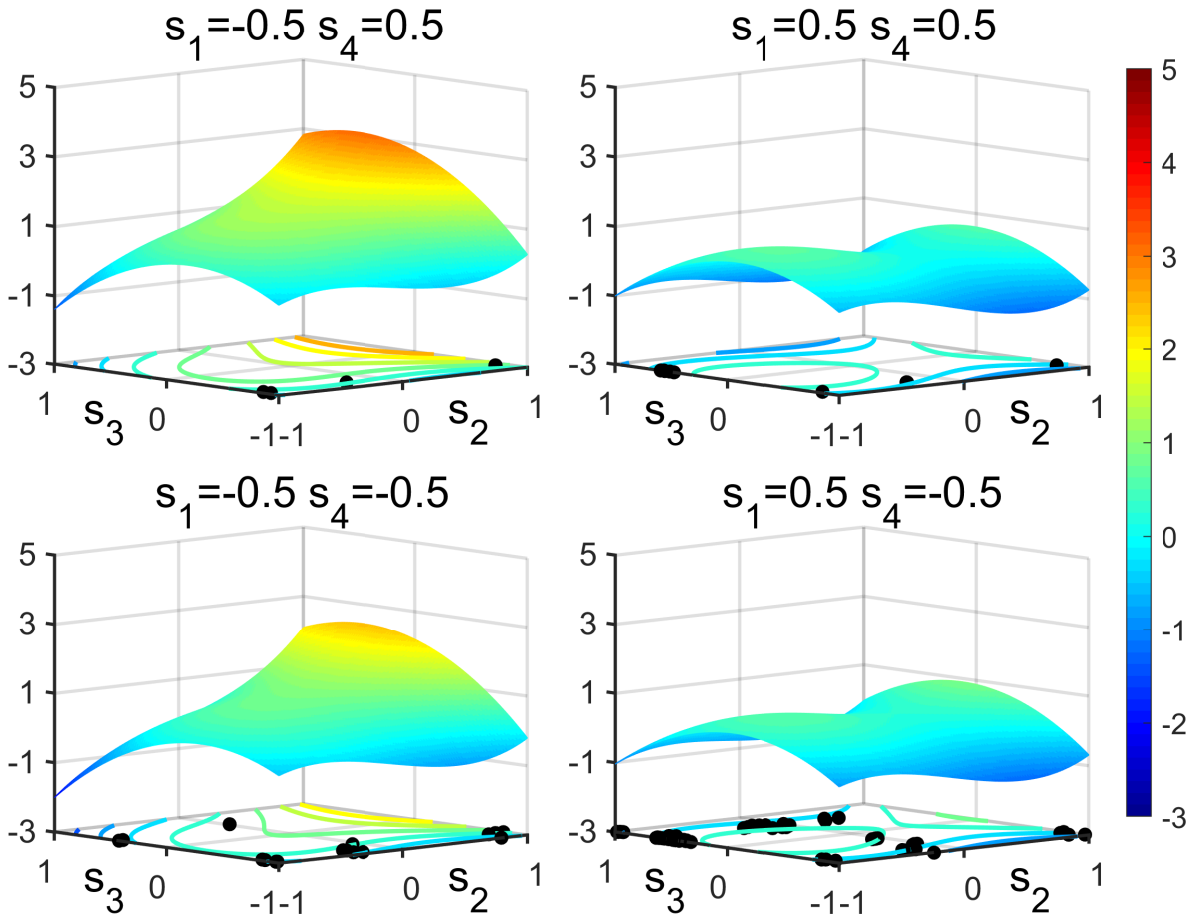

Figure 6.5: Discrepancy function $\delta(s_1 - s_4; 3)$ in the projected s_2-s_3 space at fixed s_1-s_4 value pairs. Black points represent scenario conditions of quantities of interest (QOIs) in the dataset.

Although $\delta(s_1 - s_5; 2)$ exhibits the largest partial derivative value with respect to s_5, it is computed and plotted in the projected space of s_2-s_3 considering the observed extremely bifurcated distribution of s_5 in the training set. The results are presented in Figure 6.6. The two scenario parameters not shown in each subfigure were set to zero. The function surface displays a moderately small curvature in most of the cases, except at $s_5 = 0.75$, where the function value decreases quickly toward the $[s_2 = 1, s_3 = -1]$ corner. The results suggest that, with an average value of H_2 to CO ratio and initial temperature and a relatively high

fuel to oxygen ratio, the discrepancy function exhibits a considerable negative correction to the model output at high initial pressures with small temperature increase. In this last case, the function value experiences larger changes in regions where no training data exist.

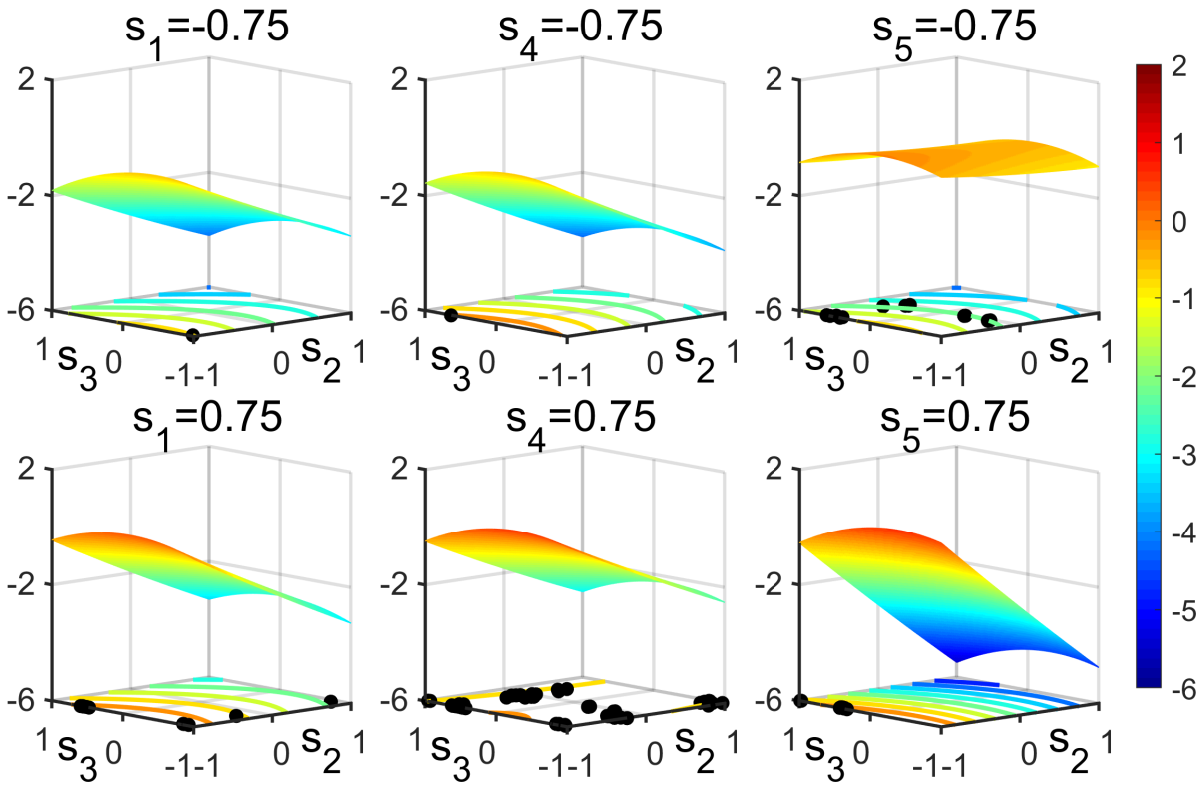

Figure 6.6: Discrepancy function $\delta(s_1 - s_5; 2)$ in the projected s_2-s_3 space at fixed $\{s_1, s_4, s_5\}$ value sets. Black points represent scenario conditions of quantities of interest (QOIs) in the dataset.

6.8 Feasible Set Analysis

The modified feasible set $\widetilde{\mathcal{F}}$ (i.e., the projection of the joint feasible set on the model parameter space) was examined with the four discrepancy functions discussed in the previous section. For comparison, the feasible set of D_{VCM} was also included in the analysis. The prediction interval for each model parameter was calculated by substituting x_i into the objective function in Equations (5.8) and (5.9) or Equations (2.7) and (2.8). The computed outer-bound intervals are plotted in Figure 6.7 for rate multipliers whose posterior uncertainty bounds are reduced compared to the prior uncertainty bounds.

The results demonstrate that the prediction intervals are similar to each other if $\delta(s_1 - s_3; 4)$, $\delta(s_1 - s_4; 3)$, $\delta(s_1 - s_5; 2)$, and D_{VCM} are used. When $\delta(s_1, s_3; 4, 5, 4)$ was used, the

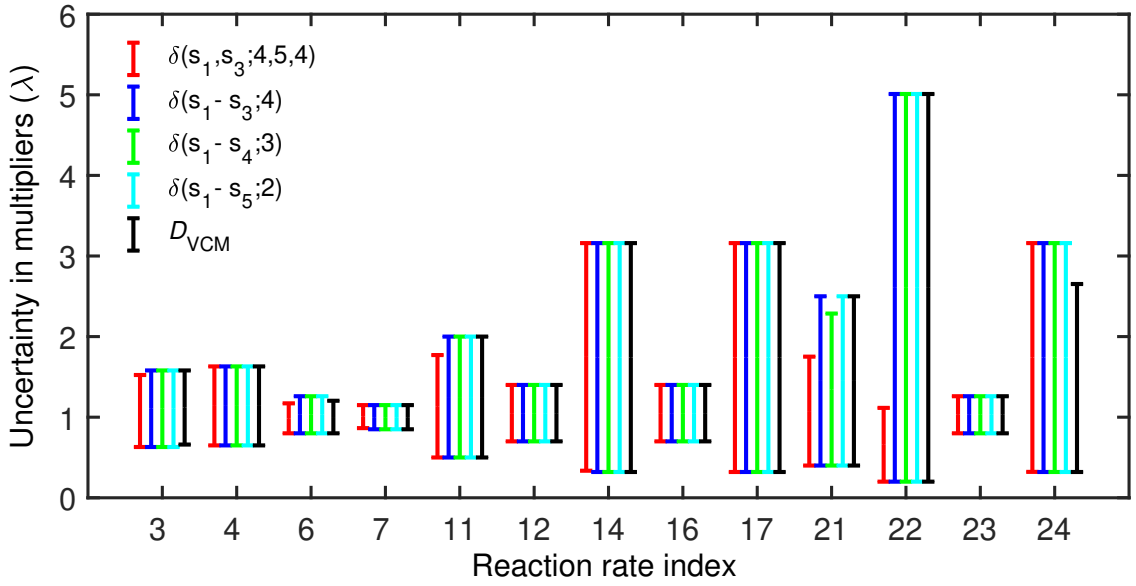

Figure 6.7: Bound-to-bound data collaboration predicted outer-bound intervals for reaction rate multipliers whose posterior uncertainty is smaller than the prior uncertainty.

upper uncertainty bound was significantly reduced for multipliers of reaction $HO_2 + HO_2 \rightarrow H_2O_2 + O_2$ (#21) and $CO + O_2 \rightarrow CO_2 + O$ (#22). No systematic difference was observed in the predicted model parameter intervals computed using a discrepancy function or D_{VCM}.

A uniform distribution assumption was then selected for the joint feasible set for a statistical analysis. A total of 3×10^5, 4×10^5, 4×10^5, 5×10^5, and 10^5 samples were generated for cases with $\delta(s_1, s_3; 4, 5, 4)$, $\delta(s_1 - s_3; 4)$, $\delta(s_1 - s_4; 3)$, $\delta(s_1 - s_5; 2)$ and D_{VCM} by applying the Gibbs sampler discussed in Section 3.3. The convergence of the samples was monitored and ensured using the test method detailed in Section 3.4. The two-sigma confidence interval of each model parameter, truncated by the prior uncertainty bounds, is estimated using the samples and plotted in Figure 6.8.

For the four cases where a discrepancy function was used, the estimated confidence intervals are consistent overall. The majority of them overlap for each multiplier, except λ_{18}, the multiplier associated with reaction $OH + H_2O_2 \rightarrow HO_2 + H_2O$, where the confidence intervals with $\delta(s_1 - s_4; 3)$ and $\delta(s_1 - s_5; 2)$ barely intersect. In general, the length of the confidence interval for $\delta(s_1, s_3; 4, 5, 4)$ is the longest and that of either $\delta(s_1 - s_4; 3)$ or $\delta(s_1 - s_5; 2)$ is the shortest. The estimated confidence interval for D_{VCM}, however, exhibits a noticeable difference for λ_3, λ_{17}, λ_{18}, λ_{21}, and λ_{22}, whose associated reactions are listed in Table 6.11.

In addition to the confidence interval, the 1D marginal empirical probability density function (PDF) of each model parameter was computed. The results for the six parameters appeared most frequently as active parameters for the 112 training QOIs are given in

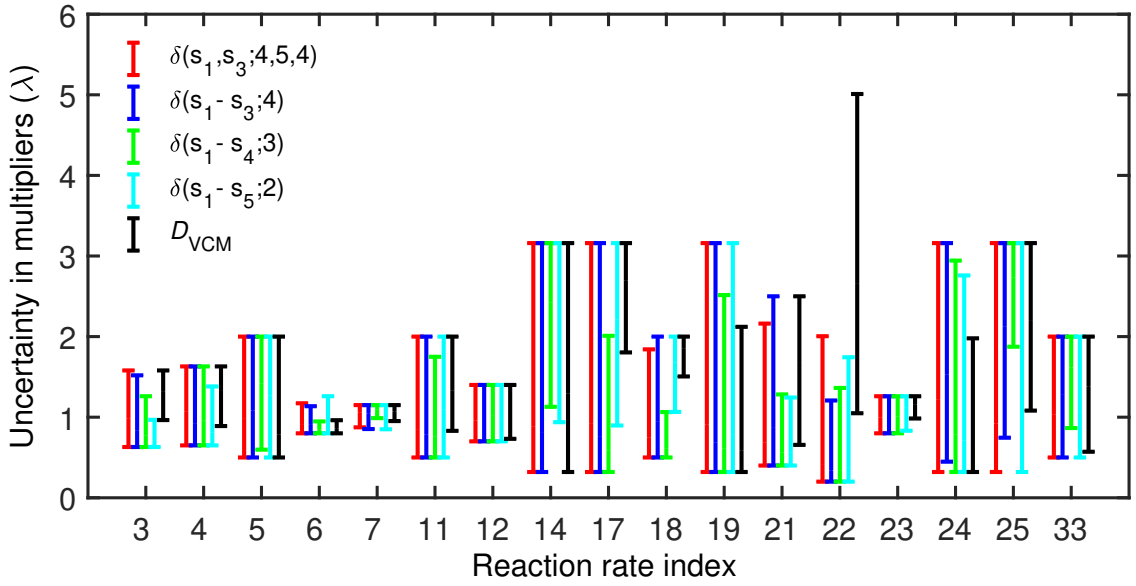

Figure 6.8: Estimated two-sigma confidence interval truncated by prior uncertainty bounds for reaction rate multipliers whose posterior uncertainty is smaller than the prior uncertainty.

Table 6.11: Reactions whose estimated posterior confidence interval in the multipliers are different for D_{VCM} compared to using discrepancy functions.

Index	Reaction
3	$H_2 + O \rightarrow OH + H$
17	$HO_2 + OH \rightarrow H_2O + O_2$
18	$OH + H_2O_2 \rightarrow HO_2 + H_2O$
21	$HO_2 + HO_2 \rightarrow H_2O_2 + O_2$
22	$CO + O_2 \rightarrow CO_2 + O$

Figure 6.9. The associated reactions are listed in Table 6.12.

Examination of the results shows some differences in the empirical PDFs generated from the dataset with discrepancy functions and from D_{VCM}. In the following discussion, the description about the relative magnitude of the reaction rate values is regarding their nominal values (i.e., a multiplier with value 1). Both VCM and discrepancy function methods result in higher probabilities in lower rate values of reaction $O_2 + H \rightarrow OH + O$ (λ_6) and higher rate of reaction $O_2 + H \rightarrow HO_2$ (λ_7). However, for reactions $H_2 + O \rightarrow OH + H$ (λ_3) and $CO + O_2 \rightarrow CO_2 + O$ (λ_{22}), the VCM method produces a PDF with higher probabilities for higher rate values whereas the opposite is observed in PDFs generated from the discrepancy method, except for the case with $\delta(s_1, s_3; 4, 5, 4)$ where a relatively flat PDF is produced. For reaction $HO_2 + H \rightarrow H_2 + O_2$ (λ_{11}), the PDF produced by the VCM method displays

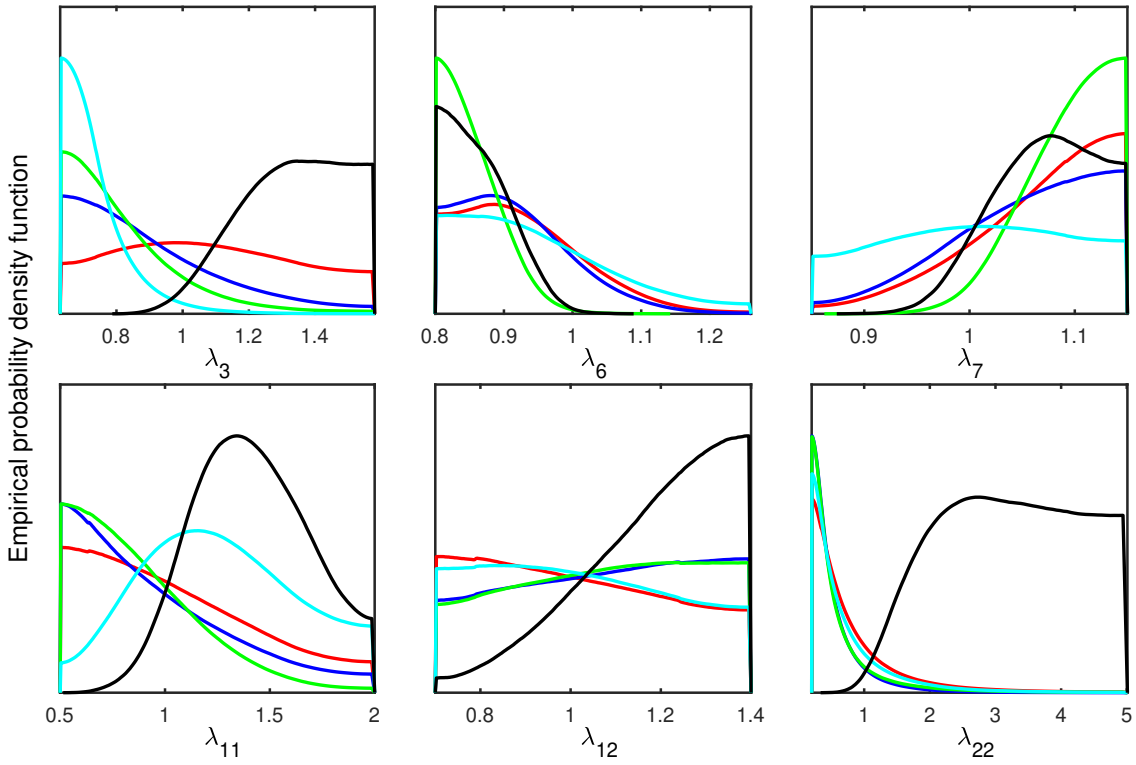

Figure 6.9: Estimated marginal probability density for multipliers λ_3, λ_6, λ_7, λ_{11}, λ_{12}, λ_{22}. The color codes are red lines: $\delta(s_1, s_3; 4, 5, 4)$; blue lines: $\delta(s_1 - s_3; 4)$; green lines: $\delta(s_1 - s_4; 3)$; cyan lines: $\delta(s_1 - s_5; 2)$; and black lines: D_{VCM}.

Table 6.12: Reactions whose multipliers appear most frequently in the surrogate models as active parameters for the 112 training quantities of interest.

Index	Reaction
3	$H_2 + O \rightarrow OH + H$
6	$O_2 + H \rightarrow OH + O$
7	$O_2 + H \rightarrow HO_2$
11	$HO_2 + H \rightarrow H_2 + O_2$
12	$HO_2 + H \rightarrow OH + OH$
22	$CO + O_2 \rightarrow CO_2 + O$

a bell shape centered at a higher rate value whereas the PDFs generated by the discrepancy function method, except for the case with $\delta(s_1 - s_5; 2)$, show higher probabilities in lower rate values. For the case with $\delta(s_1 - s_5; 2)$, the PDF exhibits a bell shape centered at a different location. For reaction $HO_2 + H \rightarrow OH + OH$ (λ_{12}), the VCM method generates a PDF with higher probabilities in higher rate values whereas the discrepancy function method produces

relatively flat PDFs.

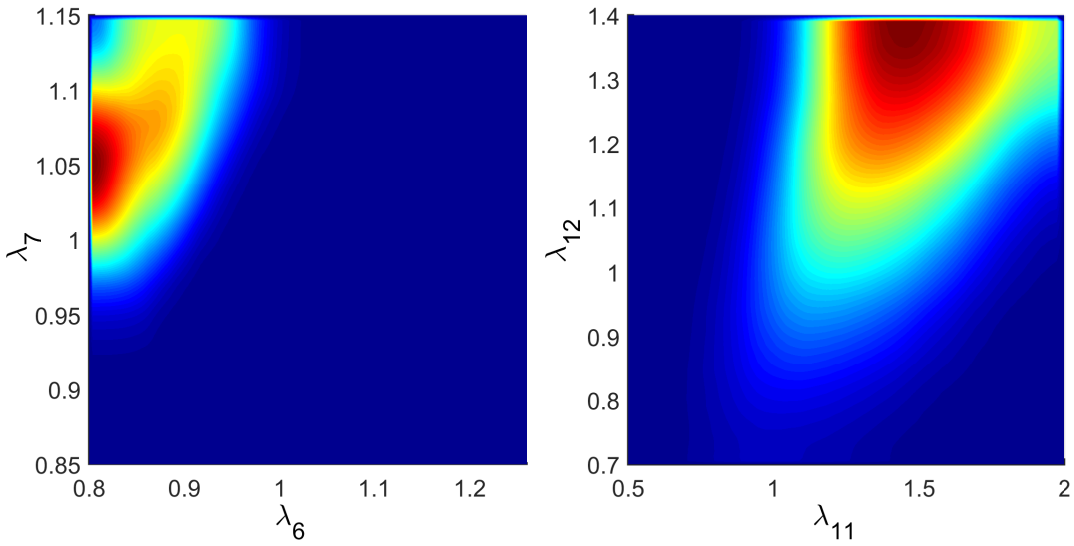

Figure 6.10: Estimated two-dimensional probability density functions in the λ_6-λ_7 and λ_{11}-λ_{12} space based on samples generated with D_{VCM}. The axis limits are the prior uncertainty bounds.

The 2D correlated PDFs on the projected λ_6-λ_7 and λ_{11}-λ_{12} spaces were computed and the results are given in Figures 6.10 to 6.12. The two reactions associated with λ_6 and λ_7, $O_2 + H \rightarrow OH + O$ and $O_2 + H \rightarrow HO_2$, compete over the same reactants. The PDF resulted from the VCM method exhibits a high probability in the parameter region that moderately enhances reaction $O_2 + H \rightarrow HO_2$ and strongly suppresses reaction $O_2 + H \rightarrow OH + O$, pushing the reaction rate value close to the lower uncertainty bound. For discrepancy functions $\delta(s_1, s_3; 4, 5, 4)$ and $\delta(s_1 - s_3; 4)$, the resulted PDFs have a high probability in the parameter region that inhibits reaction $O_2 + H \rightarrow OH + O$ mildly and reinforces substantially reaction $O_2 + H \rightarrow HO_2$. For $\delta(s_1 - s_4; 3)$, the resulting PDF has a high probability region that suppresses reaction $O_2 + H \rightarrow OH + O$ and enhances reaction $O_2 + H \rightarrow HO_2$ both significantly and push the reaction rate values to the respective lower and upper uncertainty bounds. For $\delta(s_1 - s_5; 2)$, the produced PDF covers a large parameter region with noticeable probabilities. The region with the highest probability, however, indicates a suppression on both reaction rates.

The two reactions associated with λ_{11} and λ_{12}, $HO_2 + H \rightarrow H_2 + O_2$ and $HO_2 + H \rightarrow OH + OH$, also compete over the same reactants. The VCM method generates a PDF that has a high probability in the parameter region that enhances reaction $HO_2 + H \rightarrow OH + OH$ strongly and reaction $HO_2 + H \rightarrow H_2 + O_2$ weakly. For $\delta(s_1, s_3; 4, 5, 4)$, completely distinct from the VCM result, the produced PDF has a high probability in the parameter region that suppresses both reactions substantially. For $\delta(s_1 - s_3; 4)$ and $\delta(s_1 - s_4; 3)$, the

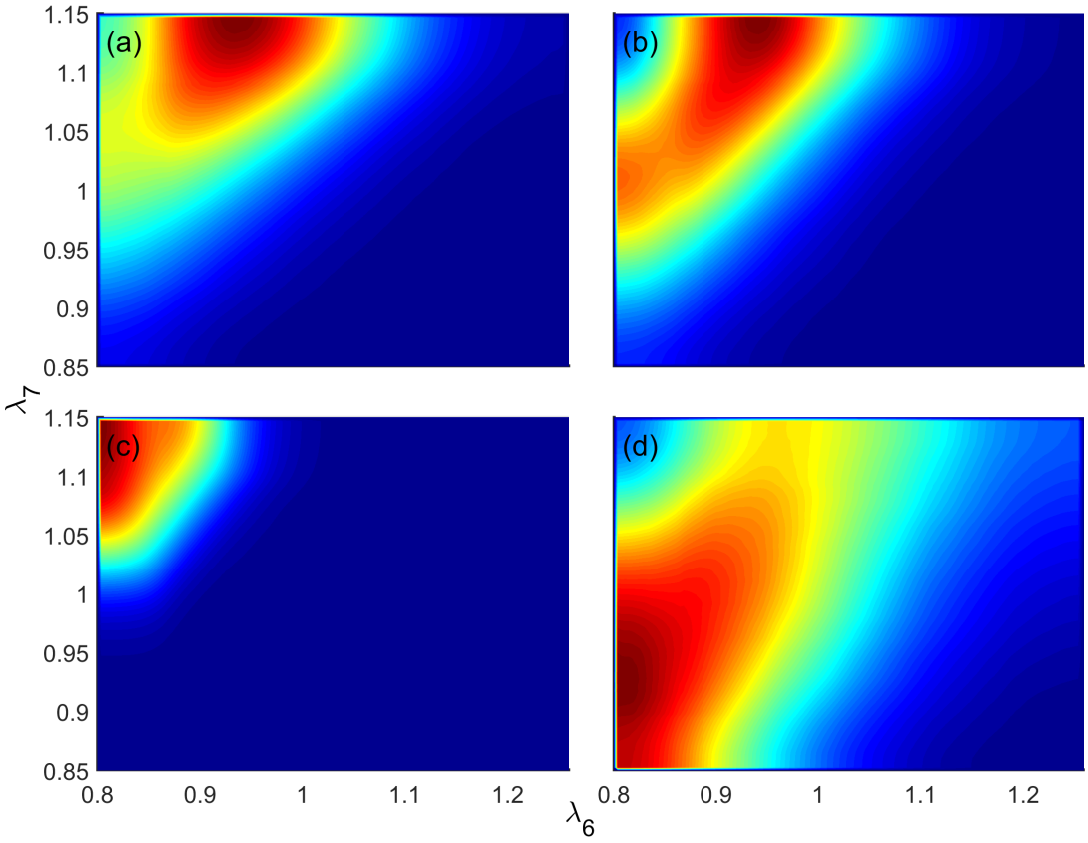

Figure 6.11: Estimated two-dimensional probability density functions in the λ_6-λ_7 space based on samples generated using a (a) dataset with $\delta(s_1, s_3; 4, 5, 4)$, (b) dataset with $\delta(s_1 - s_3; 4)$, (c) dataset with $\delta(s_1 - s_4; 3)$, and (d) dataset with $\delta(s_1 - s_5; 2)$. The axis limits are the prior uncertainty bounds.

resulting PDFs have a high probability in inhibiting reaction $HO_2 + H \rightarrow H_2 + O_2$ but do not display a observable preference in increasing or decreasing the reaction rate of $HO_2 + H \rightarrow OH + OH$. For $\delta(s_1 - s_5; 2)$, the obtained PDF has a high probability in the parameter region that mildly enhances reaction $HO_2 + H \rightarrow H_2 + O_2$ and suppresses reaction $HO_2 + H \rightarrow OH + OH$. The PDF also demonstrates a noticeable positive correlation between the two reaction rate values.

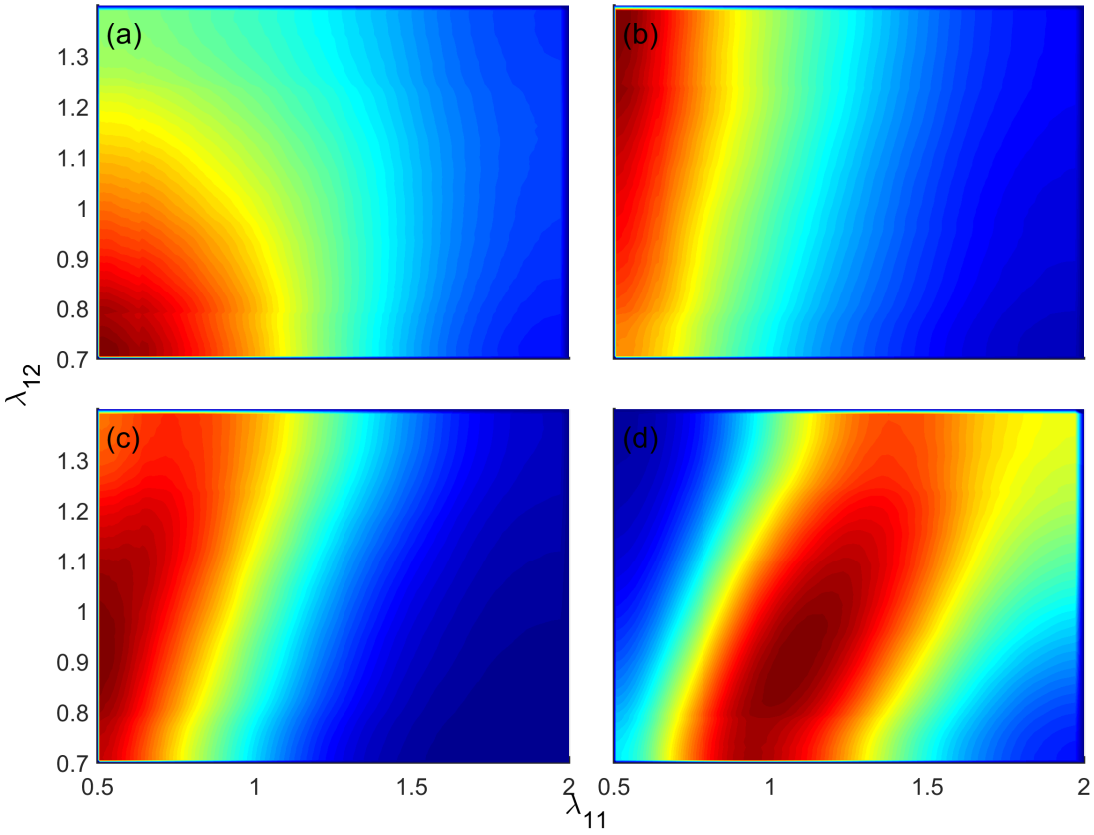

Figure 6.12: Estimated two-dimensional probability density functions in the λ_{11}-λ_{12} space based on samples generated with a (a) dataset with $\delta(s_1, s_3; 4, 5, 4)$, (b) dataset with $\delta(s_1 - s_3; 4)$, (c) dataset with $\delta(s_1 - s_4; 3)$, and (d) dataset with $\delta(s_1 - s_5; 2)$. The axis limits are the prior uncertainty bounds.

6.9 Chapter Summary

In this chapter, a syngas combustion dataset consisted of only ignition delay time data was constructed. The CONSTVA model, which is adequate at ideal experimental conditions, was selected as the original simulation models for the ignition delay time QOIs. Both the VCM method and the method of including a discrepancy function were applied to resolve the initial dataset inconsistency. The discrepancy function method was able to obtain dataset consistency without removing experimental data. The selection of combinations of scenario parameters that can recover dataset consistency is not unique, nor are the choices of the basis functions. However, the method may fail with certain basis functions if important scenario parameters are not included in the analysis. The resulting dataset consistency is significantly less vulnerable to addition of extra data compared to that obtained by removing the VCM-identified QOIs. The sensitivity analysis revealed that the initial pressure, temperature increment and fuel-to-oxygen ratio are important scenario parameters for the

discrepancy function. The latter two scenario parameters were reported in [87] as effective contributors to the experimentally observed inhomogeneous circumferential ignition. Therefore, the experimental data included in this study are likely subject to such nonideal ignition phenomena. The discrepancy function exhibited relatively regularized behavior in regions where data exist but can change quickly outside this training domain. Although the training data density dilutes quickly as the dimension of the scenario parameters increases, the discrepancy function with more scenario parameters and lower order polynomial basis functions exhibits an overall flatter surface in the 2D projected scenario parameter spaces.

The 1D prediction intervals of model parameters are qualitatively similar between the feasible sets obtained by applying the discrepancy function method and the VCM method, and among feasible sets obtained by applying different discrepancy functions. However, the sample-based credible intervals and lower-dimensional (1D and 2D) empirical PDFs of the model parameters can differ from each other. The difference is more substantial between the two methods than among different discrepancy functions. The empirical PDFs from feasible sets obtained using the two methods can exhibit different, sometimes opposite results for rate values of reactions that are important to syngas ignition delay times. Therefore, a careful assessment of the source for dataset inconsistency is crucial for UQ as the correspondingly selected resolution method has significant influence on the computed results.

In this study, the scenario parameters were selected based on our prior knowledge about shock-tube ignition experiments. They are factors with physical meanings. In practice, correlations can and are likely to exist in these scenario parameters, as shock-tube experiments are usually conducted with a similar mixture composition at different temperatures and pressures. The temperature increment is also related to pressure and mixture composition through thermodynamic laws. Future work may focus on developing more efficient rules for selecting scenario parameters and potentially uncorrelated linear combinations of physically defined scenario parameters.

Chapter 7

Summary and Conclusions

This dissertation explored and expanded the method of Bound-to-Bound Data Collaboration (B2BDC) in uncertainty quantification (UQ). The B2BDC framework combines models and experimental data with assessed uncertainty to systematically improve the knowledge of the underlying physical process. The updated uncertainty after data collaboration is characterized by the feasible set, a generally smaller region in the parameter space compared to its prior uncertainty region. The feasible set is mathematically defined by inequality constraints that are derived by requiring model outputs at a set of model parameter vectors to be within the assessed experimental uncertainties. The dataset is inconsistent when the feasible set is empty, and this inconsistency must be resolved before moving to predictions. When the dataset is consistent, uncertainty in other quantities of interest (QOIs) can be computed. Dataset consistency is determined by the sign of the scalar consistency measure, which is calculated by solving a constrained optimization problem. The QOI predictions are calculated by solving a pair of constrained minimization and maximization problems. The Solution Mapping technique is used to create quadratic, rational quadratic, and polynomial surrogate models that replace the original simulation models in B2BDC computations. The difficulty in finding a globally optimal solution to NP-hard nonconvex optimization problems is alleviated by computing an interval that contains the global optimum. The bounds of the interval are calculated by finding a local solution to the nonconvex problem and finding a solution to a convex semidefinite programming problem, which is derived from the nonconvex problem via convex relaxation approaches.

Compared to the optimization-based B2BDC framework, Bayesian inference method can provide a more informative assessment about the underlying problem with more informative assumptions. In a Bayesian inference, a prior distribution and a likelihood function need to be selected to characterize the prior knowledge of the model parameters and the model describing the measurement error. The Gaussian and the uniform measurement error assumptions are two statistical models inspired by realistic experimental setups. Numerical study presented in Chapter 3 based on a 2D toy example and the 102-dimensional GRI-Mech dataset shows that, with the uniform prior distribution, these two likelihood assumptions

generate a growing and noticeably larger difference in their posterior distributions and QOI predictions in a higher dimensional application. Therefore, careful evaluation and validation of the selected statistical models are crucial to guarantee the quality of a Bayesian inference application in realistic engineering problems. The Bayesian framework with the uniform prior distribution and uniform likelihood assumption generates a posterior distribution that is uniformly distributed over the feasible set. Numerical studies show that this Bayesian posterior distribution, while providing a quantifiable measure (the probability) to each QOI value, can generate noticeably less-conservative credible intervals compared to B2BDC prediction intervals, particularly for higher dimensional problems.

Dataset inconsistency indicates a provable disagreement among the collected model and experimental data. Strategies resolving dataset inconsistency are developed focusing on different scenarios. For example, the developed vector consistency measure (VCM) method [52] focuses on identifying the fewest experimental data points, adjusting/removing which recovers a consistent dataset. The model discrepancy function method presented in Chapter 5 focuses on adding a scenario-dependent correction to model output that resolves dataset inconsistency without modifying experimental data and their assessed uncertainty. In the VCM method, different weights can be assigned to different model parameters and experimental data points to reflect domain expertise. In the model discrepancy function method, expert opinions can be included by choosing different sets of basis functions or scenario parameters. The development enriches the B2BDC framework and enables an analyst, when the dataset is inconsistent, to design and choose resolution strategies that better reflect his/her understanding of the specific application. More importantly, the comparison analysis for a syngas combustion dataset shown in Chapter 6 demonstrates that different resolution strategies can produce quite different UQ results, highlighting the necessity of incorporating application-specific information in the analysis and the ability of the B2BDC framework to provide such an option.

The practical value of the B2BDC framework in realistic engineering problems is reiterated in the DLR syngas combustion dataset presented in Chapter 4. The initial dataset inconsistency can be resolved by removing VCM-identified QOIs. The B2BDC analysis on the obtained consistent dataset generates improved understanding of the uncertainty in the reaction rate parameters of the syngas combustion mechanism. The B2BDC prediction intervals show that some parameters have a shorter uncertainty than their prior uncertainty interval. The uniform samples from the feasible set visualize correlations among different parameters/QOIs. Optimized sets of model parameters obtained from the feasible set exhibit better performance compared to those obtained from the prior uncertainty region, especially in predictions at relatively extreme conditions not reflected by experimental data points in the dataset. The result highlights the essence of the B2BDC framework, which gradually and systematically improves our knowledge of the system with an expanding dataset by forming the converging feasible set.

The field of UQ has by no means found a solution that is agreed upon by all researchers.

In the author's opinion, three main challenges remain for future study: 1) How can we identify all sources of uncertainty in an underlying system? 2) How can we accurately quantify and characterize each uncertainty source in the analysis? 3) How can we practically realize the analysis? These points are reflected on throughout this dissertation. For example, considering the first question, model discrepancy, an uncertainty source that has received growing attention recently, is included in the B2BDC framework to resolve dataset inconsistency as shown in Chapter 5. However, there could be other sources that contribute to the disagreement in the system, whether detected or not.

Appendix A

GRI-Mech Dataset

Table A.1: Quantities of interest in the GRI-Mech dataset [113]. Measurements from the same research institute are grouped together.

Label	QOI
IG.1a, IG.1b, IG2, IG.St3a, IG.St3b	Ignition delay measurement in shock tube
IG.6a, IG.6b	Ignition delay measurement in shock tube
IG.T1	Ignition delay measurement in shock tube
IG.T2, IG.St1a, IG.St1b	Ignition delay measurement in shock tube
IG.St4a, IG.St4b	Ignition delay measurement in shock tube
CH3.C1a, CH3.C1b, CH3.C2, CH3.C4	Maximum CH3 concentration
CH3.T1a, CH3.T1b, CH3.T2	Time of CH3 maximum
CH3.C3	Maximum CH3 concentration
CH3.T4, CH3.StC6, CH3.StC7, CH3.T3	Time of CH3 maximum
OH.1a, OH.1b, OH.2	Time to half of OH maximum
OH.3a, OH.3b, OH.3c, OH.3d, OH.ST8	Time to half of OH maximum
CO.C1a, CO.C1b, CO.C1c, CO.C1d, CO.SC8,CO.T1a, CO.T1b, CO.T1c	Maximum CO concentration
BCO.T1, BCO.T2, BCO.T3, BCO.T4, BCO.T5, BCO.T6, BCO.T7	Time to half of CO maximum

Table A.1 (continued)

Label	QOI
BCH2O.T1, BCH2O.T2, BCH2O.T3	Time to half of CO maximum
SR.10c	Temperature where [CO2] = 500ppm
F1, StF8	Laminar flame speed
F2, F3	Laminar flame speed
F4	Laminar flame speed
F5, F6	Laminar flame speed
SF7	Laminar flame speed
SNO.C11	NO (2 cm) concentration
SCH.C11	Maximum CH concentration
SCH.C12, SCH.C13	Maximum CH concentration
CH.St	Maximum of CH concentration without NO doping
NFR1	HCN relative concentration
NFR2	NO relative concentration
NFR3	N2O relative concentration
NF6	Maximum NO mole fraction
NF7	Maximum CN mole fraction
NF11	Ratio of CH maximum concentrations at two levels of NO doping
NF12/13	Ratio of CN maximum concentrations for NO and N2O doping
NFR4	NO mole fraction at reactor exit
NFR5	HCN mole fraction at reactor exit
CHNO.St	Maximum of CH concentration with NO doping

Table A.2: Active model parameters in GRI-Mech dataset [113]

Index	Reaction/Species	Parameter type
1	$O_2 + CH_2O \rightarrow HO_2 + HCO$	log pre-exponential factor
2	$H + O_2 \rightarrow O + OH$	log pre-exponential factor
3	$H + HO_2 \rightarrow O_2 + H_2$	log pre-exponential factor
4	$H + HO_2 \rightarrow OH + OH$	log pre-exponential factor
5	$OH + OH + M \rightarrow H_2O_2 + M$	log pre-exponential factor
6	$OH + CH_2O \rightarrow HCO + H_2O$	log pre-exponential factor

Table A.2 (continued)

Index	Reaction/Species	Parameter type
7	$HO_2 + HO_2 \rightarrow O_2 + H_2O_2$	log pre-exponential factor
8	$HO_2 + CH_2O \rightarrow HCO + H_2O_2$	log pre-exponential factor
9	$HCO + M \rightarrow H + CO + M$	log pre-exponential factor
10	$HCO + O_2 \rightarrow HO_2 + CO$	log pre-exponential factor
11	$H + HCO \rightarrow H_2 + CO$	log pre-exponential factor
12	$H + CH_2O \rightarrow H_2 + HCO$	log pre-exponential factor
13	$H + HCO + M \rightarrow CH_2O + M$	log pre-exponential factor
14	$OH + HO_2 \rightarrow O_2 + H_2O$	log pre-exponential factor
15	$H_2 + CO + M \rightarrow CH_2O + M$	log pre-exponential factor
16	$O + CH_2O \rightarrow OH + HCO$	log pre-exponential factor
17	$H + O_2 + M \rightarrow HO_2 + M$	log pre-exponential factor
18	$H + CH \rightarrow H_2 + C$	log pre-exponential factor
19	$H + CH_2 + M \rightarrow CH_3 + M$	log pre-exponential factor
20	$H + CH_3 + M \rightarrow CH_4 + M$	log pre-exponential factor
21	$O_2 + CH \rightarrow O + HCO$	log pre-exponential factor
22	$CH + H_2 \rightarrow H + CH_2$	log pre-exponential factor
23	$CH + CH_3 \rightarrow H + C_2H_3$	log pre-exponential factor
24	$CH_2 + CH_3 \rightarrow C_2H_4 + H$	log pre-exponential factor
25	$CH_2(S) + H_2 \rightarrow CH_3 + H$	log pre-exponential factor
26	$CH + H_2 + M \rightarrow CH_3 + M$	log pre-exponential factor
27	$O + CH_3 \rightarrow CH_2O + H$	log pre-exponential factor
28	$O + CH_3 \rightarrow H_2 + H + CO$	log pre-exponential factor
29	$O + CH_4 \rightarrow CH_3 + OH$	log pre-exponential factor
30	$H + CH_4 \rightarrow CH_3 + H_2$	log pre-exponential factor
31	$OH + CH_3 \rightarrow CH_2(S) + H_2O$	log pre-exponential factor
32	$OH + CH_4 \rightarrow CH_3 + H_2O$	log pre-exponential factor
33	$CH_3 + CH_3 \rightarrow C_2H_5 + H$	log pre-exponential factor
34	$H + C_2H_5 + M \rightarrow C_2H_6 + M$	log pre-exponential factor
35	$H + C_2H_6 \rightarrow H_2 + C_2H_5$	log pre-exponential factor
36	$CH_2 + CH_4 \rightarrow CH_3 + CH_3$	log pre-exponential factor
37	$CH_2(S) + CH_4 \rightarrow CH_3 + CH_3$	log pre-exponential factor
38	$CH_3 + CH_3 + M \rightarrow C_2H_6 + M$	log pre-exponential factor
39	$CH_3 + C_2H_6 \rightarrow C_2H_5 + CH_4$	log pre-exponential factor
40	$OH + CH_3 \rightarrow CH_2 + H_2O$	log pre-exponential factor
41	$O_2 + CH_3 \rightarrow CH_3O + O$	log pre-exponential factor
42	$H + CH_2OH \rightarrow OH + CH_3$	log pre-exponential factor
43	$O_2 + CH_2 \rightarrow H + H + CO_2$	log pre-exponential factor
44	$H_2 + CH_2 \rightarrow CH_3 + H$	log pre-exponential factor
45	$CH + NO \rightarrow HCN + O$	log pre-exponential factor

Table A.2 (continued)

Index	Reaction/Species	Parameter type
46	$OH + CO \rightarrow CO_2 + H$	log pre-exponential factor
47	$CH_2 + O_2 \rightarrow OH + H + CO$	log pre-exponential factor
48	$CH_2(S) + N_2 \rightarrow CH_2 + N_2$	log pre-exponential factor
49	$CH_2(S) + O_2 \rightarrow H + OH + CO$	log pre-exponential factor
50	$OH + H_2 \rightarrow H_2O + H$	log pre-exponential factor
51	$O + H_2 \rightarrow H + OH$	log pre-exponential factor
52	$O + C_2H_2 \rightarrow H + HCCO$	log pre-exponential factor
53	$O_2 + CH_3 \rightarrow CH_2O + OH$	log pre-exponential factor
54	$H + CH_2O + M \rightarrow CH_3O + M$	log pre-exponential factor
55	$HO_2 + CH_3 \rightarrow O_2 + CH_4$	log pre-exponential factor
56	$CH_3O + O_2 \rightarrow HO_2 + CH_2O$	log pre-exponential factor
57	$H + O_2 + H_2O \rightarrow HO_2 + H_2O$	log pre-exponential factor
58	$HO_2 + CH_3 \rightarrow OH + CH_3O$	log pre-exponential factor
59	$H + OH + M \rightarrow H_2O + M$	log pre-exponential factor
60	$HCO + H_2O \rightarrow H + CO + H_2O$	log pre-exponential factor
61	$H + C_2H_4 + M \rightarrow C_2H_5 + M$	log pre-exponential factor
62	$C_2H_5 + O_2 \rightarrow HO_2 + C_2H_4$	log pre-exponential factor
63	$CH_3 + C_2H_5 + M \rightarrow C_3H_8 + M$	log pre-exponential factor
64	$H + C_3H_8 \rightarrow H_2 + C_3H_7$	log pre-exponential factor
65	$CH + H_2O \rightarrow CH_2O + H$	log pre-exponential factor
66	$CH_2 + NO \rightarrow H + HNCO$	log pre-exponential factor
67	$N + O_2 \rightarrow NO + O$	log pre-exponential factor
68	$N + OH \rightarrow NO + H$	log pre-exponential factor
69	$N_2O + H \rightarrow N_2 + OH$	log pre-exponential factor
70	$NH + H \rightarrow H_2 + N$	log pre-exponential factor
71	$NH + NO \rightarrow N_2O + H$	log pre-exponential factor
72	$CH_3 + N \rightarrow H_2CN + H$	log pre-exponential factor
73	$N + NO \rightarrow N_2 + O$	log pre-exponential factor
74	$NH + O \rightarrow NO + H$	log pre-exponential factor
75	$HCN + O \rightarrow NCO + H$	log pre-exponential factor
76	$H + H + H_2O \rightarrow H_2 + H_2O$	log pre-exponential factor
77	$CN + OH \rightarrow NCO + H$	log pre-exponential factor
78	$CN + H_2 \rightarrow HCN + H$	log pre-exponential factor
79	HCN	enthalpy of formation at 298K
80	$OH + OH \rightarrow H_2O + O$	log pre-exponential factor
81	$CN + H_2O \rightarrow HCN + OH$	log pre-exponential factor
82	$HCN + OH \rightarrow HOCN + H$	log pre-exponential factor
83	$NCO + O \rightarrow NO + CO$	log pre-exponential factor
84	$NCO + OH \rightarrow NO + H + CO$	log pre-exponential factor

Table A.2 (continued)

Index	Reaction/Species	Parameter type
85	$NCO + NO \rightarrow N_2O + CO$	log pre-exponential factor
86	$NCO + NO \rightarrow N_2 + CO_2$	log pre-exponential factor
87	$CH_2(S) + O_2 \rightarrow H_2O + CO$	log pre-exponential factor
88	$OCH_2(S) + H_2O \rightarrow CH_2 + H_2O$	log pre-exponential factor
89	$CH + N_2 \rightarrow HCN + N$	log pre-exponential factor
90	$O + C_2H_6 \rightarrow C_2H_5 + OH$	log pre-exponential factor
91	$H + C_2H_5 \rightarrow H_2 + C_2H_4$	log pre-exponential factor
92	$OH + C_2H_4 \rightarrow H_2O + C_2H_3$	log pre-exponential factor
93	$CH_2 + NO \rightarrow OH + HCN$	log pre-exponential factor
94	$CH_3 + NO \rightarrow HCN + H_2O$	log pre-exponential factor
95	$HCNO + H \rightarrow H + HNCO$	log pre-exponential factor
96	$HCNO + H \rightarrow OH + HCN$	log pre-exponential factor
97	$HCCO + O_2 \rightarrow OH + CO + CO$	log pre-exponential factor
98	$NH_2 + O \rightarrow H + HNO$	log pre-exponential factor
99	$NH_2 + H \rightarrow H_2 + NH$	log pre-exponential factor
100	$H + NO + M \rightarrow HNO + M$	log pre-exponential factor
101	$HNO + H \rightarrow H_2 + NO$	log pre-exponential factor
102	$HCCO + NO \rightarrow HCNO + CO$	log pre-exponential factor

Appendix B

Syngas Combustion Datasets

Table B.1: The initial syngas combustion mechanism and associated reaction rate constants [110], $k = AT^n \exp(-E_a/T)$ in units of cm^3, mol, s, and K.

Index	Reaction	A	n	E_a
1	$H_2 + O_2 \rightarrow OH + OH$	2.4E+13	0.47	35121
2	$H + H (+Ar) \rightarrow H_2 (+Ar)$	6.53E+17	-1	0
	$H + H (+H_2) \rightarrow H_2 (+H_2)$	1.0E+17	-0.6	0
	$H + H (+N_2) \rightarrow H_2 (+N_2)$	5.4E+18	-1.3	0
	$H + H (+H_2O) \rightarrow H_2 (+H_2O)$	1.00E+19	-1	0
	$H + H (+H) \rightarrow H_2 (+H)$	3.2E+15	0	0
	$H + H (+M) \rightarrow H_2 (+M)$	7.47E+17	-1	0
	Collider efficiency: CO_2=3.75, CO=1.875, He=0.87	—	—	—
3	$H_2 + O \rightarrow OH + H$	3.82E+12	0	4000
	$H_2 + O \rightarrow OH + H$	8.79E+14	0	9650
4	$H_2 + OH \rightarrow H_2O + H$	2.16E+08	1.52	1740
5	$OH + OH (+H_2O) \rightarrow H_2O_2 (+H_2O)$[1]	1.59E+13	0	0
	Low-pressure limit	1.45E+18	0	0
	$OH + OH (+M) \rightarrow H_2O_2 (+M)$[1]	1.59E+13	0	0
	Low-pressure limit	2.4E+19	-0.8	0
	Collider efficiency: H_2=2.5, CO=1.875, CO_2=3.75, Ar=0.875	—	—	—
6	$O_2 + H \rightarrow OH + O$	1.9E+14	-0.097	7560
7	$O_2 + H (+He) \rightarrow HO_2 (+He)$[2]	4.66E+12	0.44	0
	Low-pressure limit	6.13E+18	-1.2	0
	$O_2 + H (+Ar) \rightarrow HO_2 (+Ar)$[2]	4.66E+12	0.44	0

[1]Tore parameters: $a = 1$, $T^{***} = 1$, $T^* = 1$, $T^{**} = 243$
[2]Tore parameters: $a = 0.5$, $T^{***} = 1E - 30$, $T^* = 1E + 30$

Table B.1 (continued)

Index	Reaction	A	n	E_a
	Low-pressure limit	7.43E+18	-1.2	0
	$O_2 + H$ $(+O_2) \rightarrow HO_2$ $(+O_2)$[2]	4.66E+12	0.44	0
	Low-pressure limit	5.69E+18	-1.09	0
	$O_2 + H$ $(+N_2) \rightarrow HO_2$ $(+N_2)$[2]	4.66E+12	0.44	0
	Low-pressure limit	1.75E+19	-1.23	0
	$O_2 + H$ $(+H_2O) \rightarrow HO_2$ $(+H_2O)$[1]	4.66E+12	0.44	0
	Low-pressure limit	3.67E+19	-1	0
	$O_2 + H$ $(+M) \rightarrow HO_2$ $(+M)$[2]	4.66E+12	0.44	0
	Low-pressure limit	1.75E+19	-1.23	0
	Collider efficiency: H_2=1.5, CO_2=1.06	—	—	—
8	$O + O$ $(+M) \rightarrow O_2$ $(+M)$	5.4E+13	0	-899.69
	Collider efficiency: H_2=2.5, H_2O=16.25, Ar=0.87, He=0.87, CO=1.875, CO_2=3.75	—	—	—
9	$OH + H$ $(+Ar) \rightarrow H_2O$ $(+Ar)$[2]	2.511E+13	0.234	-57.5
	Low-pressure limit	3.114E+20	-1.53	185
	$OH + H$ $(+M) \rightarrow H_2O$ $(+M)$[2]	2.511E+13	0.234	-57.5
	Low-pressure limit	4.533E+21	-1.81	251
	Collider efficiency: H_2=2.5, H_2O=16.25, He=0.87, CO=1.875, CO_2=3.75	—	—	—
10	$H + O$ $(+M) \rightarrow OH$ $(+M)$	7.73E+18	-1	0
	Collider efficiency: H_2=2.5, H_2O=16.25, Ar=0.87, He=0.87, CO=1.875, CO_2=3.75	—	—	—
11	$HO_2 + H \rightarrow H_2 + O_2$	2E+14	0	1030
12	$HO_2 + H \rightarrow OH + OH$	4E+14	0	700
13	$HO_2 + H \rightarrow H_2O + O$	1.44E+12	0	0
14	$H_2O_2 + H \rightarrow H_2 + HO_2$	1.69E+12	0	1889.58
15	$H_2O_2 + H \rightarrow OH + H_2O$	1.02E+13	0	1800.58
16	$OH + OH \rightarrow H_2O + O$	3.35E+04	2.42	-970
17	$HO_2 + OH \rightarrow H_2O + O_2$	9.27E+15	0	8810
	$HO_2 + OH \rightarrow H_2O + O_2$	2.89E+13	0	-250
18	$OH + H_2O_2 \rightarrow HO_2 + H_2O$	1.64E+18	0	14800
	$OH + H_2O_2 \rightarrow HO_2 + H_2O$	1.93E+12	0	215
19	$HO_2 + O \rightarrow OH + O_2$	1.63E+13	0	-224
20	$O + H_2O_2 \rightarrow OH + HO_2$	8.43E+11	0	2000
21	$HO_2 + HO_2 \rightarrow H_2O_2 + O_2$	4.22E+14	0	6030.79
	$HO_2 + HO_2 \rightarrow H_2O_2 + O_2$	1.32E+11	0	-820.3
22	$CO + O_2 \rightarrow CO_2 + O$	1.26E+13	0	23682.94
23	$CO + OH \rightarrow CO_2 + H$	1.01E+13	0	8050
	$CO + OH \rightarrow CO_2 + H$	9.03E+13	0	2300

[1]Tore parameters: $a = 0.6$, $T^{***} = 1E - 30$, $T^* = 1E + 30$
[2]Tore parameters: $a = 0.72$, $T^{***} = 1E + 33$, $T^* = 1E + 33$

Table B.1 (continued)

Index	Reaction	A	n	E_a
	$CO + OH \rightarrow CO_2 + H$	1.01E+11	0	30
24	$CO + O (+M) \rightarrow CO_2 (+M)$	1.362E+10	0	1242
	Low-pressure limit	1.173E+24	-2.79	2095
	Collider efficiency: H_2=2, H_2O=12, Ar=0.7, He=0.7, CO=1.75, CO_2=3.6	—	—	—
25	$CO + HO_2 \rightarrow CO_2 + OH$	1.15E+05	2.28	8775
26	$HCO + O_2 \rightarrow CO + HO_2$	1.35E+10	0.68	-236
27	$HCO + O_2 \rightarrow OH + CO_2$	1.35E+10	0.68	-236
28	$HCO + H \rightarrow CO + H_2$	9E+13	0	0
29	$HCO + O \rightarrow CO + OH$	3.01E+13	0	0
30	$HCO + O \rightarrow CO2 + H$	3.01E+13	0	0
31	$HCO + OH \rightarrow CO + H_2O$	1.02E+14	0	0
32	$HCO + HO_2 \rightarrow OH + CO_2 + H$	3E+13	0	0
33	$HCO (+M) \rightarrow CO + H (+M)$	4.75E+11	0.66	7485
	Collider efficiency: H_2=2.5, H_2O=16.25, Ar=0.87, He=0.87, CO=1.87, CO_2=3.75	—	—	—
34	$HCCO + O_2 \rightarrow CO_2 + CO + H$	1.4E+09	1	0
35	$HCCO + O_2 \rightarrow CO + CO + OH$	1.63E+12	0	430.6
36	$HCCO + O_2 \rightarrow HCO + CO + O$	1.63E+12	0	430
37	$HCCO + OH \rightarrow HCO + HCO$	1E+13	0	0
38	$HCCO + O \rightarrow CO + CO + H$	9.64E+13	0	0
39	$CH + O_2 \rightarrow CO + OH$	1.66E+13	0	0
40	$CH + O_2 \rightarrow CO_2 + H$	1.66E+13	0	0
41	$CH + CO \rightarrow HCCO$	2.77E+11	0	-860
42	$CH + CO_2 \rightarrow HCO + CO$	3.43E+12	0	345.2
43	$CH + O \rightarrow CO + H$	3.97E+13	0	0
44	$CH + OH \rightarrow H + HCO$	3E+13	0	0
45	$O + H (+M) \rightarrow OH^* (+M)$	1.5E+13	0	25
	Collider efficiency: H_2=1, H_2O=6.5, O_2=0.4, Ar=0.35, N_2=0.4, CO=0.75, CO_2=1.5	—	—	—
46	$CH + O_2 \rightarrow OH^* + CO$	1.8E+11	0	0
47	$OH^* \rightarrow OH$	1.45E+06	0	0
48	$OH^* + O_2 \rightarrow OH + O_2$	2.1E+12	0.5	-242.96
49	$OH^* + H_2O \rightarrow OH + H_2O$	5.93E+12	0.5	-434.21
50	$OH^* + H_2 \rightarrow OH + H_2$	2.95E+12	0.5	-223.72
51	$OH^* + CO_2 \rightarrow OH + CO_2$	2.76E+12	0.5	-488.33
52	$OH^* + CO \rightarrow OH + CO$	3.23E+12	0.5	-396.92
53	$OH^* + OH \rightarrow OH + OH$	6.01E+12	0.5	-383.69
54	$OH^* + H \rightarrow OH + H$	1.31E+13	0.5	-84.2
55	$OH^* + Ar \rightarrow OH + Ar$	1.69E+12	0	2083.23

Table B.2: Prior uncertainty range of the reaction rate multipliers [110].

Index	Reaction	Lower bound	Upper bound
1	$H_2 + O_2 \rightarrow OH + OH$	0.1	10
2	$H + H \rightarrow H_2$	0.32	3.16
3	$H_2 + O \rightarrow OH + H$	0.63	1.58
4	$H_2 + OH \rightarrow H_2O + H$	0.65	1.63
5	$OH + OH \rightarrow H_2O_2$	0.5	2
6	$O_2 + H \rightarrow OH + O$	0.8	1.26
7	$O_2 + H \rightarrow HO_2$	0.85	1.15
8	$O + O \rightarrow O_2$	0.77	1.13
9	$OH + H \rightarrow H_2O$	0.8	1.2
10	$H + O \rightarrow OH$	0.2	5
11	$HO_2 + H \rightarrow H_2 + O_2$	0.5	2
12	$HO_2 + H \rightarrow OH + OH$	0.7	1.4
13	$HO_2 + H \rightarrow H_2O + O$	0.32	3.16
14	$H_2O_2 + H \rightarrow H_2 + HO_2$	0.32	3.16
15	$H_2O_2 + H \rightarrow OH + H_2O$	0.5	2
16	$OH + OH \rightarrow H_2O + O$	0.7	1.4
17	$HO_2 + OH \rightarrow H_2O + O_2$	0.32	3.16
18	$OH + H_2O_2 \rightarrow HO_2 + H_2O$	0.5	2
19	$HO_2 + O \rightarrow OH + O_2$	0.32	3.16
20	$O + H_2O_2 \rightarrow OH + HO_2$	0.5	2
21	$HO_2 + HO_2 \rightarrow H_2O_2 + O_2$	0.4	2.5
22	$CO + O_2 \rightarrow CO_2 + O$	0.2	5
23	$CO + OH \rightarrow CO_2 + H$	0.8	1.26
24	$CO + O \rightarrow CO_2$	0.5	2
25	$CO + HO_2 \rightarrow CO_2 + OH$	0.32	3.16
26	$HCO + O_2 \rightarrow CO + HO_2$	0.4	2.5
27	$HCO + O_2 \rightarrow OH + CO_2$	0.4	2.5
28	$HCO + H \rightarrow CO + H_2$	0.5	2
29	$HCO + O \rightarrow CO + OH$	0.5	2
30	$HCO + O \rightarrow CO2 + H$	0.5	2
31	$HCO + OH \rightarrow CO + H_2O$	0.5	2
32	$HCO + HO_2 \rightarrow OH + CO_2 + H$	0.2	5
33	$HCO \rightarrow CO + H$	0.5	2
34	$HCCO + O_2 \rightarrow CO_2 + CO + H$	0.5	2
35	$HCCO + O_2 \rightarrow CO + CO + OH$	0.2	5
36	$HCCO + O_2 \rightarrow HCO + CO + O$	0.2	5
37	$HCCO + OH \rightarrow HCO + HCO$	0.5	2

Table B.2 (continued)

Index	Reaction	Lower bound	Upper bound
38	$HCCO + O \rightarrow CO + CO + H$	0.5	2
39	$CH + O_2 \rightarrow CO + OH$	0.32	3.16
40	$CH + O_2 \rightarrow CO_2 + H$	0.32	3.16
41	$CH + CO \rightarrow HCCO$	0.8	1.25
42	$CH + CO_2 \rightarrow HCO + CO$	0.8	1.25
43	$CH + O \rightarrow CO + H$	0.32	3.16
44	$CH + OH \rightarrow H + HCO$	0.8	1.25
45	$O + H \rightarrow OH^*$	0.5	2
46	$CH + O_2 \rightarrow OH^* + CO$	0.5	2
47	$OH^* \rightarrow OH$	0.5	2
48	$OH^* + O_2 \rightarrow OH + O_2$	0.5	2
49	$OH^* + H_2O \rightarrow OH + H_2O$	0.5	2
50	$OH^* + H_2 \rightarrow OH + H_2$	0.5	2
51	$OH^* + CO_2 \rightarrow OH + CO_2$	0.5	2
52	$OH^* + CO \rightarrow OH + CO$	0.5	2
53	$OH^* + OH \rightarrow OH + OH$	0.5	2
54	$OH^* + H \rightarrow OH + H$	0.5	2
55	$OH^* + Ar \rightarrow OH + Ar$	0.5	2

Table B.3: List of ignition delay time quantities of interest and their estimated uncertainty. T_5 and P_5 are the initial temperature and pressure behind the reflected shock wave [110].

T_5 (K)	P_5 (MPa)	t_{ign} (μs)	PrIMe ID	Uncertainty (%)
916	0.11	1812	a00000179	50
954	0.12	462	a00000181	35
993	0.10	175	a00000183	30
1074	0.11	65	a00000186	30
1151	0.10	64	a00000188	30
914	0.11	2277	a00000105	50
951	0.11	687	a00000131	40
996	0.11	181	a00000132	35
1072	0.11	87	a00000133	30
1175	0.10	55	a00000135	30
1187	0.10	39	a00000136	30
1241	0.10	29	a00000107	30
900	0.06	2935	a00000110	50

Table B.3 (continued)

T_5 (K)	P_5 (MPa)	t_{ign} (μs)	PrIMe ID	Uncertainty (%)
1026	0.11	153	a00000111	30
1162	0.10	57	a00000112	30
936	0.12	1331	a00000113	40
1015	0.11	219	a00000189	30
1183	0.11	63	a00000190	30
929	0.26	2593	a00000191	50
992	0.26	1015	a00000192	40
1058	0.26	108	a00000114	30
1063	0.31	120	a00000193	30
1015	1.39	2278	a00000213	50
1114	1.51	638	a00000194	35
1190	1.70	82	a00000115	35
960	0.12	1307	a00000116	40
1052	0.11	274	a00000195	30
1197	0.11	101	a00000196	30
981	0.27	2284	a00000197	50
1048	0.25	236	a00000198	30
1118	0.25	94	a00000117	30
1063	1.45	1695	a00000199	40
1126	1.20	472	a00000200	35
1265	1.73	25	a00000118	30
968	0.12	1167	a00000307	40
1033	2.40	1760	a00000317	35
1148	2.17	380	a00000318	35
909	0.119	1900	a00000322	40
933	0.116	660	a00000323	40
947	0.121	560	a00000324	35
932	0.14	1169	a00000223	40
956	0.14	878	a00000224	35
965	0.15	629	a00000225	35
1046	1.70	4340	a00000226	30
1072	1.60	2660	a00000227	30
1132	1.64	986	a00000228	35
1107	1.64	3970	a00000229	30
1159	1.64	1350	a00000230	30
1206	1.66	588	a00000231	35
1165	1.63	3900	a00000232	30
1207	1.66	1730	a00000233	30
1259	1.61	630	a00000234	30

Table B.3 (continued)

T_5 (K)	P_5 (MPa)	t_{ign} (μs)	PrIMe ID	Uncertainty (%)
1019	1.43	3430	a00000235	30
1051	1.55	1810	a00000236	30
1097	1.58	692	a00000237	35
1048	1.62	3210	a00000238	30
1086	1.57	1310	a00000239	30
1128	1.57	374	a00000240	30
1054	1.58	3960	a00000241	30
1090	1.60	1850	a00000242	30
1140	1.61	448	a00000243	30
1057	0.11	317	a00000308	30
1263	0.11	87	a00000309	30
977	0.23	1654	a00000310	40
1149	0.20	102	a00000311	30
1304	0.17	54	a00000312	30
1110	1.29	944	a00000313	40
943	2.26	3430	a00000316	35
1299	1.22	48.8	a00000334	25
1182	1.22	93.6	a00000335	25
1096	1.22	1796.8	a00000336	30
1383	1.22	41.1	a00000337	25
1235	1.22	86.2	a00000338	25
1099	1.22	1060.8	a00000339	30
1387	1.22	83	a00000340	25
1228	1.22	191.9	a00000341	25
1116	1.22	1450.1	a00000342	35
1264	3.24	61.4	a00000343	30
1243	3.24	139.5	a00000344	30
1185	3.24	938.2	a00000345	35
1325	3.24	32.1	a00000346	30
1204	3.24	552.9	a00000347	35
1179	3.24	864.3	a00000348	35
1327	3.24	76.4	a00000349	30
1259	3.24	180.1	a00000350	30
1166	3.24	1493.8	a00000351	40
1695	0.16	51.8	a00000352	30
1351	0.16	183.9	a00000353	30
980	0.16	1467.7	a00000354	40
2004	0.16	40.2	a00000355	25
1273	0.16	311.5	a00000356	25

Table B.3 (continued)

T_5 (K)	P_5 (MPa)	t_{ign} (μs)	PrIMe ID	Uncertainty (%)
992	0.16	1640.7	a00000357	35
1975	0.16	115.4	a00000358	25
1436	0.16	296.1	a00000359	25
1027	0.16	1726	a00000360	35
996	10	5854.1	a00000510	51
1062	10	1143.6	a00000511	86
940	5	8499.6	a00000512	55
1042	5	1432.4	a00000513	90
968	15	7357	a00000514	74
1037	15	2169.5	a00000515	74
998	1.6	1444.7	a00000489	50
1146	1.6	477.37	a00000490	30
1786	1.6	71.81	a00000493	30
1397	12.5	28.544	a00000498	30
1284	12.5	48.121	a00000499	30
1100	12.5	973.24	a00000500	30
1299	32	37.8	a00000501	30
1186	32	500.37	a00000502	30
1883	1.6	55.99	a00000503	30
1008	1.6	1347.4	a00000504	50
1360	12.5	42.39	a00000505	30
1122	12.5	701.53	a00000506	30
1291	32	51.447	a00000507	30
1233	32	253.23	a00000508	30
1150	32	1459	a00000509	30
981	1.24	1360	a00000491	20
1065	1.3	182	a00000492	20
1135	1.19	83	a00000494	20
975	1.72	1720	a00000495	20
999	1.8	951	a00000496	20
1048	1.7	199	a00000497	20

Table B.4: List of laminar flame speed quantities of interest and their estimated uncertainty [110]. T_0, P_0 and ϕ are the initial temperature, pressure and equivalence ratio of the mixture.

T_0 (K)	P_0 (MPa)	ϕ	Flame speed (cm/s)	PrIMe ID	Uncertainty (%)
300	0.10	0.8	80	a00000128	10
300	0.10	1.2	151	a00000129	10
300	0.10	2.5	162	a00000130	15
300	0.51	2.0	60	a00000249	15
300	1.01	0.75	20	a00000250	15
300	1.01	1.4	47	a00000252	15
300	2.03	1.0	29	a00000253	20
300	4.05	1.4	32	a00000257	20
300	0.51	3.5	80.3	a00000124	25
300	1.01	1.0	100	a00000125	15
300	1.01	1.8	150	a00000126	15
300	1.01	3.5	42	a00000127	20
700	0.10	0.7	350	a00000282	10
700	0.10	0.9	450	a00000280	10
300	0.10	1.0	32	a00000260	10
300	0.10	1.5	47	a00000261	10
300	0.05	1.0	34	a00000269	10
300	0.10	0.6	20	a00000271	10
300	2.03	1.6	41.3	x00000460	20
300	2.03	3.0	20	x00000460	25
300	4.05	2.0	28	x00000461	25
600	1.52	0.6	60	x00000471	20
600	1.52	0.6	80	a00000471	20
298	0.51	0.7	32.1	a00000516	10
298	0.30	1.0	13.7	a00000517	10
298	0.91	0.6	32	a00000518	10
298	1.01	0.5	11.1	a00000519	15
295	0.10	0.6	35.5	a00000520	10
295	0.10	1.4	102	a00000521	10
295	0.10	1.0	73	a00000522	10
400	0.10	1.2	240	a00000523	10
298	0.10	1.2	87.21	a00000524	10
298	0.10	2.0	49.12	a00000525	12
298	0.10	0.6	20.83	a00000526	10
298	0.10	0.6	205.3	a00000527	10
298	0.10	1.2	144.86	a00000528	10
298	0.10	2.0	253.35	a00000529	10

Table B.4 (continued)

T_0 (K)	P_0 (MPa)	ϕ	Flame speed (cm/s)	PrIMe ID	Uncertainty (%)
298	0.10	1.2	160.5	a00000530	10
298	0.10	0.6	48.31	a00000531	10
373	0.10	2.5	238	a00000532	15
373	0.10	2.0	184.4	a00000533	15
373	0.10	1.2	138.4	a00000534	10
373	0.10	1.25	80.3	a00000535	10
373	0.51	1.2	105.4	a00000536	15
298	0.10	0.5	22.7	a00000537	10

Table B.5: The initial syngas combustion mechanism and associated reaction rate constants [110], $k = AT^n \exp(-E_a/T)$ in units of cm^3, mol, s, and K.

Index	Reaction	A	n	E_a
1	$H_2 + O_2 \rightarrow OH + OH$	2.4E+13	0.47	35121
2	$H + H$ (+Ar) $\rightarrow H_2$ (+Ar)	6.53E+17	-1	0
	$H + H$ (+H_2) $\rightarrow H_2$ (+H_2)	1.0E+17	-0.6	0
	$H + H$ (+N_2) $\rightarrow H_2$ (+N_2)	5.4E+18	-1.3	0
	$H + H$ (+H_2O) $\rightarrow H_2$ (+H_2O)	1.00E+19	-1	0
	$H + H$ (+H) $\rightarrow H_2$ (+H)	3.2E+15	0	0
	$H + H$ (+M) $\rightarrow H_2$ (+M)	7.47E+17	-1	0
	Collider efficiency: CO_2=3.75, CO=1.875, He=0.87	—	—	—
3	$H_2 + O \rightarrow OH + H$	3.82E+12	0	4000
	$H_2 + O \rightarrow OH + H$	8.79E+14	0	9650
4	$H_2 + OH \rightarrow H_2O + H$	2.16E+08	1.52	1740
5	$OH + OH$ (+H_2O)$\rightarrow H_2O_2$ (+H_2O)[1]	1.59E+13	0	0
	Low-pressure limit	1.45E+18	0	0
	$OH + OH$ (+M)$\rightarrow H_2O_2$ (+M)[1]	1.59E+13	0	0
	Low-pressure limit	2.4E+19	-0.8	0
	Collider efficiency: H_2=2.5, CO=1.875, CO_2=3.75, Ar=0.875	—	—	—
6	$O_2 + H \rightarrow OH + O$	1.9E+14	-0.097	7560
7	$O_2 + H$ (+He) $\rightarrow HO_2$ (+He)[2]	4.66E+12	0.44	0
	Low-pressure limit	6.13E+18	-1.2	0
	$O_2 + H$ (+Ar) $\rightarrow HO_2$ (+Ar)[2]	4.66E+12	0.44	0

[1]Tore parameters: $a = 1$, $T^{***} = 1$, $T^{*} = 1$, $T^{**} = 243$

[2]Tore parameters: $a = 0.5$, $T^{***} = 1E - 30$, $T^{*} = 1E + 30$

Table B.5 (continued)

Index	Reaction	A	n	E_a
	Low-pressure limit	7.43E+18	-1.2	0
	O_2 + H (+O_2) → HO_2 (+O_2)[2]	4.66E+12	0.44	0
	Low-pressure limit	5.69E+18	-1.09	0
	O_2 + H (+N_2) → HO_2 (+N_2)[2]	4.66E+12	0.44	0
	Low-pressure limit	1.75E+19	-1.23	0
	O_2 + H (+H_2O) → HO_2 (+H_2O)[1]	4.66E+12	0.44	0
	Low-pressure limit	3.67E+19	-1	0
	O_2 + H (+M) → HO_2 (+M)[2]	4.66E+12	0.44	0
	Low-pressure limit	1.75E+19	-1.23	0
	Collider efficiency: H_2=1.5, CO_2=1.06	—	—	—
8	O + O (+M) → O_2 (+M)	5.4E+13	0	-899.69
	Collider efficiency: H_2=2.5, H_2O=16.25, Ar=0.87, He=0.87, CO=1.875, CO_2=3.75	—	—	—
9	OH + H (+Ar) → H_2O (+Ar)[2]	2.511E+13	0.234	-57.5
	Low-pressure limit	3.114E+20	-1.51	185
	OH + H (+M) → H_2O (+M)[2]	2.511E+13	0.234	-57.5
	Low-pressure limit	4.533E+21	-1.81	251
	Collider efficiency: H_2=2.5, H_2O=16.25, He=0.87, CO=1.875, CO_2=3.75	—	—	—
10	H + O (+M) → OH (+M)	7.73E+18	-1	0
	Collider efficiency: H_2=2.5, H_2O=16.25, Ar=0.87, He=0.87, CO=1.875, CO_2=3.75	—	—	—
11	HO_2 + H → H_2 + O_2	2E+14	0	1030
12	HO_2 + H → OH + OH	4E+14	0	700
13	HO_2 + H → H_2O + O	1.44E+12	0	0
14	H_2O_2 + H → H_2 + HO_2	1.69E+12	0	1889.58
15	H_2O_2 + H → OH + H_2O	1.02E+13	0	1800.58
16	OH + OH → H_2O + O	3.35E+04	2.42	-970
17	HO_2 + OH → H_2O + O_2	9.27E+15	0	8810
	HO_2 + OH → H_2O + O_2	2.89E+13	0	-250
18	OH + H_2O_2 → HO_2 + H_2O	1.64E+18	0	14800
	OH + H_2O_2 → HO_2 + H_2O	1.93E+12	0	215
19	HO_2 + O → OH + O_2	1.63E+13	0	-224
20	O + H_2O_2 → OH + HO_2	8.43E+11	0	2000
21	HO_2 + HO_2 → H_2O_2 + O_2	4.22E+14	0	6030.79
	HO_2 + HO_2 → H_2O_2 + O_2	1.32E+11	0	-820.3
22	CO + O_2 → CO_2+ O	1.26E+13	0	23682.94
23	CO + OH → CO_2 + H	1.01E+13	0	8050
	CO + OH → CO_2 + H	9.03E+13	0	2300

[1]Tore parameters: $a = 0.6$, $T^{***} = 1E - 30$, $T^{*} = 1E + 30$
[2]Tore parameters: $a = 0.72$, $T^{***} = 1E + 33$, $T^{*} = 1E + 33$

Table B.5 (continued)

Index	Reaction	A	n	E_a
	$CO + OH \rightarrow CO_2 + H$	1.01E+11	0	30
24	$CO + O\ (+M) \rightarrow CO_2\ (+M)$	1.362E+10	0	1242
	Low-pressure limit	1.173E+24	-2.79	2095
	Collider efficiency: H_2=2, H_2O=12, Ar=0.7, He=0.7, CO=1.75, CO_2=3.6	—	—	—
25	$CO + HO_2 \rightarrow CO_2 + OH$	1.15E+05	2.28	8775
26	$HCO + O_2 \rightarrow CO + HO_2$	2.5E+10	0.68	-236
27	$HCO + O_2 \rightarrow OH + CO_2$	2E+09	0.68	-236
28	$HCO + H \rightarrow CO + H_2$	9E+13	0	0
29	$HCO + O \rightarrow CO + OH$	3.01E+13	0	0
30	$HCO + O \rightarrow CO2 + H$	3.01E+13	0	0
31	$HCO + OH \rightarrow CO + H_2O$	1.02E+14	0	0
32	$HCO + HO_2 \rightarrow OH + CO_2 + H$	3E+13	0	0
33	$HCO\ (+M) \rightarrow CO + H\ (+M)$	4.75E+11	0.66	7485
	Collider efficiency: H_2=2.5, H_2O=16.25, Ar=0.87, He=0.87, CO=1.87, CO_2=3.75	—	—	—
34	$HCCO + O_2 \rightarrow CO_2 + CO + H$	4.78E+12	-0.142	575
35	$HCCO + O_2 \rightarrow CO + CO + OH$	1.91E+11	-0.02	511
36	$HCCO + O_2 \rightarrow HCO + CO + O$	2.18E+02	2.692	1770
37	$HCCO + OH \rightarrow HCO + HCO$	1E+13	0	0
38	$HCCO + O \rightarrow CO + CO + H$	9.64E+13	0	0
39	$CH + O_2 \rightarrow CO + OH$	1.66E+13	0	0
40	$CH + O_2 \rightarrow CO_2 + H$	1.66E+13	0	0
41	$CH + CO \rightarrow HCCO$	2.77E+11	0	-860
42	$CH + CO_2 \rightarrow HCO + CO$	3.43E+12	0	345.2
43	$CH + O \rightarrow CO + H$	3.97E+13	0	0
44	$CH + OH \rightarrow H + HCO$	3E+13	0	0
45	$O + H\ (+M) \rightarrow OH^*\ (+M)$	1.5E+13	0	3007.5
	Collider efficiency: H_2=1, H_2O=6.5, O_2=0.4, Ar=0.35, N_2=0.4, CO=0.75, CO_2=1.5	—	—	—
46	$CH + O_2 \rightarrow OH^* + CO$	1.8E+11	0	0
47	$OH^* \rightarrow OH$	1.45E+06	0	0
48	$OH^* + O_2 \rightarrow OH + O_2$	2.1E+12	0.5	-242.96
49	$OH^* + H_2O \rightarrow OH + H_2O$	5.93E+12	0.5	-434.21
50	$OH^* + H_2 \rightarrow OH + H_2$	2.95E+12	0.5	-223.72
51	$OH^* + CO_2 \rightarrow OH + CO_2$	2.76E+12	0.5	-488.33
52	$OH^* + CO \rightarrow OH + CO$	3.23E+12	0.5	-396.92
53	$OH^* + OH \rightarrow OH + OH$	6.01E+12	0.5	-383.69
54	$OH^* + H \rightarrow OH + H$	1.31E+13	0.5	-84.2
55	$OH^* + Ar \rightarrow OH + Ar$	1.69E+12	0	2083.23

Table B.6: Prior uncertainty range of the reaction rate multipliers[110].

Index	Reaction	Lower bound	Upper bound
1	$H_2 + O_2 \rightarrow OH + OH$	0.1	10
2	$H + H \rightarrow H_2$	0.32	3.16
3	$H_2 + O \rightarrow OH + H$	0.63	1.58
4	$H_2 + OH \rightarrow H_2O + H$	0.65	1.63
5	$OH + OH \rightarrow H_2O_2$	0.5	2
6	$O_2 + H \rightarrow OH + O$	0.8	1.26
7	$O_2 + H \rightarrow HO_2$	0.85	1.15
8	$O + O \rightarrow O_2$	0.77	1.13
9	$OH + H \rightarrow H_2O$	0.8	1.2
10	$H + O \rightarrow OH$	0.2	5
11	$HO_2 + H \rightarrow H_2 + O_2$	0.5	2
12	$HO_2 + H \rightarrow OH + OH$	0.7	1.4
13	$HO_2 + H \rightarrow H_2O + O$	0.32	3.16
14	$H_2O_2 + H \rightarrow H_2 + HO_2$	0.32	3.16
15	$H_2O_2 + H \rightarrow OH + H_2O$	0.5	2
16	$OH + OH \rightarrow H_2O + O$	0.7	1.4
17	$HO_2 + OH \rightarrow H_2O + O_2$	0.32	3.16
18	$OH + H_2O_2 \rightarrow HO_2 + H_2O$	0.5	2
19	$HO_2 + O \rightarrow OH + O_2$	0.32	3.16
20	$O + H_2O_2 \rightarrow OH + HO_2$	0.5	2
21	$HO_2 + HO_2 \rightarrow H_2O_2 + O_2$	0.4	2.5
22	$CO + O_2 \rightarrow CO_2 + O$	0.2	5
23	$CO + OH \rightarrow CO_2 + H$	0.8	1.26
24	$CO + O \rightarrow CO_2$	0.32	3.16
25	$CO + HO_2 \rightarrow CO_2 + OH$	0.32	3.16
26	$HCO + O_2 \rightarrow CO + HO_2$	0.6	1.65
27	$HCO + O_2 \rightarrow OH + CO_2$	0.6	1.65
28	$HCO + H \rightarrow CO + H_2$	0.5	2
29	$HCO + O \rightarrow CO + OH$	0.5	2
30	$HCO + O \rightarrow CO2 + H$	0.5	2
31	$HCO + OH \rightarrow CO + H_2O$	0.5	2
32	$HCO + HO_2 \rightarrow OH + CO_2 + H$	0.2	5
33	$HCO \rightarrow CO + H$	0.5	2
34	$HCCO + O_2 \rightarrow CO_2 + CO + H$	0.5	2
35	$HCCO + O_2 \rightarrow CO + CO + OH$	0.5	2
36	$HCCO + O_2 \rightarrow HCO + CO + O$	0.5	2
37	$HCCO + OH \rightarrow HCO + HCO$	0.5	2

Table B.6 (continued)

Index	Reaction	Lower bound	Upper bound
38	$HCCO + O \rightarrow CO + CO + H$	0.5	2
39	$CH + O_2 \rightarrow CO + OH$	0.32	3.16
40	$CH + O_2 \rightarrow CO_2 + H$	0.32	3.16
41	$CH + CO \rightarrow HCCO$	0.8	1.25
42	$CH + CO_2 \rightarrow HCO + CO$	0.8	1.25
43	$CH + O \rightarrow CO + H$	0.32	3.16
44	$CH + OH \rightarrow H + HCO$	0.8	1.25
45	$O + H \rightarrow OH^*$	0.5	2
46	$CH + O_2 \rightarrow OH^* + CO$	0.5	2
47	$OH^* \rightarrow OH$	0.5	2
48	$OH^* + O_2 \rightarrow OH + O_2$	0.5	2
49	$OH^* + H_2O \rightarrow OH + H_2O$	0.5	2
50	$OH^* + H_2 \rightarrow OH + H_2$	0.5	2
51	$OH^* + CO_2 \rightarrow OH + CO_2$	0.5	2
52	$OH^* + CO \rightarrow OH + CO$	0.5	2
53	$OH^* + OH \rightarrow OH + OH$	0.5	2
54	$OH^* + H \rightarrow OH + H$	0.5	2
55	$OH^* + Ar \rightarrow OH + Ar$	0.5	2

Appendix C

The MATLAB Toolbox

The framework of Bound-to-Bound Data Collaboration (B2BDC) and the methods developed in previous Chapters are implemented in computer programs. MATLAB is selected as the programming language considering its comprehensive list of well maintained toolboxes relevant to our applications. The collection of all the relevant codes is referred to as the B2BDC toolbox hereafter and can be found using the Github link `https://github.com/B2BDC/`. In this appendix, we introduce the main objects and functions of the B2BDC toolbox. A class diagram of the toolbox is given in Figure C.1 for illustration. As the toolbox is developed using object-oriented programming style, the following sections are ordered by different objects in the toolbox.

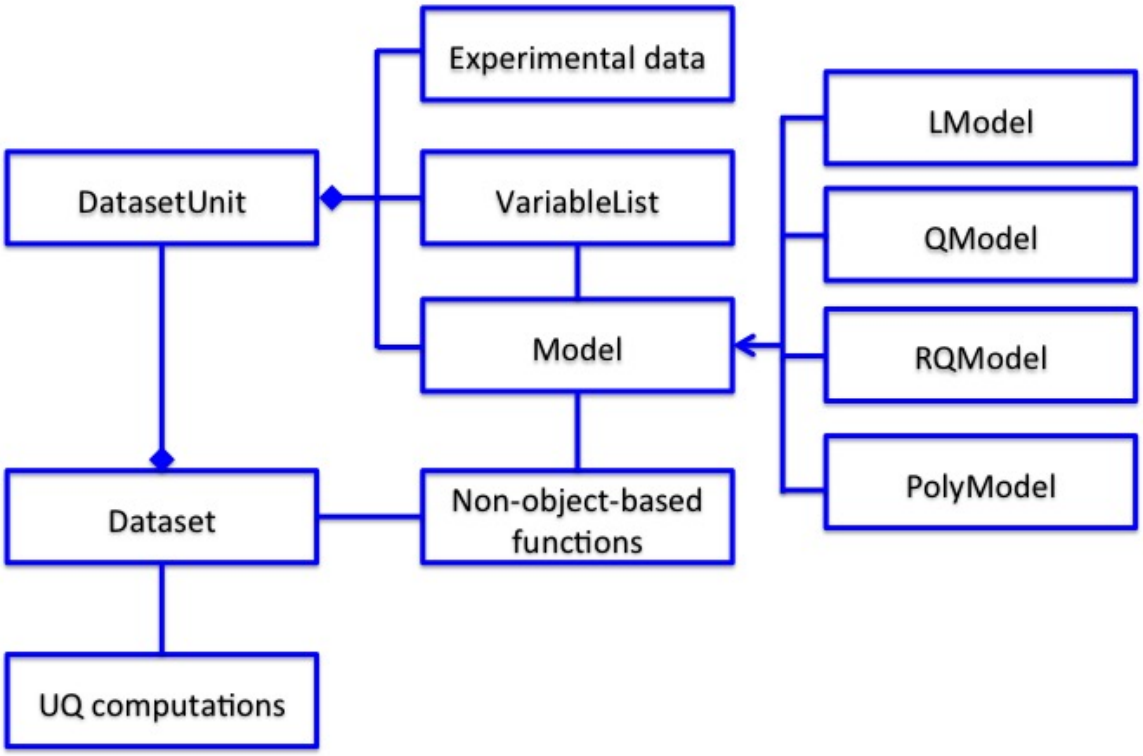

Figure C.1: The class diagram of the B2BDC toolbox.

B2BDC.B2Bvariables.ModelVariable

This object represents a single parameter.

Properties

- NominalValue: the nominal value of the parameter.
- LowerBound: the lower uncertainty bound of the parameter.
- UpperBound: the upper uncertainty bound of the parameter.
- Name: the name of the parameter.

B2BDC.B2Bvariables.VariableList

This object represents a list of parameters.

Properties

- ExtraLinConstraint: save the information of linear constraints of the parameter vector in addition to the specified interval uncertainty of each individual parameter.
- Length: the number of parameters in the list.
- Value: the array of B2BDC.B2Bvariables.ModelVariable objects.

Functions

newobj = addList(obj, varList)

Input:

- obj: a B2BDC.B2Bvariables.VariableList object.
- varList: a B2BDC.B2Bvariables.VariableList object.

Output:

- newobj: a B2BDC.B2Bvariables.VariableList object.

Cases:

- newobj = addList(obj,varList) adds the variable list saved in varList to the variable list saved in obj and returns the extended variable list as newobj. If any parameters are in common between obj and varList, the intersection of their respective uncertainties is used in the extended parameter list.

xSample = makeDesignSample(obj, nSample, method)

Input:

- obj: B2BDC.B2Bvariables.VariableList object.
- nSample: number of design points you want to generate.

- method: a character array specifying the approach using which the samples are generated ('lhs', 'sobol', or 'uniform', case insensitive).

Output:

- xSample: a 2-D array containing the design points (each row corresponds to a design point).

Cases:

- xSample = makeDesignSample(obj, nSample, method) generates nSample i.i.d (independently and identically distributed) samples using the approach specified by method.
- xSample = makeDesignSample(obj, nSample) generates nSample i.i.d samples using the latin hypercube design approach.

newobj = deleteVariable(obj, varIdx)

Input:

- obj: B2BDC.B2Bvariables.VariableList object.
- varIdx: a character array or a scalar.

Output:

- newobj: B2BDC.B2Bvariables.VariableList object.

Cases:

- newobj = deleteVariable(obj, varIdx) removes the variable specified by varIdx in the variable list specified by obj. The new variable list is returned as newobj.

varBD = calBound(obj)

Input:

- obj: B2BDC.B2Bvariables.VariableList object.

Output:

- varBD: a 2-D numerical array.

Cases:

- varBD = calBound(obj) returns the prior interval uncertainty of each individual variable as a 2-D array varBD. The first and second columns of varBD are the lower and upper bounds, respectively.

varOB = calNominal(obj)

Input:

- obj: B2BDC.B2Bvariables.VariableList object.

Output:

- varOB - a 1-D column array.

Cases:

- varOB = calBound(obj) returns the nominal value of each individual variable as a 1-D column array varOB.

newobj = changeBound(obj, newBD, idx)

Input:

- obj: B2BDC.B2Bvariables.VariableList object.
- newBD: a 2-D numerical array.
- idx: a 1-D cell array or a 1-D numerical array.

Output:

- newobj: B2BDC.B2Bvariables.VariableList object

Cases:

- newobj = changeBound(obj, newBD, idx) updates the uncertainty bounds (if newBD has two columns) and the nominal values (if newBD has three columns and the last column corresponds to the new nominal value) in obj and returns the updated variable list as newobj. The variables updated are specified by the input idx, a cell array of the variable names or a numerical array of the positions of the variables in the list.
- newobj = changeBound(obj, newBD) updates the uncertainty bounds (if newBD has two columns) and the nominal values (if newBD has three columns and the last column corresponds to the new nominal value) of all variables in obj and returns the updated variable list as newobj.

newVar = addLinearConstraint(obj, A, b, c)

Input:

- obj: B2BDC.B2Bvariables.VariableList object.
- A: a 2-D numerical array.
- b: a 1-D numerical array.
- c: a 1-D numerical array.

Output:

- newVar: B2BDC.B2Bvariables.VariableList object.

Cases:

- newVar = addLinearConstraint(obj,A,b) adds linear constraints to the variables such that Ax¡=b. Since the constraints are saved as LB¡=Ax¡=UB in the object, the corresponding lower bounds are calculated by solving a linear programming.
- newVar = addLinearConstraint(obj,A,b,c) adds linear constraints to the variables such that b¡=Ax¡=c.

newVar = makeSubset(obj, varIdx)

Input:

- obj: B2BDC.B2Bvariables.VariableList object.
- varIdx: a 1-D cell array or 1-D numerical array.

Output:

- newVar: B2BDC.B2Bvariables.VariableList object

Cases:

- newVar = makeSubset(obj,varIdx) generates a new variable list that contains a subset of the original variable list. The subset is specified by the names contained in the cell array varIdx or by the index contained in the numerical array varIdx.

xNew = changeCoordinate(obj, xOld, newVList)

Input:

- obj: B2BDC.B2Bvariables.VariableList object.
- xOld: a 2-D numerical array.
- newVList: B2BDC.B2Bvariables.VariableList object.

Output:

- xNew: a 2-D numerical array.

Cases:

- xNew = changeCoordinate(obj,xOld,newVList) creates a new 2D numerical array xNew, whose corresponding parameter values are assigned from the input xOld for those overlapped between the two variable lists. Parameters not overlapped are assigned to zeros.

B2BDC.B2Bmodels.Model

This object represents the abstract prototype of any models used in B2BDC.

Properties

- Variables: a B2BDC.B2Bvariables.VariableList object contains the parameters of the model.
- ErrorStats: a strcuture array contains the estimated fitting error, if relevant, of the surrogate model.

- VarRanges: a 2-D numerical array contains the prior uncertainty interval of the parameters.
- VarNames: a 1-D cell array contains the names of the parameters.

Functions

y = eval(obj,X,varObj)

Input:

- obj: B2BDC.B2Bmodels.Model object.
- X: a 2-D numerical array.
- varObj: B2BDC.B2Bvariables.VariableList object.

Output:

- y: a 1-D column array.

Cases:

- y = eval(obj, X) evaluates the model output at input design points specified by X. Each row of X corresponds to a design point.
- y = eval(obj, X, varObj) evaluates the model output at input design points specified by X and varObj. Each row of X corresponds to a design point. The column of X is specified by the given input varObj.

B2BDC.B2Bmodels.LModel

This object represents a linear surrogate model. It is a subclass of B2BDC.B2Bmodels.Model object.

Properties

- CoefVec: a 1-D column array contains the coefficient of the linear model.

B2BDC.B2Bmodels.QModel

This object represents a quadratic surrogate model. It is a subclass of B2BDC.B2Bmodels.Model object.

Properties

- CoefMatrix: a 2-D symmetric array contains the coefficient of the quadratic model.
- Hessian: a 2-D symmetric array contains the Hessian of the quadratic model.

Functions

pModel = convertToPoly(obj)

Input:

- obj: B2BDC.B2Bmodels.QModel object.

Output:

- pModel: B2BDC.B2Bmodels.PolyModel object.

Cases:

- pModel = convertToPoly(obj) converts a B2BDC.B2Bmodels.QModel object to a B2BDC.B2Bmodels object.

B2BDC.B2Bmodels.RQModel

This object represents a rational quadratic surrogate model. It is a subclass of B2BDC.B2Bmodels.Mode object.

Properties

- Numerator: a 2-D symmetric array contains the coefficient of the numerator quadratic of the model.
- Denominator: a 2-D symmetric array contains the coefficient of the denominator quadratic of the model.
- K: the regulatory constant for the denominator.

B2BDC.B2Bmodels.PolyModel

This object represents a general polynomial surrogate model. It is a subclass of B2BDC.B2Bmodels.Mod object.

Properties

- SupportMatrix: a 2-D array contains the list of monomials. Each row corresponds to a monomial: its coefficient specifies the order of the corresponding parameter in the monomial.
- Coefficient: a 1-D column array contains the coefficient of each monomial in the polynomial model.
- Degree: the degree of the polynomial model.

Functions

sparsePoly = createSparsePOP(obj, flag)

Input:

- obj: B2BDC.B2Bmodels.PolyModel object.
- flag: a numerical scalar.

Output:

- sparsePoly: a structure array.

Cases:

- sparsePoly = createSparsePOP(obj) creates a structure array that is compatible for sparsePOP toolbox. The input obj corresponds to an inequality or objective polynomial.
- sparsePoly = createSparsePOP(obj, flag) creates a structure array that is compatible for sparsePOP toolbox. The input obj corresponds to an inequality constraint or objective polynomial if flag is 1 and corresponds to an equality constraint polynomial otherwise.

newPoly = expandDimension(obj, newVar)

Input:

- obj: B2BDC.B2Bmodels.PolyModel object.
- newVar: B2BDC.B2Bvariables.VariableList object.

Output:

- newPoly: B2BDC.B2Bmodels.PolyModel object.

Cases:

- newPoly = expandDimension(obj, newVar) replaces the variable list in obj by the input newVar.

B2BDC.B2Bdataset.DatasetUnit

This object represents a dataset unit of B2BDC.

Properties

- Name: a character array contains the name of the dataset unit.
- LowerBound: a scalar specifies the lower bound of the dataset unit.
- ObservedValue: a scalar specifies the nominal value of the dataset unit.
- UpperBound: a scalar specifies the upper bound of the dataset unit.
- SurrogateModel: a B2BDC.B2Bmodels.Model object contains the surrogate model of the dataset unit.
- VariableList: a B2BDC.B2Bvariables.VariableList object that contains the parameters of the surrogate model.
- ScenarioParameter: a structure array contains the scenario parameter information.

Functions

y = changeBounds(obj, newbd)

Input:

- obj: B2BDC.B2Bdataset.DatasetUnit object.
- newbd: a 1-D numerical array.

Output:

- y: B2BDC.B2Bdataset.DatasetUnit object.

Cases:

- y = changeBounds(obj, newbd) changes the lower and upper bounds of the dataset unit if newbd has 2 elements; it changes the lower and upper bound, as well as the nominal value if newbd has 3 elements.

newOBJ = setScenarioParameter(oldOBJ, sv, sname)

Input:

- obj: B2BDC.B2Bdataset.DatasetUnit object.
- sv: a 1-D numerical array.
- sname: a 1-D cell array.

Output:

- newOBJ: B2BDC.B2Bdataset.DatasetUnit object.

Cases:

- newOBJ = setScenarioParameter(oldOBJ, sv, sname) sets the scenario parameter of the dataset unit. The values and names of the scenario parameters are specified by sv and sname, respectively.

y = eval(obj,x, varObj)

Input:

- obj: B2BDC.B2Bdataset.DatasetUnit object.
- x: a 2-D numerical array.
- varObj: B2BDC.B2Bvariables.VariableList object.

Output:

- y: a 1-D column array.

Cases:

- y = eval(obj, x) evaluates the model output at input design points specified by X. Each row of X corresponds to a design point.
- y = eval(obj, x, varObj) evaluates the model output at input design points specified by X and varObj. Each row of X corresponds to a design point. The column of X is specified by the given input varObj.

B2BDC.B2Bdataset.DatasetUnitList

This object represents a list of dataset units.

Properties

- Length: a scalar specifies the length of the list.
- Values: a 1-D array of B2BDC.B2Bdataset.DatasetUnit objects.

B2BDC.B2Bdataset.Dataset

This object represents a B2BDC dataset.

Properties

- Name: a character array specifies the name of the dataset.
- DatasetUnits: a B2BDC.B2Bdataset.DatasetUnitList object contains the list of dataset units.
- Variables: a B2BDC.B2Bvariables.VariableList object specifies the parameter list of the dataset.
- FeasiblePoint: a 1-D column array contains a feasible point if there exists one returned from consistency measure calculation.
- Length: a scalar specifies the number of QOIs in the dataset.
- VarNames: a cell array contains the name of the parameters.
- QOINames: a cell array contains the name of the QOIs.
- ConsistencyMeasure: a 1-D numerical array contains the scalar consistency measure.
- ConsistencySensitivity: a structure array contains the sensitivity of the scalar consistency measure with respect to parameter and QOI uncertainty bounds.
- ModelDiscrepancy: a structure array contains the information related to the considered model discrepancy.
- FeasibleFlag: a logical scalar indicates whether the fitting error is included in the analysis.
- ModelDiscrepancyFlag: a logical scalar indicates whether model discrepancy is considered in the analysis.

Functions

addDSunit(obj, dsUnitObj)

Input:

- obj: B2BDC.B2Bdataset.Dataset object.
- dsUnitObj: B2BDC.B2Bdataset.DatasetUnit object.

Cases:

- addDSunit(obj, dsUnitObj) adds a dataset unit, specified by the input dsUnitObj, to the dataset.

y = isConsistent(obj, opt)

Input:

- obj: B2BDC.B2Bdataset.Dataset object.
- opt: B2BDC.Option.Option object.

Output:

- y: a logical scalar.

Cases:

- y = isConsistent(obj, opt) calculates the scalar consistency measure of the dataset with user-specified option opt, and returns dataset consistency in y.
- y = isConsistent(obj) calculates the scalar consistency measure of the dataset with the default option, and returns dataset consistency in y.

deletedUnits = deleteUnit(obj, id)

Input:

- obj: B2BDC.B2Bdataset.Dataset object.
- id: a 1-D column cell array or 1-D column numerical array.

Output:

- deletedUnits: a 1-D B2BDC.B2Bdataset.DatasetUnit array.

Cases:

- deletedUnits = deleteUnit(obj, id) removes the QOIs specified by the input id from the dataset and retures these QOIs in deletedUnits.

changeBound(obj, newBD, idx)

Input:

- obj: B2BDC.B2Bdataset.Dataset object.
- newBD: a 2-D numerical array with 2 or 3 columns.
- idx: a 1-D cell array or 1-D numerical array.

Cases:

- changeBound(obj, newBD) updates the QOI uncertainty bounds by the input newBD. If newBD has 2 columns, they correspond to the lower and upper uncertainty bounds; if newBD has 3 columns, the third column corresponds to the nominal value.
- changeBound(obj, newBD, idx) updates the uncertainty bounds of the QOIs specified by input idx. If newBD has 2 columns, they correspond to the lower and upper uncertainty bounds; if newBD has 3 columns, the third column corresponds to the nominal value.

changeVarBound(obj, newBD, idx)

Input:

- obj: B2BDC.B2Bdataset.Dataset object.
- newBD: a 2-D numerical array with 2 or 3 columns.
- idx: a 1-D cell array or 1-D numerical array.

Cases:

- changeVarBound(obj, newBD) updates the parameter uncertainty bounds by the input newBD. If newBD has 2 columns, they correspond to the lower and upper uncertainty bounds; if newBD has 3 columns, the third column corresponds to the nominal value.
- changeVarBound(obj, newBD, idx) updates the uncertainty bounds of the parameters specified by input idx. If newBD has 2 columns, they correspond to the lower and upper uncertainty bounds; if newBD has 3 columns, the third column corresponds to the nominal value.

[units, unitIdx] = findDSunit(obj, unitName)

Input:

- obj: B2BDC.B2Bdataset.Dataset object.
- unitName: a 1-D column cell array.

Output:

- units: a B2BDC.B2Bdataset.DatasetUnit array.
- unitIdx: a 1-D numerical array.

Cases:

- [units, unitIdx] = findDSunit(obj, unitName) finds the target QOIs specified by unitName in the dataset. The dataset units are returned in units and their indices returned in unitIdx.

dsNew = clone(obj)

Input:

- obj: B2BDC.B2Bdataset.Dataset object.

Output:

- dsNew: B2BDC.B2Bdataset.Dataset object.

Cases:

- dsNew = clone(obj) makes a copy of the dataset object and returns it as dsNew.

bounds = calBound(obj)

Input:

- obj: B2BDC.B2Bdataset.Dataset object.

Output:

- bounds: a 2-D numerical array.

Cases:

- bounds = calBound(obj) calculates the QOI uncertainty bounds.

observes = calObserve(obj)

Input:

- obj: B2BDC.B2Bdataset.Dataset object.

Output:

- observes: a 1-D column array.

Cases:

- observes = calObserve(obj) calculates the measured QOI values.

y = eval(obj, X, DSIdx)

Input:

- obj: B2BDC.B2Bdataset.Dataset object.
- X: a 2-D numerical array.
- DSIdx: a 1-D column cell array or 1-D column numerical array.

Output:

- y: a 2-D numerical array.

Cases:

- y = eval(obj, X) evaluates all QOI outputs at input design points specified by X. Each row of X corresponds to a design point. Each column of y corresponds to a QOI.
- y = eval(obj, X, DSIdx) evaluates some QOI outputs, specified by DSIdx, at input design points specified by X. Each row of X corresponds to a design point. Each column of y corresponds to a QOI.

clearConsis(obj)

Input:

- obj: B2BDC.B2Bdataset.Dataset object.

Cases:

- clearConsis(obj) clears consistency-related properties of the dataset.

clearModelDiscrepancy(obj)

Input:

- obj: B2BDC.B2Bdataset.Dataset object.

Cases:

- clearModelDiscrepancy(obj) clears discrepancy-related properties of the dataset.

[sv, sname] = getScenarioParameter(obj)

Input:

- obj: B2BDC.B2Bdataset.Dataset object.

Output:

- sv: a 2-D numerical array.
- sname: a 1-D cell array.

Cases:

- [sv, sname] = getScenarioParameter(obj) calculates the scenario-parameter values and names of the dataset.

clearFeasiblePoint(obj)

Input:

- obj: B2BDC.B2Bdataset.Dataset object.

Cases:

- clearFeasiblePoint(obj) clears the saved feasible point.

makeSubset(obj, idx)

Input:

- obj: B2BDC.B2Bdataset.Dataset object.
- idx: a 1-D column cell array or 1-D column numerical array.

Cases:

- makeSubset(obj, idx) updates the dataset by keeping only the QOIs specified by input idx.

[isFeas, xFea] = isFeasiblePoint(obj, point, addError)

Input:

- obj: B2BDC.B2Bdataset.Dataset object.
- point: a 2-D numerical array.
- addError: a logical scalar.

Output:

- isFeas: a 1-D logical array.
- xFea: a 2-D numerical array.

Cases:

- [isFeas, xFea] = isFeasiblePoint(ds, point) returns a logical array isFeas corresponds to whether the input point is feasible or not. Each row of point corresponds to a parameter vector of the dataset. The subset of feasible points are returned in xFea.
- [isFeas, xFea] = isFeasiblePoint(ds, point, addError) returns a logical array corresponds to whether the input point is feasible or not. Each row of point corresponds to a parameter vector of the dataset. The estimation includes fitting error if addError is true. The subset of feasible points are returned in xFea.

[vcReport, EXITFLAG] = vectorConsistency(dsObj, wY, wX, opt)

Input:

- dsObj: B2BDC.B2Bdataset.Dataset object.
- wY: a 2-D numerical array or a character array.
- wX: a 2-D numerical array or a character array.
- opt: a B2BDC.Option.Option object.

Output:

- vcReport: a structure array.
- EXITFLAG: a numerical scalar.

Cases:

- [vcReport, EXITFLAG] = vectorConsistency(dsObj, wY, wX) calculates the vector consistency measure of the dataset. When wY and wX are 2-column numerical arrays, they specify the weights associated with QOI and parameter uncertainty bounds, respectively. When they are charracter arrays, they specify certain types of weights: 'perc' for percentage weights; 'uwidth' for uncertanty width weights; 'unit' for unit weights and 'null' for zero weights. In this case, the option variable is the default B2BDC.Option.Option object. The vector consistency measure results are stored in vcRport whereas EXITFLAG indicates the solution status of the inner bound from fmincon.
- [vcReport, EXITFLAG] = vectorConsistency(dsObj, wY, wX, opt) calculates the vector consistency measure of the dataset. When wY and wX are 2-column numerical arrays, they specify the weights associated with QOI and parameter uncertainty bounds, respectively. When they are charracter arrays, they specify certain types of weights:

'perc' for percentage weights; 'uwidth' for uncertanty width weights; 'unit' for unit weights and 'null' for zero weights. In this case, the option variable is specified by opt. The vector consistency measure results are stored in vcRport whereas EXITFLAG indicates the solution status of the inner bound from fmincon.

[QOIrange, QOISensitivity, xOpt] = predictQOI(obj, QOIobj, B2Bopt, QOIcorrection)

Input:

- obj: B2BDC.B2Bdataset.Dataset object.
- QOIobj: B2BDC.B2Bmodels.Model object.
- B2Bopt: B2BDC.Option.Option object.
- QOIcorrection: a structure array.

Output:

- QOIrange: a structure array.
- QOISensitivity: a structure array.
- xOpt: a structure array.

Cases:

- [QOIrange, QOISensitivity, xOpt] = predictQOI(obj, QOIobj, B2Bopt) predicts the uncertainty interval of the QOI specified by QOIobj using the dataset obj. The option variable is specified by B2Bopt. The calculated uncertainty interval, sensitivity, and optimal points for the inner bounds, are saved in QOIrange, QOISensitivity, and xOpt, respectively.
- [QOIrange, QOISensitivity, xOpt] = predictQOI(obj, QOIobj, B2Bopt, QOIcorrection) predicts the uncertainty interval of the QOI specified by QOIobj using the dataset obj. Model discrepancy is considered in the analysis and the corresponding information of the QOI is specified by QOIcorrection. The option variable is specified by B2Bopt. The calculated uncertainty interval, sensitivity, and optimal points for the inner bounds, are saved in QOIrange, QOISensitivity and xOpt, respectively.

dsUnitList = checkSelfConsistency(obj, opt)

Input:

- obj: B2BDC.B2Bdataset.Dataset object.
- opt: B2BDC.Option.Option object.

Output:

- dsUnitList: a B2BDC.B2Bdataset.DatasetUnit array.

Cases:

- dsUnitList = checkSelfConsistency(obj) calculates self-inconsistent dataset units in the dataset. The option variable is the default B2BDC option object.
- dsUnitList = checkSelfConsistency(obj,opt) calculates self-inconsistent dataset units in the dataset. The option variable is specified by the input opt.

xPos = calVarBounds(obj, index, opt)

Input:

- obj: B2BDC.B2Bdataset.Dataset object.
- index: a 1-D cell array or 1-D numerical array.
- opt: B2BDC.Option.Option object.

Output:

- xPos: a 2-D numerical array.

Cases:

- xPos = calVarBounds(obj) calculates the posterior uncertainty bound of all parameters. The option variable is set to be the default B2BDC option.
- xPos = calVarBounds(obj, index) calculates the posterior uncertainty bound of the parameters specified by index. The option variable is set to be the default B2BDC option.
- xPos = calVarBounds(obj, index, opt) calculates the posterior uncertainty bound of the parameters specified by index. The option variable is specified by opt.

qoiPos = calQOIBounds(obj, index, opt)

Input:

- obj: B2BDC.B2Bdataset.Dataset object.
- index: a 1-D cell array or 1-D numerical array.
- opt: B2BDC.Option.Option object.

Output:

- qoiPos: a 2-D numerical array.

Cases:

- qoiPos = calQOIBounds(obj) calculates the posterior uncertainty bound of all QOIs in the dataset. The option variable is set to be the default B2BDC option.
- qoiPos = calQOIBounds(obj, index) calculates the posterior uncertainty bound of the QOIs specified by index. The option variable is set to be the default B2BDC option.
- qoiPos = calQOIBounds(obj, index, opt) calculates the posterior uncertainty bound of the QOIs specified by index. The option variable is specified by opt.

addScenarioParameter(obj, Svalue, Sname)

Input:

- obj: B2BDC.B2Bdataset.Dataset object.
- Svalue: a 2-D numerical array.
- Sname: a 1-D cell array.

Cases:

- addScenarioParameter(obj,Svalue,Sname) adds the input scenario parameters to the dataset. The values and names of the scenario parameters are specified by the input Svalue and Sname, respectively.

changeScenarioParameter(obj, Svalue, Sname, QOIindex)

Input:

- obj: B2BDC.B2Bdataset.Dataset object.
- Svalue: a 2-D numerical array.
- Sname: a 1-D cell array.
- QOIindex: a 1-D numerical array.

Cases:

- changeScenarioParameter(obj,Svalue,Sname) updates the values of existing scenario parameters in the dataset for all QOIs. The values and names of the scenario parameters are specified by the input Svalue and Sname, respectively.
- changeScenarioParameter(obj,Svalue,Sname,QOIindex) updates the values of existing scenario parameters in the dataset for QOIs specified by QOIindex. The values and names of the scenario parameters are specified by the input Svalue and Sname, respectively.

clearScenarioParameter(obj)

Input:

- obj: B2BDC.B2Bdataset.Dataset object.

Cases:

- clearScenarioParameter(obj) clears all existing scenario parameters in the dataset.

setModelDiscrepancy(obj, QOIindex, fMD, Range)

Input:

- obj: B2BDC.B2Bdataset.Dataset object.
- QOIindex: a 1-D numerical array or a 1-D cell array.
- fMD: a function handle or a 1-D cell array.
- Range: a numerical scalar or a 1-D numerical array.

Cases:

- setModelDiscrepancy(obj, QOIindex, fMD) sets the discrepancy-function, specified by fMD, to the QOIs specified by QOIindex. If QOIindex and fMD are cell arrays, they correspond to different QOI groups. In this case, the discrepancy-function coefficients have a default prior uncertainty range of [-10 10].
- setModelDiscrepancy(obj, QOIindex, fMD, Range) sets the discrepancy-function, specified by fMD, to the QOIs specified by QOIindex. If QOIindex and fMD are cell arrays, they correspond to different QOI groups. In this case, the prior uncertainty range of discrepancy-function coefficients is specified by Range.

[xSample, status] = collectSample(obj, N, x0, opt)

Input:

- obj: B2BDC.B2Bdataset.Dataset object.
- N: a numerical scalar.
- x0: a 1-D numerical array.
- opt: B2BDC.Option.Option object.

Output:

- xSample: a structure array.
- status: a structure array.

Cases:

- [xSample,status] = collectSample(obj, N) computes uniformly distributed samples from the (joint) feasible set. The samples and associated sampler information are saved in xSample and status, respectively. In this case, the chain starts at the SCM point and the option variable is the default B2BDC option.
- [xSample, status] = collectSample(obj, N, x0) computes uniformly distributed samples from the (joint) feasible set. The samples and associated sampler information are saved in xSample and status, respectively. In this case, the option variable is the default B2BDC option.

- [xSample, status] = collectSample(obj, N, x0, opt) computes uniformly distributed samples from the (joint) feasible set. The samples and associated sampler information are saved in xSample and status, respectively. In this case, the option variable is specified by opt.

[xopt, yopt] = optimize_Parameter(obj, logFlag, weight,opt)

Input:

- obj: B2BDC.B2Bdataset.Dataset object.
- logFlag: a 1-D logical array or an empty array.
- weight: a 1-D numerical array.
- opt: B2BDC.Option.Option object.

Output:

- xopt: a 1-D numerical array.
- yopt: a numerical scalar.

Cases:

- [xopt, yopt] = optimize_Parameter(obj, logFlag, weight) calculates an optimized parameter vector based on a specified criteria. The logFlag indicates whether the response surface of the corresponding QOI is in the log scale. The minimized object function is specified by the option variable and the weights asscoiated with individual terms in the object function is specified by weight. In this case, the option variable is the default B2BDC option. The calculated optimal parameter vector and minimized object value are saved in xopt and yopt.
- [xopt, yopt] = optimize_Parameter(obj, logFlag, weight, opt) calculates an optimized parameter vector based on a specified criteria. The logFlag indicates whether the response surface of the corresponding QOI is in the log scale. The minimized object function is specified by the option variable and the weights asscoiated with individual terms in the object function is specified by weight. In this case, the option variable is specified by opt. The calculated optimal parameter vector and minimized object value are saved in xopt and yopt.

B2BDC.Option.Option

This object represents a general B2BDC option variable.

Properties

- ConsistencyMeasure: a character array, 'relative' or 'absolute', indicates which scalar consistency measure is calculated.
- ExtraLinFraction: a scalar between 1 to 100 indicates the percentage of extra quadratic inequalities generated by combining two linear inequalities, or -1 indicates that extra quadratic inequalities whose influence factor are greater than 5% of the most influential quadratic inequality are included.
- Display: a logical scalar indicates whether to show the computation details during the process.
- AddFitError: a logical scalar indicates whether to inlcude fitting error in the calculation.
- Prediction: a character array, 'inner', 'outer', or 'both', specifying which uncertainty bounds to calculate.
- SampleOption: a B2BDC.Option.SampleOption object contains optional information related to sampling.
- POPOption: a B2BDC.Option.POPOption object contains optional information related to polynomial optimization.
- OptimOption: a B2BDC.Option.OptimOption object contains optional information related to optimized parameter vector calculation.

B2BDC.Option.SampleOption

This object represents a B2BDC option variable related to sampling.

Properties

- SampleMethod: a character array, 'Gibbs', 'HR', 'AM', or 'CWAM', indicates which sampler to use.
- StepInterval: a numerical scalar specifies the thinning parameter, i.e., the number of samples that are discarded between two returning sampled points.

- WarmStart: a structure array specifies the recorded sampling information related to the AM sampler.

B2BDC.Option.POPOption

This object represents a B2BDC option variable related to polynomial optimization.

Properties

- relaxOrder: a numerical scalar specifies the relaxation order.
- sparseSW: a numerical scalar indicates the relaxation type: 1 - use sparse relaxation; 0 - use dense relaxation; 2 - use a smaller dense relaxation; 3 - use a smaller sparse relaxation.
- perturbation: a numerical scalar, typically very small such as 10^{-5}, that is added to the objective polynomial.
- SDPsolver: a character array specifies the name of the SDP solver.
- printFileName: a numerical scalar or a character array for how to print the solution information: 0 - save no solution information; 1 - save solution information; a character array of the file name - print the solution in the file.
- printLevel: a numerical array contains 2 elements, [a, b], where a and b specifies what information to be saved in the result and in the file, respectively: 0 - no information on the computational result; 1 - some information without an optimal solution; 2 - detailed solution information.
- POPsolver: a character array specifies the solver used for computing the inner bound.
- mex: a numerical scalar indicates whether to use C++ subroutines (1) or not (0).

B2BDC.Option.OptimOption

This object represents a B2BDC option variable related to optimizing parameter vectors.

Properties

- OptimizationMethod: a character array, 'LSF', 'LSH', or '1NF', specifies the type of the optimization framework.

- PenaltyWeight: a character array, 'relative', 'absolute', or 'user-defined', specifies the type of the weight.
- RandomStart: a numerical scalar specifies the number of starting points.
- Logtype: a character array, 'nature' or 'log10', specifies the type of the log scale.

Appendix D

B2BDC Application: GRI-Mech

Application of Bound-to-Bound Data Collaboration (B2BDC) to a realistic problem typically includes dataset construction, dataset consistency determination, dataset inconsistency resolution if encountered and uncertainty quantification for a consistent dataset. The process is abstractly summarized in Figure D.1.

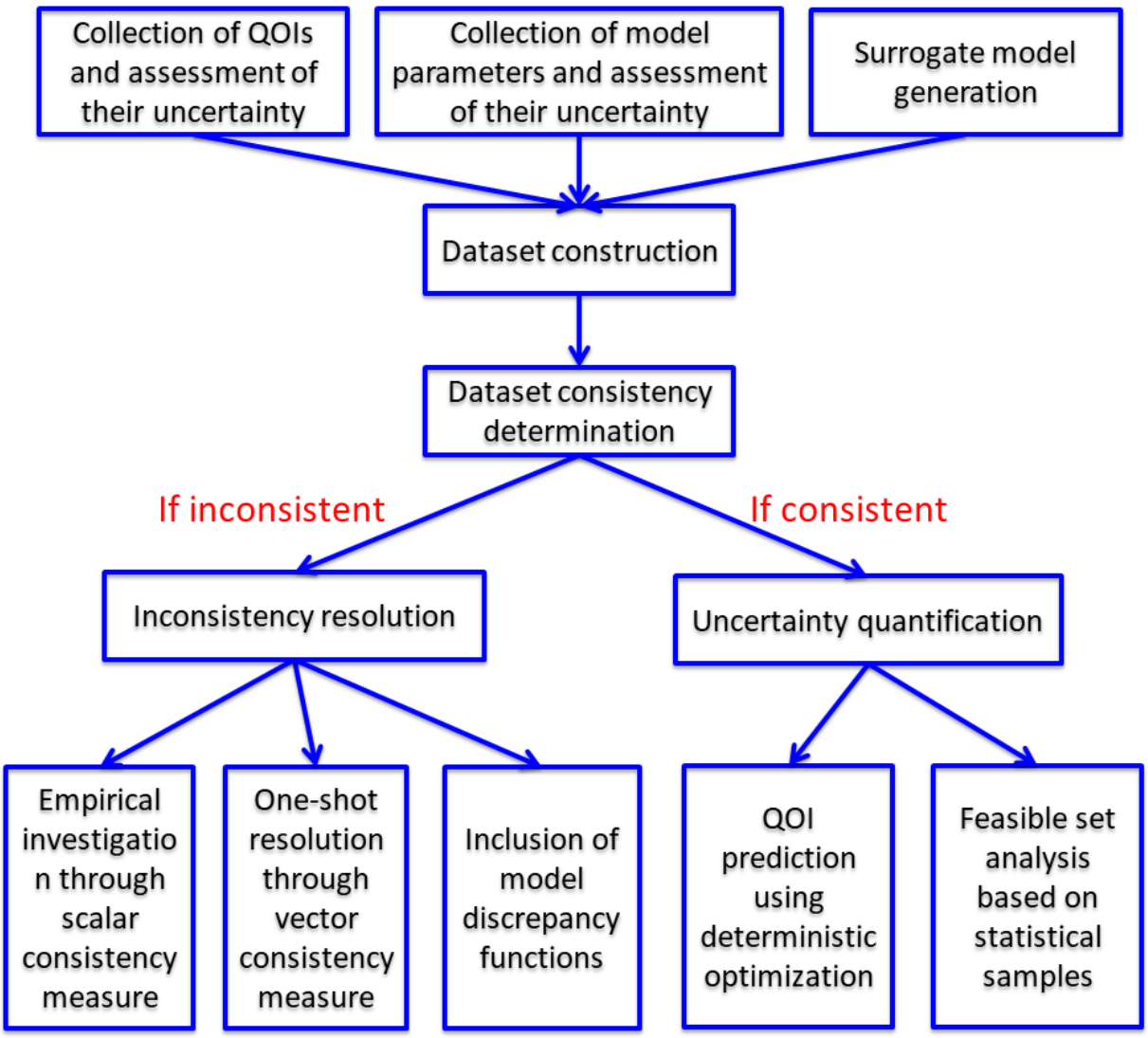

Figure D.1: Procedures of application of Bound-to-Bound Data Collaboration to engineering problems.

The MATLAB source codes used to generate the results presented in Section 2.8 are given as follows. The 'data.mat' file can be found at `https://github.com/B2BDC/B2BDC/tree/master/GRIexample`.

```
% B2BDC example: GRI-Mech 3.0
% In this example file, we assume the QOIs and the model parameters are
% given with their assessed uncertainty, as well as the quadratic surrogate
% models for simulating the QOIs
%% set a seed number
rng(1);
%% load data
load('GRI_data.mat');
QOINames = data.QOINames;  % a 77-by-1 cell array containing the name of ...
    the QOIs
VariableNames = data.VariableNames;  % a 102-by-1 cell array containing ...
    the name of the model parameters
QOIInfo = data.QOIInfo;  % a 77-by-3 numerical array containing the lower ...
    and upper bounds, and the measured value of the QOIs
VariableInfo = data.VariableInfo;  % a 77-by-3 numerical array containing ...
    the lower and upper bounds, and the measured value of the QOIs
ModelCoefficients = data.ModelCoefficients;  % a 77-by-1 cell array ...
    containing the coefficient matrix of the quadratic surrogate model for ...
    the QOIs
ActiveVariables = data.ActiveVariables;  % a 77-by-1 cell array containing ...
    the indices of the active variable for the QOIs
%% dataset construction
dsGRI = generateDataset('GRI-Mech 3.0');  % create a ...
    B2BDC.B2Bdataset.Dataset object
variable_list_GRI = ...
    generateVar(VariableNames,VariableInfo(:,1:2),VariableInfo(:,3));  % ...
    create the B2BDC.B2Bvariables.VariableList object containing all 102 ...
    model parameters
nQOI = 77;
for i = 1:nQOI
   CoefMatrix = ModelCoefficients{i};
   active_variable_id = ActiveVariables{i};
   variable_list_current_QOI = ...
       variable_list_GRI.makeSubset(active_variable_id);  % create the ...
       B2BDC.B2Bvariables.VariableList object containing active variables ...
       for the current QOI
   model_current_QOI = ...
       generateModel(CoefMatrix,variable_list_current_QOI);  % create the ...
       B2BDC.B2Bmodel.QModel object for the current QOI
   datasetunit_current_QOI = ...
       generateDSunit(QOINames{i},model_current_QOI,QOIInfo(i,1:2),QOIInfo(i,3)); ...
        % create the B2BDC.B2Bdataset.DatasetUnit object for the current QOI
   dsGRI.addDSunit(datasetunit_current_QOI);  % add the dataset unit to ...
       the dataset object
end
```

```
%% dataset consistency determination
B2B_option = generateOpt('AddFitError',false);  % create a ...
    B2BDC.Option.Option object, no fitting error is included in this analysis
dsGRI.isConsistent(B2B_option);  % calculate the scalar consistency ...
    measure (SCM)
scm = dsGRI.ConsistencyMeasure  % check the SCM value
%% plot of the sensitivity of SCM to QOI and model parameter uncertainty ...
    bounds
dsGRI.plotConsistencySensitivity;
%% remove QOI f5 to obtain a consistent dataset
removed_unit = dsGRI.deleteUnit('f5');
%% dataset consistency calculation
dsGRI.isConsistent(B2B_option);
scm = dsGRI.ConsistencyMeasure
%% B2BDC prediction interval of model parameters
nVar = 102;
x_posterior_bounds = dsGRI.calVarBounds(1:nVar,B2B_option);  % calculates ...
    the posterior bounds
x_posterior_bounds_inner = x_posterior_bounds.InnerBound;  % the ...
    inner-bound prediction intervals
x_posterior_bounds_outer = x_posterior_bounds.OuterBound;  % the ...
    outer-bound prediction intervals
%% leave-one-out prediction
nQOI = 76;
QOI_prediction_inner = zeros(nQOI,2);
QOI_prediction_outer = zeros(nQOI,2);
for i = 1:nQOI
    dsGRI_new = dsGRI.clone;  % copy the GRI-dataset with 76 QOIs
    pred_QOI = dsGRI_new.deleteUnit(i);  % remove the prediction QOI from ...
        the dataset (leave-one-out)
    prediction_result = ...
        dsGRI.predictQOI(pred_QOI.SurrogateModel,B2B_option);  % calculate ...
        B2BDC prediction interval
    QOI_prediction_inner(i,:) = [prediction_result.min(2) ...
        prediction_result.max(1)];  % the inner-bound prediction intervals
    QOI_prediction_outer(i,:) = [prediction_result.min(1) ...
        prediction_result.max(2)];  % the outer-bound prediction intervals
end
```

Bibliography

[1] M. J. Bayarri, J. O. Berger, R. Paulo, J. Sacks, J. A. Cafeo, J. Cavendish, C.-H. Lin, and J. Tu, *A framework for validation of computer models*, Technometrics, 49 (2007), pp. 138–154.

[2] R. L. Belford and R. A. Strehlow, *Shock tube technique in chemical kinetics*, Annual Review of Physical Chemistry, 20 (1969), pp. 247–272.

[3] C. J. Bélisle, H. E. Romeijn, and R. L. Smith, *Hit-and-run algorithms for generating multivariate distributions*, Mathematics of Operations Research, 18 (1993), pp. 255–266.

[4] H. Berbee, C. Boender, A. R. Ran, C. Scheffer, R. L. Smith, and J. Telgen, *Hit-and-run algorithms for the identification of nonredundant linear inequalities*, Mathematical Programming, 37 (1987), pp. 184–207.

[5] A. Boneh and A. Golan, *Constraints' redundancy and feasible region boundedness by random feasible point generator (rfpg)*, in Third European congress on operations research (EURO III), Amsterdam, 1979.

[6] G. Box and R. D. Meyer, *Some new ideas in the analysis of screening designs*, Journal of Researct of the National Bueau of Standards, 90 (1985).

[7] G. E. Box and W. G. Hunter, *The experimental study of physical mechanisms*, Technometrics, 7 (1965), pp. 23–42.

[8] S. Boyd and L. Vandenberghe, *Convex optimization*, Cambridge university press, 2004.

[9] P. Bratley and B. L. Fox, *Algorithm 659: Implementing sobol's quasirandom sequence generator*, ACM Transactions on Mathematical Software (TOMS), 14 (1988), pp. 88–100.

[10] S. P. Brooks and A. Gelman, *General methods for monitoring convergence of iterative simulations*, Journal of Computational and Graphical Statistics, 7 (1998), pp. 434–455.

[11] J. Brynjarsdóttir and A. O'Hagan, *Learning about physical parameters: The importance of model discrepancy*, Inverse Problems, 30 (2014), p. 114007.

[12] L. Cai and H. Pitsch, *Mechanism optimization based on reaction rate rules*, Combustion and Flame, 161 (2014), pp. 405–415.

[13] G. Casella and E. I. George, *Explaining the gibbs sampler*, The American Statistician, 46 (1992), pp. 167–174.

[14] M. Chaos and F. L. Dryer, *Chemical-kinetic modeling of ignition delay: Considerations in interpreting shock tube data*, International Journal of Chemical Kinetics, 42 (2010), pp. 143–150.

[15] M.-H. Chen and B. Schmeiser, *Performance of the gibbs, hit-and-run, and metropolis samplers*, Journal of Computational and Graphical Statistics, 2 (1993), pp. 251–272.

[16] L. Chisci, A. Garulli, and G. Zappa, *Recursive state bounding by parallelotopes*, Automatica, 32 (1996), pp. 1049–1055.

[17] P. S. Craig, M. Goldstein, A. H. Seheult, and J. A. Smith, *Pressure matching for hydrocarbon reservoirs: a case study in the use of bayes linear strategies for large computer experiments*, in Case studies in Bayesian statistics, Springer, 1997, pp. 37–93.

[18] A. K. Das, K. Kumar, and C.-J. Sung, *Laminar flame speeds of moist syngas mixtures*, Combustion and Flame, 158 (2011), pp. 345–353.

[19] D. Davidson and R. Hanson, *Interpreting shock tube ignition data*, International Journal of Chemical Kinetics, 36 (2004), pp. 510–523.

[20] S. G. Davis, A. V. Joshi, H. Wang, and F. Egolfopoulos, *An optimized kinetic model of H_2/CO combustion*, Proceedings of the Combustion Institute, 30 (2005), pp. 1283–1292.

[21] D. E. Edwards, D. Y. Zubarev, A. Packard, W. A. Lester Jr, and M. Frenklach, *Interval prediction of molecular properties in parametrized quantum chemistry*, Physical Review Letters, 112 (2014), p. 253003.

[22] R. Feeley, M. Frenklach, M. Onsum, T. Russi, A. Arkin, and A. Packard, *Model discrimination using data collaboration*, The Journal of Physical Chemistry A, 110 (2006), pp. 6803–6813.

[23] R. Feeley, P. Seiler, A. Packard, and M. Frenklach, *Consistency of a reaction dataset*, The Journal of Physical Chemistry A, 108 (2004), pp. 9573–9583.

[24] R. P. Feeley, *Fighting the curse of dimensionality: A method for model validation and uncertainty propagation for complex simulation models*, University of California, Berkeley, 2008.

[25] E. Fogel and Y.-F. Huang, *On the value of information in system identification—bounded noise case*, Automatica, 18 (1982), pp. 229–238.

[26] M. Frenklach, *Modeling*, in Combustion chemistry, W. C. Gardiner, ed., Springer, 1984, pp. 423–453.

[27] M. Frenklach, *Systematic optimization of a detailed kinetic model using a methane ignition example*, Combustion and Flame, 58 (1984), pp. 69–72.

[28] M. Frenklach, *Transforming data into knowledge—process informatics for combustion chemistry*, Proceedings of the Combustion Institute, 31 (2007), pp. 125–140.

[29] M. Frenklach, *Reaction Lab*, 2017, `https://github.com/PrimeKinetics/ReactionLab`.

[30] M. Frenklach, C. Li Kwok Cheong, and E. Oran, *LDV measurements of gas flow behind reflected shocks*, Dynamics of Flames and Reactive Systems, (1985), pp. 722–735.

[31] M. Frenklach and D. Miller, *Statistically rigorous parameter estimation in dynamic modeling using approximate empirical models*, AIChE Journal, 31 (1985), pp. 498–500.

[32] M. Frenklach, A. Packard, and R. Feeley, *Optimization of reaction models with solution mapping*, Comprehensive Chemical Kinetics, 42 (2007), pp. 243–291.

[33] M. Frenklach, A. Packard, G. Garcia-Donato, R. Paulo, and J. Sacks, *Comparison of statistical and deterministic frameworks of uncertainty quantification*, SIAM/ASA Journal on Uncertainty Quantification, 4 (2016), pp. 875–901.

[34] M. Frenklach, A. Packard, and P. Seiler, *Prediction uncertainty from models and data*, in Proceedings of the 2002 American Control Conference (IEEE Cat. No. CH37301), vol. 5, IEEE, 2002, pp. 4135–4140.

[35] M. Frenklach, A. Packard, P. Seiler, and R. Feeley, *Collaborative data processing in developing predictive models of complex reaction systems*, International Journal of Chemical Kinetics, 36 (2004), pp. 57–66.

[36] M. Frenklach, H. Wang, and M. J. Rabinowitz, *Optimization and analysis of large chemical kinetic mechanisms using the solution mapping method-combustion of methane*, Progress in Energy and Combustion Science, 18 (1992), pp. 47–73.

[37] A. Garulli, A. Vicino, and G. Zappa, *Conditional central algorithms for worst case set-membership identification and filtering*, IEEE Transactions on Automatic Control, 45 (2000), pp. 14–23.

[38] A. Gelman, J. B. Carlin, H. S. Stern, D. B. Dunson, A. Vehtari, and D. B. Rubin, *Bayesian data analysis*, Chapman and Hall/CRC, 2013.

[39] A. Gelman and D. B. Rubin, *Inference from iterative simulation using multiple sequences*, Statistical Science, 7 (1992), pp. 457–472.

[40] S. Geman and D. Geman, *Stochastic relaxation, gibbs distributions, and the bayesian restoration of images*, IEEE Transactions on Pattern Analysis and Machine Intelligence, (1984), pp. 721–741.

[41] S. Gersen, H. Darmeveil, and H. Levinsky, *The effects of CO addition on the autoignition of H_2, CH_4 and CH_4/H_2 fuels at high pressure in an RCM*, Combustion and Flame, 159 (2012), pp. 3472–3475.

[42] E. G. Golstein, *Theory of convex programming*, vol. 36, American Mathematical Soc., 2008.

[43] M. Goswami, R. Bastiaans, A. A. Konnov, and L. De Goey, *Laminar burning velocity of lean H_2–CO mixtures at elevated pressure using the heat flux method*, International Journal of Hydrogen Energy, 39 (2014), pp. 1485–1498.

[44] M. Goswami, J. Van Griensven, R. Bastiaans, A. A. Konnov, and L. De Goey, *Experimental and modeling study of the effect of elevated pressure on lean high-hydrogen syngas flames*, Proceedings of the Combustion Institute, 35 (2015), pp. 655–662.

[45] K. Grogan, Q. Wang, and M. Ihme, *Modeling gas dynamic effects in shock-tubes for reaction kinetics measurements*, in 53rd AIAA Aerospace Sciences Meeting, 2015, p. 0414.

[46] K. P. Grogan and M. Ihme, *Weak and strong ignition of hydrogen/oxygen mixtures in shock-tube systems*, Proceedings of the Combustion Institute, 35 (2015), pp. 2181–2189.

[47] H. Haario, E. Saksman, and J. Tamminen, *Componentwise adaptation for high dimensional MCMC*, Computational Statistics, 20 (2005), pp. 265–273.

[48] M. Han, Y. Ai, Z. Chen, and W. Kong, *Laminar flame speeds of H_2/CO with CO_2 dilution at normal and elevated pressures and temperatures*, Fuel, 148 (2015), pp. 32–38.

[49] R. Hanson and D. Davidson, *Recent advances in laser absorption and shock tube methods for studies of combustion chemistry*, Progress in Energy and Combustion Science, 44 (2014), pp. 103–114.

[50] M. Hassan, K. Aung, and G. Faeth, *Properties of laminar premixed CO/H/air flames at various pressures*, Journal of Propulsion and Power, 13 (1997), pp. 239–245.

[51] Y. He, Z. Wang, W. Weng, Y. Zhu, J. Zhou, and K. Cen, *Effects of CO content on laminar burning velocity of typical syngas by heat flux method and kinetic modeling*, International Journal of Hydrogen Energy, 39 (2014), pp. 9534–9544.

[52] A. Hegde, W. Li, J. Oreluk, A. Packard, and M. Frenklach, *Consistency analysis for massively inconsistent datasets in bound-to-bound data collaboration*, SIAM/ASA Journal on Uncertainty Quantification, 6 (2018), pp. 429–456.

[53] D. Henrion and A. Garulli, *Positive polynomials in control*, vol. 312, Springer Science & Business Media, 2005.

[54] J. Herzler and C. Naumann, *Shock tube study of the ignition of lean CO/H_2 fuel blends at intermediate temperatures and high pressure*, Combustion Science and Technology, 180 (2008), pp. 2015–2028.

[55] D. Higdon, M. Kennedy, J. C. Cavendish, J. A. Cafeo, and R. D. Ryne, *Combining field data and computer simulations for calibration and prediction*, SIAM Journal on Scientific Computing, 26 (2004), pp. 448–466.

[56] S. Iavarone, J. Oreluk, S. T. Smith, A. Hegde, W. Li, A. Packard, M. Frenklach, P. J. Smith, F. Contino, and A. Parente, *Application of bound-to-bound data collaboration approach for development and uncertainty quantification of a reduced char combustion model*, Fuel, 232 (2018), pp. 769–779.

[57] V. R. Joseph and S. N. Melkote, *Statistical adjustments to engineering models*, Journal of Quality Technology, 41 (2009), pp. 362–375.

[58] D. M. Kalitan, J. D. Mertens, M. W. Crofton, and E. L. Petersen, *Ignition and oxidation of lean CO/H_2 fuel blends in air*, Journal of Propulsion and Power, 23 (2007), pp. 1291–1301.

[59] R. J. Kee, F. M. Rupley, and J. A. Miller, *Chemkin-II: A Fortran chemical kinetics package for the analysis of gas-phase chemical kinetics*, tech. report, Sandia National Labs., Livermore, CA (USA), 1989.

[60] M. C. Kennedy and A. O'Hagan, *Bayesian calibration of computer models*, Journal of the Royal Statistical Society: Series B (Statistical Methodology), 63 (2001), pp. 425–464.

[61] A. Kéromnès, W. K. Metcalfe, K. A. Heufer, N. Donohoe, A. K. Das, C.-J. Sung, J. Herzler, C. Naumann, P. Griebel, and O. Mathieu, *An experimental and detailed chemical kinetic modeling study of hydrogen and syngas mixture oxidation at elevated pressures*, Combustion and Flame, 160 (2013), pp. 995–1011.

[62] J. Kiefer and J. Wolfowitz, *Optimum designs in regression problems*, The Annals of Mathematical Statistics, 30 (1959), pp. 271–294.

[63] W. Kleiber, S. R. Sain, M. J. Heaton, M. Wiltberger, C. S. Reese, and D. Bingham, *Parameter tuning for a multi-fidelity dynamical model of the magnetosphere*, The Annals of Applied Statistics, 7 (2013), pp. 1286–1310.

[64] R. Kohavi, *A study of cross-validation and bootstrap for accuracy estimation and model selection*, in Ijcai, vol. 14, Montreal, Canada, 1995, pp. 1137–1145.

[65] M. C. Krejci, O. Mathieu, A. J. Vissotski, S. Ravi, T. G. Sikes, E. L. Petersen, A. Kérmonès, W. Metcalfe, and H. J. Curran, *Laminar flame speed and ignition delay time data for the kinetic modeling of hydrogen and syngas fuel blends*, Journal of Engineering for Gas Turbines and Power, 135 (2013), p. 021503.

[66] D. Lapalme and P. Seers, *Influence of CO_2, CH_4, and initial temperature on H_2/CO laminar flame speed*, International Journal of Hydrogen Energy, 39 (2014), pp. 3477–3486.

[67] H. Li, Z. Owens, D. Davidson, and R. Hanson, *A simple reactive gasdynamic model for the computation of gas temperature and species concentrations behind reflected shock waves*, International Journal of Chemical Kinetics, 40 (2008), pp. 189–198.

[68] H.-M. Li, G.-X. Li, Z.-Y. Sun, Z.-H. Zhou, Y. Li, and Y. Yuan, *Effect of dilution on laminar burning characteristics of $H_2/CO/CO_2$/air premixed flames with various hydrogen fractions*, Experimental Thermal and Fluid Science, 74 (2016), pp. 160–168.

[69] J. Li, Z. Zhao, A. Kazakov, M. Chaos, F. L. Dryer, and J. J. Scire Jr, *A comprehensive kinetic mechanism for CO, CH_2O, and CH_3OH combustion*, International Journal of Chemical Kinetics, 39 (2007), pp. 109–136.

[70] X. Li, X. You, F. Wu, and C. K. Law, *Uncertainty analysis of the kinetic model prediction for high-pressure H_2/CO combustion*, Proceedings of the Combustion Institute, 35 (2015), pp. 617–624.

[71] L. Lovász, *Hit-and-run mixes fast*, Mathematical Programming, 86 (1999), pp. 443–461.

[72] L. Lovász and S. Vempala, *Hit-and-run from a corner*, SIAM Journal on Computing, 35 (2006), pp. 985–1005.

[73] A. B. Mansfield and M. S. Wooldridge, *High-pressure low-temperature ignition behavior of syngas mixtures*, Combustion and Flame, 161 (2014), pp. 2242–2251.

[74] F. J. Massey Jr, *The kolmogorov-smirnov test for goodness of fit*, Journal of the American statistical Association, 46 (1951), pp. 68–78.

[75] O. Mathieu, M. Kopp, and E. Petersen, *Shock-tube study of the ignition of multi-component syngas mixtures with and without ammonia impurities*, Proceedings of the Combustion Institute, 34 (2013), pp. 3211–3218.

[76] M. D. McKay, R. J. Beckman, and W. J. Conover, *Comparison of three methods for selecting values of input variables in the analysis of output from a computer code*, Technometrics, 21 (1979), pp. 239–245.

[77] I. C. McLean, D. B. Smith, and S. C. Taylor, *The use of carbon monoxide/hydrogen burning velocities to examine the rate of the CO+OH reaction*, in Symposium (International) on Combustion, vol. 25, Elsevier, 1994, pp. 749–757.

[78] J. D. Mertens, D. M. Kalitan, A. B. Barrett, and E. L. Petersen, *Determination of the rate of $H+O_2+M \rightarrow HO_2+M$ ($M= N_2$, Ar, H_2O) from ignition of syngas at practical conditions*, Proceedings of the Combustion Institute, 32 (2009), pp. 295–303.

[79] J. Meyer and A. Oppenheim, *On the shock-induced ignition of explosive gases*, in Symposium (International) on Combustion, vol. 13, Elsevier, 1971, pp. 1153–1164.

[80] M. Milanese and A. Vicino, *Optimal estimation theory for dynamic systems with set membership uncertainty: an overview*, Automatica, 27 (1991), pp. 997–1009.

[81] D. Miller and M. Frenklach, *Sensitivity analysis and parameter estimation in dynamic modeling of chemical kinetics*, International Journal of Chemical Kinetics, 15 (1983), pp. 677–696.

[82] G. Mittal, C.-J. Sung, and R. A. Yetter, *Autoignition of H_2/CO at elevated pressures in a rapid compression machine*, International Journal of Chemical Kinetics, 38 (2006), pp. 516–529.

[83] R. Myers, D. Montgomery, and C. Anderson-Cook, *Response Surface Methodology: Process and Product Optimization Using Designed Experiments*, Wiley Series in Probability and Statistics, Wiley, 2009.

[84] R. Myers, D. Montgomery, and C. Anderson-Cook, *Response Surface Methodology: process and Product Optimization Using Designed Experiments*, Wiley Series in Probability and Statistics, Wiley, 2016.

[85] J. Natarajan, Y. Kochar, T. Lieuwen, and J. Seitzman, *Pressure and preheat dependence of laminar flame speeds of $H_2/CO/CO_2/O_2/He$ mixtures*, Proceedings of the Combustion Institute, 32 (2009), pp. 1261–1268.

[86] J. Natarajan, T. Lieuwen, and J. Seitzman, *Laminar flame speeds of H_2/CO mixtures: effect of CO_2 dilution, preheat temperature, and pressure*, Combustion and Flame, 151 (2007), pp. 104–119.

[87] E. Ninnemann, B. Koroglu, O. Pryor, S. Barak, L. Nash, Z. Loparo, J. Sosa, K. Ahmed, and S. Vasu, *New insights into the shock tube ignition of H_2/O_2 at low to moderate temperatures using high-speed end-wall imaging*, Combustion and Flame, 187 (2018), pp. 11–21.

[88] W. L. Oberkampf and C. J. Roy, *Verification and validation in scientific computing*, Cambridge University Press, 2010.

[89] A. O'Hagan and M. West, *The Oxford handbook of applied Bayesian analysis*, Oxford University Press, 2010.

[90] S. Park, E. Serpedin, and K. Qaraqe, *Gaussian assumption: The least favorable but the most useful [lecture notes]*, IEEE Signal Processing Magazine, 30 (2013), pp. 183–186.

[91] P. A. Parrilo, *Semidefinite programming relaxations for semialgebraic problems*, Mathematical Programming, 96 (2003), pp. 293–320.

[92] J. Pedel, J. N. Thornock, and P. J. Smith, *Ignition of co-axial turbulent diffusion oxy-coal jet flames: Experiments and simulations collaboration*, Combustion and Flame, 160 (2013), pp. 1112–1128.

[93] W. Peschke and L. J. Spadaccini, *Determination of autoignition and flame speed characteristics of coal gases having medium heating values*, The Institute, 1985.

[94] E. L. Petersen and R. K. Hanson, *Nonideal effects behind reflected shock waves in a high-pressure shock tube*, Shock Waves, 10 (2001), pp. 405–420.

[95] E. L. Petersen, D. M. Kalitan, A. B. Barrett, S. C. Reehal, J. D. Mertens, D. J. Beerer, R. L. Hack, and V. G. McDonell, *New syngas/air ignition data at lower temperature and elevated pressure and comparison to current kinetics models*, Combustion and Flame, 149 (2007), pp. 244–247.

[96] M. Plumlee, *Bayesian calibration of inexact computer models*, Journal of the American Statistical Association, 112 (2017), pp. 1274–1285.

[97] P. Z. Qian and C. J. Wu, *Bayesian hierarchical modeling for integrating low-accuracy and high-accuracy experiments*, Technometrics, 50 (2008), pp. 192–204.

[98] Z. Qin, V. V. Lissianski, H. Yang, W. C. Gardiner, S. G. Davis, and H. Wang, *Combustion chemistry of propane: a case study of detailed reaction mechanism optimization*, Proceedings of the Combustion Institute, 28 (2000), pp. 1663–1669.

[99] T. Russi, A. Packard, R. Feeley, and M. Frenklach, *Sensitivity analysis of uncertainty in model prediction*, The Journal of Physical Chemistry A, 112 (2008), pp. 2579–2588.

[100] T. Russi, A. Packard, and M. Frenklach, *Uncertainty quantification: Making predictions of complex reaction systems reliable*, Chemical Physics Letters, 499 (2010), pp. 1–8.

[101] T. M. Russi, *Uncertainty quantification with experimental data and complex system models*, PhD thesis, UC Berkeley, 2010.

[102] J. Sacks, W. J. Welch, T. J. Mitchell, and H. P. Wynn, *Design and analysis of computer experiments*, Statistical Science, (1989), pp. 409–423.

[103] A. Saltelli, S. Tarantola, F. Campolongo, and M. Ratto, *Sensitivity Analysis in Practice: A Guide to Assessing Scientific Models*, Halsted Press, New York, NY, USA, 2004.

[104] P. Saxena and F. A. Williams, *Testing a small detailed chemical-kinetic mechanism for the combustion of hydrogen and carbon monoxide*, Combustion and Flame, 145 (2006), pp. 316–323.

[105] F. Schweppe, *Recursive state estimation: unknown but bounded errors and system inputs*, IEEE Transactions on Automatic Control, 13 (1968), pp. 22–28.

[106] P. Seiler, M. Frenklach, A. Packard, and R. Feeley, *Numerical approaches for collaborative data processing*, Optimization and Engineering, 7 (2006), pp. 459–478.

[107] A. Shapiro, *Directional differentiability of the optimal value function in convex semi-infinite programming*, Mathematical Programming, 70 (1995), pp. 149–157.

[108] D. A. Sheen and H. Wang, *Combustion kinetic modeling using multispecies time histories in shock–tube oxidation of heptane*, Combustion and Flame, 158 (2011), pp. 645–656.

[109] D. A. Sheen, X. You, H. Wang, and T. Løvås, *Spectral uncertainty quantification, propagation and optimization of a detailed kinetic model for ethylene combustion*, Proceedings of the Combustion Institute, 32 (2009), pp. 535–542.

[110] N. A. Slavinskaya, M. Abbasi, J. H. Starcke, R. Whitside, A. Mirzayeva, U. Riedel, W. Li, J. Oreluk, A. Hegde, A. Packard, M. Frenklach, G. Gerasimov, and O. Shatalov, *Development of an UQ-predictive chemical*

reaction model for syngas combustion, Energy & Fuels, 31 (2017), pp. 2274–2297, https://doi.org/10.1021/acs.energyfuels.6b02319.

[111] N. A. Slavinskaya, U. Riedel, S. B. Dworkin, and M. J. Thomson, *Detailed numerical modeling of pah formation and growth in non-premixed ethylene and ethane flames*, Combustion and Flame, 159 (2012), pp. 979–995.

[112] G. P. Smith, M. Frenklach, R. Feeley, A. Packard, and P. Seiler, *A system analysis approach for atmospheric observations and models: Mesospheric hox dilemma*, Journal of Geophysical Research: Atmospheres, 111 (2006).

[113] G. P. Smith, D. M. Golden, M. Frenklach, N. W. Moriarty, B. Eiteneer, M. Goldenberg, C. T. Bowman, R. K. Hanson, S. Song, J. W. C. Gardiner, V. V. Lissianski, and Z. Qin, *GRI-Mech 3.0*. http://combustion.berkeley.edu/gri_mech/.

[114] R. L. Smith, *Monte carlo procedures for generating random feasible solutions to mathematical programs*, in A Bulletin of the ORSA/TIMS Joint National Meeting, Washington, DC, vol. 101, 1980.

[115] R. L. Smith, *Efficient monte carlo procedures for generating points uniformly distributed over bounded regions*, Operations Research, 32 (1984), pp. 1296–1308.

[116] A. Starik, N. Titova, A. Sharipov, and V. Kozlov, *Syngas oxidation mechanism*, Combustion, Explosion, and Shock Waves, 46 (2010), pp. 491–506.

[117] P. B. Stark, *Constraints versus priors*, SIAM/ASA Journal of Uncertainty Quantification, 3 (2015), pp. 586–598.

[118] M. L. Stein, *Interpolation of spatial data: some theory for kriging*, Springer Science & Business Media, 2012.

[119] P. Stoica and P. Babu, *The gaussian data assumption leads to the largest cramér-rao bound [lecture notes]*, IEEE Signal Processing Magazine, 28 (2011), pp. 132–133.

[120] M. Stone, *Cross-validatory choice and assessment of statistical predictions*, Journal of the Royal Statistical Society: Series B (Methodological), 36 (1974), pp. 111–133.

[121] C. B. Storlie, W. A. Lane, E. M. Ryan, J. R. Gattiker, and D. M. Higdon, *Calibration of computational models with categorical parameters and correlated outputs via bayesian smoothing spline ANOVA*, Journal of the American Statistical Association, 110 (2015), pp. 68–82.

[122] J. F. Sturm, *Using SeDuMi 1.02, a MATLAB toolbox for optimization over symmetric cones*, Optimization Methods and Software, 11 (1999), pp. 625–653.

[123] H. Sun, S. Yang, G. Jomaas, and C. K. Law, *High-pressure laminar flame speeds and kinetic modeling of carbon monoxide/hydrogen combustion*, Proceedings of the Combustion Institute, 31 (2007), pp. 439–446.

[124] S. Sun, S. Meng, Y. Zhao, H. Xu, Y. Guo, and Y. Qin, *Experimental and theoretical studies of laminar flame speed of CO/H_2 in O_2/H_2O atmosphere*, International Journal of Hydrogen Energy, 41 (2016), pp. 3272–3283.

[125] L. D. Thi, Y. Zhang, and Z. Huang, *Shock tube study on ignition delay of multi-component syngas mixtures–effect of equivalence ratio*, International Journal of Hydrogen Energy, 39 (2014), pp. 6034–6043.

[126] T. Varga, C. Olm, T. Nagy, I. G. Zsély, É. Valkó, R. Pálvölgyi, H. J. Curran, and T. Turányi, *Development of a joint hydrogen and syngas combustion mechanism based on an optimization approach*, International Journal of Chemical Kinetics, 48 (2016), pp. 407–422.

[127] S. S. Vasu, D. F. Davidson, and R. K. Hanson, *Shock tube study of syngas ignition in rich CO_2 mixtures and determination of the rate of $H+O_2+CO_2 \rightarrow HO_2+CO_2$*, Energy & Fuels, 25 (2011), pp. 990–997.

[128] E. Walter and H. Piet-Lahanier, *Estimation of parameter bounds from bounded-error data: a survey*, Mathematics and Computers in Simulation, 32 (1990), pp. 449–468.

[129] S. Wang, W. Chen, and K.-L. Tsui, *Bayesian validation of computer models*, Technometrics, 51 (2009), pp. 439–451.

[130] Z. Wang, W. Weng, Y. He, Z. Li, and K. Cen, *Effect of H_2/CO ratio and N_2/CO_2 dilution rate on laminar burning velocity of syngas investigated by direct measurement and simulation*, Fuel, 141 (2015), pp. 285–292.

[131] W. Weng, Z. Wang, Y. He, R. Whiddon, Y. Zhou, Z. Li, and K. Cen, *Effect of N_2/CO_2 dilution on laminar burning velocity of H_2–CO–O_2 oxy-fuel premixed flame*, International Journal of Hydrogen Energy, 40 (2015), pp. 1203–1211.

[132] F. A. Williams, *Detailed and reduced chemistry for hydrogen autoignition*, Journal of Loss Prevention in the Process Industries, 21 (2008), pp. 131–135.

[133] Y. Xie, J. Wang, N. Xu, S. Yu, and Z. Huang, *Comparative study on the effect of CO_2 and H_2O dilution on laminar burning characteristics of CO/H_2/air mixtures*, International Journal of Hydrogen Energy, 39 (2014), pp. 3450–3458.

[134] Y. Xie, J. Wang, N. Xu, S. Yu, M. Zhang, and Z. Huang, *Thermal and chemical effects of water addition on laminar burning velocity of syngas*, Energy & Fuels, 28 (2014), pp. 3391–3398.

[135] X. You, A. Packard, and M. Frenklach, *Process informatics tools for predictive modeling: Hydrogen combustion*, International Journal of Chemical Kinetics, 44 (2012), pp. 101–116.

[136] X. You, T. Russi, A. Packard, and M. Frenklach, *Optimization of combustion kinetic models on a feasible set*, Proceedings of the Combustion Institute, 33 (2011), pp. 509–516.

[137] Z. B. Zabinsky, R. L. Smith, J. F. McDonald, H. E. Romeijn, and D. E. Kaufman, *Improving hit-and-run for global optimization*, Journal of Global Optimization, 3 (1993), pp. 171–192.

[138] Y. Zhang, W. Shen, M. Fan, H. Zhang, and S. Li, *Laminar flame speed studies of lean premixed H_2/CO/air flames*, Combustion and Flame, 161 (2014), pp. 2492–2495.